Thermal evolution of neutron stars
by Letao Qin

A thesis submitted in partial fulfillment of the requirements for the degree of Doctor of Philosophy in Physics
Montana State University

Abstract:
The neutron star thermal calculation is to simulate how temperatures of neutron stars will evolve with time. The ultrahigh density of neutron stars (1015g cm~3) is a physical condition that cannot be realized in a laboratory so far, and that implies serious theoretical difficulties. Our work on neutron star thermal evolution is to calculate the cooling history of the star and to eliminate some theoretical uncertainties by comparing with the observational data. Among them, the thermal effects of strong magnetic fields, crust breaking, axion emission and neutrino magnetic dipole moment are the four projects we have worked on.

The results we obtained are encouraging for all four cases. We found that a magnetic neutron star will maintain a relatively high temperature for a period longer than a non-magnetic star. In the case of crust breaking, our calculations show that for an ideal lattice, the heating due to crust breaking is significant, while for an imperfect lattice, it is not. By including axion emission and effects of neutrino magnetic dipole moment into the neutron star cooling calculations and by comparing with the observational data, we are able to obtain limits on some theoretical parameters, i.e. the mass of axions and neutrino magnetic dipole moment.

Also we developed a new way to connect theoretical calculations and observational data through light curves. Theoretical constructions of light curves and comparison with observational data enable us to determine the configurations of magnetic fields and the mechanisms of the emission near the surface of neutron stars.

THERMAL EVOLUTION OF NEUTRON STARS

by

Letao Qin

A thesis submitted in partial fulfillment

of the requirements for the degree

of

Doctor of Philosophy

in

Physics

MONTANA STATE UNIVERSITY

Bozeman, Montana

December 1995

APPROVAL

of a thesis submitted by

Letao Qin

This thesis has been read by each member of the thesis committee and has been found to be satisfactory regarding content, English usage, format, citations, bibliographic style, and consistency, and is ready for submission to the College of Graduate Studies.

12/1/95

Date — Chairperson, Graduate Committee

Approved for the Major Department

12-1-95

Date — Head, Major Department

Approved for the College of Graduate Studies

12/20/95

Date — Graduate Dean

STATEMENT OF PERMISSION TO USE

In presenting this thesis in partial fulfillment of the requirements for a doctoral degree at Montana State University, I agree that the Library shall make it available to borrowers under rules of the Library. I further agree that copying of this thesis is allowable only for scholarly purposes, consistent with "fair use" as prescribed in the U.S. Copyright Law. Requests for extensive copying or reproduction of this thesis should be referred to University Microfilms International, 300 North Zeeb Road, Ann Arbor, Michigan 48106, to whom I have granted "the exclusive right to reproduce and distribute my dissertation in and from microform, along with the non-exclusive right to reproduce and distribute my abstract in any format in whole or in part."

Signature

Date Dec. 3, 1995.

ACKNOWLEDGMENTS

The author wants to thank Dr. Tsuruta for the guidance she has provided during the course of this research; Dr. Tsuruta and Dr. Link for their careful review of this thesis and valuable suggestions, and the members of my commitee (Dr. Tsuruta, Dr. Lindblom, Dr. Link, Dr. Hermanson & Dr. Cone) for their support.

Thanks are also due to the physics department. Without the precious opportunity it offered to me and its excellent research environment, the work here would not have been possible.

TABLE OF CONTENTS

TABLE OF CONTENTS — Continued

TABLE OF CONTENTS — Continued

LIST OF TABLES

LIST OF FIGURES

LIST OF FIGURES — Continued

LIST OF FIGURES — Continued

LIST OF FIGURES — Continued

LIST OF FIGURES — Continued

ABSTRACT

The neutron star thermal calculation is to simulate how temperatures of neutron stars will evolve with time. The ultrahigh density of neutron stars ($10^{15} g\ cm^{-3}$) is a physical condition that cannot be realized in a laboratory so far, and that implies serious theoretical difficulties. Our work on neutron star thermal evolution is to calculate the cooling history of the star and to eliminate some theoretical uncertainties by comparing with the observational data. Among them, the thermal effects of strong magnetic fields, crust breaking, axion emission and neutrino magnetic dipole moment are the four projects we have worked on.

The results we obtained are encouraging for all four cases. We found that a magnetic neutron star will maintain a relatively high temperature for a period longer than a non-magnetic star. In the case of crust breaking, our calculations show that for an ideal lattice, the heating due to crust breaking is significant, while for an imperfect lattice, it is not. By including axion emission and effects of neutrino magnetic dipole moment into the neutron star cooling calculations and by comparing with the observational data, we are able to obtain limits on some theoretical parameters, i.e. the mass of axions and neutrino magnetic dipole moment.

Also we developed a new way to connect theoretical calculations and observational data through light curves. Theoretical constructions of light curves and comparison with observational data enable us to determine the configurations of magnetic fields and the mechanisms of the emission near the surface of neutron stars.

Chapter 1

Introduction

The possible existence of neutron stars was first proposed by Walte Baade and Fritz Zwicky in 1934 (1934). A little more than 30 years later, radio pulsars were discovered in Cambridge by Anthony Hewlish and Jocelyn Bell (1968). Because of the peculiar property of neutron stars, ultrahigh density ($10^{15} g\ cm^{-3}$), theoretical uncertainties, such as the equation of state of matters with density higher than nucleon density, the effect of magnetic fields, the presence of exotic particles, e.g. axion, pion, kaon, etc, are overwhelming. Fortunately modern X-ray satellites have been able to observe X-ray pulsars, and to some degree, the observational data helps us eliminate the theoretical uncertainties.

My PhD research projects are neutron star thermal evolution calculations. In Chapter 1, I will give a brief introduction to the study of neutron stars. In Chapters 2 and 3, I will present our simulations of the thermal evolution of magnetized neutron stars. In Chapter 4 and Chapter 5, I will introduce several examples of how particle and solid state theories are tested in the neutron star laboratory, mainly three projects we worked on: starquakes, neutrino magnetic dipole moment and axion emissions. In Chapters 2 through 5, the validity and uncertainty of theoretical predictions are discussed by comparing with observational data. In Chapter 6, I will describe the current status of X-ray observations of pulsars and demonstrate how theoretical light curve calculations are able to determine the observational parameters.

In this chapter, section §1.1 summarize the discovery of neutron stars. Section §1.2 describes neutron star interior. In section §1.3, we discuss neutron star magnetic fields and the possible existence of superfluid in the interior.

1.1 Discovery of Pulsars

At the beginning of this century, it gradually became clear to physicists that the Sun is powered by nuclear reactions. One of the basic nuclear reactions inside a star is $4H \longrightarrow He + \gamma + \nu$. Once the mechanism by which stars shine was understood, the question that naturally followed was: what would happen to the stars when their main fuel, hydrogen, was exhausted? One possibility is that the star becomes a white dwarf. The first white dwarf, Sirius B, was discovered by W.S. Adams in 1914 (1915). Sirius B has very high density. Its mass is about 1 solar mass, its radius is only about 20,000 km, 10^{-2} of the radius of the sun ($R_{\odot} = 7 \times 10^5$km). The average density of white dwarfs is $10^7 gcm^{-3}$. In ordinary stars, the pressure resulting from collisions maintains hydrostatic equilibrium. In white dwarfs, the density is so high that the pressure required to balance gravity is tremendous, impossible to be explained by ideal gas law.

In 1926, Fowler solved this puzzle by applying Fermi-Dirac statistics to the electrons inside neutron stars. Because electrons are fermions, their distribution satisfies the Fermi-Dirac function. When the number density n is large, the electrons will be forced to populate high energy levels. These electrons at high energy levels have large velocities, and the pressure provided by such electrons provides the major part of the pressure required to balance gravity.

In 1932, Chadwick discovered neutrons. Neutrons are fermions, have spin $\frac{1}{2}$ and no charge. In 1932, after he learned about the discovery of neutrons, Landau (1932) applied Fermi-Dirac statistics to "neutron stars", stars supposed to consist primarily of neutrons, and obtain a mass limit for neutron stars. In 1934, Walter Baade and Fritz Zwicky proposed the idea that neutron stars would be the end point of stellar evolution. In their paper, they wrote:

with all reserve we advance the view that a supernovae represents the transition of an ordinary star into a neutron star, consisting mainly of neutrons. Such a star may possess a very small radius and an extremely high density.

It seemed impossible to confirm such a claim at that time. Only some 30 years later, when neutron stars astoundingly presented themselves as radio pulsars, the idea of neutron stars began to be accepted by astrophysicists.

Nevertheless during those years, some pioneer theoretical calculations on neutron stars were carried out. Oppenheimer and Volkoff (1939) first calculated the structure of neutron stars. Their calculations showed that a neutron star could have a central density as high as 10^{15}gcm^{-3} when the mass of the neutron star is about 0.7 solar mass. Following that, Harrison, Wakano and Wheeler (1958), Cameron (1959a), Ambartsumyan and Saakyan (1960), and Hamada and Salpeter (1961) discussed in detail the equation of state and neutron star models. Tsuruta (1964) first carried out thermal evolution calculations of neutron stars. A neutron star is a product of supernova explosion. When it is born, its temperature is very high, above 1 MeV. Afterwards, it is cooled by neutrino emission and photon emission. In her thesis, Tsuruta calculated how the surface temperatures of neutron stars would evolve with time.

In 1967, Hewlish, a radio astronomer, and his student Bell at Cambridge discovered an extremely regular pulse series. The period of the signal was about 1.377 seconds. In their paper (1968), they pointed out that the radio signal must be from outside the solar system and that the rapidity of the pulsation showed that the source must be very small, probably a condensed star, presumably either a white dwarf or a neutron star. The identity of radio pulsars as neutron stars was soon established by Gold (1968).

When the cause of pulsating is mechanical, the fundamental physical quantities describing such a system would be the total mass M and density ρ of this system. The characteristic dynamical time τ should be:

$$\tau \propto (G\rho)^{-2} \tag{1.1}$$

If τ is ~ 0.1 second, ρ would be $\sim 10^{12} gcm^{-3}$. This density is much higher than the densities of all known objects at that time. The average density of a white dwarf is only $10^{7} gcm^{-3}$, far smaller than $10^{12} gcm^{-3}$, while an ordinary star has $\rho \sim 1 gcm^{-3}$.

But according to the calculations of Oppenheimer and Volkoff, neutron stars could have densities as high as $10^{15} gcm^{-3}$.

If the pulsar is a neutron star, how are the radio signals produced? Gold (1968) suggested that the radio signals from a neutron star are caused by the magnetic fields around the star. When a neutron star is rotating, carrying a strong dipolar magnetic field with it, it acts as a very energetic electric generator, and provides a source of energy for radiation. The radiation from a rotating dipole is

$$\frac{dE}{dt} = \frac{2}{3c^3} \mid \frac{d^2\overrightarrow{m}}{dt^2} \mid^2, \tag{1.2}$$

where $\overrightarrow{m}$ is the magnetic dipole moment. For a rotating dipolar field, $\mid \overrightarrow{m} \mid = B_p R^3/2$, $d\overrightarrow{m}/dt$ is

$$\frac{d\overrightarrow{m}}{dt} = \vec{m} \times \vec{\Omega} \sim \frac{B_P R^3}{2} \Omega \sin\alpha, \tag{1.3}$$

with $\vec{\Omega}$ as the angular velocity, α the angle between $\vec{m}$ and $\vec{\Omega}$, and

$$\frac{d^2\overrightarrow{m}}{dt^2} = \frac{B_P R^3}{2} \Omega^2 \sin^2\alpha. \tag{1.4}$$

So

$$\frac{dE}{dt} = \frac{B_P^2 R^6 \Omega^4}{6c^3} \sin^4\alpha. \tag{1.5}$$

Since the energy is being lost, Gold predicted that the rotation period of the neutron star will increase and the rate of increase would be:

$$\frac{d(\frac{1}{2} I \Omega^2)}{dt} = -\dot{E}, \tag{1.6}$$

so that,

$$I\Omega\dot{\Omega} = -\dot{E}, \tag{1.7}$$

$$\dot{\Omega} = -\frac{\dot{E}}{I\Omega} = -\frac{B_P^2 R^6 \Omega^3}{6c^3 I}\sin^4\alpha. \tag{1.8}$$

In 1975, when the Crab Pulsar was discovered, a slow increase of the period was detected. At that time, the period of the Crab Pulsar was 33ms, and the rate of increase of the period was $dP/dt = 1.2589 \times 10^{-15}$. If we assume this increase of the period is due to the radiation of the magnetic dipole, then B_p should be about $5 \times 10^{12}G$. Thus, the increase of the period of the Crab pulsar suggests the presence of strong magnetic fields associated with neutron stars. Further evidence, the emission line from HerX-1, will be discussed in §1.3.

With their ultrahigh densities, neutron stars have been attracting attentions of physicists. Neutron stars have become a testing ground for nuclear, particle and solid state theories. Different theories can be incorporated into the thermal calculation of neutron stars, and compared with the observational data in order to be tested.

By now neutron stars are not only being observed through radio telescopes, but also in X-rays and Gamma-rays. Even before the discovery of radio pulsars, a rocket-borne X-ray experiment on board observed Sco X-1, a powerful X-ray source. This X-ray source is now known to be a binary star system. One member of this binary system is a neutron star, and X-rays come from the accretion of materials from an ordinary star onto the neutron star. Later with X-ray satellites, such as UHURU, Einstein and ROSAT, more and more pulsars are studied in the X-ray range. The surface temperatures of these pulsars then can be deduced from the flux intensity and spectrum of the soft X-rays from the surfaces of neutron stars, and comparisons between the observational data and theoretical thermal calculations can be made.

Such comparisons are necessary in order to make judgement on several alternative theories.

1.2 Structure of Neutron Stars

1.2.1 Basic Equations

The mass of a neutron star is usually around 1 solar mass, and the radius of a neutron star is about 10 km, about 10 times the Shwarzchild radius. Hence general relativistic effects are relevant in determining the star's structure.

The hydrostatic equations governing the structure of neutron stars are called the Oppenheimer-Volkoff equations. They can be expressed as the following:

$$\frac{dm}{dr} = 4\pi r^2 \rho, \tag{1.9}$$

$$\frac{dP}{dr} = -\frac{\rho m}{r^2}(1+\frac{P}{\rho})(1+\frac{4\pi P r^3}{m})(1-\frac{2m}{r})^{-1}, \tag{1.10}$$

$$\frac{d\Phi}{dr} = -\frac{1}{\rho}\frac{dP}{dr}(1+\frac{P}{\rho})^{-1}, \tag{1.11}$$

where r is the local radial distance from the stellar center, m(r) the mass inside radius r, $\rho(r)$ the density, $P(r)$ the pressure, $\Phi(r)$ the gravity potential. There are three equations and four variables. If the above set of equations is supplied with the equation of state, $P = P(\rho)$, and the boundary conditions given at the center $r = 0$ as $M(0) = 0$ and $\rho(0) = \rho_c$, integration from the center toward the boundary yields a density profile. The radius of the neutron star is defined to be at $r = R_0$ where $P(R_0) = 0$.

Unfortunately, the equation of state of matters above nuclear density is poorly understood. Below the nuclear density, we believe that we have fairly good understanding of the equation of state through solid state physics.

1.2.2 Equation of State

Several models, mainly phenomenological, exist, giving quite different equations of state.

Below Nuclear Density

Below the nuclear density, the pressure can be expressed as $P = P_{ion} + P_e + P_n$, the sum of the pressures from ions, free neutrons and free electrons. When they are treated as a perfect gas, the pressures from the electrons and neutrons P_e and P_n can be calculated from the following basic equation:

$$P = \frac{1}{3}\int pvn(p)d^3p, \tag{1.12}$$

with $n(p)$ as particle number density and $v = \frac{p}{m}/[1+(p/mc)^2]^{1/2}$ relativistically, or $v = p/m$ nonrelativistically.

If the electrons are degenerate, the number density as a function of momentum can be expressed as :

$$n(p)d^3p = \frac{2}{h^3}\frac{4\pi p^2 dp}{\exp(\frac{E-\mu}{kT})+1}, \tag{1.13}$$

or for a complete degeneracy,

$$n(p)d^3p = \begin{cases} \frac{2}{h^3}4\pi p^2 dp & p < p_F \\ 0 & p > p_F, \end{cases} \tag{1.14}$$

where μ is the chemical potential, which is a known function of ρ and T, and p_F is Fermi momentum. The energy E can be expressed as $p^2/2m$ non-relativistically or $\sqrt{p^2c^2 + m^2c^4}$ relativistically.

In the relativistically and degenerate regime:

$$\begin{aligned} P &= \frac{1}{3}\int_0^{p_F} \frac{\frac{p^2}{m}}{[1+(\frac{p}{mc})^2]^{1/2}} \frac{2}{h^3} 4\pi p^2 dp \\ &= \frac{8\pi}{3mh^3}\int_0^{p_F} \frac{p^4 dp}{[1+(\frac{p}{mc})^2]^{1/2}}, \end{aligned} \tag{1.15}$$

In the non-relativistically and degenerate regime, $v = p/m$, and the pressure is

$$\begin{aligned} P &= \frac{1}{3}\int_0^{p_F} \frac{p^2}{m}\frac{2}{h^3} 4\pi p^2 dp \\ &= \frac{8\pi}{3mh^3}\int_0^{p_F} p^4 dp \\ &= \frac{8\pi}{15mh^3} p_F^5. \end{aligned} \tag{1.16}$$

In the non-relativistic and partially degenerate regime, the pressure can be expressed as:

$$\begin{aligned} P &= \frac{1}{3}\int_0^{\infty} p\frac{p}{m}\frac{8\pi p^2 dp}{h^3(\exp(\frac{E-\mu}{kT})+1)} \\ &= \frac{8\pi}{3mh^3}\int_0^{\infty} \frac{p^4 dp}{\exp(\frac{E-\mu}{kT})+1}. \end{aligned} \tag{1.17}$$

Note that the criterion used to judge whether the particles are relativistic or non-relativistic is (Clayton 1968)

$$\xi_r = (\frac{\rho}{7.3 \times 10^6 gm/cm^3})\mu_e. \tag{1.18}$$

If ξ_r is $\gg 1$, it is relativistic. If ξ_r is $\ll 1$, it is non-relativistic. The criterion for degeneracy is

$$\xi_d = (\frac{\rho}{2.4 \times 10^{-8}})\mu_e T^{3/2}. \tag{1.19}$$

If ξ_d is $\gg 1$ ($\ll 1$), it is degenerate (non-degenerate). For T is $< 10^9 K$, as is the case during most of the life time of a neutron star, the criterion for the relativistic case is more strict than the criterion for degeneracy. Therefore in the extremely relativistic regions, the matter is also degenerate, and in the regions where it is partially degenerate, it is non-relativistic.

The above expressions are derived under the assumption that particles inside neutron stars are perfect gases. However, free electrons experience Coulomb forces, while free neutrons and protons experience nuclear forces. These forces affect the pressure. To calculate the corrections to the pressure caused by the interactions between the particles, we start with the basic thermodynamic equation (Shapiro & Teukolsky 1983):

$$P = P_{perfect} + n^2 \frac{\partial}{\partial n}(\varepsilon). \tag{1.20}$$

Here $P_{perfect}$ is the pressure of an ideal gas, n is the particle number density, ε is the energy of the interactions per particle. ε can be expressed as $\varepsilon = \varepsilon_c + \varepsilon_n$, with ε_c as the energy due to Coulomb interaction and ε_n as the energy due to nuclear interaction. For the Coulomb interaction, ε_c can be expressed as:

$$\varepsilon_c = \varepsilon_{e-e} + \varepsilon_{e-i}, \tag{1.21}$$

where ε_{e-e} is the potential energy due to Coulomb interactions between electrons and ε_{e-i} is the potential energy due to Coulomb interactions between electrons and ions.

Suppose that the gas is divided into neutral spheres of radius r_0 about each nucleus, which contains Z electrons nearby. Then ε_{e-e} and ε_{e-i} can be calculated by

$$\begin{aligned} \varepsilon_{e-e} &= \frac{1}{Z}\int_0^{r_0} \frac{qdq}{r} \\ &= \frac{3}{5}\frac{Ze^2}{r_0}, \end{aligned} \tag{1.22}$$

with $q = Ze\frac{r^3}{r_0^3}$, and

$$\begin{aligned} \varepsilon_{e-i} &= -\frac{1}{Z}\int_0^{r_0} \frac{Ze}{r}dq \\ &= -\frac{3}{2}\frac{Ze^2}{r_0}. \end{aligned} \tag{1.23}$$

For nuclear interaction, ε_n can be expressed as an integral:

$$\varepsilon_n = \frac{1}{2}\int\int f(\mid \overrightarrow{r_1} - \overrightarrow{r_2} \mid, \overrightarrow{s_1}, \overrightarrow{s_2}, \overrightarrow{L}) d\mathcal{V}_1 d\mathcal{V}_2, \tag{1.24}$$

where $f(\mid \overrightarrow{r_1} - \overrightarrow{r_2} \mid, \overrightarrow{s_1}, \overrightarrow{s_2}, \overrightarrow{L})$ is the nuclear potential between two nucleons. It is a function of the distance bewtween these two nucleons, and spins and angular momenta of these two nucleons. A simple approximation for the nuclear potential is a Yukawa potential.

If the ions are free gases, then P_{ion} is just nkT, because the ions are too heavy to be degenerate or relativistic. If the ions solidify and form a lattice, then P_{ion} is caused by phonons and Coulomb interactions between the ions (see §2.3.1).

Above Nuclear Density

When calculating the equation of state, $P = P(\rho)$, in the high density regions, the nuclear potential is required. Inside the core, the composition is primarily neutrons, plus a small amount of protons and electrons. In the central region, the density is so high and the distance between two nucleons so short that nuclear interactions cannot be neglected. Our current knowledge about nuclear interactions are basically phenomenological, and are only tested in the regions where the density is below and near nuclear density. To extend to the regime where the density is significantly higher than nuclear density, the only way is by extrapolation. Among the theoretical alternatives for the dense matter equation of state are the FP Model, which was proposed by Friedman and Pandharipande (1981), and the Baym-Bethe-Pethick equation of state (Baym, Bethe and Pethick 1971), the BPS Model (Baym, Pethick and Sutherland 1971), and the PS Model(Pandharipande and Smith 1976), etc.

1.2.3 Density Profile

Once the equation of state is known, given an initial central pressure P_c, we can integrate the hydrostatic equations from the center outward, and obtain a structure profile. In Fig(1.1), we show the density profile for the FP Model.

Different nuclear energy potential models will give different equations of state. In Fig(1.2) and Fig(1.3), we show two neutron star structures obtained with the BPS Model and PS Model. Compared with the FP model in Fig(1.1), the BPS Model is softer, that is $P_{BPS} < P_{FP}$ for the same value of ρ, so with the same mass, the FP Model has a larger radius, thus a lower density than the BPS Model. On the other hand, the PS Model is the stiffest among the three models, it has the largest radius and the lowest density. The FP Model is of intermediate stiffness.

From these figures, we can see that the density is nearly constant in the interior,

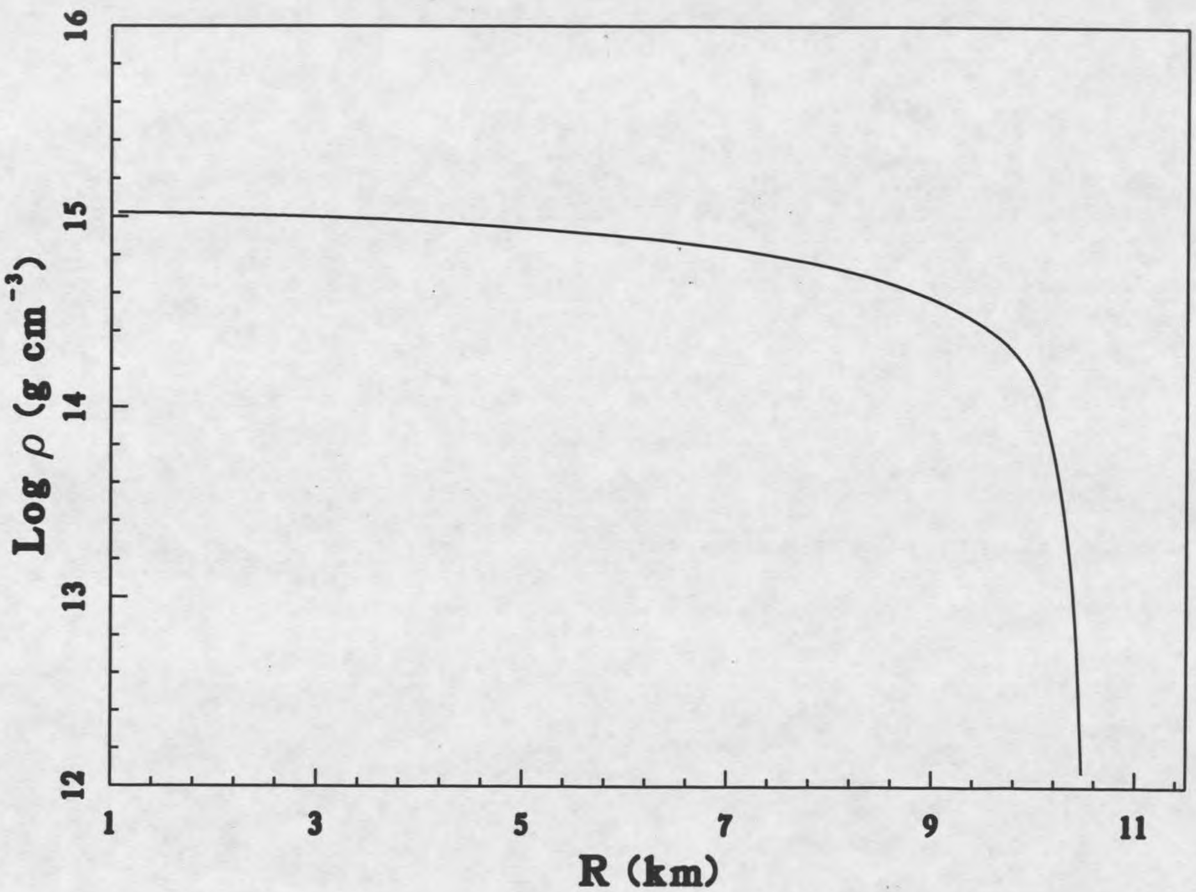

Fig(1.1) Density Profile for FP Type Neutron Stars

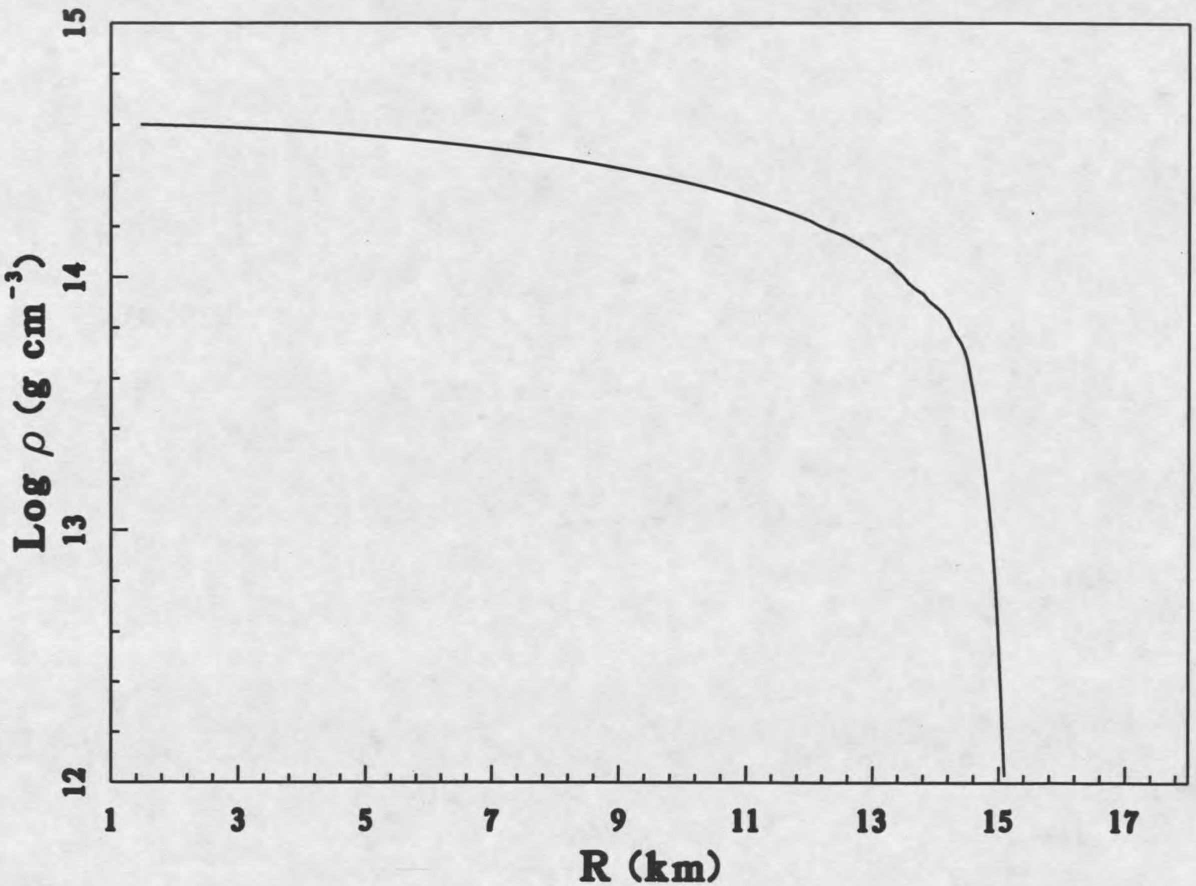

Fig(1.2) Density Profile for PS Type Neutron Stars

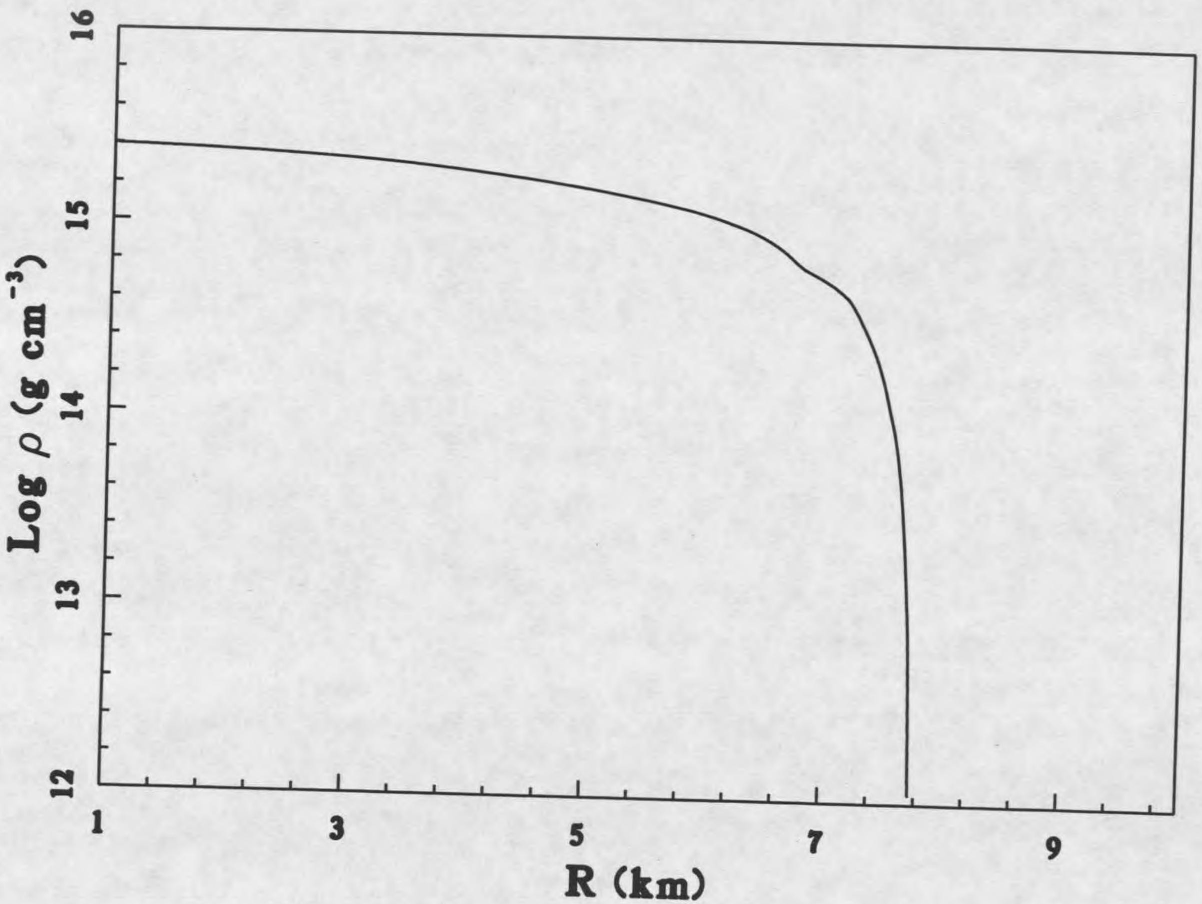

Fig(1.3) Density Profile for BPS Type Neutron Stars but near the surface, the density drops drastically from $10^7 gcm^{-3}$ to zero in a region of about 1 meter thick. This region is called the envelope. The region from $4.3 \times 10^{11} gcm^{-3}$ to the outmost envelope is called the outer crust. Above $4.3 \times 10^{11} gcm^{-3}$, neutron drip occurs, and a gas of free neutrons coexists with a lattice of neutron rich nuclei. The region between $2.8 \times 10^{14} gcm^{-3}$ and $4.3 \times 10^{11} gcm^{-3}$ is called the inner crust. Above $2.8 \times 10^{14} gcm^{-3}$, it is the core. Inside the core, the nuclei dissolve. The core consists mostly of neutrons and a small percentage of protons and electrons.

1.3 Magnetic Field and Superfluidity

1.3.1 Magnetic Field

In §1.1, we discussed one evidence for the existence of strong magnetic fields around neutron stars. Further evidence is provided by the 58 kev emission line from X-ray Pulsar Her X-1.

The origin of this 58 kev emission line can be understood in the following way. Suppose there is a uniform $\overrightarrow{B}$ field. A charged particle moves inside $\overrightarrow{B}$ with a velocity $\overrightarrow{v}$, which has a component v_0 in the plane perpendicular to $\overrightarrow{B}$. The particle will move in a circular orbit due to the influence of the $\overrightarrow{B}$ field. The velocity of the particle satisfies:

$$eBv_0 = m\frac{v_0^2}{r}, \tag{1.25}$$

which leads to:

$$r = \frac{mv_0}{eB}, \tag{1.26}$$

r is the radius of the circular orbit, and is inversely proportional to the magnetic field strength B.

In the case of neutron stars, the magnetic field can exceed 1×10^{12}Gauss. Then, for electrons with $m_e = 9.1 \times 10^{-31} kg$ and $e = 1.6 \times 10^{-19} C$, if the velocity v_0 is $c/10$, r would be $\sim 10^{-11} m$, which is comparable to the de Broglie wavelength λ. Thus, the quantum effects are important.

Let us redo the problem quantum-mechanically. The Lagrangian L for an electron in a magnetic field is

$$L = \frac{1}{2} m v^2 + \frac{e}{c} \overrightarrow{v} \cdot \overrightarrow{A}, \tag{1.27}$$

with $\overrightarrow{A} = \frac{1}{2} \overrightarrow{B} \times \overrightarrow{r}$. The momentum $\overrightarrow{p}$ is

$$\begin{aligned} \overrightarrow{p} &= \frac{\partial L}{\partial \overrightarrow{v}} \\ &= m \overrightarrow{v} + \frac{e}{c} \overrightarrow{A} \\ &= \frac{1}{2} m \overrightarrow{v}. \end{aligned} \tag{1.28}$$

The Bohr quantization condition is

$$\oint L_\theta d\theta = nh. \tag{1.29}$$

Since $L_\theta = \vec{P} \times \vec{r} = \frac{1}{2} m v r$, then

$$\oint \frac{1}{2} m v r d\theta = \pi m v r = nh, \tag{1.30}$$

and because

$$r = \frac{v}{\omega_0}, \tag{1.31}$$

where $\omega_0 = eB/m$, we have:

$$\frac{mv^2}{\omega_0} = 2n\hbar. \tag{1.32}$$

The kinetic energy E can be expressed as:

$$E = \frac{1}{2}mv^2 = n\hbar\omega_0. \tag{1.33}$$

It is quantized, and the differences between two consecutive energy levels are

$$\Delta E = \hbar\omega_0. \tag{1.34}$$

As the electrons jump from one level to the next, photons of energy $\hbar\omega_0$ will be emitted. If $B = 1 \times 10^{12} Gauss$, $\omega_0 = 2 \times 10^{19} s^{-1}$, and $\Delta E = \hbar\omega_0 \approx 10 keV$. The 58 keV photons from Her X-1 imply that the magnetic field strength is about $5 \times 10^{12} Gauss$. Usually the magnetic field inside neutron stars is assumed to be dipolar. The field lines of a dipolar field are shown in Fig(1.4). As the magnetic field corotates with the star, electric fields are induced. In the region that is within a radius R_{lc} from the star, where $R_{lc} = \Omega/c$, the magnetic field has an overwhelming influence over the charged particles. This cylindrical region within R_{lc} is called the light cylinder. The field lines 1, 2, 3 and 1', 2', 3' are closed field lines, and the field lines 0 and 0' are open.

How is the strong radiation produced on the surfaces of neutron stars? The radio emission originates from a region that is $\sim$ 10 stellar radii away from the surface. The beam is radiated by high energy particles constrained to move along the field lines over the magnetic poles. The individual radio pulses are often highly polarized indicating the presence of strong magnetic fields. The intensities of the emitted radio emission are so high that they cannot be due to thermal emissions or incoherent synchrotron radiation, only coherent radiation can produce such high intensities. When the radiation is coherent, the total energy is proportional to N^2, not N, with N as the number density of the particles. Because the electrons are constrained to move together, they act as one particle of charge Ne. When a charged particle with charge q is accelerating, the radiated power is

$$\frac{dE}{dt} = \frac{8\pi^2}{3}(\frac{eB}{mc})^2\frac{v^2}{c^3}q^2. \tag{1.35}$$

For N electrons radiating noncoherently, the total energy radiated will be $N\frac{dE}{dt}$. If N electrons are synchronised, then the total energy radiated is

$$\begin{aligned}\frac{dE_{total}}{dt} &= -\frac{8\pi^2}{3}(\frac{NeB}{mc})^2\frac{v^2}{c^3} \\ &= N^2\frac{dE_e}{dt}.\end{aligned} \tag{1.36}$$

The intensity is enhanced by N^2 times.

As to understanding how charged particles are accelerating along the field lines, we need to turn to the electrodynamics of a rotating magnetic neutron star, which is a very difficult problem, as yet incompletely solved. Goldreich and Julian (1969) assumed the magnetic dipole moment is aligned with the rotating axis, and the neutron star is a good electric conductor. If the interior of a neutron star is a good conductor, then:

$$E' = 0\ , \tag{1.37}$$

where E' is the electric field in the rotating frame. Changing to the inertial frame, we have inside the neutron star,

$$\overrightarrow{E} + (\frac{\overrightarrow{\Omega} \times \overrightarrow{r}}{c}) \times \overrightarrow{B} = 0, \tag{1.38}$$

where $\overrightarrow{\Omega}$ is the angular velocity vector. Since neutron stars are good conductors, we can assume there are no currents on the stellar surfaces. Then $\overrightarrow{B}$ inside is a static dipole field,

$$\overrightarrow{B} = \frac{B_0 R^3}{2r^3}(2\hat{r}\cos\theta + \hat{\theta}\sin\theta). \tag{1.39}$$

Substitute the expression for $\overrightarrow{B}$ into Equation(1.38), we get:

$$\overrightarrow{E} = -\frac{B_0 R\Omega \sin\theta}{2c}(-\hat{r}\sin\theta + 2\hat{\theta}\cos\theta). \tag{1.40}$$

Integrating $\overrightarrow{E} \cdot d\overrightarrow{r}$ from the center toward the surface, we obtain

$$\begin{aligned} \Phi_{in} &= \int_0^R \overrightarrow{E} \cdot d\overrightarrow{r} \\ &= \frac{B_0 R^2 \Omega}{2c}\sin^2\theta + C. \end{aligned} \tag{1.41}$$

Suppose outside the star it is a vacuum. Then the Possion Equation $\nabla^2\Phi_{out} = \rho$ becomes the Laplace Equation.

$$\nabla^2\Phi_{out} = 0. \tag{1.42}$$

With the boundary conditions:

$$\begin{aligned} & r \longrightarrow \infty, \qquad \Phi_{out} \longrightarrow 0 \\ \text{and} & \\ & r = R, \qquad \Phi_{out}\mid_R = \Phi_{in}\mid_R, \end{aligned} \tag{1.43}$$

we get:

$$\Phi_{out}(r,\theta) = \frac{B_0 R^5 \Omega}{2r^3 c}(\sin^2\theta - \frac{2}{3}) + C'. \tag{1.44}$$

Is the above solution stable under the circumstance of the neutron star?

Since the electric field is so strong compared to gravity, any surface charge will be pulled off the surface by the strong electric field. As is shown below, the above solution gives a non-zero surface charge density. That indicates it is not a stable solution.

From Equation(1.39), we know $\overrightarrow{B} \cdot \hat{r} \neq 0$ when $\theta \neq 90°$, and

$$\overrightarrow{B} \cdot \overrightarrow{E} = 0 \tag{1.45}$$

for $r < R$, also

$$\overrightarrow{B} \cdot \overrightarrow{E} = -\frac{B_0^2 R^8 \Omega}{r^7 c} \cos^3 \theta \tag{1.46}$$

for $r > R$. Since the tangential component of the electric field is continuous,

$$\Phi_{out} \mid_R = \Phi_{in} \mid_R, \tag{1.47}$$

then

$$\overrightarrow{E} \cdot \hat{r} \mid_{R-} \neq \overrightarrow{E} \cdot \hat{r} \mid_{R+} . \tag{1.48}$$

That means there will be surface charges, which will be flowing into the vacuum until the surface charges disappear, and the interior and exterior $\overrightarrow{E}$ field become continuous. Then Equation(1.40) for $\overrightarrow{E}$ would apply for both the interior and exterior. The charge density outside the neutron star would be

$$\begin{aligned} \rho_e &= \frac{\nabla \cdot \overrightarrow{E}}{4\pi} \\ &= -\frac{\overrightarrow{B} \cdot \overrightarrow{\Omega}}{2\pi c} \\ &= \frac{B_0 R^3 \Omega}{4\pi r^3 c}(\sin^2 \theta - 2\cos^2 \theta). \end{aligned} \tag{1.49}$$

It implies a particle density of $\sim 10^{11}cm^{-3}$, which is very small, compared to the particle density on the surface of $10^{20}cm^{-3}$. A small amount of accretion of charged plasma would neutralize the charged density in the space and cause charged particles to stream out of the surface. The charged particles will move along the $\overrightarrow{B}$ field lines. There are two kinds of $\overrightarrow{B}$ field lines, one is open and the other is closed, as shown in Fig(1.4). When the particles are moving along the closed field lines, they will eventually come back to the stellar surface. When the particles are moving along the open field lines, they will form beamed winds.

Why is the radio radiation from the neutron stars generally pulsed? The pulsation can be understood by using a lighthouse as a model. As the pulsar rotates, the two beams radiating out of the two poles of the neutron star will sweep through the observer. Depending on the angle between the magnetic field and rotating axes, and also depending on the size of the beam, the observer may receive one or two pulses during each period.

The existence of magnetic fields affects the thermal conductivity of neutron star matters and will change the cooling rate of neutron stars. Under strong magnetic fields, the thermal conductivity becomes a tensor, the conductivities along and perpendicular to the magnetic field become different, and the cooling problem becomes a 2-dimensional problem. The cooling calculations of neutron stars with strong magnetic fields will be discussed in detail in Chapters 2 and 3.

1.3.2 Superfluidity

For a Bose system, when the temperature drops below the critical temperature

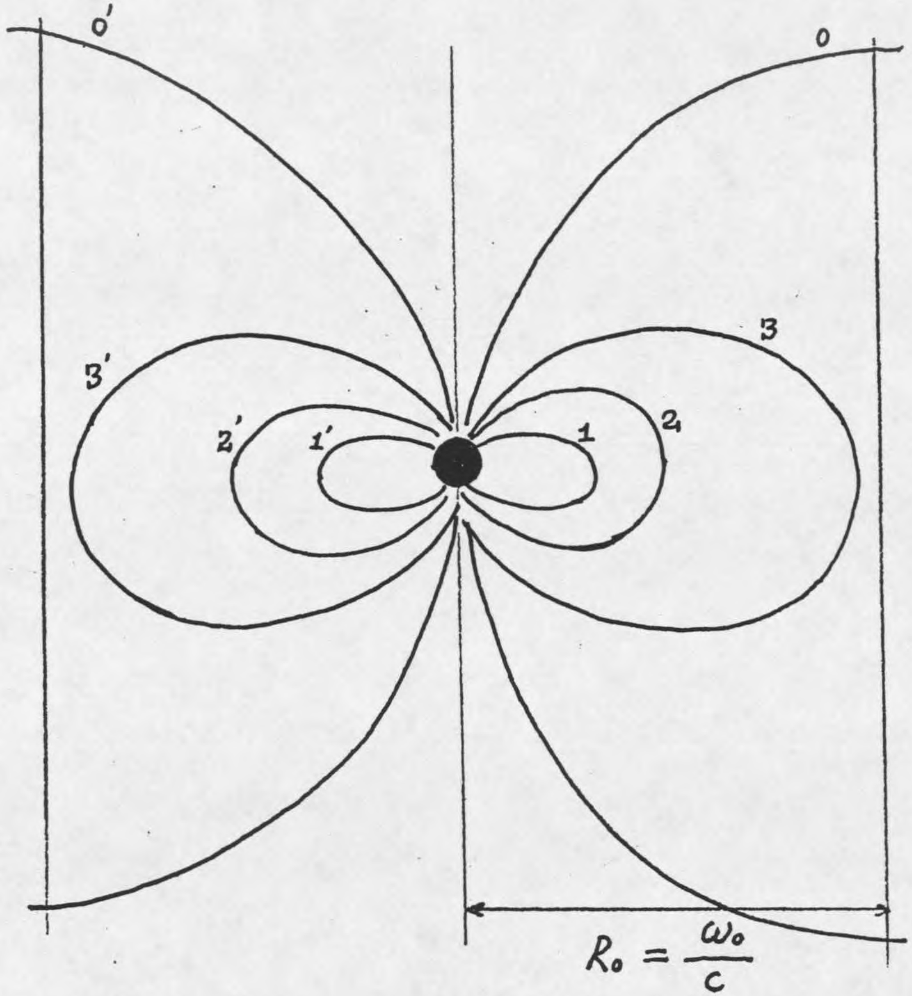

Fig(1.4) Illustration of a Dipolar Magnetic Field

T_{crit},

$$T_{crit} = \frac{2\pi\hbar^2}{mk_B}(\frac{n}{2.612})^{2/3}, \tag{1.50}$$

the system will undergo a second-order phase transition, Bose condensation, from the normal state to the superfluid state.

The number density of particles in the ground state after the Bose condensation is

$$n_T = n_0[1 - (\frac{T}{T_{crit}})^{3/2}]. \tag{1.51}$$

Here n_0 is the total number density of the particles. If $T \sim 0.1T_{crit}$, then $n_T \sim n_0$, so most of the particles are in the ground state when T is lower than the critical temperature. Because friction is caused by momentum transfer between particles, we expect the friction to disappear when the particles are in the same state.

For a system of fermions, if there are attractive interactions between them, under certain conditions, fermions can pair and form bosons. When the temperature is low enough, Bose condensation can be realized in a Fermi system too. These pairs of fermions are called the Cooper Pairs. Below we give a brief explanation of how the Cooper pairs can form. The idea is from Baym (1973).

Let H be the Hamiltonian of two fermions with the attractive interaction,

$$H = \frac{p_1^2}{2m} + \frac{p_2^2}{2m} + V, \tag{1.52}$$

where V is non-positive, because of the attractive nature of the interaction. Let $\mid \phi >$ be the wave function of this two-fermion system. The Shrödinger equation is

$$H \mid \phi >= E \mid \phi > . \tag{1.53}$$

Consider two electrons outside the fermi surface. Between these two electrons, when their momenta are within a certain range above the fermi sea, i.e when their momenta are larger than the fermi momentum p_f and smaller than p_a, with p_a as a momentum slightly higher than p_f, there will be a weak attractive force between them. This kind of attractive force is caused by the attractive Coulomb forces between the ions and the two electrons.

For two free electrons, the total wavefunction is simply:

$$\Psi(\overrightarrow{r_1}, \overrightarrow{r_2}, t) = \frac{e^{i\overrightarrow{k_1}\cdot\overrightarrow{r_1}}}{\sqrt{L^3}} e^{-i\frac{\epsilon_{k_1}}{\hbar}t} \cdot \frac{e^{i\overrightarrow{k_2}\cdot\overrightarrow{r_2}}}{\sqrt{L^3}} e^{-i\frac{\epsilon_{k_2}}{\hbar}t}, \tag{1.54}$$

with L^3 as the total volumn and $k_i = p_i/h$. The wavefunction of these two weakly interacting electrons can be written as a sum of the wavefunctions of two non-interacting electrons.

$$\Psi(\overrightarrow{r_1}, \overrightarrow{r_2}, t) = \sum_{\overrightarrow{k_1}, \overrightarrow{k_2}} a_{\overrightarrow{k_1}\overrightarrow{k_2}} \frac{e^{i\overrightarrow{k_1}\cdot\overrightarrow{r_1}}}{\sqrt{L^3}} \frac{e^{i\overrightarrow{k_2}\cdot\overrightarrow{r_2}}}{\sqrt{L^3}} e^{-i\frac{E}{\hbar}t}. \tag{1.55}$$

Here E is the total energy of the two-fermion system. The Shrödinger equation then becomes

$$\left(\frac{p_1^2}{2m} + \frac{p_2^2}{2m} + V(p_1, p_2)\right) \sum_{p_1', p_2'} a_{p_1'p_2'} \mid p_1'p_2' >= E \sum_{p_1'p_2'} a_{p_1'p_2'} \mid p_1'p_2' > . \tag{1.56}$$

By multiplying both sides by $< p_1p_2 \mid$ and summing over p_1 and p_2, we get:

$$\sum a_{p_1p_2}\left[\frac{p_1^2 + p_2^2}{2m} - E\right] + \sum_{p_1'p_2'} a_{p_1'p_2'} \sum_{p_1p_2} < p_1p_2 \mid V(p_1p_2) \mid p_1'p_2' >= 0. \tag{1.57}$$

Assume $V(x) = -V_0\delta(x)$, then $V(p_1p_2) = -V_0$. So:

$$\sum_{p_1'p_2'} a_{p_1'p_2'} \sum_{p_1p_2} < p_1p_2 \mid V(p_1, p_2) \mid p_1'p_2' >= -V_0 \sum_{p_1'p_2'} a_{p_1'p_2'} \tag{1.58}$$

Substitute Equation(1.58) back into Equation(1.57), and we get:

$$\sum_{p_1p_2} \frac{p_1^2+p_2^2}{2m} - E = V_0, \tag{1.59}$$

or

$$1 = \sum_{p_1p_2} \frac{V_0}{\frac{p_1^2+p_2^2}{2m} - E}. \tag{1.60}$$

The equation (1.60) is a condition to determine the possible eigenvalues of the total energy E. Notice that p_1 and p_2 are restricted to have values between p_f and p_a. Given a total momentum $p = p_1 + p_2$, with each possible $\varepsilon_{p_1} + \varepsilon_{p_2}$ when $p_f < p_1, p_2 < p_a$, Equation(1.60) has a pole. Let $f(E) = -\sum_{p_1p_2} V_0/(\frac{p_1^2+p_2^2}{2m} - E)$, Fig(1.5) gives a graphic solution of $f(E)$. From Fig(1.5), we can see that the ground state of the paired fermions is lower than the simply degenerate state $2\varepsilon_f$. The ground state energy E_{GS} can be approximated by:

$$E_{GS} \approx 2E_F - 2\Delta, \tag{1.61}$$

where $\Delta = E_F \exp[-2/(g_0V_0)]$ with $g_0 = (L^3/4\pi^2)[(2m)^{2/3}/h^3]\sqrt{E_F}$. When the fermions pair up, they form bosons. If the temperature is sufficiently low, i.e. lower than the critical temperature of the boson system, Bose condensation will take place, and the superfluidity will appear. If the particles have charges, the superfluidity implies superconductivity.

In the central interior region of neutron stars where the density is above $2 \times 10^{14} gm/cm^3$, the corresponding fermi temperature is $10^{12}K$, while the actual temperature is around 10^9K, far lower than the fermi temperature. The theoretical

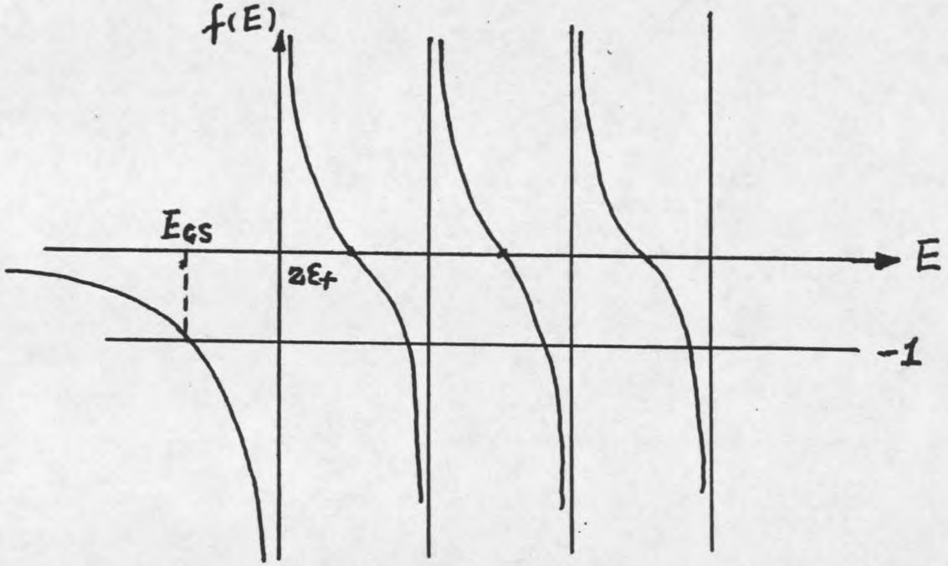

Fig(1.5) Solution of f(E)

arguments, that explain why the terrestrial matter have superfluidity when the temperature is below $10^{-3}T_{fermi}$, predict that neutron stars should have superfluid interiors. In the inner crust of neutron stars where the density is above the neutron drip, there will be free neutrons. The central core consists mainly of neutrons with a small percentage of protons and electrons. The origin of the attraction between these fermions is the nucleon-nucleon interaction, which can be expressed as:

$$V_{nn} = V_{central}(|\overrightarrow{r}|) + V_{so}(|\overrightarrow{r}|)\overrightarrow{s}\cdot\overrightarrow{l}, \tag{1.62}$$

where the central part of the potential is attractive at the long range $r > \frac{1}{2}fm$, due to the exchange of pions, and is repulsive at the short distance due to the exchange of the ω meson. This same vector meson is also responsible for the spin-orbit interaction, which becomes strong at short distances.

Through scattering experiments, we can determine the phase-shift of free neutrons, and from the phase shifts, we can obtain the information about the interaction between two neutrons. A positive phase shift indicates an attractive interaction, while a negative phase shift a repulsive interaction. The larger the phase shift, the greater the attraction. The greater the attraction, the more stable the state. The scattering experiments show that at low densities, the $^1S_0$ state will dominate, while at high densities, the $^3P_2$ state dominates. So inside neutron stars, neutrons in the central core will be in the $^3P_2$ state, while neutrons in the inner crust and protons inside the core will be in the $^1S_0$ state.

When the interior of neutron stars is in the superfluid state, both their thermal properties and hydrostatic properties will be different from those in the normal state. Here we will only discuss the influence of superfluidity on thermal properties of neutron stars.

Using neutron-scattering experiments the excitation spectrum of a Bose gas can be measured. The excitation consist of a mixture of phonons and rotons. The spectrum is suggested by Landau(1941,1947), as:

$$\epsilon = \begin{cases} \Delta + \frac{(p-p_0)^2}{2\mu_r} & \text{roton} \\ c_1 p & \text{phonon} \,, \end{cases} \tag{1.63}$$

where c_1 and p_0 are two constants, p is the momentum, μ_r is a constant which can be regarded as the mass of rotons, and Δ is the energy gap. The contribution by phonons and rotons to the thermal properties, such as specific heat, may be calculated separately and then added together. For the phonon gas the Bose-Einstein distribution is appropriate, but the roton distribution function includes an extra factor $\exp(-\Delta/k_BT)$. In the cooling calculations of neutron stars, we consider only the roton excitations' contribution to the superfluid component and include the phonon excitations into the specific heat of the normal components.

The number density of rotons is

$$N_{roton} = \frac{2p_0^2(\mu_r k_B T)^{1/2}}{(2\pi)^{3/2}h^3} \exp(-\Delta/k_BT), \tag{1.64}$$

assuming Maxwell-Boltzman statistics. The extra factor $\exp(-\Delta/k_BT)$ implies that the neutrino emissivity and the specific heat will be reduced by $\exp(\Delta/k_BT)$. These two effects at a certain level would cancel each other out, and make the overall effects of superfluidity on the thermal evolution of neutron stars not very important.

In Fig(1.6), we show the effects of superfluidity on neutron star thermal evolution.

The cooling profile is calculated for the FP Model. The solid curve is the cooling curve without the superfluids, the dashed one is with the superfluids. The superfluidity slightly changes the temperatures of neutron stars. For a detailed discussion of the cooling curves of neutron stars, see §2.2.

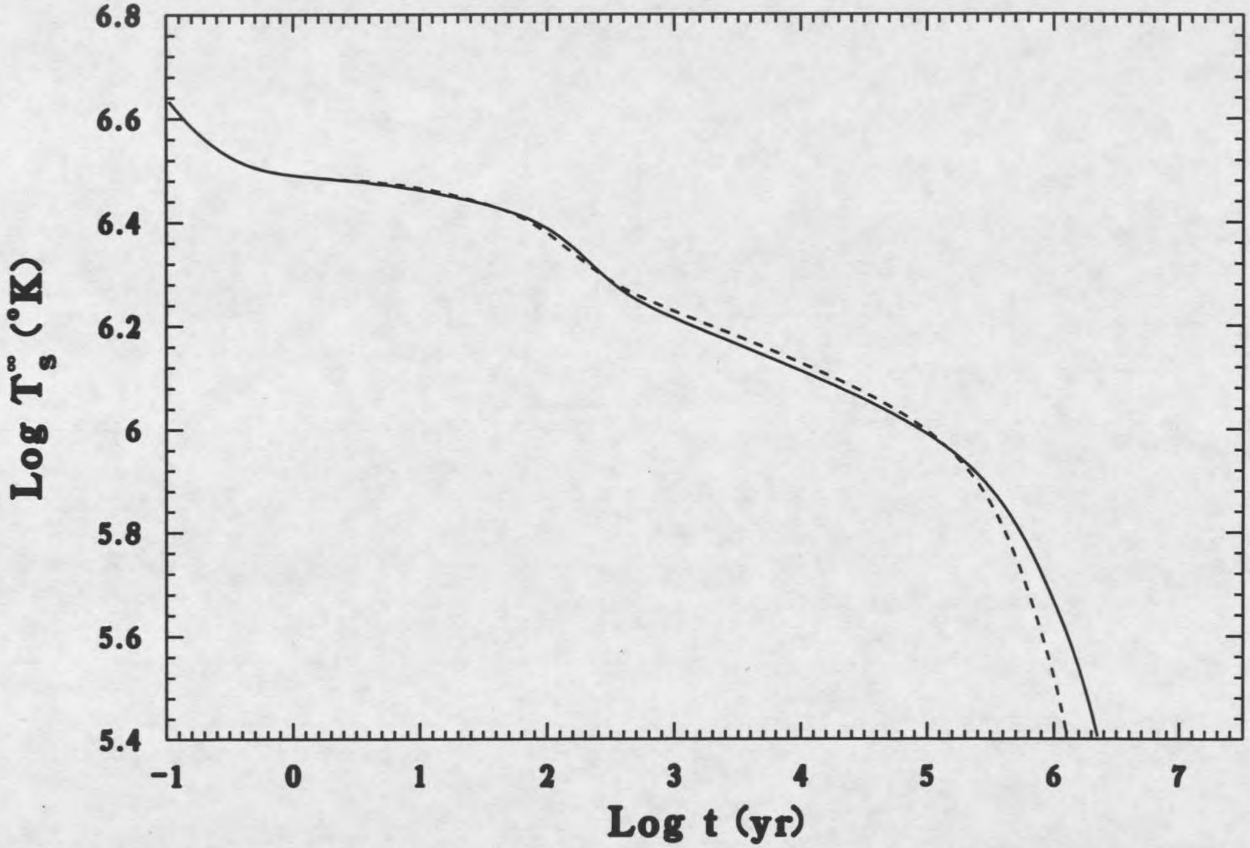

Fig(1.6) Effects of Superfluidity on Neutron Star Cooling, the FP Model

Chapter 2

One Dimensional Cooling Calculation

2.1 Introduction

Neutron stars are produced in type II supernovae. When they are born, neutron stars are very hot, having temperatures around $10^{10} \sim 10^{11} K$. Different neutrino emission processes, such as modified URCA, bremsstrahlung and plasma neutrino processes, take place. Since the neutrino's mean free path is much longer than the neutron star size, neutrinos will escape and carry away energy. Also photon emission occurs at the star's surface.

Tsuruta (1964) was one of the first to solve the thermal evolution problem of neutron stars. In her pioneering work, the isothermal method is employed. The isothermal method assumes that the temperature of the core is uniform and the thin envelope outside the core has constant photon luminosity. The finite conduction time through the crust is neglected. The core temperature is determined by the neutrino emission, thermal conduction calculation from the core to the surface in the envelope determines the surface temperature. Later, Malone and Richardson (Richardson et al 1982) used the evolutionary method. They solved the equations of stellar evolution as a mixed initial-boundary value problem. But since the equations of state they used were medium to soft, the crustal shell was very thin, and they found that the effect of the finite conduction time lasted only 1 $\sim$ 30 years. More recently, Nomoto and Tsuruta carried out the exact evolutionary calculations of neutron stars with updated inputs of neutrino emissivity and opacity, and stiff equations of state as well as soft equations of state (Nomoto & Tsuruta 1987, thereafter referred as NT87). In their paper, the effect of the mass of neutron stars and superfluidity were thoroughly explored, and they found that the thermal relaxation time was significantly longer than the results of Richardson et al. For the PS Model, which has a stiff equation of state, it takes $\sim 6 \times 10^4$ yr to reach the thermal equilibrium. For an intermediate model (e.g. FP), it takes $\sim$ 600 yr. For a soft model (e.g. BPS), the thermal relaxation time is $\sim$ 300 yr. All the time scales are found to be longer than the previous results.

The works above are confined to non-magnetic neutron stars. The effects of strong magnetic fields on neutron star cooling have also been considered by a number of authors (Tsuruta et al 1972; Tsuruta 1974, 1975, 1979; Nomoto & Tsuruta 1981; Glen & Sutherland 1980; Yakovlev & Upin 1981). In Greenstein & Hartke (1983), they derived the $\sqrt{|\cos\theta|}$ surface temperature modulation for magnetized neutron stars. Hernquist (1985) estimated the longitudinal cooling, and he found that the polar temperature of a magnetic neutron star is slightly higher than in the non-magnetic case. This, together with the $\sqrt{|\cos\theta|}$ relation, made him conclude that the total luminosity of a magnetic neutron star at a given age would not differ significantly from the non-magnetic stars. It was Shaaf (1990) who actually calculated the transverse surface temperatures. He used the envelope calculation, and he found that in thermal equilibrium there is a significant difference between the longitudinal and transverse core temperatures for a given surface temperature. He claimed that the surface-core temperature relations and the resulting time-dependent cooling behaviors would change for magnetic neutron stars. Nevertheless, Shaaf's method is not evolutionary. A major focus of this thesis is to calculate how the temperature of a magnetized neutron star evolves with time and to compare the results with the observational data.

In this chapter, we will first discuss the exact method of neutron star cooling calculations (§2.2). In §2.3, the physical inputs, such as opacity and neutrino emissivity will be discussed. In §2.4, we explain how the magnetic fields change the opacities of neutron star matter. Due to the presence of strong magnetic fields, the heat conductivity is anisotropic. To fully take into account the effect of the magnetic field, the two-dimensional (radial and tangential) cooling code (2D code) is needed. Before constructing a fully 2D model, we use a 1D approximation to explore the influence of the magnetic field, which could offer us insight and help us to understand the important change of the thermal history of magnetic neutron stars from the non-magnetic case later. In §2.5 and §2.6, the cooling profiles of magnetic neutron stars obtained from 1D approximation method, are presented (Qin, Tsuruta & Umeda 1995a). The

2D cooling calculations of magnetic neutron stars will be discussed and the results will be presented in Chapter 3.

2.2 Methods of Neutron Star Cooling Calculations

2.2.1 Isothermal Method

When the neutron star cooling problem was first attacked, the isothermal method was used (Tsuruta 1964). In the isothermal method, a neutron star is treated as consisting of two parts, an isothermal core and a thin envelope; the hydrodynamic and thermodynamic equations are decoupled. The core integration of the former determines the stellar mass and radius, while the core temperature is determined by energy balance equation,

$$c_v \frac{dT_c}{dt} = \varepsilon_\nu, \tag{2.1}$$

during the neutrino cooling era. Here T_c is the core temperature, c_V is the specific heat, and ε_ν is the neutrino emissivity. Determination of the surface temperature is then a heat transport problem. Fig(2.1) is a cooling profile of neutron stars obtained with the isothermal method taken from Tsuruta's doctoral thesis(1964). From Fig(2.1), we see that after the age of $t \sim 10^5$ yr, the surface temperature takes sudden drops. During the neutrino cooling era, i.e. before $t \sim 10^5$ yr, the stellar cooling rate is determined by the energy loss due to neutrino emission, while during the photon cooling era, i.e. after $t \sim 10^5$ yr, it is determined by photon emission.

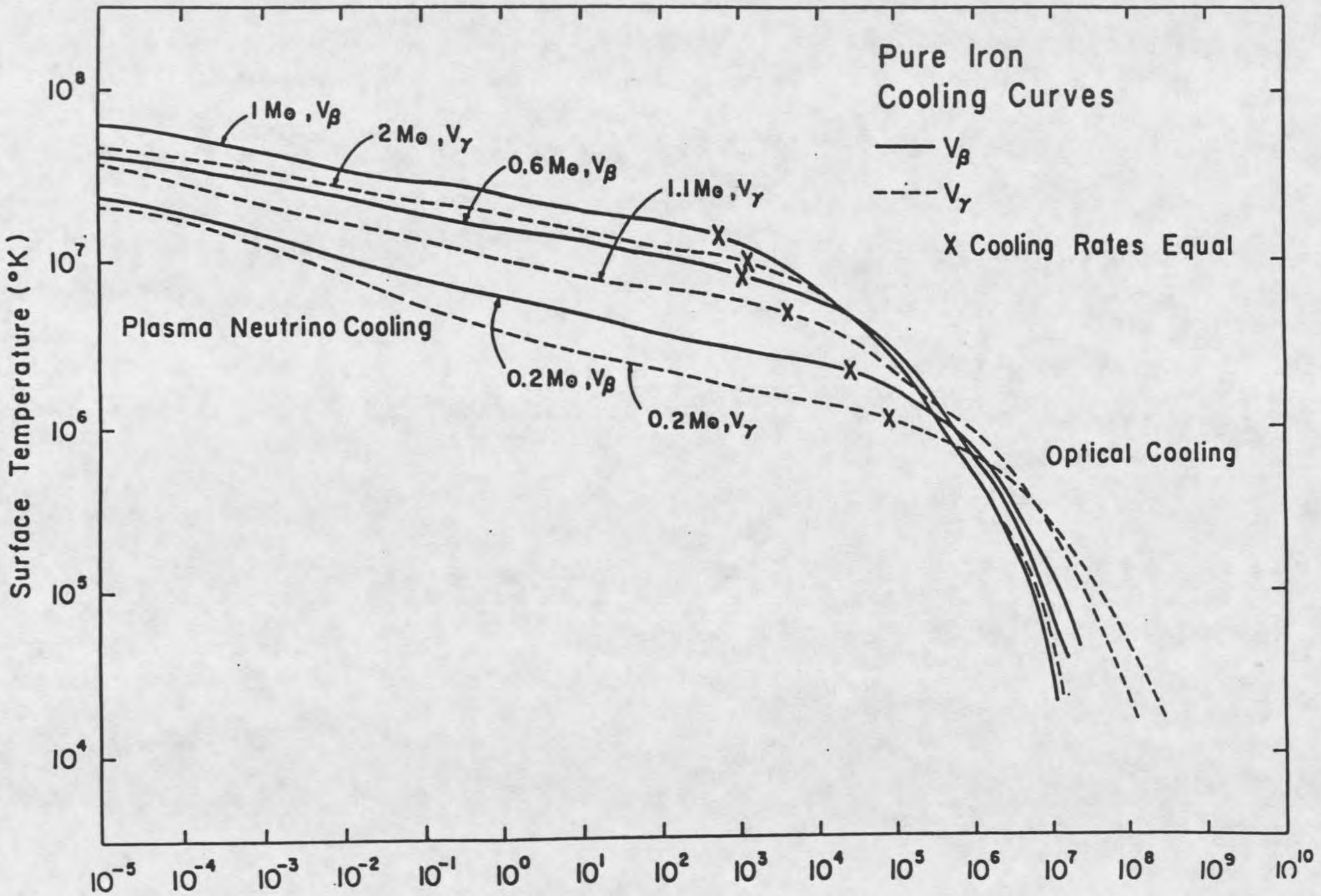

Fig(2.1) Cooling Profile from Isothermal Method

The energy loss rate due to the neutrino emissions can be written as (NT87):

$$L_\nu = L_\nu{}^{modified\ URCA} + L_\nu{}^{brem} + L_\nu{}^{plasm} + L_\nu{}^{photon-neutrino} + L_\nu{}^{e^+e^-}. \quad (2.2)$$

Generally $L_\nu^{modified\ URCA}$ is the most important among these five processes. Thus we consider $L_\nu{}^{modifiedURCA}$ only, which can be written approximately as (Shapiro & Teukolsky 1983):

$$L_\nu{}^{URCA} = 5.3 \times 10^{39} ergs^{-1} \frac{\dot{M}}{M_\odot} (\frac{\rho_{nuc}}{\rho})^{\frac{1}{3}} T_9^8. \quad (2.3)$$

Here $T_9 = T/10^9$, and $\rho_{nucl.}$ is the nuclear density, $\rho_{nucl.} = 2.8 \times 10^{14} gm/cm^3$. The total stellar energy content is (Shapiro & Teukolsky 1983)

$$\dot{U_n} = 6 \times 10^{47} erg(M/M_\odot)(\rho/\rho_{nuc})^{-\frac{2}{3}} T_9^2. \quad (2.4)$$

The energy balance requires that

$$\frac{dU_n}{dt} = -L_\nu^{modified\ URCA}. \quad (2.5)$$

Substituting Equations(2.3) and (2.4) into Equation(2.5), we obtain

$$T_9^{-7} \frac{dT_9}{dt} = -4.4 \times 10^{-13} (\frac{\rho_{nuc}}{\rho})^{-\frac{1}{3}}. \quad (2.6)$$

Integrating the differential Equation(2.5), we get:

$$T_9^{-6} = 2.64 \times 10^{-12} (\frac{\rho_{nuc}}{\rho})^{-\frac{1}{3}} t + c. \quad (2.7)$$

Here t is the age of the neutron star, c is a integration constant. On the other hand, the energy loss rate due to the surface blackbody emission is

$$L_\gamma = 4\pi R^2 \sigma T_s{}^4. \quad (2.8)$$

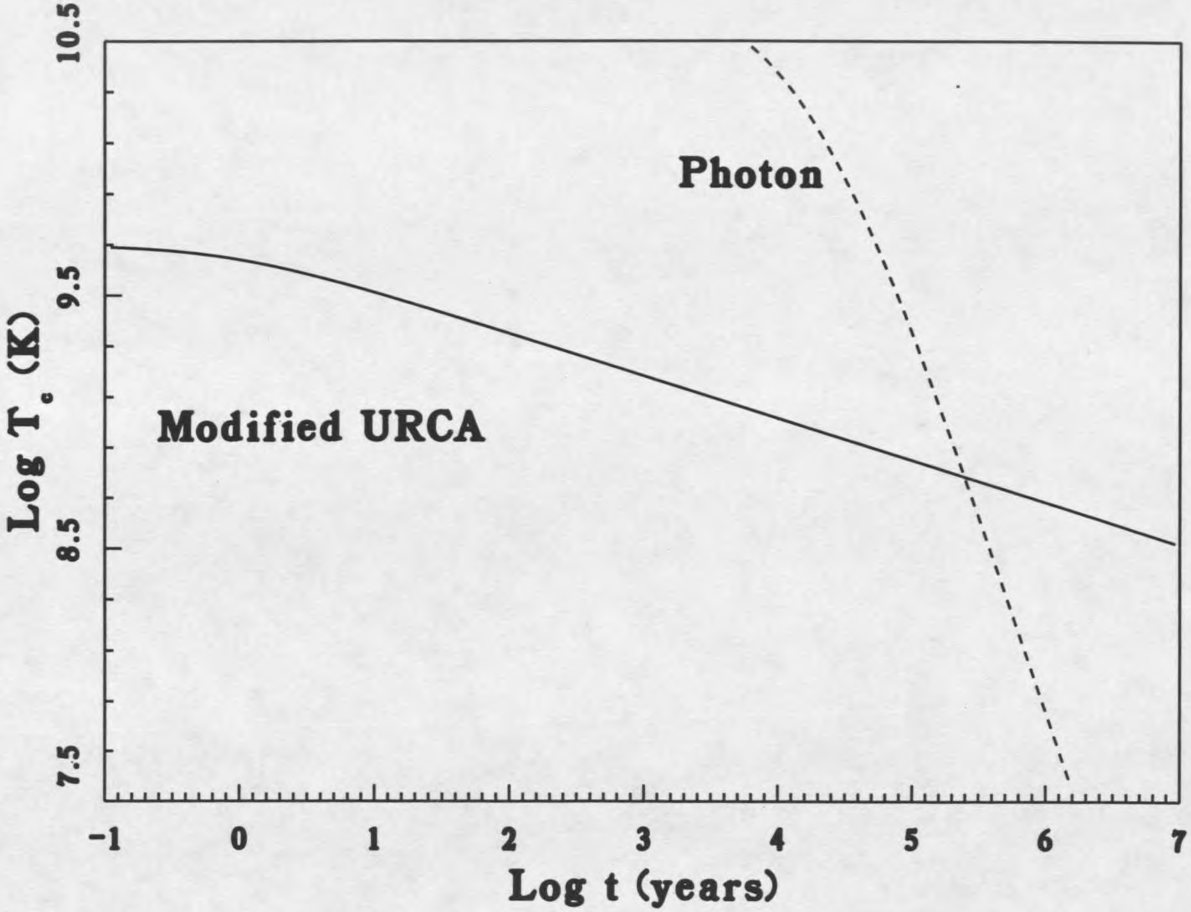

Fig(2.2) T_c vs. t (zero field)

The relation between T_s and T_c can be expressed as $T_s = 4.64 \times T_c^{\frac{2}{3}}$ according to Tsuruta (1974). After some calculations, we obtain the cooling rate due to the photon emission as:

$$T_c^{-\frac{2}{3}} = 4.648 \times 10^{-4}(\frac{M}{M_\odot})^{-\frac{1}{3}}t + c. \qquad (2.9)$$

In Fig(2.2), we show the T_c vs. t relation for the modified URCA process and the blackbody emission. Before the age $t \sim 10^5$ yr, the modified URCA process dominates the blackbody emission, while after $t \sim 10^5$ yr, the blackbody cooling takes over. This can be understood through the fact that the modified URCA emissivity has a temperature dependence of T^8, while the blackbody emissivity goes $\propto T^{2.7}$. Thus, at higher temperatures, the modified URCA process is more important than the blackbody cooling, while as the temperature decreases, the modified URCA emissivity decreases more rapidly than the photon emissivity, and at lower temperatures, the blackbody cooling takes over. Fig(2.2) quantitatively explains Fig(2.1).

2.2.2 Exact Evolutionary Method

The exact method of neutron star cooling calculations is to solve the differential equations of stellar evolution. In NT87, the structure and thermal evolution equations are solved simultaneously. The full set of the structure evolution equations may be expressed as follows.

The hydrostatic equations: given by Eq.(1.9), (1.10), (1.11).

The thermodynamic equations:

$$\frac{d(Te^{\phi})}{dt} = -\frac{n}{c_v}\frac{d(Le^{2\phi})}{da} - e^{2\phi}\frac{\epsilon_\nu}{c_v} \qquad (2.10)$$

$$Le^{2\phi} = -\frac{16\sigma}{3}\frac{T^3}{\kappa\rho}(4\pi r^2)^2 n e^{\phi}\frac{d(Te^{\phi})}{da}, \tag{2.11}$$

with

$$\frac{da}{dr} = \frac{4\pi r^2 n}{\sqrt{1-\frac{2Gm}{c^2 r}}}. \tag{2.12}$$

Here r is the radius, $\rho(r)$ is the mass density, $P(r)$ is the pressure, $m(r)$ is the gravitational mass enclosed within r, $T(r)$ is the temperature, $\phi(r)$ is the gravitational potential, $n(r)$ is the baryon number density, $a(r)$ is the baryon number enclosed within r, c_v is the specific heat per unit volume with a unit of erg/cm^3K, ϵ_ν is the neutrino emissivity per unit volume with a unit of erg/cm^3s, $L(r)$ is the luminosity, and κ is the opacity.

However, since $T_{fermi} = 10^{12}K \gg$ the actual temperature inside the neutron stars, the structures of neutron stars will only change slightly when the stellar temperature decreases. So we can decouple the hydrostatic equations and thermodynamic equations by assuming $P = P(\rho)$, a function independent of temperature T.

In my research, I adopt the results of the hydrostatic structures of a neutron star from NT87, and solve only the thermodynamic equations.

When the stellar structure does not change significantly with time, the thermodynamic equations can be simplified to:

$$\frac{dT}{dt} = -\frac{1}{4\pi r^2 c_v e^{2\phi}}\frac{d(Le^{2\phi})}{dr} - e^{\phi}\frac{\epsilon_\nu}{c_v}, \tag{2.13}$$

$$L = -\frac{16\sigma}{3}\frac{T^3}{\kappa\rho}(4\pi r^2)e^{-2\phi}\frac{d(Te^{\phi})}{dr}. \tag{2.14}$$

To solve these nonlinear differential equations numerically, we use fully implicit differential scheme.

We first build up a mesh as shown in Fig(2.3). We divide the whole range from $r = 0$ to $r = 10km$ into 150 zones. At each zone, we place the luminosity variables L_{2k} at the ends of each zone, and the temperature variables T_{2k+1} at the middle points. Then the finite difference equations become

$$\begin{aligned}\frac{T_{2k+1} - T_{2k+1}^{old}}{\Delta t} &= -\frac{1}{4\pi R_k^2 c_v e^{2\phi}} \frac{L_{2k+2} e^{2\phi_{k+1}} - L_{2k} e^{2\phi_k}}{R_{k+1} - R_k} - \\ & \quad e^{2\phi_k} \frac{\epsilon_\nu}{c_v},\end{aligned} \tag{2.15}$$

$$\begin{aligned}L_{2k} &= -\frac{16\sigma}{3} \frac{(\frac{T_{2k+1}+T_{2k-1}}{2})^3}{\kappa \rho_k} \\ & \quad (4\pi R_k^2) e^{-2\phi_k} \frac{T_{2k+1} e^{\phi_{k+1}} - T_{2k-1} e^{\phi_k}}{R_{k+1} - R_k}.\end{aligned} \tag{2.16}$$

The quantities κ, ϵ_ν and c_v are evaluated at the middle points of each zone. The finite difference equations are fully implicit. The left side of Equation (2.15) includes the current temperatures, thus unknown, and depends on the gradient of luminosity. Equation(2.16) tells us the luminosities are functions of the current temperatures. Also the parameters such as κ, ϵ_ν, c_v are functions of the current temperatures too. To solve Equations (2.15) and (2.16), i.e, to find the values of T_{2k+1} and L_{2k}, we start with a set of trial values. Surely, this set of trial values will not satisfy Equations (2.15) and (2.16). Define $\delta L_{2k} \equiv {L_{2k}}^{true} - {L_{2k}}^{trial}$, and $\delta T_{2k+1} \equiv {T_{2k+1}}^{true} - {T_{2k+1}}^{trial}$. The superscript "true" means the values that will satisfy Equations(2.15) and (2.16). Solve for δL_{2k}, δT_{2k+1} with the boundary conditions supplied. Then add δL_{2k} and δT_{2k+1} to the trial values, that will give us a new set of T_{2k+1} and L_{2k}, which are closer to the true values. We iterate, until $\mid \delta L_{2k}/L_{2k} \mid$ and $\mid \delta T_{2k+1}/T_{2k+1} \mid$ are smaller than

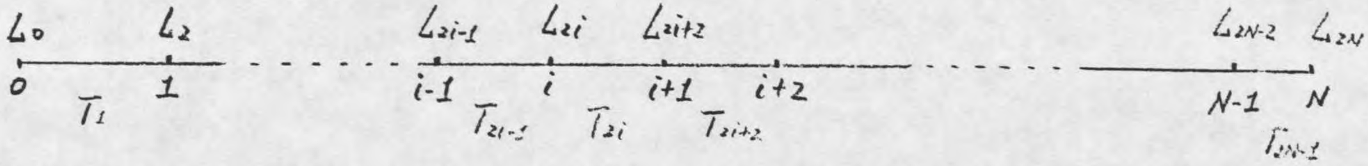

Fig(2.3) Mesh in 1D Calculation

a certain limit, ε. Then we finish one step calculation, and the temperatures and luminosities at the current time are found. To go to time $t + \Delta t$, we use the set of values we just obtained as trial values, then repeat the above procedure to find a set of solutions for time $t + \Delta t$.

When we substitute $\delta L_{2k} + L_{2k}{}^{trial}$ and $\delta T_{2k+1} + T_{2k+1}{}^{trial}$ into Equations (2.15) and (2.16), we get:

$$\begin{aligned} &\frac{\delta T_{2k+1} + T_{2k+1} - T_{2k+1}{}^{old}}{\Delta t} = \\ &-\frac{1}{4\pi R_k^2 c_v e^{2\phi}} \frac{(L_{2k+2} + \delta L_{2k+2})e^{2\phi_{k+1}} - (L_{2k} + \delta L_{2k})e^{2\phi_k}}{R_{k+1} - R_k} - \\ &e^{2\phi_k}\frac{\epsilon_\nu}{c_v}, \end{aligned} \tag{2.17}$$

$$\begin{aligned} L_{2k} + \delta L_{2k} &= -\frac{16\sigma}{3\kappa\rho}\left(\frac{T_{2k+1} + \delta T_{2k+1} - T_{2k-1} - \delta T_{2k-1}}{2}\right)^3 \\ &(4\pi R_k{}^2)e^{-2\phi_k}\frac{(T_{2k+1} + \delta T_{2k+1})e^{\phi_{k+1}} - (T_{2k-1} - \delta T_{2k-1})e^{\phi_k}}{R_{k+1} - R_k} \end{aligned} \tag{2.18}$$

Note that c_v, ϵ_ν and κ are functions of $T_{2k+1} + \delta T_{2k+1}$. Approximate $\frac{1}{c_v}$, ϵ_ν and κ with

$$\frac{1}{c_v(T_{2k+1})} - \frac{1}{c_v{}^2(T_{2k+1})}\frac{dc_v}{dT}\delta T_{2k+1}, \tag{2.19}$$

$$\epsilon_\nu(T_{2k+1}) + \frac{d\epsilon_\nu}{dT}\delta T_{2k+1}, \tag{2.20}$$

$$\kappa(T_{2k+1}) + \frac{d\kappa}{dT}\delta T_{2k+1}. \tag{2.21}$$

Substitute Equations (2.19), (2.20) and (2.21) back into Equations (2.17) and (2.18), and rearrange them, then we get the following two linear equations (accurate to the first order):

$$A_{2k+1,2k+1}\delta T_{2k+1} + A_{2k+1,2k+2}\delta L_{2k+2} + A_{2k+1,2k}\delta L_{2k} = F_{2k+1}, \tag{2.22}$$

$$A_{2k,2k}\delta L_{2k} + A_{2k,2k+1}\delta T_{2k+1} + A_{2k,2k-1}\delta T_{2k-1} = F_{2k}. \tag{2.23}$$

$$k = 0, 1, \cdots, 150. \tag{2.24}$$

The coefficients $A_{i,j}$ and F_i are given in Appendix A. The boundary conditions are: for $k = 0$, $L_{2k} = 0$, and for $k = N$, $T_{2k+1} = T_0$, where T_0 is determined by the integration inside the envelope, which will be discussed in the latter part of this section.

The remaining problem then is to solve the set of linear equations(2.22) and (2.23). This set of equations when written in a matrix form, becomes:

$$\vec{A} \times \begin{pmatrix} \delta L_0 \\ \delta T_1 \\ \delta L_2 \\ \delta T_3 \\ \cdot \\ \cdot \\ \cdot \\ \delta L_{2N} \end{pmatrix} = \vec{F}. \tag{2.25}$$

Matrix $\vec{A}$ is a tridiagonal matrix. Solving the set of linear equations then reduces to invert matrix $\vec{A}$. To invert $\vec{A}$, we use a standard tridiagonal inversion subroutine (Numerical Recipes §2.6).

To calculate the temperatures and luminosities at the new time, we first evaluate the elements of the matrix, then invert the matrix, and solve for $(\delta L_{2k}, \delta T_{2k+1})$. The increments are added to the corresponding trial values, the matrix is then evaluated and solved for $(\delta L_{2k}, \delta T_{2k+1})$ again, and so on, until the increments or the corrections are less than a set accuracy. In our 1D code, $\mid \delta L_{2i}/L_{2i} \mid$ is set to be less than 10^{-6} and $\mid \delta T_{2i+1}/\delta T_{2i+1} \mid$ less than 10^{-8}. The step size is kept small enough such that during each step the changes of the temperatures are less than 2%. The above method is called the Henyey-type stellar evolutionary code. The computing time depends heavily on the speed of matrix inversion. The time it takes to invert a matrix is proportional to N^2, where N is the dimension of the matrix. If we divide the whole range from $r = 0$ to $r = R$ into 150 zones, where R is the stellar radius, then the matrix has dimension 300, because each zone has two variables: temperature and luminosity. The initial model with the central temperature $T_c = 1 \times 10^{10} K$ was constructed by suppressing neutrino emission and choosing a long enough time step to reach the thermally-relaxed state.

The boundary conditions help us to evaluate the matrix elements F_0, $A_{0,0}$, $A_{0,1}$ and F_N, $A_{N,N}$,$A_{N-1,N}$. The boundary condition at $r = 0$ is :

$$L = 0, \text{ at } r = 0. \tag{2.26}$$

This tells us $\delta L_0 = 0$, i.e. $F_0 = 0$, $A_{0,0} = 1$ $A_{0,1} = 0$. The boundary condition at the outside boundary is rather complicated. In the last zone, L_{2N} is a function of $(T_{2N+1} - T_{2N})/(\Delta R)$. T_{2N+1} is a variable outside the mesh. To find T_{2N+1}, the envelope calculation is needed. The envelope is defined as a thin layer outside the outer crust. Inside the envelope, the flux can be regarded as constant. Inverting the heat transfer equation, we have:

$$\frac{dT}{dr} = -\frac{3}{16\sigma}\frac{\kappa\rho}{T^3}\frac{L}{4\pi R^2\sqrt{1-\frac{2GM}{Rc^2}}}. \tag{2.27}$$

The hydrostatic equation is

$$\frac{dP}{dr} = -\frac{GM\rho}{R^2}\frac{1}{1-\frac{2GM}{Rc^2}}, \tag{2.28}$$

together they give:

$$\frac{dT}{dP} = \frac{3}{16}\frac{\kappa}{T^3}\frac{{T_s}^4}{g_s}, \tag{2.29}$$

where T_s is the surface temperature, which is related to the flux by

$$L = 4\pi R^2 \sigma {T_s}^4, \tag{2.30}$$

and g_s is the surface gravity,

$$g_s = \frac{GM}{R^2}\frac{1}{\sqrt{1-\frac{2GM}{Rc^2}}}. \tag{2.31}$$

Integrate Equation(2.28) from P_s, the pressure at the surface, to P_0, the pressure at the outmost zone of the mesh, with T_s as the initial value, we then can find out what T_{2N+1} is. The surface is defined to be at optical depth $\tau = \frac{2}{3}$, where τ is defined by $d\tau = -\kappa\rho dr$. Then:

$$\frac{dP}{d\tau} = -\frac{GM}{R^2\kappa}\frac{1}{1-\frac{2GM}{Rc^2}} = -\frac{g_s}{\kappa}. \tag{2.32}$$

Assuming the opacity to be constant and integrating the above equation from $\tau = 0$ to $\tau = 2/3$ ($P = 0$ at $\tau = 0$), we get:

$$P_s = \frac{2g_s}{3\kappa_s}. \tag{2.33}$$

The opacity κ is a function of the surface temperature T_s and surface density ρ_s, and pressure P_s is related to density ρ_s by the equation of state. So Equation(2.32) is a transcendental equation about ρ_s. To solve this equation, we use the bisection method. We choose two bracketing values as $\rho_l = 10^{-4} gm/cm^3$ and $\rho_u = 10^2 gm/cm^3$, which safely bracket all possible surface densities for the temperatures we are interested in. From ρ_s, T_s and the equation of state $P_s(\rho_s, T_s)$,, we can calculate the surface pressure. Fig(2.4) shows the surface pressure P_s we find for different temperatures by solving Equation(2.32). The integration of Equation(2.28) is done by the fourth order Runger-Kutta method. Fig(2.5) shows the results of the integration. It gives the temperature vs. pressure relation in the envelope layer. The integration will yield the temperature T_{2N+1}, which is the boundary temperature we are looking for. We evaluate T_{2N+1} at the beginning of each new time calculation, and during each iteration, we keep this temperature fixed. The coefficients $A_{2N,j}$, F_{2N} then can be calculated by equations in Appendix A.

In the next section, we discuss the basic physical inputs such as, the equation of state, neutrino emissivity, specific heat and opacity needed for the calculation.

2.3 Physical Input

2.3.1 Equation of State & Specific Heat

In order to understand a system's thermal properties, we begin with the free energies. In Richardson et al (1982), they used the Helmhotz free energy $A(N,V,T)$. In terms of the Helmhotz free energy, the equation of state, entropy and specific heat can be expressed as :

$$P = -\left(\frac{\partial A}{\partial V}\right)_{N,T}, \tag{2.34}$$

$$S = -\left(\frac{\partial A}{\partial T}\right)_{N,V}, \tag{2.35}$$

$$c_V = T\left(\frac{\partial S}{\partial T}\right)_{N,V}. \tag{2.36}$$

The equation of state and specific heat can be obtained from the entropy $S(N,V,E)$

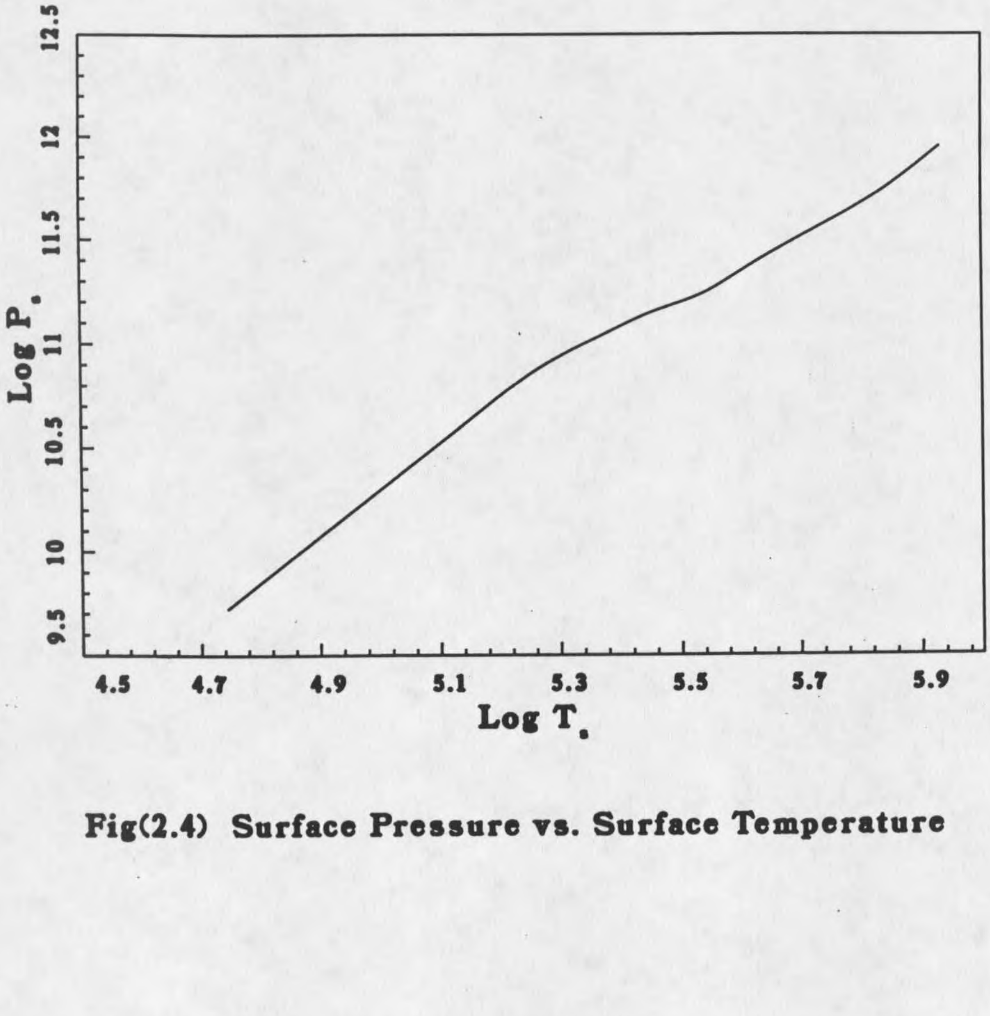

Fig(2.4) Surface Pressure vs. Surface Temperature

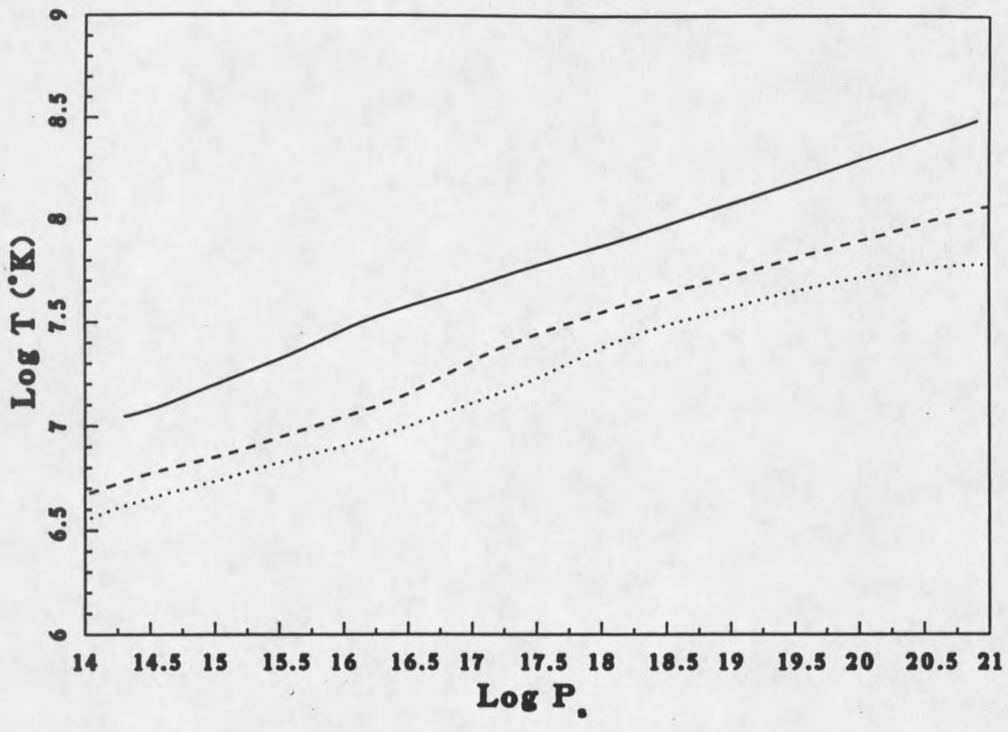

Fig(2.5) Structures of the Envelope

also. In terms of the entropy, P and c_V are:

$$P = T(\frac{\partial S}{\partial V})_{N,E}, \tag{2.37}$$

$$c_V = T(\frac{\partial S}{\partial T})_{N,V}. \tag{2.38}$$

Since neutron stars are rather "cold", we assume the composition of the neutron star interior to be of cold catalyzed matter which depends on the density only. Table(2.1) is taken from Tsuruta (1964). It lists the most stable elments corresponding to different densities. Near the surface, the most stable element is ^{56}Fe. As the density increases, we find more and more neutron-rich nuclei. When the density reaches $4.3 \times 10^{11} gcm^{-3}$, free neutrons will drip out of the nuclei. In this region, free neutrons, free electrons and neutron-rich nuclei exist together. When the density exceeds $2.8 \times 10^{14} gcm^{-3}$, nuclei dissolve into free neutrons. The composition is dominated by neutrons with a small fraction of protons and electrons. At still higher density, it is possible that muons, pions, hyperons and quark matter may appear. In our study, we use the "standard model"; that is, inside the stellar core, we do not assume the presence of exotic particles, such as muons, pions or quarks. (For non-standard cooling, see Umeda, Tsuruta and Nomoto 1994). In the remainder of this section, we will discuss the equations of state and specific heat in different regions separately.

Outer Crust ($\rho < 4.3 \times 10^{11} gm/cm^3$)

The outer crustal region of neutron stars consists of electrons and heavy ions. While throughout the outer crust region electrons are in partially degenerate and partially relativistic, the state of ions changes from an ideal gas to a solid lattice, Table (2.1) Compositions Of Neutron Star Matter

Temperature	E_F (MeV)	ρ	A_m	Z_m
5×10^9 °K	0.17	3.86×10^5	4	2
	5	2.17×10^9	66	28
	10	1.87×10^{10}	82	32
	15	6.70×10^{10}	78	28
	20	1.78×10^{11}	80	28
	23	2.72×10^{11}	80	28
	25	8.18×10^{11}	118	36
2×10^9 °K	0.17	3.64×10^5	56	26
	5	2.15×10^9	66	28
	10	1.87×10^{10}	82	32
	15	6.31×10^{10}	80	30
	20	1.70×10^{11}	80	28
	23	2.79×10^{11}	120	38
	25	6.81×10^{11}	118	36

as temperature drops from $10^8 K$ at the inner boundary of the outercrust to $10^7 K$ at the surface. For electrons, the equation of state and specific heat can be found in Sugimoto & Nomoto 1975. For ions, the equation of state and specific heat are different for the liquid state and the ideal gas state. The transition from the liquid phase to the solid phase takes place when

$$\Gamma = \frac{Z^2 e^2}{akT} \sim 170, \tag{2.39}$$

where Z is the atomic number and a is the radius of ions. The parameter Γ is defined as the ratio of the Coulomb potential to the thermal energy. When T is low, $\Gamma \gg 1$, the Coulomb energy dominates the thermal energy, and the ions will tend to form a lattice structure. When T is high, $\Gamma \ll 1$, the thermal energy is much higher than the Coulomb energy, the ions will be able to overcome the Coulomb attraction, destroy the lattice structure and become a gas. At the intermediate temperature, the ions comprise a Coulomb liquid. The value of Γ for the liquid-solid phase transition is found by using Monte Carlo simulations (Slattery, Doolen and Dewitt 1982). When the ions are in the gas phase, we assume that it is an ideal gas, the equation of state and the specific heat can be easily written down. For ions in the liquid phase, from Monte Carlo simulations, the fitted formula for the Helmholtz energy is available in Slattery, Doolen and Dewitt 1982. When the ions are in the solid phase, the Helmholtz free energy contributed by the ions includes the potential energy of Coulomb force, and the phonons of a bcc lattice (Richardson et al 1982).

$$A_{phonon} = nkT \sum_{q,j} [\frac{1}{2} \frac{h\omega_j \vec{q}}{kT} + \ln\{1 - \exp(-\frac{h\omega_j \vec{q}}{kT})\}, \tag{2.40}$$

where $\omega_j(\vec{q})$ are the normal mode frequencies corresponding to wave vector $\vec{q}$ with j specifying the three excitation modes (two transverse and one longitudinal). The potential energy is

$$A_{potential} = nkT(-0.895929\Gamma - \frac{1750}{\Gamma^2}). \qquad (2.41)$$

The first term is the temperature independent static energy of a bcc lattice, while the second term is the classical anharmonic term. From the Helmholtz free energy, the pressure can be calculated.

Inner Crust ($4.3 \times 10^{11} gm/cm^3 < \rho < 2.8 \times 10^{14} gm/cm^3$)

Here the composition is heavy ions, free neutrons and free electrons. The electrons are in the relativistic, completely degenerate state, the ions are in the ideal gas state and the neutrons are in the partially degenerated partially relatistic state. The equation of state at this region is taken from Negele and Vantherin (1972).

Around the regions where the density is about $4.3 \times 10^{11} gm/cm^3$, we use interpolation to fit P smoothly into the outer crust region.

Core ($\rho > 2.8 \times 10^{14} gm/cm^3$)

Inside this region, free neutrons are the major constituent, plus a small fraction of protons and electrons. For densities below $2.8 \times 10^{14} gm/cm^3$, the physical properties of dense matter are fairly well understood. But for the regions where the density is above $2.8 \times 10^{14} gm/cm^3$, our knowledge is rather poor; not only because the correct forms of the nuclear potential are still under investigation, but also because a satisfactory many-body computational method for solving the non-local Shrödinger equation remains to be developed.

Yukowa potential is the simpliest model for the nuclear potential, but it is far from adequate. A more complicated model is the Reid type potential. The Reid type potential is a sum of Yukowa functions of different ranges and strengths. The coefficients in the Reid type potential were separately adjusted to fit the nucleon-nucleon scattering data. Different nuclear potential models made different assumptions for nuclear interactions. In some of our calculations, we chose three representative nuclear potential models: FP, PS and BPS model (See section §1.2) in order to see the effect of these different assumptions.

Table (2.2) shows the pressure vs. density relation for the three models which we adopt, in the range of $10^{11} \sim 1 \times 10^{16} gcm^{-3}$.

2.3.2 Neutrino Emissivity

Neutrinos are produced during the various neutrino processes (discussed below). Because the cross sections for the interactions between the neutrinos and neutron star matter are so small, just after the temperature drops down to 10^9 K, the mean free path of the neutrinos will be larger than the radius of neutron stars. So the neutrinos will pass through the stars unimpeded. The neutrinos carry away the thermal energy of neutron stars, and the star cools.

When the neutrinos pass through a neutron star, there are two kinds of reactions between the neutrinos and the neutron star matter: charged current interactions and neutral current interactions. The charged current interactions are the following three

Table(2.2) Equation Of State For Model FP, PS, BPS

Log(ρ)	Model FP Log(P)	Model PS	Model BPS
11.02	29.17468	29.17465	29.17468
11.32	29.51720	29.51716	29.51720
11.63	29.89241	29.89237	29.89241
11.93	30.04269	30.04265	30.04269
12.15	30.21929	30.21925	30.21929
12.43	30.42488	30.42484	30.42488
12.65	30.62630	30.62626	30.62630
12.98	31.03850	31.03852	31.03856
13.20	31.36316	31.36312	31.43889
13.42	31.69965	31.69961	31.76297
13.69	32.12194	32.12190	32.1700
13.91	32.46582	32.80718	32.55143
14.24	33.08502	33.62062	33.14720
14.46	33.65866	34.15431	33.56186
14.70	34.29170	34.76411	34.07811
14.80	34.56619	35.01718	34.40704
15.00	35.13920		34.80771
15.32	36.17873		35.79082
15.58	36.93885		36.46370
15.72			36.46370

reactions:

$$\nu_e + n \longrightarrow p + e^-, \tag{2.42}$$

$$\overline{\nu_e} + p \longrightarrow n + e^+, \tag{2.43}$$

$$\overline{\nu_e} + p + n \longrightarrow n + n + e^+. \tag{2.44}$$

The neutral current interactions are:

$$n + \nu_e \longrightarrow n + \nu_e, \tag{2.45}$$

$$n + \nu_\mu \longrightarrow n + \nu_\mu. \tag{2.46}$$

For the charged current interactions, the cross section of the interaction is

$$\sigma_e = \chi\sigma_0(\frac{E_\nu}{m_e c^2})^2 \frac{E_\nu}{E_F(e)}, \tag{2.47}$$

where $\sigma_0 \equiv \frac{4}{\pi}(h/m_e c^2)^{-4}(G_F/m_e c^2)^2 = 1.76 \times 10^{-14} cm^2$ with G_F as the Fermi coupling constant, and $\chi = 0.06$ (Weinberg-Salam-Glashow (WSG) theory). The cross section for the neutral current interactions is

$$\sigma_n = \frac{1}{4}\sigma_0(\frac{E_\nu}{m_e c^2})^2, \tag{2.48}$$

where σ_0 is the same as above. The mean free path of neutrinos is

$$\lambda = (\sigma n)^{-1}. \tag{2.49}$$

Here n is the particle number density, and σ is the cross section. For the charged current interaction:

$$\lambda_c = (\sigma_e n_e)^{-1} \sim (9 \times 10^7 km)(\frac{\rho_{nuc}}{\rho})^{4/3}(\frac{100keV}{E_\nu})^3, \tag{2.50}$$

where $\rho_{nucl.}$ is the nuclear density, ρ is the density of the neutron star matter. E_ν is the energy of neutrinos. For the neutral current interaction:

$$\lambda_n = (\sigma_n n_n)^{-1} \sim 300km(\frac{\rho_{nuc}}{\rho})(\frac{100keV}{E_\nu})^2. \tag{2.51}$$

The effective mean free path is

$$\begin{aligned} \lambda_{eff} &= (\lambda_c \lambda_n)^{1/2} & (2.52) \\ &\sim 2 \times 10^5 km(\frac{\rho_{nuc}}{\rho})^{7/6}(\frac{100keV}{E_\nu})^{5/2}. & (2.53) \end{aligned}$$

The neutrinos are thermal, so E_ν is about $kT \sim 100keV$. Thus $100keV/E_\nu^{\frac{5}{2}} \sim 10^{-3}$ and inside the core $(\rho_{nuc}/\rho)^{\frac{7}{6}}$ is about 1. λ_{eff} then is $\sim 100km$, much longer than the radius of the neutron star $\sim 10km$. Consequently the neutron star interior is basically transparent to the neutrinos.

Inside neutron stars, the neutrinos are produced both inside the core and in the crustal region. Inside the core, the basic processes are the modified URCA process, and neutron-neutron and neutron-proton bremsstrahlung processes. Inside the crust, the major processes are the electron-ion neutrino bremsstrahlung process and the direct coupled electron-neutrino processes, such as plasmon-neutrino, photon-neutrino and electron-positron pair neutrino processes.

The modified URCA process proceeds as follows:

$$n + n \longrightarrow n + p + e^- + \overline{\nu_e}, \tag{2.54}$$

$$n + p + e^- \longrightarrow n + n + \nu_e. \tag{2.55}$$

The direct URCA process, $n \longrightarrow p + e^- + \overline{\nu_e}$, is usually considered as highly impossible inside the core of neutron stars, because of the energy restriction. But if there is a bystander particle present to absorb the momentum of neutrons, a modified URCA process is possible, as shown in Equations (2.53) and (2.54). Fig(2.6) gives the modified URCA emissivity vs. temperatures at different densities.

The nn and np bremsstrahlung processes are

$$n + n \longrightarrow n + n + \nu + \overline{\nu}, \tag{2.56}$$

$$n + p \longrightarrow n + n + \nu + \overline{\nu}, \tag{2.57}$$

and the emissivity due to nn and np bremsstrahlung processes is given in Fig(2.7). In the crust, the electron-ion neutrino bremsstrahlung is due to the collisions between electrons and nuclei,

$$e^- + (Z, A) \longrightarrow e^- + (Z, A) + \nu_e + \overline{\nu_e}. \tag{2.58}$$

The kinetic energies of the participating particles are transformed into neutrino-antineutrino pairs. The direct coupled electron-neutrino processes are:

$$\gamma_{plasmon} \longrightarrow \nu_e + \overline{\nu_e} \qquad \text{plasma neutrino} \tag{2.59}$$

$$\gamma + e^- \longrightarrow e^- + \nu_e + \overline{\nu_e} \qquad \text{photo neutrino} \tag{2.60}$$

$$e^+ + e^- \longrightarrow \nu_e + \overline{\nu_e} \quad \text{electron positron pair neutrino} \tag{2.61}$$

In Fig(2.8), we show how the plasma neutrino emissivity varies with temperature and density. Fig(2.8) indicates that the plasma emissivity drops more quickly with the decrease of temperatures than either the modified URCA process or the nn, np

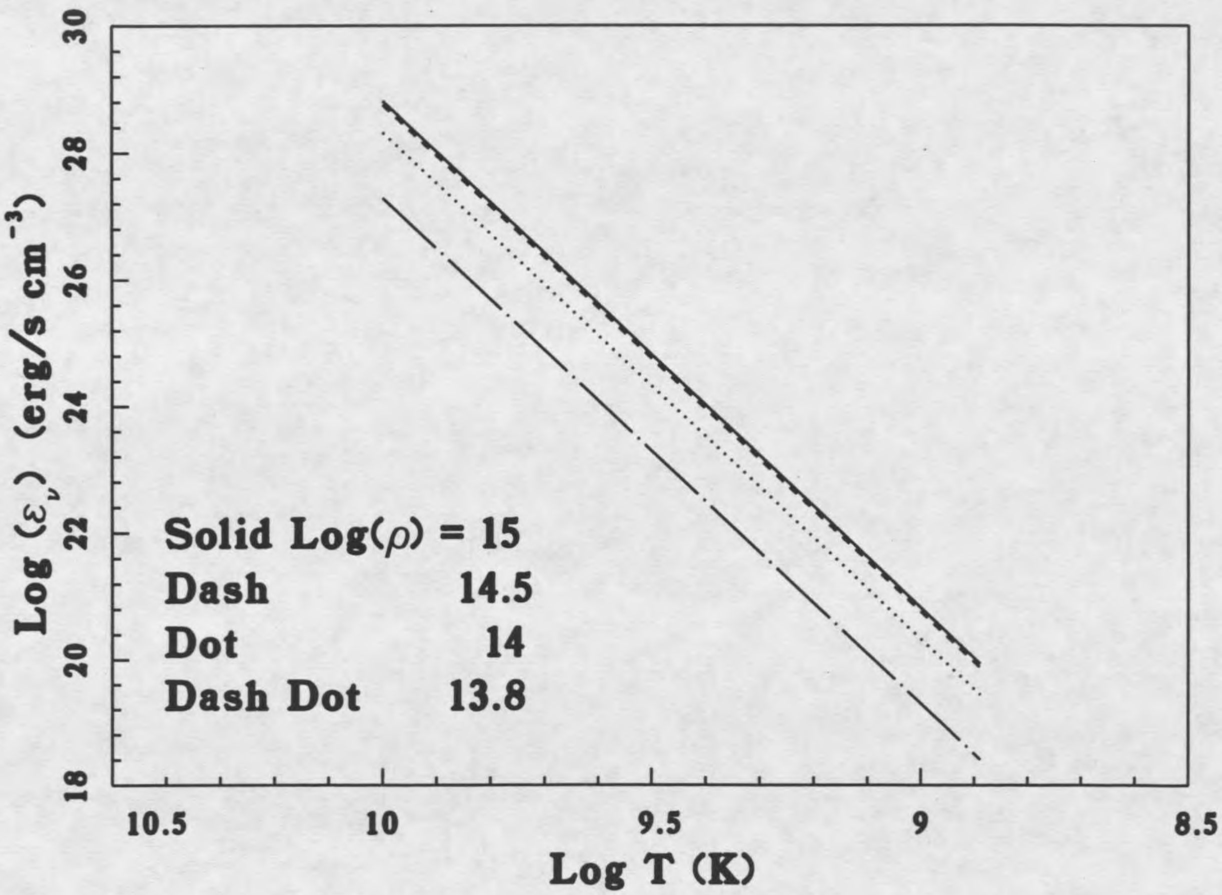

Fig(2.6) Emissivity of Modified URCA Process

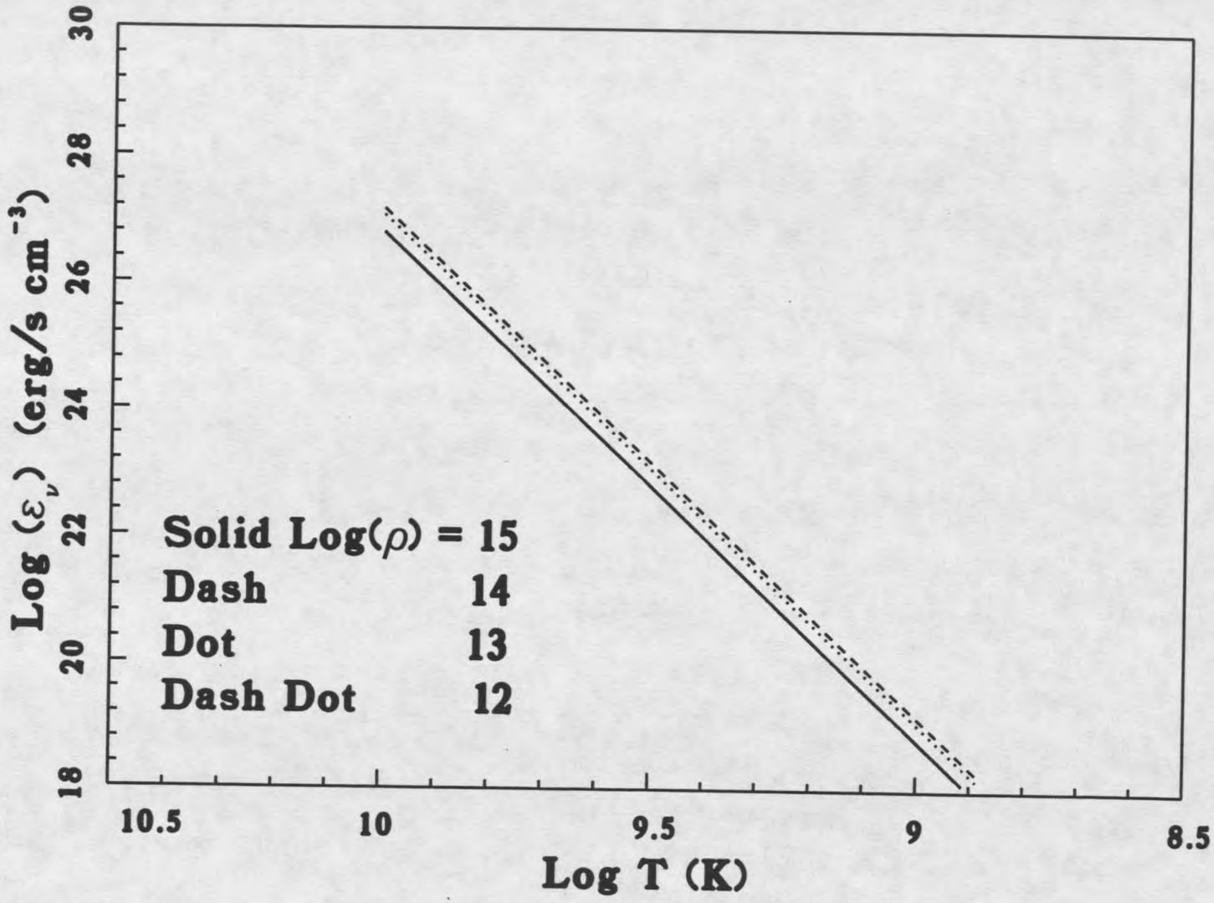

Fig(2.7) Emissivity of Bremsstrahlung Process

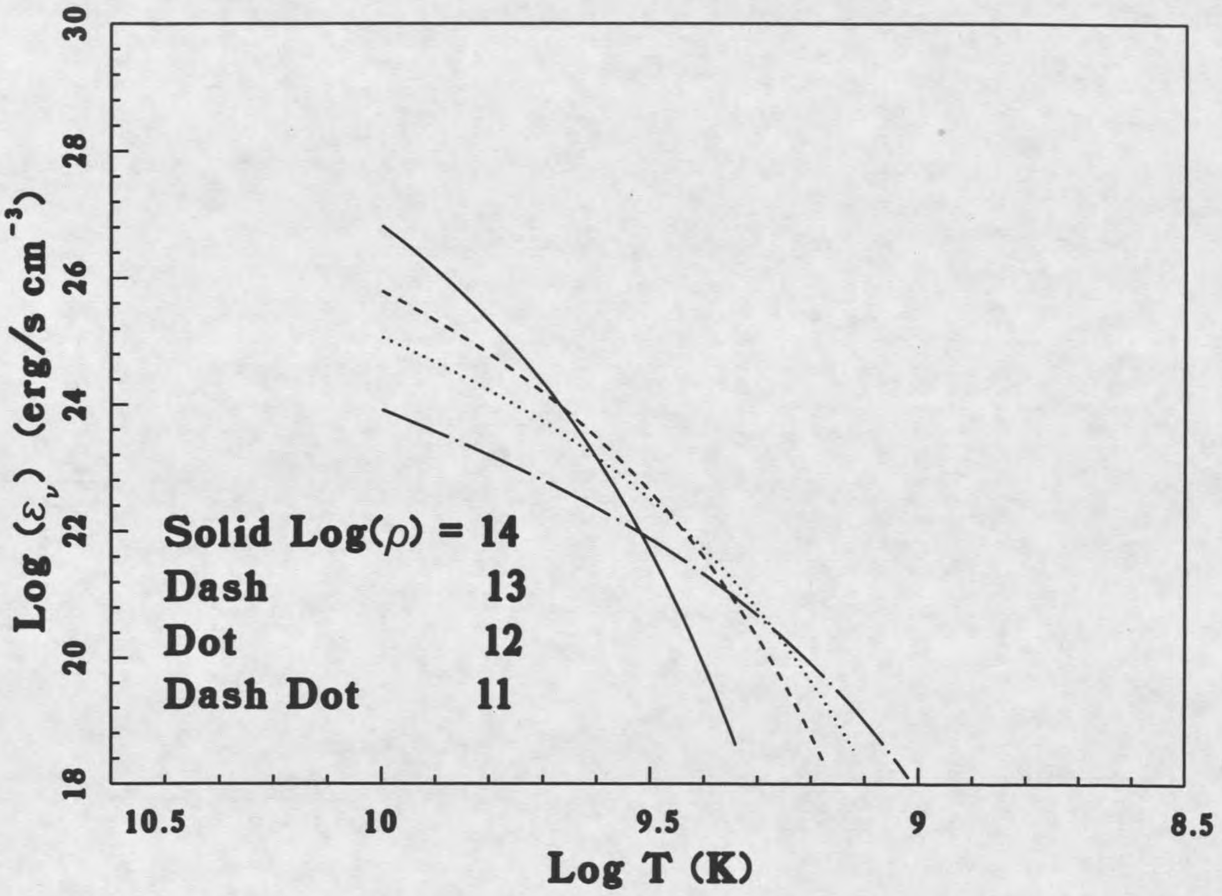

Fig(2.8) Emissivity of Plasmon Neutrino Process

bremsstrahlung processes. By comparing Fig(2.8) with Fig(2.7) and Fig(2.6), we see that at high densities the plasma emissivity is about two orders of magnitude lower than the other two emissivities; the plasma neutrino emission is less important than the other two processes.

We use the results from Friman and Maxwell (1979) for the neutrino processes inside the core. Inside the crust, the neutrino emissivity due to the electron ion neutrino bremsstrahlung process is different in the liquid region than in the solid region. In the liquid phase, the various neutrino emissivities can be found in Kohyama 1983 and Itoh et al 1984a. The neutrino emissivities in the solid phase are given in Itoh et al 1984b,c. For the direct-coupled electron-neutrino processes, we take the emissivity given by Munakata, Kohyana and Itoh (1985).

2.3.3 Opacity

Inside neutron stars, there are two ways to transfer energy from the interior to the surface: radiation and conduction. The energy transfer equation is

$$L = -\frac{16\sigma}{3}\frac{T^3}{\kappa\rho}(4\pi r^2)ne^{-2\phi}\frac{d(Te^{\phi})}{dr}. \tag{2.62}$$

Here κ is the opacity, which is related to conductivity λ as:

$$\kappa = \frac{4acT^3}{3\rho\lambda}, \tag{2.63}$$

with

$$a = \frac{4\sigma}{c}, \tag{2.64}$$

where σ is Stefan-Boltzman constant.

The total opacity is determined by the radiative opacity and the heat conductivity through the relation:

$$\frac{1}{\kappa} = \frac{1}{\kappa_r} + \frac{1}{\kappa_c}. \tag{2.65}$$

Here κ_r stands for the opacity due to the radiative transfer, and κ_c the opacity due to the heat conductivity.

We follow Richardson et al (1982) for the treatment of opacities. The radiative opacity is given by analytic formula fitted to the numerical results. The radiative opacity can be divided into three parts,

$$\kappa_r = \kappa_{bf} + \kappa_{ff} + \kappa_{es}, \tag{2.66}$$

where κ_{bf} is the opacity due to the bound free transition, κ_{ff} is the opacity due to the free-free transition, κ_{es} is the opacity due to the electron scattering.

The conductive opacity κ_c is completely dominated by the contribution from the electrons. There are four processes which contribute to κ_c: the electron-electron scattering κ_{ee}, the electron-impurity scattering κ_{ei}, the electron-phonon scattering κ_{ep} and the electron- neutron scattering κ_{en}. In the low density region ($\rho < 1.04 \times 10^4 gcm^{-3}$), the heat conductivity is of a nonrelativistic, degenerate gas (Clayton 1968, p.250). In the moderate-density region ($1.04 \times 10^4 gcm^{-3} < \rho < 1.33 \times 10^{14} gcm^{-3}$), we use the tabulated heat conductivity given by Flowers and Itoh (1976). In the high density region ($\rho > 1.33 \times 10^{14} gcm^{-3}$), the heat conductivity is taken from Baym, Pethick and Pines (1969). The total opacity κ then can be calculated by using

$$\frac{1}{\kappa} = \frac{1}{\kappa_r} + \frac{1}{\kappa_c}$$

$$= \frac{1}{\kappa_{bf} + \kappa_{ff} + \kappa_{es}} + \frac{1}{\kappa_c}. \tag{2.67}$$

Fig(2.9) shows the total opacity as a function of density at different temperatures.

In this section, we introduced the physical inputs necessary for the thermal calculations of neutron stars: the equation of state, the neutrino emissivity and opacity. The results of the cooling calculations of non-magnetic neutron stars are presented in Fig(2.10). The solid curve is for the FP Model, the dashed curve is for the PS Model, and the dotted curve is for the BPS Model. The detailed discussion can be found in NT87. In Fig(2.10), we also plot the most recent observational data. Among the 13 pulsars shown, three are detections. They are PSR0656+14, PSR1055-52 and Geminga. Others are upper limits. For the Crab Pulsar, there are two upper limits. The higher one is for the PS Model, the lower one is for the FP Model.

So far we have neglected the effects of a magnetic field on the opacities. The magnetic field causes anisotropy of opacities, causing the temperature variations over the surface, and changes in the core-surface temperature relation. In the next section, we will discuss how the opacities are altered under strong magnetic fields. In §2.4, we will present our results from 1-dimensional cooling calculations for magnetized neutron stars.

2.4 Effects of Magnetic Fields on Opacity

2.4.1 General Consideration

Strong magnetic fields ($10^9 \sim 10^{13} Gauss$) are believed to exist near the surface of neutron stars (See §1.3). The presence of the magnetic fields will alter the physical

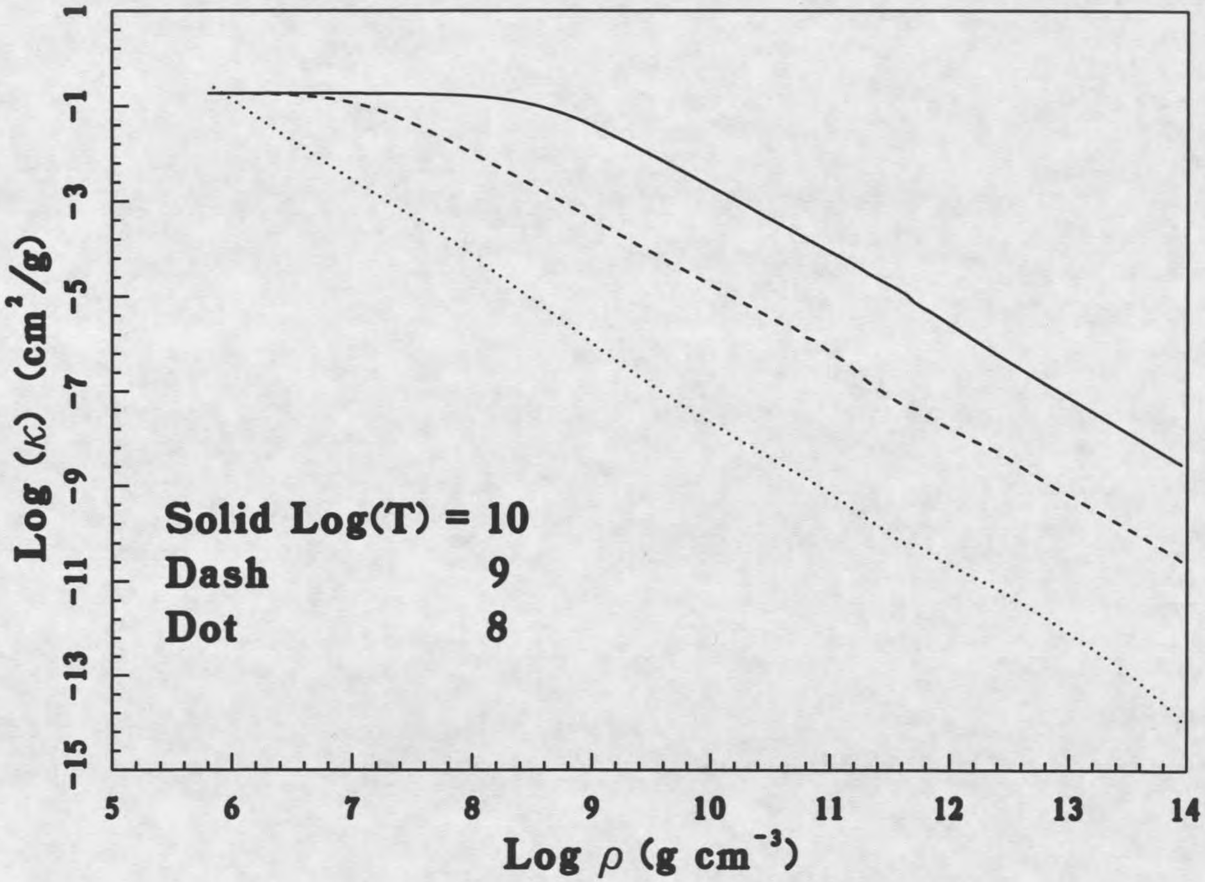

Fig(2.9) Total Opacity κ vs. Density ρ

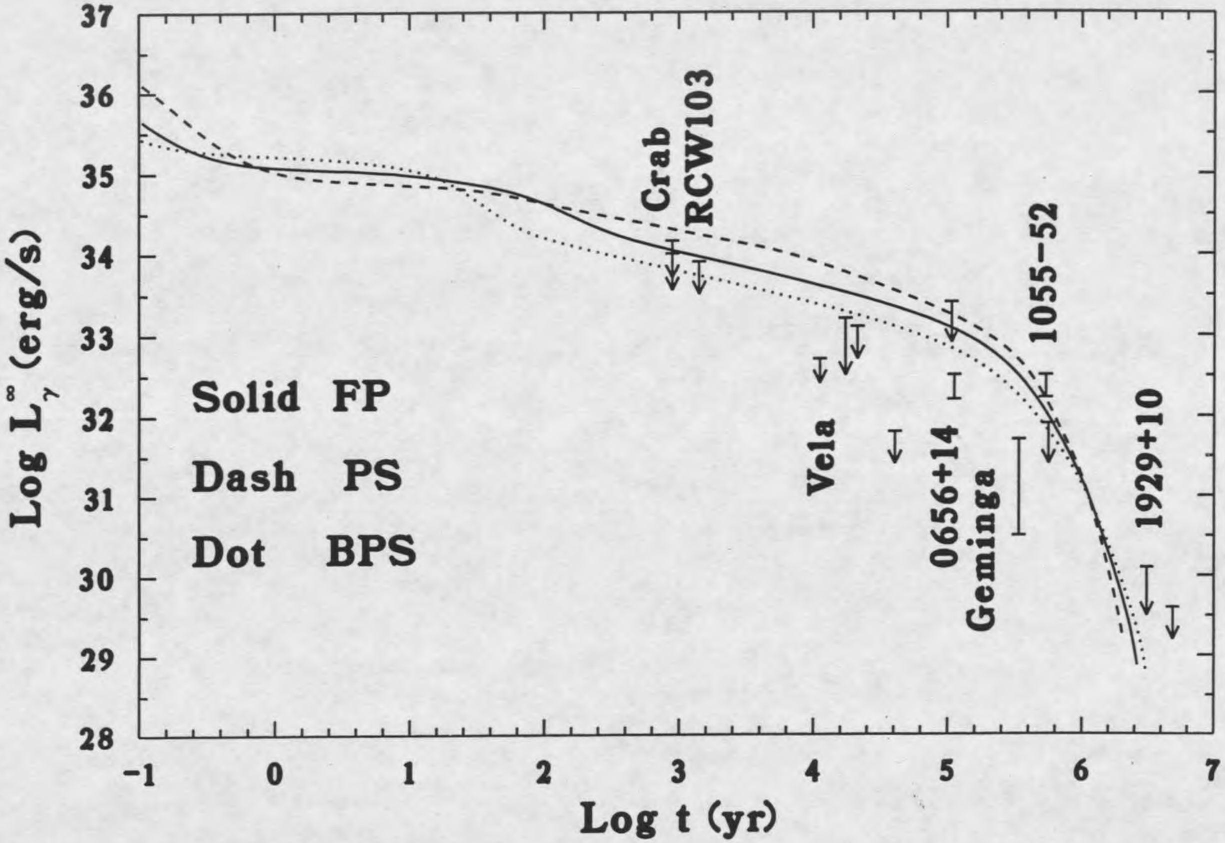

Fig(2.10) Cooling Curves of the FP, PS, BPS Models conditions and transport properties on the surface and in the crustal layers of neutron stars (Tsuruta et al 1972, Tsuruta 1974, 1975, 1979, Glen and Sutherland 1980, Nomoto and Tsuruta 1981, Yakovlev and Urpin 1981). Hernquist (1984) derived the thermal conductivities of dense matter under strong magnetic fields, and carried out longitudinal cooling calculations. He concluded that the magnetic field had negligible effect on the thermal evolution of neutron stars. Later, using a 1-dimensional approach, Shaaf (1990) performed the envelope calculations for different directions with respect to the magnetic axis. His results show that the equatorial temperature is much lower than the the polar temperature for the same core temperature. In other words, the core-surface temperature relation is significantly different for the longitudinal and transverse directions. A few years ago, Umeda carried some preliminary investigations on this subject using a 1-dimensional approximation method, and he was able to obtain some interesting results. Recently, I began construction of a 2-dimensional code to extensively investigate the influences of magnetic fields.

As a starting point, I constructed an "exact" 1-dimensional (1D) cooling code. I then carried out the calculations along different directions with respect to the magnetic axis with the 1D approach. The interior temperatures in different directions are very different, and the differences in temperatures along different directions will cause heat flows along tangential directions. In the 1D approximation, we ignore such heat flows. Both Hernquist and Shaaf used only a 1D approximation; our 1D results agree with theirs. However, as explained below, the 1D model is far from adequate. In the second stage of my research, I constructed a 2D code to take into account the tangential heat flows. The 2D code will be described in Chapter 3. Here I will first discuss how magnetic fields chanon stars. In

§2.4, I will present the results from 1D calculations.

As pointed out in section §1.3, the energy of electrons is quantized under strong magnetic fields. The energy spectrum of Landau levels is given by:

$$\epsilon = (p_z^2c^2 + m_e^2c^4 + 2n\hbar\omega_B m_e c^2)^{1/2}, \; n = 0, 1, 2, \cdots \tag{2.68}$$

with p_z as the momentum along the field, and

$$\omega_B = \frac{eB}{m_e c}. \tag{2.69}$$

The energy levels are doubly degenerate for $n \neq 0$ and non-degenerate for $n = 0$.

When electrons are distributed among various Landau levels, the number density of a free electron gas is

$$n_e = \frac{m_e\omega_B}{(2\pi\hbar)^2} \sum_{n_s} g_n \int_{-\infty}^{\infty} \frac{1}{1 + \exp(\frac{\epsilon-\mu}{k_BT})} dp_z. \tag{2.70}$$

$g_n = 1$ when $n = 0$, and $g_n = 2$ when $n \neq 0$. The summation is over all the populated Landau levels. The integral is over 1-dimensional momentum space p_z. How many Landau levels will be populated by the electrons depends on the temperature and density. The above equation can be also written as:

$$\sum_{n_s} g_n \int_{-\infty}^{\infty} \frac{1}{1 + \exp(\frac{\epsilon-\mu}{k_BT})} dp_z = \frac{n_e(2\pi\hbar)^2}{m_e\omega_B}. \tag{2.71}$$

Given the electron number density n_e and temperature T, we can determine from the above equation how many Landau levels will be populated. Let us analyze several situations with different combinations of T and ρ. At fairly low temperatures, the thermal energy of the electrons is less than the spacing between the Landau levels. In low density regions, most of electrons will reside in the ground level, and the electrons will be difficult to excite by the thermal motions. In this case, the magnetic field is strongly quantized, while in high density regions, electrons will populate many Landau levels. In this case, the magnetic field is slightly quantized.

At high temperatures, the electron thermal energy is larger than the spacing between two consecutive Landau levels, and the magnetic field will not be quantized due to the smearing of the electron thermal motions.

We define T_B as the corresponding temperature of the energy difference between two consecutive energy levels, $T_B \equiv \hbar\omega_B/k_B$ where k_B is the Boltzmann constant. We define ρ_B as $2.066 \times 10^6(B/B_c)^{\frac{3}{2}}\mu_e$, with B_c as $4.44 \times 10^{13}G$. When $T < T_B$ and $\rho > \rho_B$, the magnetic field is slightly quantized. Such conditions prevail in the crust of a neutron star through most of the star's life. When $T < T_B$ and $\rho < \rho_B$, the magnetic field is strongly quantized, this is the situation inside the envelope of neutron stars. When $T > T_B$, as in the core, the field is non-quantized. We define T_F as $T_F = T(\sqrt{1+x_B^2}-1)$, with $x_B = p_F/m_e c$. T_F is the temperature corresponding to the electron Fermi energy E_F, and when $T \ll T_F$, the electrons will be highly degenerate. The quantity x_B generally depends on the B field. When $\rho \gg \rho_B$, strongly degenerate electrons populate many Landau levels, and the Fermi energy becomes independent of B.

Quantized magnetic fields affect the thermodynamic properties of the matter.

The bulk thermodynamic quantities, such as pressure and chemical potential, are determined by all electrons. Accordingly, these quantities are only affected by the strongly quantized fields, and will not be affected by weakly quantized fields. The quantities determined by thermal electrons near the Fermi surface, such as the heat capacity, entropy, and transport properties, show large oscillations under the action of quantized fields (the de Hass-van Alphen effect (Pathria 1986)). The oscillatory nature of these physical properties can be explained by the grand partition function $\mathcal{Q}$ of the system, which is given by the usual formula

$$\ln \mathcal{Q} \equiv \frac{PV}{kT} = \int_0^\infty \ln\{1 + ze^{-\beta\epsilon}\} a(\epsilon) d\epsilon, \tag{2.72}$$

where $z = \exp(\mu/kT)$, $\beta = 1/kT$ and $a(\epsilon)$ denotes the density of states of the system about the energy value ϵ. Integrating twice by parts, we find

$$\ln \mathcal{Q} = -\beta \int_0^\infty \Omega(\epsilon) \{ \frac{\partial}{\partial \epsilon} (\frac{1}{z^{-1} e^{\beta\epsilon} + 1}) \} d\epsilon, \tag{2.73}$$

where $\Omega(\epsilon)$ is

$$\Omega(\epsilon) = -V \frac{2(2\pi m)^{3/2}}{h^3} (\frac{\mu B}{h^3})^{5/2} \sum_{l=1}^{\infty} \frac{(-1)^l}{l^{5/2}} \cos(\frac{l\pi\epsilon}{\mu B} - \frac{\pi}{4}). \tag{2.74}$$

Note that as ϵ changes, $\Omega(\epsilon)$ oscillates. In order that the oscillatory term be significant, the field strength is required to be of the order of $10^5 T$ Gauss. In the envelope and the crust of neutron stars, this condition is satisfied. Therefore in these regions, it is necessary to eliminate the oscillations of the physical quantities and find fitted smooth functions.

As pointed out by Hernquist (1984), the corrections to the equation of state for free electrons due to the magnetic field are negligible for the relation between the core and surface temperatures, and therefore, in the rest of this section, we will concentrate on how the magnetic field changes the transport properties.

2.4.2 Heat Transport Under Strong Magnetic Fields

Both means of heat transport, radiative transfer and electron conduction, are greatly influenced by magnetic fields. In the presence of a magnetic field, the radiative transfer equation does not involve only radiation intensity, e.g. through the following equation (Chandrasekhar 1938):

$$\frac{dI_\nu}{\rho ds} = j_\nu - \kappa_\nu I_\nu. \tag{2.75}$$

Instead, we must use $\rho_{\alpha\beta}(\overrightarrow{n}, \omega(\overrightarrow{r}))$, the polarization matrix of the radiation field, where $\overrightarrow{n}$ is the direction of the propagation, $\omega(\overrightarrow{r})$ is the cyclic frequency of the radiation, and α and β are the polarization indices (Pavlov & YakovloHev 1977). If the local thermodynamic equilibrium is assumed, the equation for radiative transfer is (scattering not included):

$$\begin{aligned} (\overrightarrow{n} \cdot \nabla)\rho_{\alpha\beta} &= -\frac{1}{2}\sum_\gamma (T_{\alpha\gamma}\rho_{\gamma\beta} + \rho_{\alpha\gamma}T^+_{\gamma\beta}) + \\ &\quad \frac{1}{4}(T_{\alpha\beta} + T^+_{\alpha\beta})B_\omega, \end{aligned} \tag{2.76}$$

where B_ω is the Planck function, $B_\omega(T) = (\hbar\omega^3/2c\pi^2)[1/(e^{\hbar\omega/kT} - 1)]$, with $T_{\alpha\beta}(\overrightarrow{n}, \omega(\overrightarrow{r}))$ as the absorption coefficients matrix. If we assume that the radiation field differs only slightly from the local thermodynamic equilibrium, which is described by the Plank function, $\rho_{\alpha\beta}$ can be expressed as the Planck function plus small corrections,

$$\rho_{\alpha\beta} = \frac{1}{2}\delta_{\alpha\beta}B_\omega + \Delta\rho_{\alpha\beta}. \tag{2.77}$$

Substitute Equation(2.76) into the transfer equation(2.75), and we then have:

$$\delta_{\alpha\beta}(\overrightarrow{n}\cdot\nabla)B_\omega = -\sum_\gamma(T_{\alpha\gamma}\Delta\rho_{\gamma\beta} + \Delta\rho_{\alpha\gamma}T^+_{\gamma\beta}). \tag{2.78}$$

$T_{\alpha\gamma}$ and $T^+_{\alpha\gamma}$ are known matrices from the properties of the material. Suppose

$$T_{\alpha\gamma}u_{\gamma j} = T_j u_{\alpha j}, \tag{2.79}$$

where $u_{\alpha j}$ and T_j are eigenvectors and eigenvalues of the matrix $T_{\alpha\gamma}$. Then,

$$T_{\alpha\gamma} = T_j u_{\alpha j}u^{-1}_{\gamma j}. \tag{2.80}$$

Bring Equation(2.79) back into Equation(2.77), and obtain

$$\begin{aligned}\delta_{\alpha\beta}(\overrightarrow{n}\cdot\overrightarrow{\nabla})B_\omega &= -\sum_\gamma T_j u_{\alpha j}u^{-1}_{\gamma j}\Delta\rho_{\gamma\beta} \\ &\quad -\sum_\gamma \Delta\rho_{\alpha\gamma}T^*_j(u^{-1}_{\gamma j})^+(u_{\alpha j})^+.\end{aligned} \tag{2.81}$$

The solution of the above equation is

$$\Delta\rho_{\alpha\beta} = -\chi_{\alpha\beta}(\overrightarrow{n}\cdot\overrightarrow{\nabla})B_\omega, \tag{2.82}$$

with

$$\chi_{\alpha\beta} = \sum_{jk\gamma} u_{\alpha j}u^{-1+}_{j\gamma}u^{-1}_{\gamma k}u^+_{k\beta}/(T_j + T^*_k). \tag{2.83}$$

The intensity of the radiation field then is :

$$\begin{aligned}I(\overrightarrow{n},\omega(\overrightarrow{r})) &= \sum_\alpha \rho_{\alpha\alpha} \\ &= B_\omega - (\sum_\alpha \chi_{\alpha\alpha})(\overrightarrow{n}\cdot\overrightarrow{\nabla})B_\omega \\ &= B_\omega - (\sum_\alpha \chi_{\alpha\alpha})\frac{\partial B_\omega}{\partial T}\overrightarrow{n}\cdot\nabla T\end{aligned} \tag{2.84}$$

The value of $\sum_\alpha \chi_{\alpha\alpha}$ is a function of the elements of the matrix $T_{\alpha\beta}$, which depends on the properties of the material and the environment the photons travel through.

From $I(\vec{n}, \omega(\vec{r}))$, the flux parallel to the field $j_\parallel$ and the flux perpendicular to the field $j_\perp$ can be calculated by multiplying $I(\vec{n}, \omega(\vec{r}))$ by $\cos\theta$ for $j_\parallel$ and $\sin\theta$ for $j_\perp$, and integrating over all frequencies and over all directions. Thus

$$j_\parallel = -D_\parallel \nabla_\parallel T, \tag{2.85}$$

with

$$D_\parallel = 4\pi \int_0^\infty \frac{\partial B_\omega}{\partial T} d\omega \; l_\parallel(\omega, \theta), \tag{2.86}$$

and

$$j_\perp = -D_\perp \nabla_\perp T \tag{2.87}$$

with

$$D_\perp = 4\pi \int_0^\infty \frac{\partial B_\omega}{\partial T} d\omega \; l_\perp(\omega), \tag{2.88}$$

where $l_\parallel(\omega)$ and $l_\perp(\omega)$ are:

$$l_\parallel(\omega) = \int l(\omega, \overrightarrow{n}) \cos^2\theta \sin\theta d\theta, \tag{2.89}$$

$$l_\perp(\omega) = \frac{1}{2}\int_0^{\pi/2} l(\omega, \overrightarrow{n}) \sin^2\theta \sin\theta d\theta. \tag{2.90}$$

Here $l(\omega, \vec{n})$ is the mean free path of photons with frequency ω propagating along the direction $\vec{n}$. Define ω_B as $\hbar B/m_e c$. For $\omega_B \ll \omega$, the magnetic field only slightly influences the photon mean free path. For $\omega_B \gg \omega$, i.e. $\beta \gg 1$, the magnetic field strongly influences the photon mean free path.

In the absence of a magnetic field,

$$l_{\parallel} = l_{\perp}, \tag{2.91}$$

$$D_{\parallel} = D_{\perp} = D_0, \tag{2.92}$$

$$\overrightarrow{j} = -D\nabla T. \tag{2.93}$$

Radiative Conductivity

For the free-free transition, the radiative conductivity $\overrightarrow{\lambda}$ under strong magnetic fields can be expressed as:

$$\lambda_{ff\parallel} = A_{ff\parallel}\lambda_{ff,0}, \tag{2.94}$$

$$\lambda_{ff\perp} = A_{ff\perp}\lambda_{ff,0}, \tag{2.95}$$

where $\lambda_{ff,0}$ is the conductivity of zero magnetic field due to the free free transitions. The coefficients $A_{ff\parallel}$ and $A_{ff\perp}$ can be found in Pavlov and Yakovlev 1977.

The radiative conductivity due to the bound-free transition does not depend on B (Shaaf 1990), but the radiative conductivity due to the electron scattering λ_{es} is influenced by B, similar to the free-free transition case. The conductivity longitudinal to the field $\lambda_{es\parallel}$ and transverse to the field $\lambda_{es\perp}$ due to electron scattering can be written as:

$$\lambda_{es\parallel} = A_{es\parallel}\lambda_{es,0}, \tag{2.96}$$

$$\lambda_{es\perp} = A_{es\perp}\lambda_{es,0}, \tag{2.97}$$

where $\lambda_{es,0}$ is the zero field conductivity due to the electron scattering process.

The total radiative opacity then is

$$\kappa_{r,\|\perp} = \kappa_{bf} + \frac{\kappa_{ff\|,\perp}}{A_{ff\|,\perp}} + \frac{\kappa_{es\|,\perp}}{A_{es\|,\perp}}. \tag{2.98}$$

The coefficients $A_{es,\|,\perp}$ are adopted from Shaff (1990).

Electron Conductivity

Next, we will consider how the electron conductivity will be affected by the magnetic field. The macroscopic transport equations for the electric current density $\overrightarrow{j}$ and heat current density $\overrightarrow{F}$ for electrons are:

$$\begin{aligned} \overrightarrow{j} &= \sum_v (-e) n_e v = L_{11}\vec{E} + L_{12}\nabla T, & (2.99) \\ \overrightarrow{F} &= \sum_v (\epsilon - \mu) n_e v = L_{21}\vec{E} + L_{22}\nabla T, & (2.100) \end{aligned}$$

where E is the electric field, ∇T is the temperature gradient. and L_{ij} are the so called linear transport coefficients. Here L_{11} is the electric conductivity, usually denoted as σ, L_{22} is the thermal conductivity, usually written as λ.

The crusts of neutron stars are very good conductors, so $\overrightarrow{j} = 0$, which gives:

$$\vec{E} = -\frac{L_{12}}{L_{11}}\nabla T. \tag{2.101}$$

Substitute this expression back into the expression for $\overrightarrow{F}$, and it yields:

$$\begin{aligned} \overrightarrow{F} &= -\frac{L_{12}L_{21}}{L_{11}}\nabla T + L_{22}\nabla T \\ &= -\lambda_{el}\nabla T, & (2.102) \end{aligned}$$

with

$$\lambda_{el} = -L_{22} + \frac{L_{12}L_{21}}{L_{11}}, \tag{2.103}$$

where λ_{el} is the needed electron conductivity. The coefficients L_{ij} can be expressed as (Shaaf 1988):

$$\begin{pmatrix} L_{11} \\ L_{12} \\ L_{21} \\ L_{22} \end{pmatrix} = \frac{1}{3\pi^2 c\hbar^3} \int_0^\infty d\epsilon \phi^{(1)}(\epsilon)\tau(\epsilon) \begin{pmatrix} -e^2 \\ -e(\epsilon-\mu)/T \\ e(\epsilon-\mu) \\ (\epsilon-\mu)^2/T \end{pmatrix} \frac{\partial f_0(\epsilon)}{\partial \epsilon}, \tag{2.104}$$

where

$$\phi^{(1)}(\epsilon) = \frac{[\epsilon(\epsilon + 2m_e c^2)]^{3/2}}{\epsilon + m_e c^2}, \tag{2.105}$$

$\tau(\epsilon)$ is called the relaxation time of transport processes, and $f_0(\epsilon)$is the distribution function. For $B = 0$ and $T = 0$, the zero-field complete degeneracy case, the results are well known. For the strong magnetic field, $L_{\alpha\beta}$ can be expressed as the following:

longitudinal:

$$\begin{pmatrix} L_{11} \\ L_{12} \\ L_{21} \\ L_{22} \end{pmatrix} = \frac{2m_e\omega_B k_B^2 T}{(2\pi\hbar)^2 \sigma_B n_i} \int_0^\infty du \phi(u, \beta_B) g_0(u) \begin{pmatrix} -e^2/k_B^2T^2 \\ -e(u-u_0) \\ e(u-u_0)/T \\ (u-u_0)^2 \end{pmatrix} \frac{\partial f_0(\epsilon)}{\partial \epsilon}, \tag{2.106}$$

transverse:

$$\begin{pmatrix} L_{11} \\ L_{12} \\ L_{21} \\ L_{22} \end{pmatrix} = \frac{n_i \sigma_B k_B^2 T}{2\pi^2 \hbar} \int_0^\infty du Q(u, \beta_B) g_0(u) \begin{pmatrix} -e^2/k_B^2T^2 \\ -e(u-u_0) \\ e(u-u_0)/T \\ (u-u_0)^2 \end{pmatrix} \frac{\partial f_0(\epsilon)}{\partial \epsilon} \tag{2.107}$$

with $u = \epsilon/k_BT$, $u_0 = \mu/k_BT$ and

$$\beta_B = \frac{\hbar\omega_B}{m_e c^2}. \tag{2.108}$$

Because of the quantization of the electrons' orbits, the functions ϕ and Q are not well behaved. In his paper, Shaaf (1988) numerically fitted the functions for ϕ and Q, smearing out the oscillations. In our research, we adopt his results.

2.4.3 Effects of Magnetic Fields on 1D Cooling

Because of the magnetic field, the thermal conductivity is a tensor. The longitudinal and transverse thermal conductivities are different. The expressions for thermal conductivities along and perpendicular to the field were discussed in the last section. Along an arbitrary direction $\vec{n}$, the conductivity can be expressed as:

$$\lambda = \lambda_{\parallel} \cos^2 \Phi + \lambda_{\perp} \sin^2 \Phi, \tag{2.109}$$

where $\lambda_{\parallel}$ is the conductivity along the magnetic field, $\lambda_{\perp}$ is the conductivity along the direction perpendicular to the field, and Φ is the angle between the field and $\vec{n}$. For a uniform field configuration, $\Phi = \theta$.

Let us first analyze what will happen if we incorporate the effects of the strong magnetic fields on the thermal conductivities into the cooling calculation of neutron stars (Greenstein & Hartke 1983, Hernquist 1985).

The heat conduction equation is

$$q_i = -\sum_j \lambda_{ij} \partial_j T, \tag{2.110}$$

where (q_i) is the heat flux vector, (λ_{ij}) is the thermal conductivity tensor,

$$(\lambda_{ij}) = \begin{pmatrix} \lambda_{11} & \lambda_{12} \\ \lambda_{21} & \lambda_{22} \end{pmatrix}, \tag{2.111}$$

with

$$\lambda_{11} = \lambda_{\parallel}\cos^2\Phi + \lambda_{\perp}\sin^2\Phi, \tag{2.112}$$

$$\lambda_{12} = \lambda_{21} = (\lambda_{\parallel} - \lambda_{\perp})\cos\Phi\sin\Phi, \tag{2.113}$$

$$\lambda_{22} = \lambda_{\parallel}\sin^2\Phi + \lambda_{\perp}\cos^2\Phi. \tag{2.114}$$

The heat flux along the radial direction is

$$q_1 = -\lambda_{11}\frac{\partial T}{\partial r} - \lambda_{12}\frac{1}{r}\frac{\partial T}{\partial \theta}. \tag{2.115}$$

To order of magnitude,

$$\frac{\partial T}{\partial \theta} \sim \frac{T}{R}, \tag{2.116}$$

$$\frac{\partial T}{\partial r} \sim \frac{T}{\Delta h}, \tag{2.117}$$

where R is the radius of the star, and Δh is the thickness of the crust. Because $R \gg \Delta h$,

$$\frac{T}{\Delta h} \gg \frac{T}{R}. \tag{2.118}$$

So $q_1 \approx -\lambda_{11}\frac{\partial T}{\partial r}$. Define the effective temperature T_e as:

$$\sigma T_e^4 = q_1, \tag{2.119}$$

thus:

$$\begin{aligned} \sigma T_e^4 &= -(\lambda_{\parallel}\cos^2\Phi + \lambda_{\perp}\sin^2\Phi)\frac{\partial T}{\partial r} \\ &= -(\cos^2\Phi + \frac{\lambda_{\perp}}{\lambda_{\parallel}}\sin^2\Phi)\lambda_{\parallel}\frac{\partial T}{\partial r}. \end{aligned} \tag{2.120}$$

Since $\lambda_\perp \ll \lambda_\parallel$,

$$\sigma T_e^4 \approx -\cos^2\Phi \lambda_\parallel \frac{\partial T}{\partial r}. \tag{2.121}$$

When $\Phi = 0$, $T_e = T_{e,pole}$ and $\sigma {T_{e,pole}}^4 = -\lambda_\parallel \partial T/\partial r$. T_e at any other Φ can be expressed in terms of $T_{e,pole}$ as:

$$\frac{T_e}{T_{e,pole}} = \sqrt[4]{\cos^2\Phi} = \sqrt{|\cos\Phi|}. \tag{2.122}$$

Hernquist (1985) argued that if the surface temperature of a neutron star with a strong magnetic field has the $\sqrt{|\cos\theta|}$ distribution ($\Phi = \theta$ in the uniform field case), then the integrated flux, i.e. the total luminosity, can be expressed as follows,

$$\begin{aligned}
L_{tot} &= \int \sigma T_e^4 ds \\
&= 2\sigma {T_{e,pole}}^4 R^2 \int_0^{2\pi}\int_0^{\pi/2} \sin\theta\cos^2\theta d\theta d\phi \\
&= 2\sigma {T_{e,pole}}^4 R^2 \cdot 2\pi \int_0^{\pi/2}(-\cos^2\theta) d(\cos\theta) \\
&= 2\sigma {T_{e,pole}}^4 R^2 \cdot 2\pi \frac{1}{3} \\
&= \frac{1}{3}(4\pi R^2 \sigma {T_{e,pole}}^4).
\end{aligned} \tag{2.123}$$

Hernquist showed that $\lambda_\parallel$ is slightly higher than the non-magnetic field case, and the longitudinal flux is about 3 times larger than the zero field value when the field is about 10^{12} Gauss. Then ${T_{e,pole}}^4$ is about 3 times higher than the zero field case. From Equation(2.123) we can see that the net effect of strong magnetic fields on the total luminosity of neutron stars will not be significant from the above consideration. As we will show later, this argument is valid only in the early stage, i.e. before 10^4 yr, when the thermal communications between different directions can be neglected.

2.5 Results from 1D Cooling Calculations

We choose two field configurations in our calculations. The first is a uniform field and the second is a dipolar field. For the uniform field case, the B field has the same magnitude and direction everywhere inside the crust of the neutron star. For the dipolar field case, the strength of the B field is

$$B = \frac{B_{pole}}{2}\sqrt{3+\cos^2\Phi}, \tag{2.124}$$

where Φ is the angle between the field direction and the cooling direction. Φ is related to the polar angle θ as

$$\tan\Phi = 2\tan\theta. \tag{2.125}$$

Fig(2.11) and Fig(2.12) summarize the results from our 1D cooling calculations for the uniform field and the dipolar field cases. In these two figures, the solid curves represent the direction $\theta = 0°$, the dashed curves represent the direction $\theta = 30°$, the dotted curve 50°, the dash dotted curve 70°, the chain dashed curve 90°. Both figures show that the curves corresponding to small angles stay quite close to one another, and they are similar to the cooling curves of a non-magnetic neutron star. Notice also that the spaces between different curves in Fig(2.11), the uniform field case, are larger than the spaces in Fig(2.12), the dipolar field case. The reason behind this is that in the dipolar field case, the field strength at any angle θ is smaller than in the uniform field case except at $\theta = 0°$, so the influences of magnetic fields on the cooling are relatively weaker in the dipolar field case. The most striking feature of these two figures is the cooling curves of $\theta = 90°$. Two curves in both figures are much lower

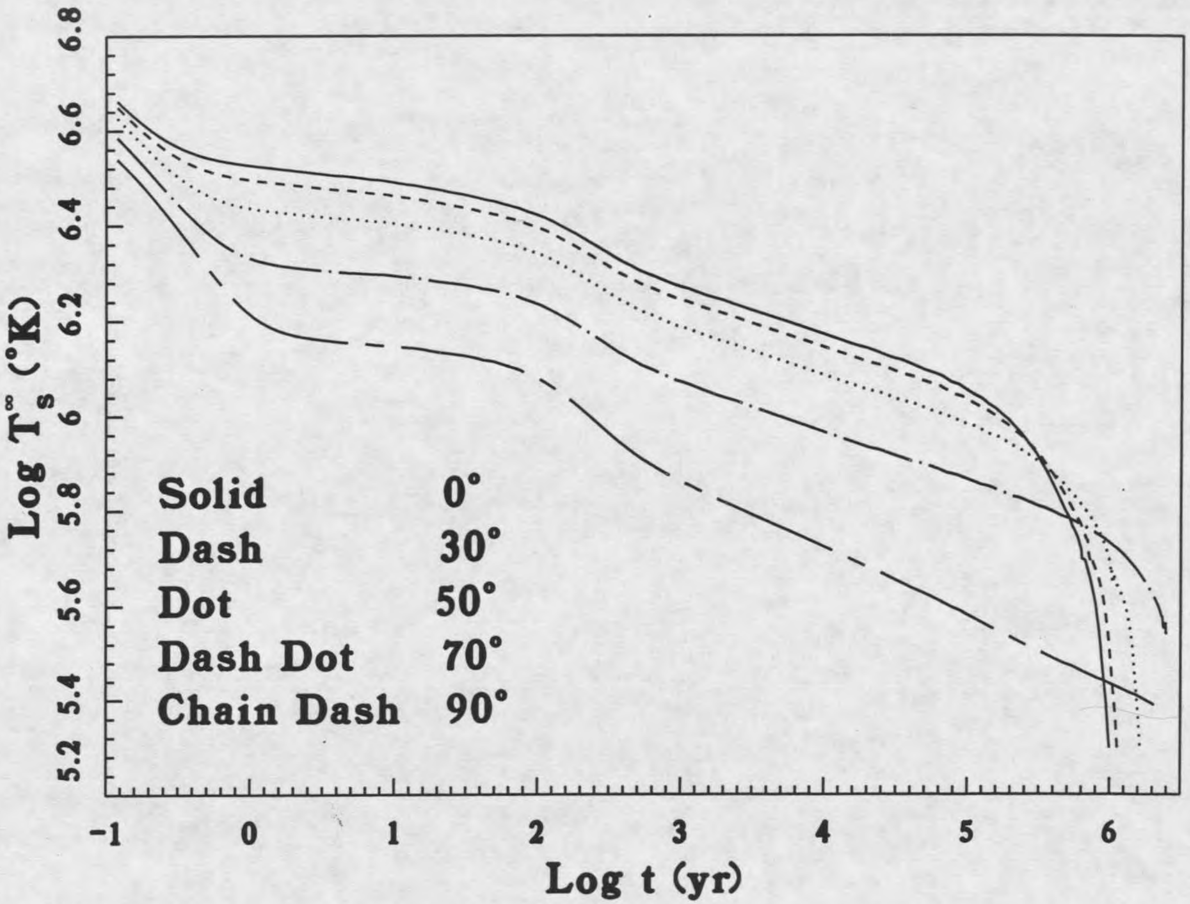

Fig(2.11) Cooling of Neutron Stars with Uniform Fields

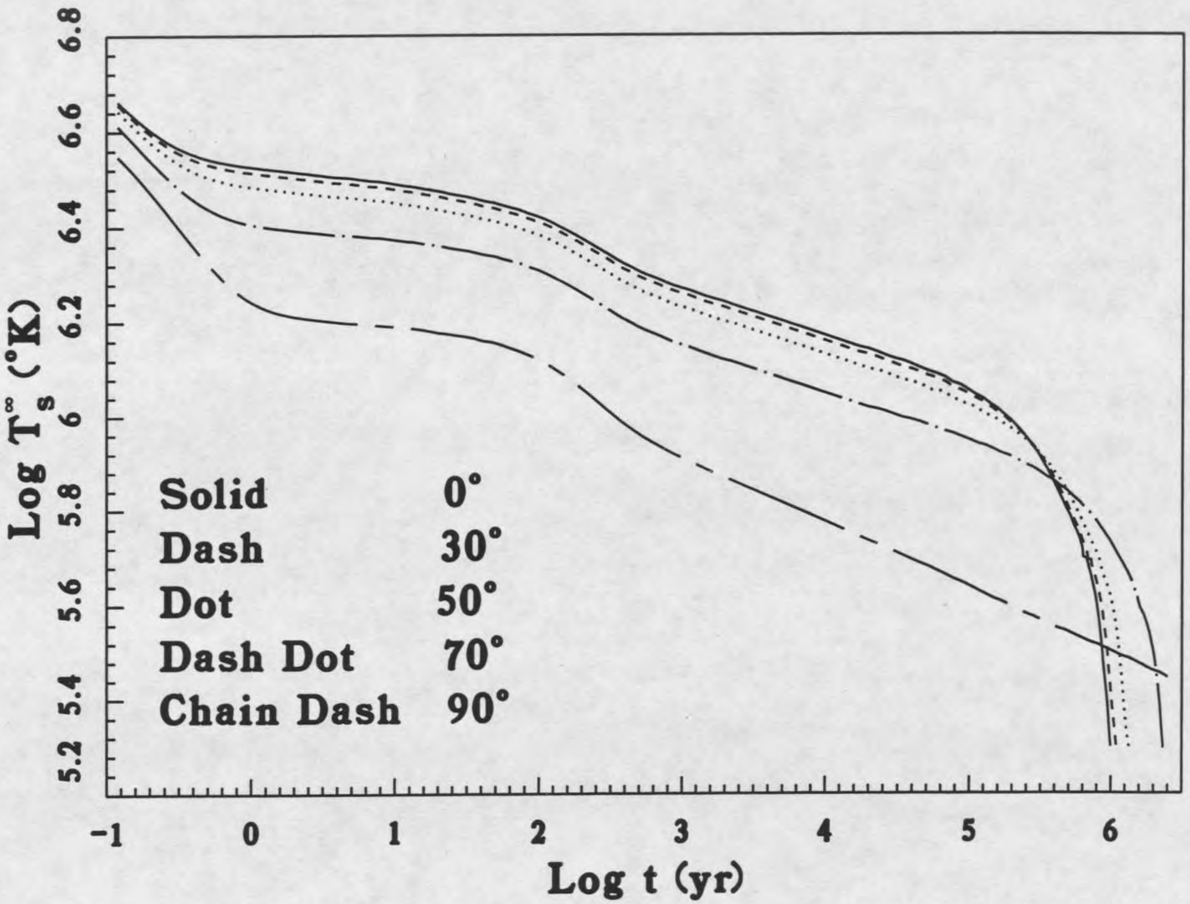

Fig(2.12) Cooling of Neutron Stars with Dipolar Fields

than the other curves, and they lack the abrupt drop of the temperatures caused by the take-over of the photon cooling.

The $T(\theta)/T_{pole}$ vs. θ relation is shown in Fig(2.13). We can see that our $T(\theta)/T_{pole}$ vs. θ curves satisfy the relation $T(\theta)/T_{pole} = \sqrt{|\cos\theta|}$, which is shown by the black dots, for a large range of θ, but the deviation is significant near 90° and both at very early and late stages. This is because in the theoretical derivation of the angular dependence, $\lambda_\perp$ is assumed to be zero, but in fact at θ near 90°, $\lambda_\perp \sin\Phi$ is even more important than $\lambda_\| \cos\Phi$. At the early stage, that $T(\theta)/T_{pole} \neq \sqrt{|\cos\theta|}$ simply because the initial conditions we give are isotropic. As shown in section §2.4.5, the $\sqrt{|\cos\theta|}$ relation is derived assuming that the surface temperatures are determined by the core temperature through heat conduction. At very late stages the photon cooling overtakes the neutrino cooling, and then it is the surface temperature that determines the core temperature. Therefore it is not a surprise that the surface temperatures no longer satisfy the $\sqrt{|\cos\theta|}$ relation.

2.6 Discussions

In section §2.2, we show that after the age $t \sim 10^5$ years, the surface photon cooling dominates other cooling mechanisms. This can be understood from the fact that the neutrino emissivity is proportional to T^8, while the photon cooling rate has a much lower temperature dependence. At higher temperatures, the neutrino emissivity dominates, while at low temperatures, the photon cooling dominates.

For the blackbody radiation, the photon emissivity is given by $L_\gamma = 4\pi R^2 \sigma T_s^4$,

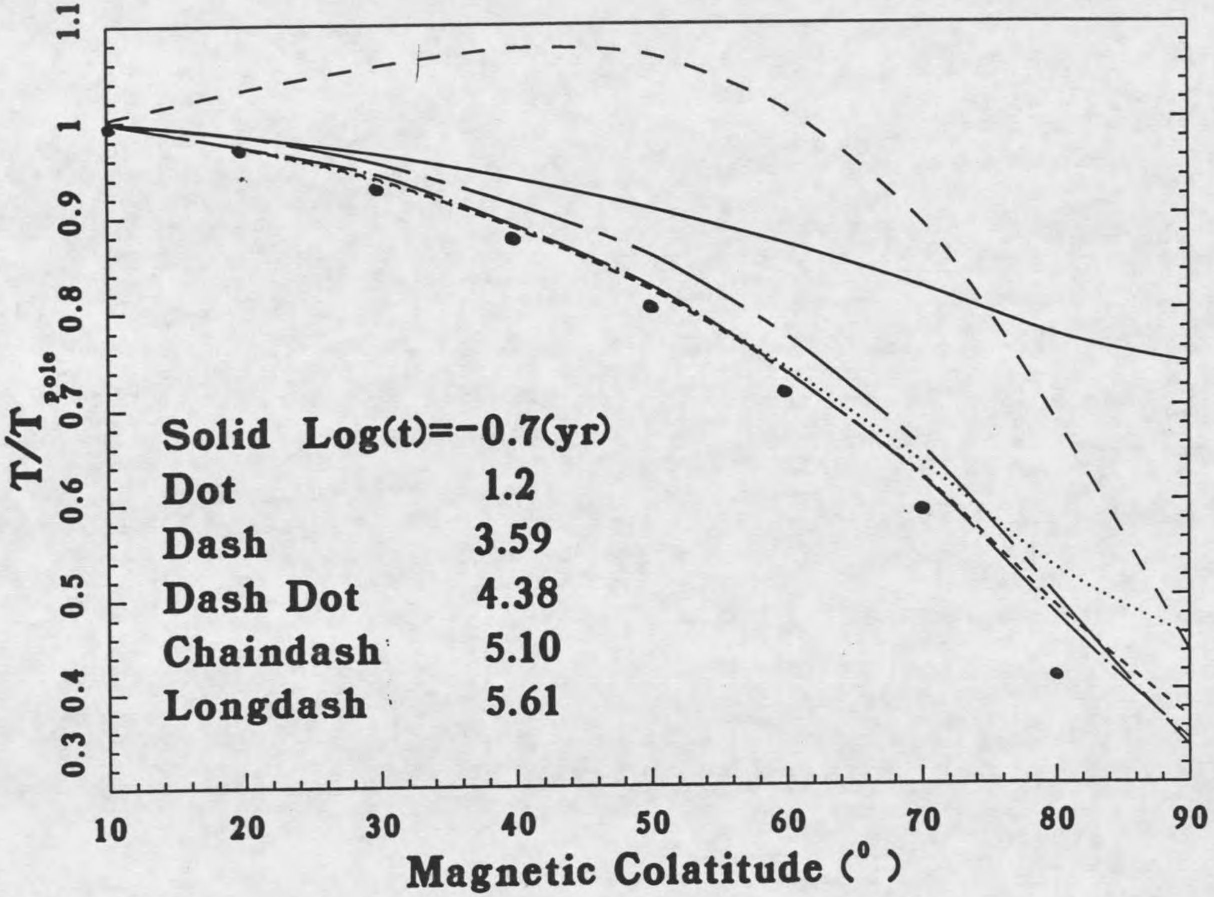

Fig(2.13) T/T_{pole} vs. Magnetic Colatitude where T_s is the surface temperature. The core temperature T_c and the surface temperature T_s are related by $T_s = \alpha T_c^{\beta}$ (see section §2.2). For the zero field case, $\alpha \sim 4.64$, $\beta \sim 0.67$, substitute these values into the expression for the total photon luminosity to find

$$L_\gamma = 4\pi R^2 \sigma (463.52\, T_c^{2.67}). \tag{2.126}$$

Therefore the cooling rate due to the blackbody emission, in the case of the zero field, is proportional to $T_c^{2.67}$ (see Fig(2.2)). Under strong magnetic fields, the relation between T_c and T_s along the longitudinal direction is not modified much, and so we expect almost the same feature as in the non-magnetic field case, i.e. the sudden temperature drop around 10^5 yr (see Fig(2.11), 2.12).) But along the directions that are perpendicular to the field or close to the perpendicular direction, the field changes the relation between the surface temperature T_s and the core temperature T_c. In the equatorial plane, the relation between T_c and T_s can be expressed as

$$T_s = \alpha' T_c^{\beta'}, \tag{2.127}$$

with $\alpha \sim 0.05$, $\beta' \sim 0.81$. Then the cooling rate due to the surface blackbody emission in the equatorial plane is proportional to $6.25 \times 10^{-6} T_c^{3.24}$. The cooling curve of the photon emission becomes flatter and it crosses the neutrino cooling curve at a later age as shown in Fig(2.14). Fig(2.14) explains the flatter cooling curves of larger angle θ when the age is longer than 10^5 yr.

We calculate the total luminosity by intergrating over the entire surface and compare it with the total luminosity of a non-magnetic neutron star. The result is shown in Fig(2.15). The solid curve represents the total photon luminosity of a magnetic

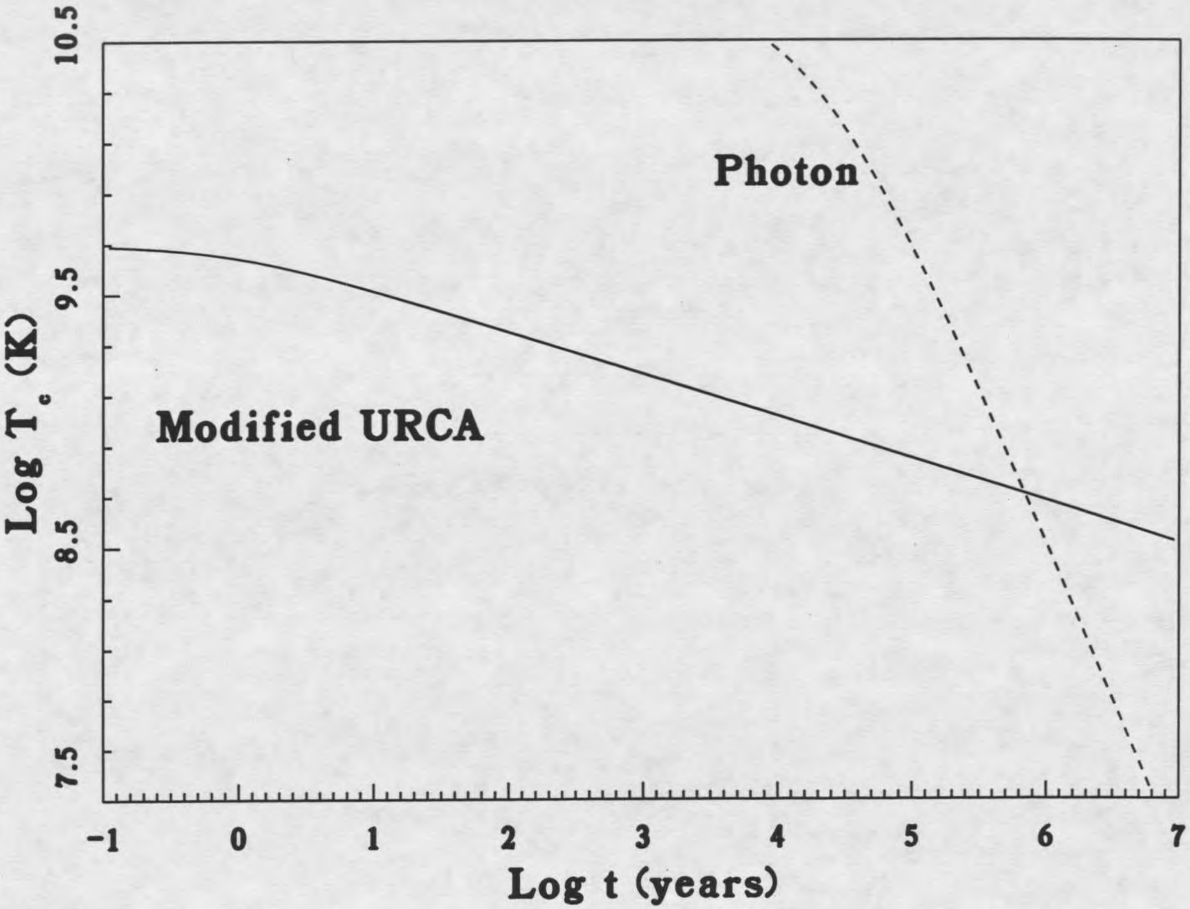

Fig(2.14) T_c vs. t (equatorial)

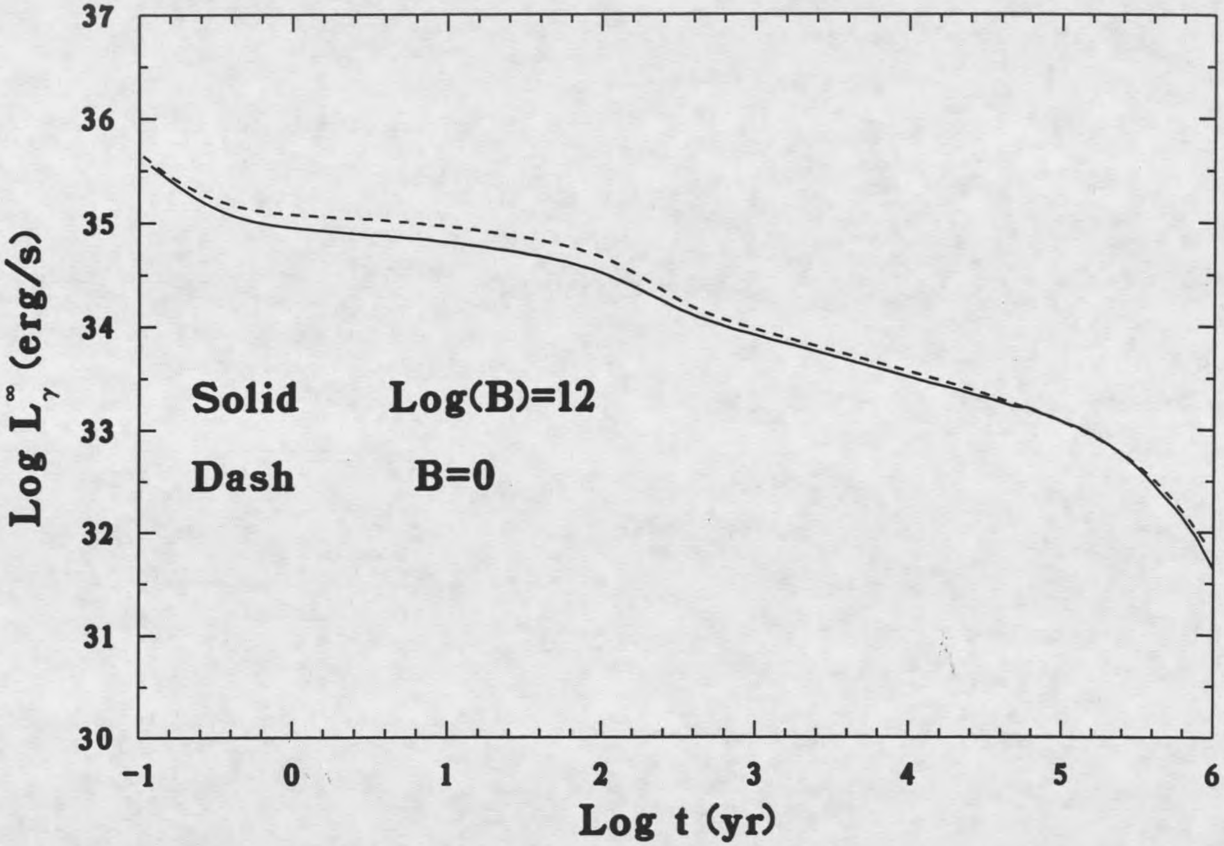

Fig(2.15) Total Luminosity of Magnetic (1D) and Non-Magnetic Neutron Stars

neutron star with a uniform field configuration and the field strength is 10^{12} Gauss, the dashed curve a non-magnetic neutron star. The two curves are close to each other with the solid curve being slightly lower than the dashed curve, confirming the prediction of Hernquist (1985).

In the 1D calculations, we calculated the thermal evolution along each direction separately, ignoring the thermal conductions in transverse directions. The results from 1D calculations show us how the magnetic field changes the neutron star thermal profile in the following sense: it slightly increases the polar temperature, and greatly reduces the equatorial temperature, while the total luminosity is almost unaffected.

The 1D approximation, however, is far from adequate. The core of a neutron star consists of highly degenerate neutrons, and the heat conduction coefficient λ is $\sim 10^{20} erg/cmsK$. The characteristic time for heat conduction inside the core is

$$\tau \sim \frac{l^2 c_v}{\lambda}. \tag{2.128}$$

Here l is the characteristic length ($\sim 1km$), and c_v is the specific heat. Inside the core $c_v \sim 10^{20} erg/cm^3K$. That will give τ about 10^{10} seconds, i.e. 100 years. Therefore, if there exists a difference in temperatures between two points inside the core, after about 100 yr, due to the heat conduction, the temperatures of these two points will become equal. In Fig(2.16), we show the core temperature vs. time relation at two different angles, $\theta = 0°$ and $\theta = 90°$. At $t = 10^5 yr$, the core temperature at $\theta = 0°$ is about twice lower than the core temperature at $\theta = 90°$. So the 1D calculations give different core temperatures in different directions at ages longer than the characteristic conduction time. These unphysical results are caused by the neglect of the tangential

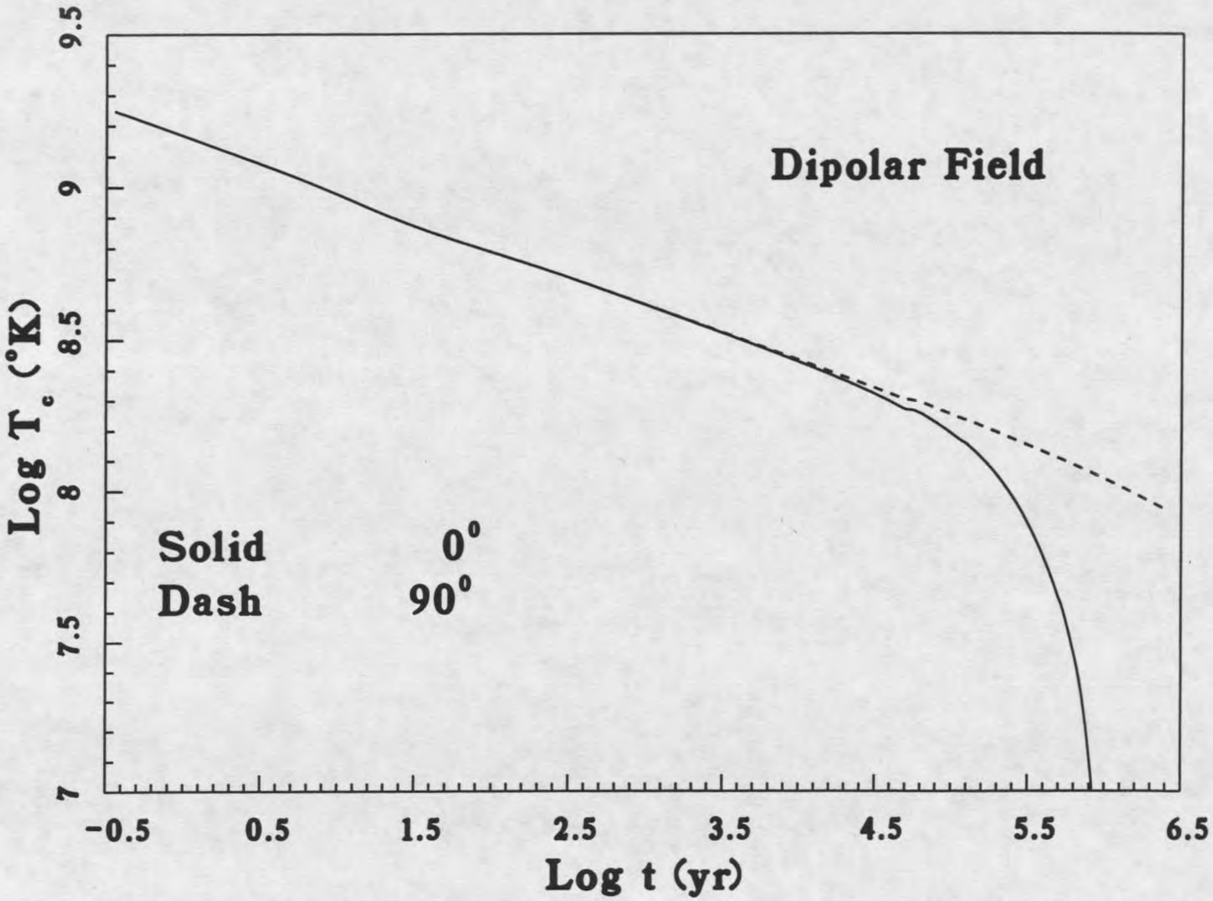

Fig(2.16) Polar and Equatorial Core Temperatures, 1D Calculation heat flows in 1D calculations. In the next chapter, we develop a 2D model to properly account for the tangential heat flows.

Chapter 3

Two Dimensional Cooling Calculation

3.1 Introduction

The anisotropy of the thermal conductivity caused by a strong magnetic field requires a two-dimensional (2D) model to simulate the thermal evolution. A full 2D model requires much computing time and storage space. If we can assume some symmetries, for instance, if the magnetic axis passes through the center of the neutron star, there will be the azimuthal symmetry and the mirror symmetry with regard to the magnetic equator, then we need simulate a quadrant instead of a whole sphere. Suppose we divide the quadrant into 10 fan shaped regions, and each fan shaped region, as in 1-dimensional calculation, is divided into 150 radial zones (see Fig(3.1)). However unlike the 1D case, where we have only two variables at each mesh point, we now have 3 variables: temperature T, radial heat flow F_r and tangential heat flow F_θ. Using the Henyey stellar evolutionary method (§2.2), the great part of the simulation is involved in matrix inversion. The time the matrix inversion takes is proportional

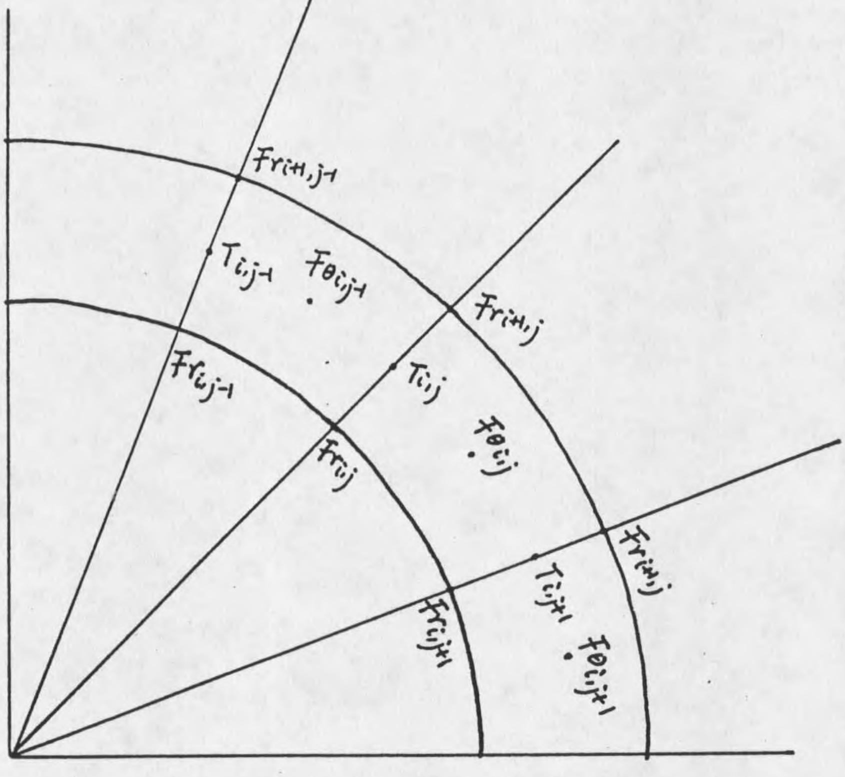

Fig(3.1)   2D Mesh

to n^3, where n is the dimension of the matrix. In 1D calculations, the dimension of the matrix is 150×2, the number of radial zones times the two variables at each zone, while in 2D calculations, the dimension of the matrix is $150 \times 3 \times 10 = 4500$, the number of radial zones in each fan shaped region times the three variables at each zone, times the number of fan shaped regions. Since the dimension of the matrix in the 2D case is 15 times larger than that in the 1D case, the speed of 2D calculation should be $15^3 = 3375$ times slower. For example, with our 1D program, it takes about 60 minutes for one calculation with our HP workstation, about half of the time is spent on the evaluation of coefficients and the computation of the boundary conditions (root-finding and integration). So the inversion of the matrix takes about half an hour in the 1D case. In the 2D case, the time becomes $0.5 \times 3375 = 1688$ hours, and the actual time will be even longer. Also the 0.5 hour in the 1D case is the optimized time, because in the 1D case, we have a tridiagonal matrix. In the 2D case, the matrix is not tridiagonal, no matter how we number the mesh points: either each row of the matrix corresponding to one radial line or one arch. As stated, the 2D problem requires a supercomputer. Fortunately, the matrix in the 2D case is "tridiagonal" in terms of the matrix blocks. If we can fully utilize this feature, we can greatly reduce the required computer time.

In this chapter, I will first introduce the set of two-dimensional thermal evolution equations in §2. In §3, the finite differential scheme and the method of the matrix inversion will be discussed. In §4, the results of the 2D calculations will be presented.

3.2 2-D Thermal Evolutional Equations

The thermal evolutionary equation in the 1D case can be written in the following form:

$$\vec{\mathcal{F}} = -\lambda \vec{\nabla} \mathcal{T}, \tag{3.1}$$

$$c_v \frac{d\mathcal{T}}{dt} = \vec{\nabla} \cdot \vec{\mathcal{F}} - \epsilon_\nu, \tag{3.2}$$

where $\mathcal{T}$ represents temperatures measured by an observer at infinity.

In the 2D case, the heat conductivity is a tensor, and the tangential symmetry no longer exists. The set of thermal evolution equations becomes

$$\vec{\mathcal{F}} = -\vec{\lambda} \cdot \vec{\nabla} \mathcal{T}, \tag{3.3}$$

$$c_v \frac{d\mathcal{T}}{dt} = \vec{\nabla} \cdot \vec{\mathcal{F}} - \epsilon_\nu, \tag{3.4}$$

with the thermal conductivity tensor $\vec{\lambda}$ as

$$\begin{pmatrix} \lambda_{11} & \lambda_{12} \\ \lambda_{21} & \lambda_{22} \end{pmatrix}. \tag{3.5}$$

In the zero field case, $\lambda_{21} = \lambda_{12} = 0$, and $\lambda_{11} = \lambda_{22}$. But when there is strong magnetic fields, λ_{11} and λ_{22} become different, and λ_{21} and λ_{12} are no longer zero (see section §2.3.5).

In the local inertial frame, the energy transport equation now is

$$\begin{aligned} \vec{\mathcal{F}} &= -\vec{\lambda} \cdot \vec{\nabla} \mathcal{T} \\ &= -\vec{\lambda} \cdot \begin{pmatrix} \frac{\partial \mathcal{T}}{\partial \tilde{r}} \\ \frac{1}{r} \frac{\partial \mathcal{T}}{\partial \theta} \end{pmatrix}, \end{aligned} \tag{3.6}$$

where $\tilde{r}$ and $\tilde{\theta}$ are coordinates of the local inertial frame and untilded coordinates are Schwarzchild coordinates. So the expressions for the radial and tangential flux become

$$\mathcal{F}_{\tilde{r}} = -\lambda_{11}\frac{\partial \mathcal{T}}{\partial \tilde{r}} - \lambda_{12}\frac{1}{r}\frac{\partial \mathcal{T}}{\partial \tilde{\theta}}, \tag{3.7}$$

$$\mathcal{F}_{\tilde{\theta}} = -\lambda_{21}\frac{\partial \mathcal{T}}{\partial \tilde{r}} - \lambda_{22}\frac{1}{r}\frac{\partial \mathcal{T}}{\partial \tilde{\theta}}. \tag{3.8}$$

Define:

$$\kappa_{rr} \equiv \frac{16\sigma T^3}{3\rho\lambda_{11}}, \tag{3.9}$$

$$\kappa_{r\theta} \equiv \frac{16\sigma T^3}{3\rho\lambda_{12}}, \tag{3.10}$$

$$\kappa_{\theta\theta} \equiv \frac{16\sigma T^3}{3\rho\lambda_{22}}, \tag{3.11}$$

and express the above two equations in terms of the Schwarzchild coordinates to obtain

$$e^{2\phi}F_r = -\frac{16\sigma T^3}{3\rho\kappa_{rr}}e^{2\phi}\frac{\partial(e^{\phi}T)}{\partial r} - \frac{16\sigma T^3}{3\rho\kappa_{r\theta}}e^{\phi}\frac{1}{r}\frac{\partial(e^{\phi}T)}{\partial\theta}, \tag{3.12}$$

$$e^{2\phi}F_\theta = -\frac{16\sigma T^3}{3\rho\kappa_{r\theta}}e^{2\phi}\frac{\partial(e^{\phi}T)}{\partial r} - \frac{16\sigma T^3}{3\rho\kappa_{\theta\theta}}e^{\phi}\frac{1}{r}\frac{\partial(e^{\phi}T)}{\partial\theta}. \tag{3.13}$$

The energy conservation equation becomes:

$$\begin{aligned}\frac{d(e^{\phi}T)}{dt} = & -\frac{1}{r^2 c_v}e^{\phi}\frac{\partial}{\partial r}(r^2 e^{2\phi}F_r) \\ & -\frac{1}{r\sin\theta c_v}\frac{\partial}{\partial\theta}(\sin\theta e^{2\phi}F_\theta) - e^{2\phi}\frac{\epsilon_\nu}{c_v}.\end{aligned} \tag{3.14}$$

In the next section, we will discuss how to solve the set of Eq.(3.12), (3.13) and (3.14).

3.3 Numerical Method

We first make the approximation that the gravitational potential ϕ is not a function of time, which follows from our previous assumption that the dynamic structure is static (section §2.2). Then Equation (3.14) becomes

$$\frac{dT}{dt} = -\frac{1}{r^2 c_v}\frac{\partial}{\partial r}(r^2 e^{2\phi} F_r) - \frac{1}{r\sin\theta c_v} e^{\phi}\frac{\partial}{\partial\theta}(\sin\theta F_\theta) - e^{\phi}\frac{\epsilon_\nu}{c_v}. \tag{3.15}$$

Let

$$X \equiv \frac{1}{r^2 c_v}, \tag{3.16}$$

$$Y \equiv \frac{e^{\phi}}{r\sin\theta c_v}, \tag{3.17}$$

$$Z \equiv \frac{e^{\phi}\epsilon_\nu}{c_v}, \tag{3.18}$$

then

$$\frac{dT}{dt} = -X\frac{\partial}{\partial r}(r^2 e^{2\phi} F_r) - Y\frac{\partial}{\partial\theta}(\sin\theta F_\theta) - Z. \tag{3.19}$$

Equation (3.13) becomes

$$F_\theta = -\frac{16\sigma T^3}{3\rho\kappa_{\theta r}}\frac{\partial(e^{\phi}T)}{\partial r} - \frac{16\sigma T^3}{3\rho r\kappa_{\theta\theta}} e^{-\phi}\frac{\partial(e^{\phi}T)}{\partial\theta}. \tag{3.20}$$

Define

$$U \equiv \frac{16\sigma}{3\rho\kappa_{\theta r}}, \tag{3.21}$$

$$V \equiv \frac{16\sigma}{3\rho r\kappa_{\theta\theta} e^{\phi}}, \tag{3.22}$$

then

$$F_\theta = -UT^3\frac{\partial(e^{\phi}T)}{\partial r} - VT^3\frac{\partial(e^{\phi}T)}{\partial\theta}. \tag{3.23}$$

Equation(3.12) becomes:

$$F_r = -\frac{16\sigma T^3}{3\rho\kappa_{rr}}\frac{\partial(e^{\phi}T)}{\partial r} - \frac{16\sigma T^3}{3\rho r\kappa_{r\theta}e^{\phi}}\frac{\partial(e^{\phi}T)}{\partial\theta} \tag{3.24}$$

Define

$$Q \equiv \frac{16\sigma}{3\rho\kappa_{rr}}, \tag{3.25}$$

$$W \equiv \frac{16\sigma}{3\rho r\kappa_{r\theta}e^{\phi}}, \tag{3.26}$$

then

$$F_r = -QT^3\frac{\partial(e^{\phi}T)}{\partial r} - WT^3\frac{\partial(e^{\phi}T)}{\partial\theta}. \tag{3.27}$$

To solve the set of Equations(3.19), (3.23) and(3.27), we change the differential equations to finite difference equations. We build our mesh as shown in Fig(3.1), and place the physical variables at the appropriate positions. In Fig(3.1), i is the index for the radial direction, and j is the index for the tangential direction. In our program, the number of zones along radial directions, NME, is set to be 150, and the number of fan shaped regions, NN, varies from 3 to 10. Our calculations show that whether NN is 3 or 10 makes little difference. We place $T_{i,j}$ between the mesh points (i,j) and $(i+1,j)$, and place $L_{i,j}$ at the mesh points (i,j), just as we did in the 1D case. We place $F_{\theta i,j}$ between the mesh points (i,j) and $(i,j+1)$.

After we build our grid system, we can change the differential equations into the finite-difference equations.

Equation(3.19) then becomes:

$$\frac{T_{i,j} - T_{i,j}^{old}}{\Delta t} =$$

$$-X_{i,j}\frac{R_{i+1}^2 e^{2\phi(R_{i+1})}F_{r\,i+1,j}-R_i^2 e^{2\phi(R_i)}F_{r\,i,j}}{\Delta r} -$$
$$\frac{Y_{i,j}}{2}\frac{\sin\theta_j F_{\theta\,i+1,j}-\sin\theta_{j-1}F_{\theta\,i+1,j-1}}{\theta_j-\theta_{j-1}} -$$
$$\frac{Y_{i,j}}{2}\frac{\sin\theta_j F_{\theta\,i,j}-\sin\theta_{j-1}F_{\theta\,i,j-1}}{\theta_j-\theta_{j-1}} - Z_{i,j} \qquad (3.28)$$

Equation(3.23) becomes:

$$\begin{aligned} F_{\theta 2i+1,j} &= -\frac{U_{i,j}+U_{i+1,j}}{2}T_{i,j}^3\frac{e^{\phi(R'_{i+1})}T_{i+1,j}-e^{\phi(R'_i)}T_{i,j}}{R_{i+1}-R_i} - \\ &\quad \frac{V_{i,j}+V_{i+1,j}}{2}T_{i,j}^3\frac{e^{\phi(R'_{i+1})}T_{i,j+1}-e^{\phi(R'_{i+1})}T_{i,j}}{\theta_{j+1}-\theta_j}, \end{aligned} \qquad (3.29)$$

with $R'_i = \frac{R_i+R_{i-1}}{2}$. Equation (3.27) becomes:

$$\begin{aligned} F_{r2i,j} &= -\frac{Q_{i,j}+Q_{i+1,j}}{2}\left(\frac{T_{i+1,j}+T_{i,j}}{2}\right)^3\frac{e^{\phi(R_{i+1})'}T_{i+1,j}-e^{\phi(R'_i)}T_{i,j}}{R_{i+1}-R_i} - \\ &\quad \frac{W_{i,j}+W_{i+1,j}}{2}\left(\frac{T_{i+1,j}+T_{i,j}}{2}\right)^3\frac{e^{\phi(R_{i+1})'}T_{i,j+1}-e^{\phi(R'_{i+1})}T_{i,j-1}}{\theta_{j+1}-\theta_{j-1}}. \end{aligned} \qquad (3.30)$$

Since we evaluate the coefficients, such as U, V, Q, W, at the middle points of each zone, so in Equation (3.28) and (3.29), we use the averaged values, e.g. $\frac{1}{2}(V_{i,j}+V_{i+1,j})$ etc.

We impose the following boundary conditions: at $i=0$, $\delta F_{r0,j}=0$ for every j, that is there is no heat flux coming in or out of the center; at $i=NME$, $T_{2i+1,j}$ is determined by the Eddington approximation (discussed below), and at $j=1$ or NN, we assume there exist mirror symmetries, i.e.

$$\begin{aligned} F_\theta(i,j=-1) &= -F_\theta(i,j=0), \end{aligned} \qquad (3.31)$$
$$\begin{aligned} T_{i,-1} &= T_{i,1}, \end{aligned} \qquad (3.32)$$

$$F_\theta(i,j=NN+1) = -F_\theta(i,j=NN-1), \tag{3.33}$$

$$T_{i,NN+1} = T_{i,NN}. \tag{3.34}$$

We have discussed how to solve the boundary problem in section §2.2. In the 2D case, the situation is somewhat different, because of the tangential flows. In the 2D model, dP/dr is still the same as in the 1D case (see Equation(2.27)). But dT/dr is different from the 1D case. To find dT/dr, we start with

$$\begin{aligned} F_\theta &= -UT^3\frac{\partial(e^\phi T)}{\partial r} - VT^3\frac{\partial(e^\phi T)}{\partial\theta}, \\ F_r &= -QT^3\frac{\partial(e^\phi T)}{\partial r} - WT^3\frac{\partial(e^\phi T)}{\partial\theta}. \end{aligned}$$

Express $\partial(e^\phi T)/\partial r$ in terms of F_θ and F_r, and we get

$$WF_\theta - VF_r = -UWT^3\frac{\partial(e^\phi T)}{\partial r} + QVT^3\frac{\partial(e^\phi T)}{\partial r}. \tag{3.35}$$

Since e^ϕ is approximately a constant in the outmost envelope, then

$$\frac{\partial T}{\partial r} = \frac{1}{T^3}\frac{WF_\theta - VF_r}{QV-UW}e^{-\phi}. \tag{3.36}$$

Assume F_θ and F_r are kept to be constant in the envelope, and then from Equation(3.36) and Equation(2.27), we find

$$\begin{aligned} \frac{dT}{dP} &= \frac{1}{T^3}\frac{WF_\theta - VF_r}{QV-UW}e^{-\phi}\frac{\rho}{g_s} \\ &= \left(\frac{W}{QV-UW}F_\theta - \frac{V}{QV-UW}F_r\right)\frac{1}{T^3}\frac{\rho}{g_s}, \end{aligned} \tag{3.37}$$

with

$$\frac{W}{QV-UW} = \frac{\lambda_{r\theta}}{\lambda_{\theta\theta}\lambda_{rr} - \lambda_{\theta r}\lambda_{r\theta}}, \tag{3.38}$$

and

$$\frac{V}{QV - UW} = \frac{\lambda_{\theta\theta}}{\lambda_{\theta\theta}\lambda_{rr} - \lambda_{\theta r}\lambda_{r\theta}}. \tag{3.39}$$

As discussed in section §2.2.2, integrating Equation(3.37) will yield a profile of the envelope. The initial value of P_s can be found by using the same method as described in section §2.2, only the value κ in Equation(2.31) should be replaced by $\kappa_{rr} = 16\sigma T^3/3\rho\lambda_{rr}$.

We once again use the Henyey stellar evolution code and define:

$$\delta F_{ri,j} = F_{ri,j}^{true} - F_{ri,j}^{current}, \tag{3.40}$$

$$\delta F_{\theta i,j} = F_{\theta i,j}^{true} - F_{\theta i,j}^{current}, \tag{3.41}$$

$$\delta T_{i,j} = T_{i,j}^{true} - T_{i,j}^{current}. \tag{3.42}$$

Substitute Equation(3.39), (3.40) and (3.42) into Equation (3.27), (3.28) and (3.29), and after some tedious but simple steps, we could find that

$$\begin{aligned}\delta F_{ri,j} + \frac{W_{i,j}}{4\Delta\theta}(\frac{T_{i+1,j} + T_{i,j}}{2})^3 e^{\phi(R'_{i+1})}\delta T_{i,j+1} \\ -\frac{W_{i,j}}{4\Delta\theta}(\frac{T_{i+1,j} + T_{i,j}}{2})^3 e^{\phi(R'_{i+1})}\delta T_{i,j-1} \\ +\alpha\delta T_{i+1,j} + \beta\delta T_{i,j} &= B(3i+2, j+1),\end{aligned} \tag{3.43}$$

$$\begin{aligned}\delta F_{\theta i,j} - \frac{U_{i,j} + U_{i+1,j}}{2\Delta R} T_{i+1,j}^3 e^{\phi(R_{i-1})}\delta T_{i,j} + \\ \frac{V_{i,j} + V_{i+1,j}}{2\Delta\theta} T_{i+1,j}^3 e^{\phi(R_i)}\delta T_{i+1,j+1} + \\ \mu\delta T_{i+1,j} = B(3i+1, j+1),\end{aligned} \tag{3.44}$$

and

$$\begin{aligned}
\Xi\delta T_{i,j} + \frac{X_{i,j}}{\Delta R}\Delta t R_{i+1}^2 e^{2\phi(R_{i+1})}\delta F_{ri,j} - \\
\frac{X_{i,j}}{\Delta R}\Delta t R_i^2 e^{2\phi(R_i)}\delta F_{ri-1,j} + \\
\frac{Y_{i,j}}{4\Delta\theta}\Delta t \sin\theta_j \delta F_{\theta i,j} + \\
\frac{Y_{i,j}}{4\Delta\theta}\Delta t \sin\theta_{j-1} \delta F_{\theta i,j-1} \\
\frac{Y_{i,j}}{4\Delta\theta}\Delta t \sin\theta_j \delta F_{\theta i-1,j} + \\
\frac{Y_{i,j}}{4\Delta\theta}\Delta t \sin\theta_{j-1} \delta F_{\theta i-1,j-1} \\
= B(3k+3, j-1).
\end{aligned} \tag{3.45}$$

The coefficients Ξ, μ, α and β can be found in Appendix B.

Upon examination of the set of Equations(3.43), (3.44) and (3.45), we see a pattern here; the matrix of the coefficients is "tridiagonal" in terms of blocks. First, the vector for the unknown we build is

$$\begin{pmatrix} \delta F_{\theta 0,0} \\ \delta F_{r0,0} \\ \delta T_{0,0} \\ \delta F_{\theta 2,0} \\ \delta F_{r2,0} \\ \delta T_{2,0} \\ \cdot \\ \cdot \\ \cdot \\ \delta F_{\theta 0,1} \\ \delta F_{r0,1} \\ \delta T_{0,1} \\ \cdot \\ \cdot \\ \cdot \end{pmatrix} \tag{3.46}$$

The linear equations for this set of variables are illustrated in Fig(3.2). In Fig(3.2), the coefficient matrix consists of matrix blocks. Each matrix block is a 450×450 submatrix. The method we use to invert this $450j \times 450j$ matrix is explained below, using $j = 3$ as an example.

Suppose we have a matrix as follows:

$$\begin{pmatrix} \mathcal{A} & \mathcal{B} & O \\ \mathcal{C} & \mathcal{D} & \mathcal{E} \\ O & \mathcal{F} & \mathcal{G} \end{pmatrix} \tag{3.47}$$

Blocks $\mathcal{A}, \mathcal{B}, \mathcal{C}, \mathcal{D}, \mathcal{E}, \mathcal{F}, \mathcal{G}$ represent non-zero submatrices, while O indicates zero matrices. If we LU decompose it, we have:

$$\begin{pmatrix} \mathcal{A} & \mathcal{B} & O \\ \mathcal{C} & \mathcal{D} & \mathcal{E} \\ O & \mathcal{F} & \mathcal{G} \end{pmatrix} = \begin{pmatrix} 1 & O & O \\ 2 & 3 & O \\ \mathcal{X} & 4 & 5 \end{pmatrix} \begin{pmatrix} 6 & 7 & \mathcal{Y} \\ O & 8 & 9 \\ O & O & 10 \end{pmatrix} \tag{3.48}$$

Submatrices $\mathcal{X}$ and $\mathcal{Y}$ are zero matrices, because if we multiply the last row of the lower triangle matrix (L) and the first column of the upper triangle matrix (U), we get

$$\mathcal{X} \cdot 6 + 4 \cdot 0 + 5 \cdot 0 = 0. \tag{3.49}$$

Since 6 can not be a zero, X has to be zero in order to satisfy Equation(3.49) (similarly for Y).

If we already know the L and U matrices, then the solution of the linear equations in Fig(3.2) can be written down. To find the L and U matrices, we try to solve the submatrices 1, 2, 3, 4, 5, 6, 7, 8, 9, 10 in Equation(3.48). The submatrix 1 belongs to the L matrix, 1 must also be a lower triangle matrix, and 6 must have an upper triangle matrix form. Also

$$1 \cdot 6 = \mathcal{A}. \tag{3.50}$$

Fig(3.2) 2D Linear Equations

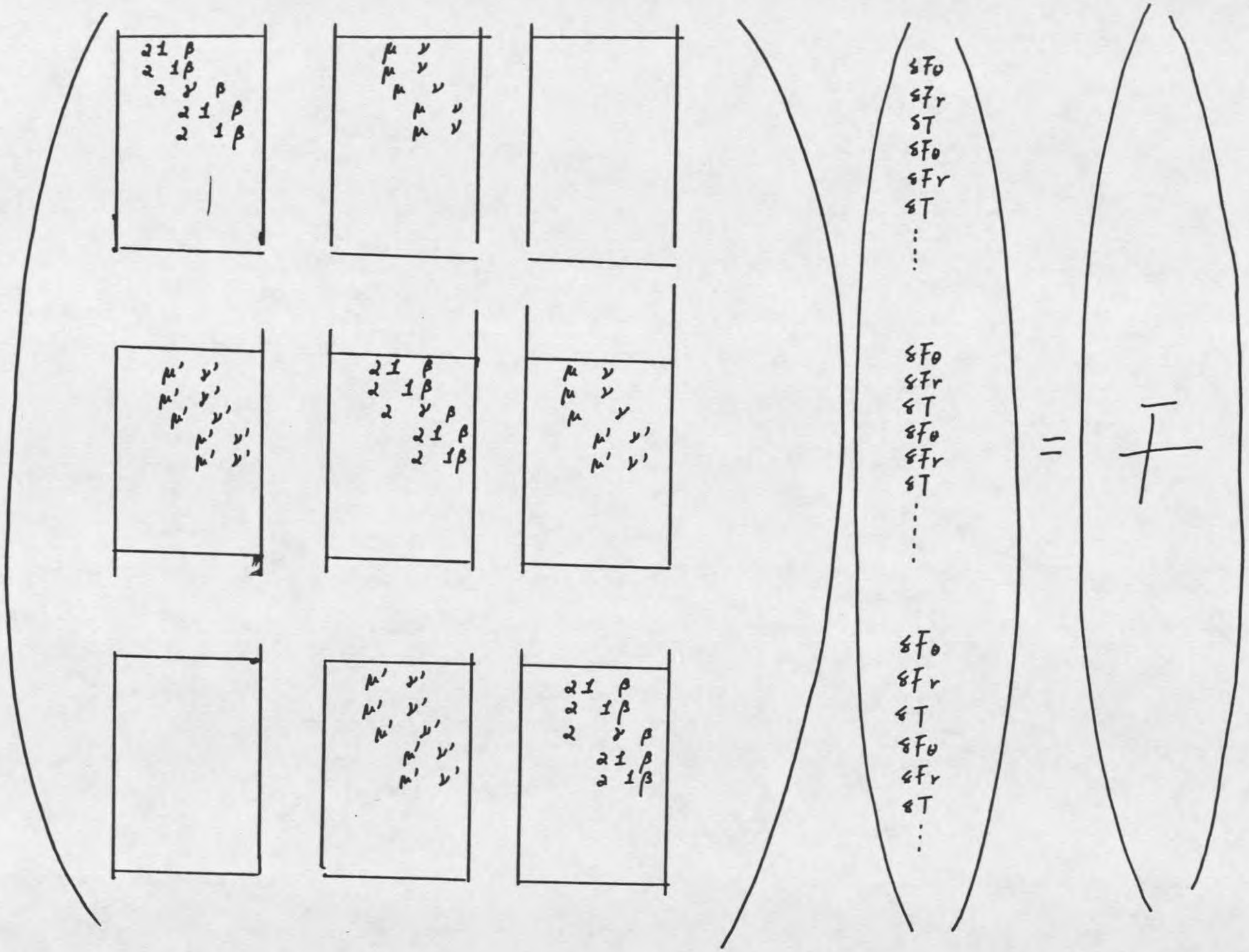

If we LU decompose $\mathcal{A}$, we can find 1 and 6. (We could use the standard LU decomposition subroutine. But since $\mathcal{A}$ is a sparse matrix, if we take advantage of this fact, we can significantly reduce computation time.) Assuming we know 1 and 6 now, then

$$1 \cdot 7 = \mathcal{B} \implies 7 = 1^{-1} \cdot \mathcal{B}, \tag{3.51}$$

and

$$2 \cdot 6 = \mathcal{C} \implies 2 = \mathcal{C} \cdot 6^{-1}. \tag{3.52}$$

We obtain submatrices 7 and 6. Multiplying the second row of the L matrix and the second column of the U matrix gives

$$3 \cdot 8 = \mathcal{D} - 2 \cdot 7. \tag{3.53}$$

3 is a L matrix, 8 is a U matrix. The LU decomposition of $\mathcal{D} - 2 \cdot 7$ yields submatrices 3 and 8. From $3 \cdot 9 = \mathcal{E}$, we could find the submatrix 9 by $9 = 3^{-1} \cdot \mathcal{E}$, and from $4 \cdot 8 = \mathcal{F}$, submatrix 4 can be calculated by $4 = \mathcal{F} \cdot 8^{-1}$. After submatrices 4 and 9 are known, by multiplying the third row of the L matrix and the third column of the U matrix, we could obtain

$$5 \cdot 10 = \mathcal{G} - 4 \cdot 9. \tag{3.54}$$

5 is a L matrix, 10 is a U matrix. From the LU decomposition of $\mathcal{G} - 4 \cdot 9$, we then could find submatrices 5 and 10. Therefore, all submatrices 1, 2, 3, 4, 5, 6, 7, 8, 9, 10 are found and the job of inversion is done.

The matrix inversion subroutines which we constructed to carry out the tasks we described above are given in Appendix C. The above method enables us to take advantage of sparseness of the huge matrix in our 2D calculations. We are able to cut the computing time by $(NN)^2$ times, with NN as the number of fan shaped regions we use. Before, according to the n^3 rule, the time of computation is proportional to $(NN \times NME \times 3)^3$, with NME as the number of zones in each fan shaped region. Now it is proportional to $NN \times (NME \times 3)^3$. So instead of half a year, only one to two days of CPU time is required.

3.4 Results and Discussions

In Fig(3.3) we show the results of 2D calculations. It shows the surface temperatures of different angles of a FP neutron star with a mass $1.4M_\odot$. The magnetic field is assumed to be dipolar, and the field strength at the pole is 10^{12} Gauss. The polar temperature is shown by the solid curve. The equatorial temperature is the dashed curve. The dotted curve is for 45°. As a comparison, the surface temperature of zero-field case is also drawn, by the dash dotted curve. We see that the equatorial surface temperature is much lower than the polar surface temperature, and the surface temperature at $\theta = 45°$ stays very close to the polar surface temperature. Also the polar surface temperature does not differ much from the zero field curve. These features exist in the 1D calculation too, and we know it is due to the $\sqrt{|\cos\theta|}$ relation of the surface temperatures (see section §2.5). In the 1D cooling calculation, the polar surface temperature has the sudden drop around 10^5 yr due to the take-over of the photon cooling. But the equatorial temperature in the 1D calculation lacks this sudden drop. The reason is also explained in §2.6. As a contrast, the 2D results

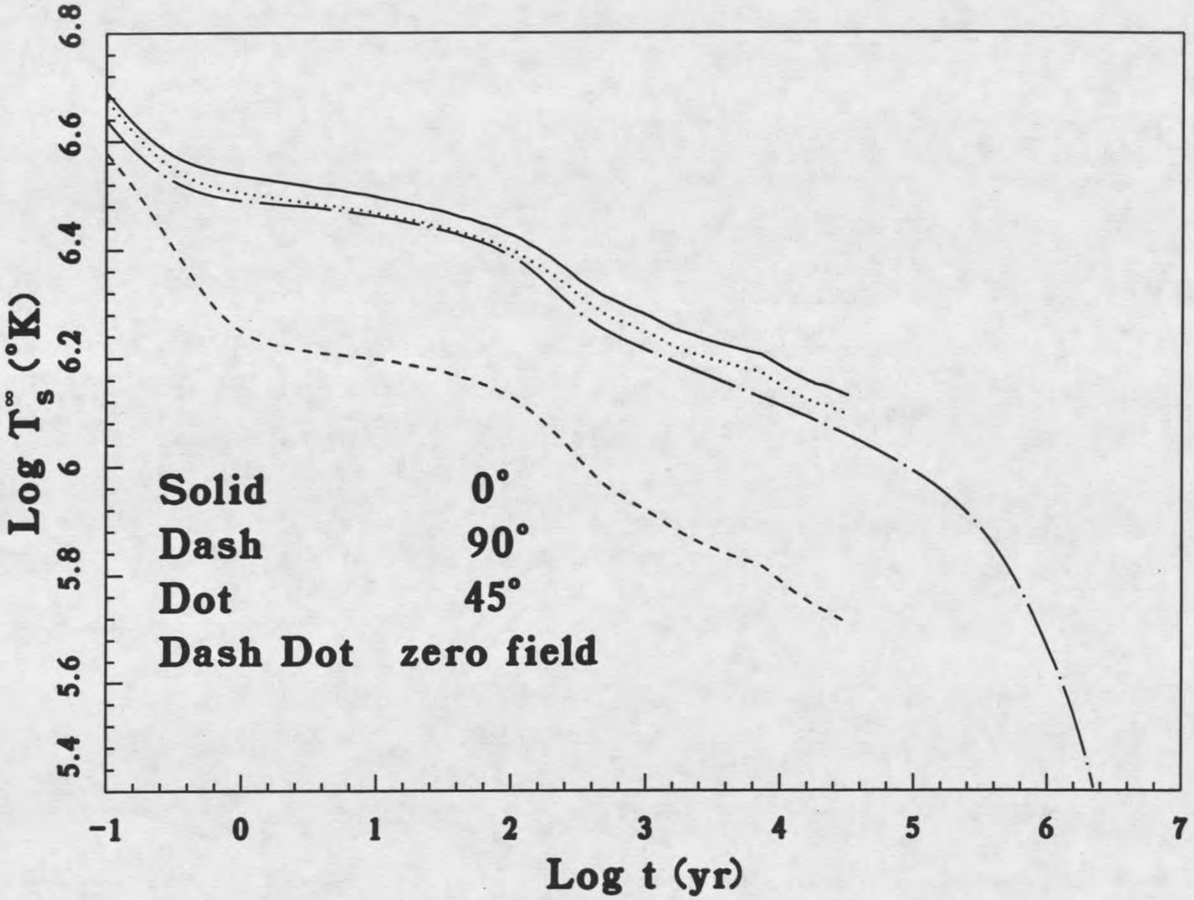

Fig(3.3) Cooling of Magnetic Neutron Stars, 2D Calculation

show that the surface temperatures for all three angles 0°, 45° and 90° remain relatively high after 10^5 yr. The high surface temperatures of neutron stars with strong magnetic fields are caused by the suppression of photon emission. The low thermal conductivity along the transverse direction restrains the heat flow from the core toward the surface.

In §2.6, we showed that in the 1D approximation calculations, the core-surface temperature relations are different for the longitudinal and transverse directions. The time when the photon emission overtakes the neutrino emission is delayed in the transverse direction, causing the core temperature of the transverse direction higher than the longitudinal core temperature at $t > 10^5 yr$. In the 2D calculation, energies will flow from the equatorial regions to the polar regions of the core, preventing the polar core temperature from dropping, as much as in the 1D calculations. In consequence, all surface temperatures stay high even after 10^6 yr in the 2D calculation.

Fig(3.4) is the core temperature vs. time. The solid curve is the 2D results. The dotted and dashed curves are the core temperatures from the 1D calculations, for 0° and 90°, respectively. As we pointed out in §2.6, the differences between the core temperatures at later times in the 1D calculations is unphysical. In our 2D calculations, we find that the core temperatures at different angles stay essentially the same through out all ages except at very early times.

In Fig(3.5), we show the evolution of the total stellar luminosity. The solid curve is the luminosity of a neutron star with a dipolar field. The field strength at the pole is 10^{12} Gauss. The dashed curve is the luminosity of a non-magnetic neutron star.

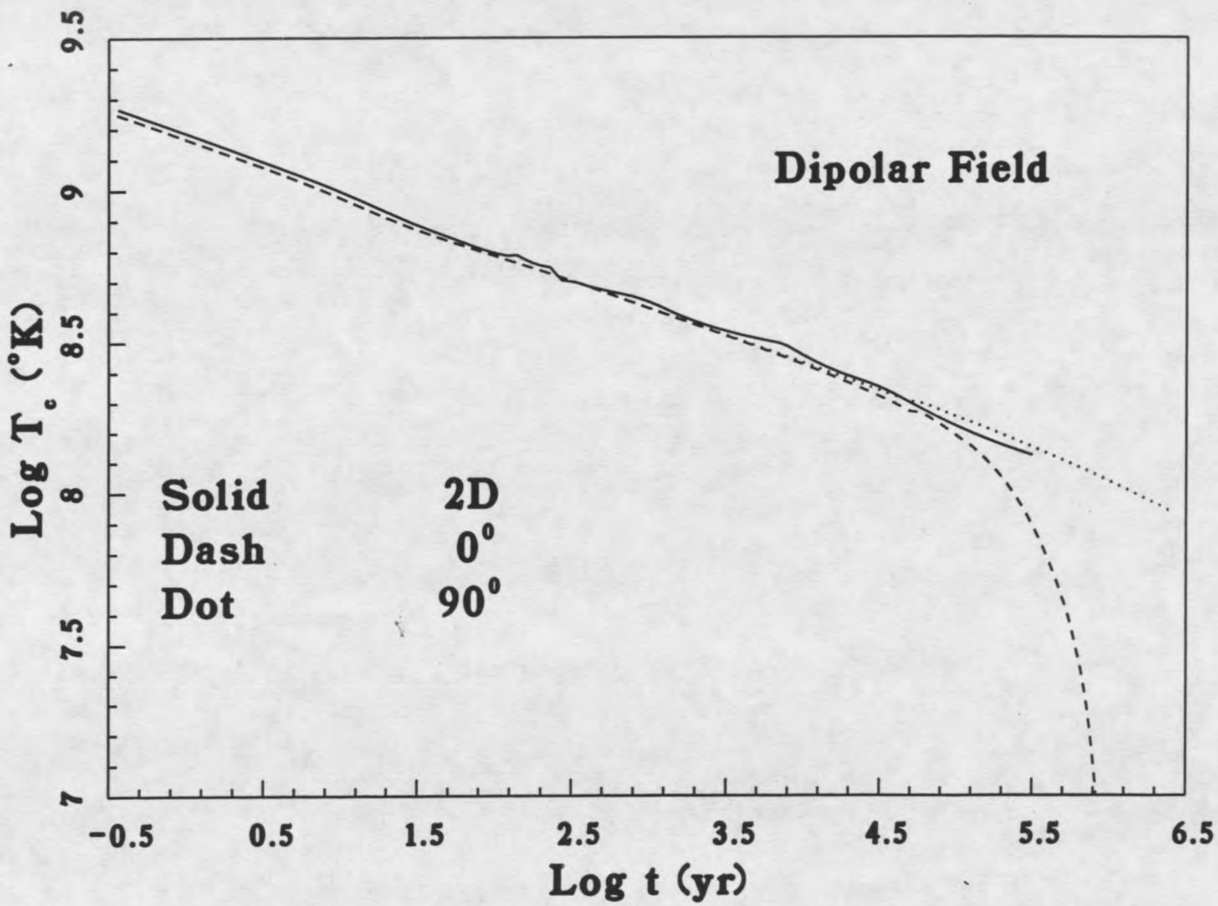

Fig(3.4) Core Temperature from 2D Calculation

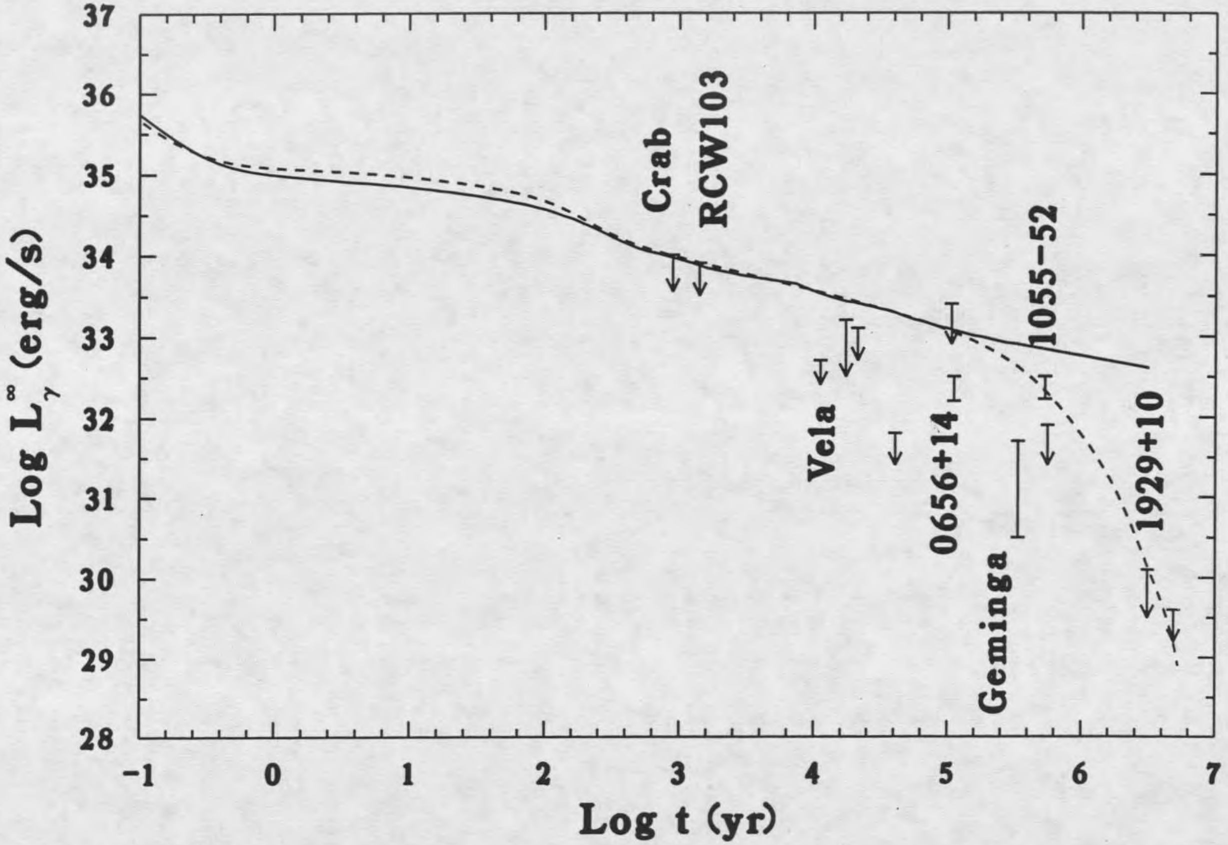

Fig(3.5) Total Luminosity of Magnetic (2D) and Non-Magnetic Neutron Stars

Before the age of 10^5 yr, these two curves are very close to one another. After 10^5 yr, the dashed curve quickly decreases while the solid curve remains rather flat. In Fig(3.5), we also plot observational data. Further discussions can be found in Qin & Tsuruta 1995b.

Chapter 4

Heating of Neutron Stars by Crust Breaking

4.1 Introduction

An evolving neutron star spins down under the external torque exerted by the magnetic field. The stellar crust deforms as stress builds up. When the stress in the solid crust exceeds a critical value, the solid crust will break, causing starquakes. Starquakes may be related to glitches of neutron stars, i.e. the sudden spin up of pulsars. According to one theory, when starquakes occur, a certain amount of energy will be released, raising the crustal temperature (Link & Epstein 1995). The temperature increase will enhance the coupling between the faster-rotating superfluid and the slower rotating rigid portions, which will speed up the slower rotating rigid portion, thus driving a glitch. In this chapter, we will study starquakes and their thermal effects on neutron stars (Qin et al 1995c).

As the spin of the neutron star slows down, the solid crust formed in the earlier stage deviates more from the new equilibrium shape, and develops stress (Baym &

Pines 1971). To describe the deformation of the crust, we define:

$$\epsilon = \frac{I_c - I_{c0}}{I_{c0}}. \tag{4.1}$$

Here I_c is the moment of inertia of the crust, and I_{c0} is the moment of inertia of the crust for a non-rotating star.

Suppose $\epsilon = \epsilon_0$ when the crust first solidifies. As time goes on, following the spin down of the pulsar, the oblateness of an equilibrium Maclarian spheroid decreases, and a finite stress is maintained. The solid crust of the star is not a perfect Maclarian spheroid. The equilibrium shape of the solid crust of neutron stars will be the least energy state.

Define A and B as follows:

$$\begin{aligned} E_{grav} &= E_{grav,0} + A\epsilon^2, &(4.2)\\ E_{strain} &= B(\epsilon - \epsilon_0)^2, &(4.3)\end{aligned}$$

where $E_{grav,0}$ is the gravitational energy of a non-rotating sphere, while E_{grav} is the gravitational energy of a rotating neutron star. E_{strain} is the strain energy. The total energy can be expressed as:

$$\begin{aligned} E &= E_{grav} + E_{strain} + E_{rotation} \\ &= E_{grav,0} + A\epsilon^2 + B(\epsilon - \epsilon_0)^2 + \frac{L^2}{2I}, &(4.4)\end{aligned}$$

where L is the total angular momentum, I is the total moment of inertia, $L^2/2I$ is the rotational energy, $L^2/2I = \frac{1}{2}I\Omega^2$, and Ω is the angular velocity. The equilibrium state is the least-energy state, and the equilibrium ϵ value is the value which satisfies $\partial E/\partial\epsilon = 0$.

$$\frac{\partial E}{\partial \epsilon} = 2B(\epsilon - \epsilon_0) + 2A\epsilon + \frac{1}{2}\Omega^2\frac{\partial I}{\partial \epsilon} = 0 \tag{4.5}$$

$$\epsilon = -\frac{\Omega^2}{4(A+B)}\frac{\partial I}{\partial \epsilon} + \frac{B\epsilon_0}{A+B}. \tag{4.6}$$

As the star slows down, Ω decreases, and ϵ will increase. The stress will grow until it reaches a critical value, and then the crust of the star breaks.

After the starquake, the strain energy is released, ϵ_0 changes to ϵ_0', and the new equilibrium configuration will be reached with:

$$\epsilon' = -\frac{\Omega^2}{4(A+B)}\frac{\partial I}{\partial \epsilon} + \frac{B\epsilon_0'}{A+B}. \tag{4.7}$$

The energy released in this starquake equals the change of the total energy:

$$\begin{aligned}\Delta E &= -\frac{\partial E}{\partial \epsilon}\Delta\epsilon - \frac{\partial E}{\partial \epsilon_0}\Delta\epsilon_0 \\ &= -\frac{\partial E}{\partial \epsilon}(\epsilon' - \epsilon) - \frac{\partial E}{\partial \epsilon_0}(\epsilon_0' - \epsilon_0).\end{aligned} \tag{4.8}$$

Since E satisfies the least energy requirement $\partial E/\partial\epsilon = 0$, ΔE reduces to:

$$\begin{aligned}\Delta E &= -\frac{\partial E}{\partial \epsilon_0}\Delta\epsilon_0 \\ &= -2B(\epsilon - \epsilon_0)\Delta\epsilon_0.\end{aligned} \tag{4.9}$$

Define $\epsilon_c = \epsilon_{max} - \epsilon_0$, where ϵ_{max} is the maximum deformation which the crust can endure before it cracks. Then during the interval between two consecutive starquakes, an amount of energy

$$\Delta E = -2B\epsilon_c\Delta\epsilon_0, \tag{4.10}$$

will be stored up in the deformed crust, where $\Delta\epsilon_0 = \epsilon_0' - \epsilon_0$. Since just after a starquake the crust will settle into a state having the least energy, ϵ_0' should equal ϵ_{max}. So $\Delta\epsilon_0 = \epsilon_c$, and this amount of energy

$$\Delta E = -2B\epsilon_c^2, \tag{4.11}$$

will be released in a starquake. The released energy will heat up the neutron star. We are interested in two questions. First, right after the starquake, how suddenly does the star's thermal emission increase? That is how much energy is required to be released in the starquake, in order to have an observable thermal pulse emerge from the star's surface? Second, by how much do frequent starquakes raise the star's surface temperature?

4.2 Physical Inputs

The short-term effect of starquakes can be simulated by adding energy ΔE in Equation(4.11) in the crust of the star at one specific time during neutron star's cooling era, and let it evolve.

To explore the long-term effect, we adopt the smooth function for the rate of energy release derived by Cheng et al (1994). The time interval between two consecutive starquakes is assumed to be $\mid \Delta t = \Omega/(d\Omega/dt) \mid$. So:

$$\frac{dE}{dt} = \frac{\Delta E}{\Delta t} = 2B\epsilon_c^2 \mid \frac{\dot{\Omega}}{\Omega} \mid, \tag{4.12}$$

where dE/dt is the long-term averaged rate of energy release by starquakes, ϵ_c is the critical value of the stress, Ω is the angular velocity, and $\dot{\Omega} = d\Omega/dt$.

Using a magnetic dipole braking model, Ω is estimated as:

$$\Omega = \frac{\sqrt{3}}{2} c^{3/2} \frac{I^{1/2}}{\mu \sin\alpha} \frac{1}{(t+\tau_{so})^{1/2}}, \tag{4.13}$$

where c is the speed of light, α is the angle between the rotation axis and magnetic field, μ is the magnetic dipole moment, t is the age of the neutron star, and τ_{so} is the characteristic spin-down time. When $t = \tau_{so}$,

$$\Omega \mid_{t=\tau_{so}} = \frac{\sqrt{3}}{2} c^{3/2} \frac{I^{1/2}}{\mu \sin\alpha} \frac{1}{\sqrt{2\tau_{so}}} = \frac{1}{\sqrt{2}} \Omega \mid_{t=0}, \tag{4.14}$$

where τ_{so} is defined as:

$$\tau_{so} = \frac{\Omega}{2\dot{\Omega}} \mid_{t=0} . \tag{4.15}$$

With this expression for Ω, we then have:

$$\frac{\dot{\Omega}}{\Omega} = \frac{1}{2(t+\tau_{so})}. \tag{4.16}$$

Substitute Equation(4.16) into Equation(4.12) to get

$$\frac{dE}{dt} = \frac{B\epsilon_c^2}{t+\tau_{so}}. \tag{4.17}$$

Equation(4.17) is the total rate of energy release in the crust. According to Baym and Pines (1971), $B = 0.5330 Z^2 e^2 n^{2/3} V$ with Z as the atomic number of the elements in the crust, e the electrical charge, n the nucleus density, and V the volume. Then the rate at which the energy density changes is

$$\frac{d\varepsilon}{dt} = \frac{b\epsilon_c^2}{t+\tau_{so}}, \tag{4.18}$$

with $\varepsilon = E/V$, and $b = B/V = 0.5330 Z^2 e^2 n^{2/3}$. An important fact which should be pointed out is that when the temperature is higher than $10^8 K$, the neutron star matter is expected to readjust its structure through plastic flow, and therefore we need a step function to take this effect into account,

$$\frac{d\varepsilon}{dt} = \frac{b\epsilon_c^2}{t+\tau_{so}}\Theta(10^8K - T). \tag{4.19}$$

To carry out the cooling calculations, we adopt the exact evolutionary method by NT87. We rewrite the energy equation as follows:

$$\begin{aligned} \frac{1}{\mathcal{R}^2}\frac{\partial(\mathcal{R}^2 L_\gamma)}{\partial m} &= -\epsilon_\nu - \frac{T}{\mathcal{R}}\frac{\partial S}{\partial t} + \\ & \frac{b\epsilon_c^2}{t+\tau_{so}}\Theta(10^8 - T)\Theta(\Gamma - 170), \end{aligned} \tag{4.20}$$

where L_γ is the photon luminosity, $\mathcal{R} = \exp(\phi/c^2)$, m(r) is the baryon mass inside r, ϵ_ν is the neutrino emissivity, T is the temperature, S is the specific heat, and t is time. The last term on the right hand side represents the energy source from starquakes. The step function $\Theta(\Gamma - 170)$ implements the condition that the heating happens only in the solid crust. Γ is a characteristic parameter of the classical one-component plasma. The fluid-solid transition takes place at $\Gamma \approx 168 \pm 4$, which was found by the Monte-Carlo simulation method (Slattery, Dooley and Dewitt 1982). We choose 170 in our calculations.

The size of the solid crust varies as the temperature of the neutron star drops. The lower the temperature, the larger the size of the solid crust. In Table(4.1), we list the crustal region of Model FP at different ages. It shows that the size of the crustal region increases with time. As we mentioned earlier, the PS Model has the stiffest equation of state, so the crustal region of the PS Model will be larger than

Table(4.1) Size Of The Crust Region At Different Ages (FP Model)

Log(t) yr	Inner Radius (km)	Outer Radius (km)
-4.00	9.51723	10.020028
-3.00	9.51723	10.43599
-1.50	9.51723	10.59036
0.50	9.51723	10.59036
3.00	9.51723	10.83402
4.6079	9.51723	10.85352
6.00	9.51723	10.89025
6.50	9.51723	10.89287
7.427	9.51723	10.89327

that of the FP Model, while the BPS Model has the softest equation of state, and hence the crustal region of the BPS model will be smaller than that of the FP Model.

The critical value of the stress ϵ_c is not well known theoretically. It was estimated to be about 10^{-5} to 10^{-4} by Smolukowoski and Welch (1970) based on the observational data of Vela and Crab's starquakes, while an ideal Coulomb lattice has ϵ_c around 10^{-2} to 10^{-1}.

4.3 Results

4.3.1 Heating due to Crust Breaking

Standard Scenario

We carried out our heating calculations using different values of ϵ_c, for a neutron star with a mass $1.4M_\odot$ and of all three models. The results are summarized in Figs(4.1), (4.2) and (4.3). Fig(4.1) is for model FP. In Fig(4.1), the solid line corresponds to $\epsilon_c = 0.01$, the dashed line $\epsilon_c = 0.005$, the dotted line $\epsilon_c = 0.003$, the dash-dotted line $\epsilon_c = 0.0008$ and the chain-dashed line, with $\epsilon_c = 0$, corresponds to cooling without internal heating effect. Fig(4.2) is for model PS, with the solid, dashed, dotted, dash-dotted and chain dashed lines corresponding to $\epsilon_c = 0.005, 0.001, 0.0008, 0.0005$ and 0, respectively. Fig(4.3) is for model BPS, with the solid, dashed, dotted, dash-dotted, chain-dashed lines corresponding to $\epsilon_c = 0.01, 0.005, 0.003, 0.001$, and 0, respectively.

Our results show that the heating effect is strongly dependent on the critical stress value ϵ_c. If the range of values $10^{-5} \le \epsilon_c \le 10^{-4}$, as estimated by Smolukowski and

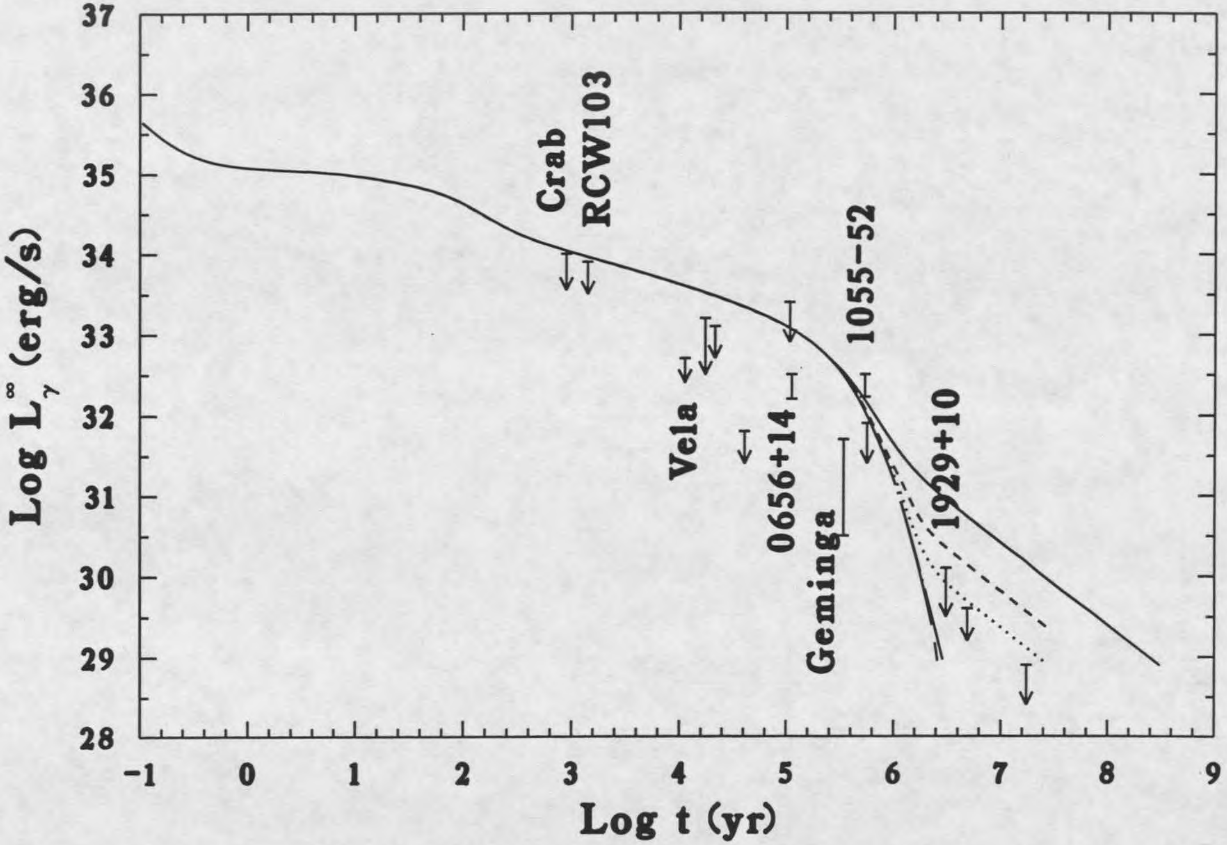

Fig(4.1) Heating by Crust Breaking, the FP Model

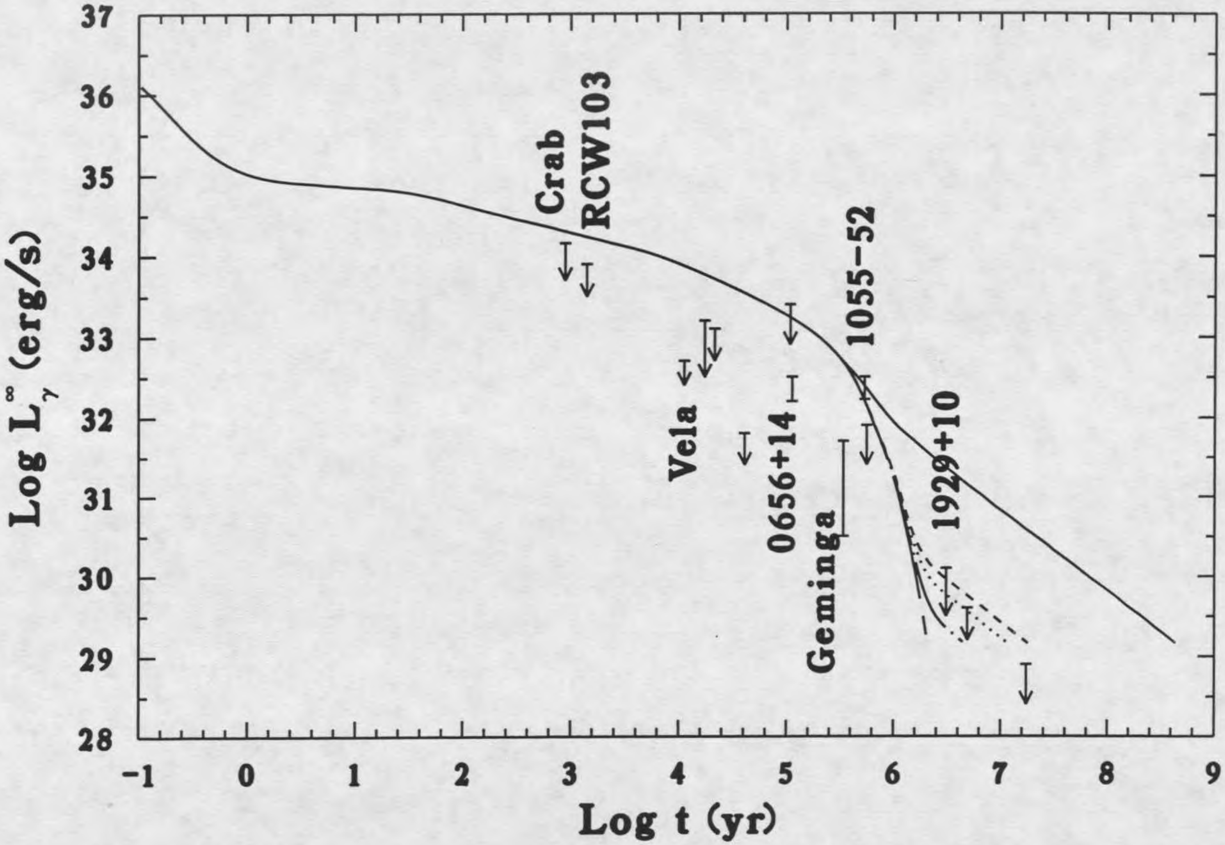

Fig(4.2) Heating by Crust Breaking, the PS Model

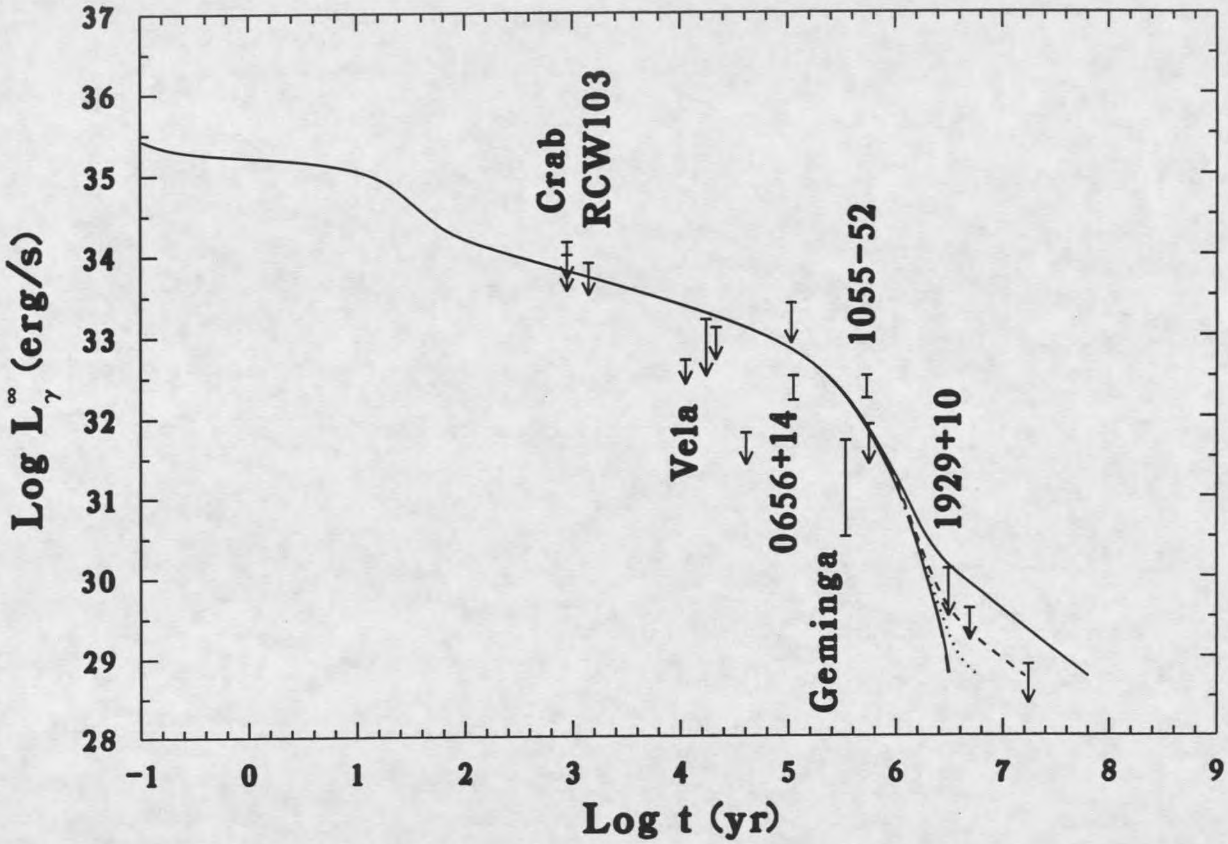

Fig(4.3) Heating by Crust Breaking, the BPS Model

Welch (1970), is correct for a neutron star, then the crust breaking will not be a very important heating mechanism. For instance, in order to alter the cooling curve distinguishably, ϵ_c must be larger than 0.0008 for the standard FP Model, 0.0005 for the PS Model and 0.001 for the BPS Model. The fact that the value of ϵ_c for the PS Model is the smallest and the value for the BPS Model is the largest is what we should expect because of the differences of the sizes of the crustal regions.

In all three models, we have considered superfluidity. We assume that protons and neutrons are in the $1S_0$ superfluid state, while neutrons in the core are in the $3P_2$ state. The superfluid model we use is Model T72 (Takatsuka & Tamagaki 1971, Takatsuka 1972).

A common feature to all three figures is that the heating effect only begins at age $t \sim 5.5 \times 10^5$ yr. This is of no surprise, because of the fact that the heating is turned on only when the temperature is less than $10^8 K$ and the size of the crust is rather small at early ages.

Non-Standard Scenario

In Fig(4.4), we show the effect of heating due to crust cracking in the non-standard scenario, where the effect of superfluidity is not included. Non-standard cooling means that there is some "exotic" fast cooling mechanism, such as direct URCA process, pion, kaon and so on. As a representative fast cooling process, we assume that the central core has the pion condensates. The presence of the pion condensate enhances neutrino emissivity through the quasi-particle URCA process. After ~ 100 years of

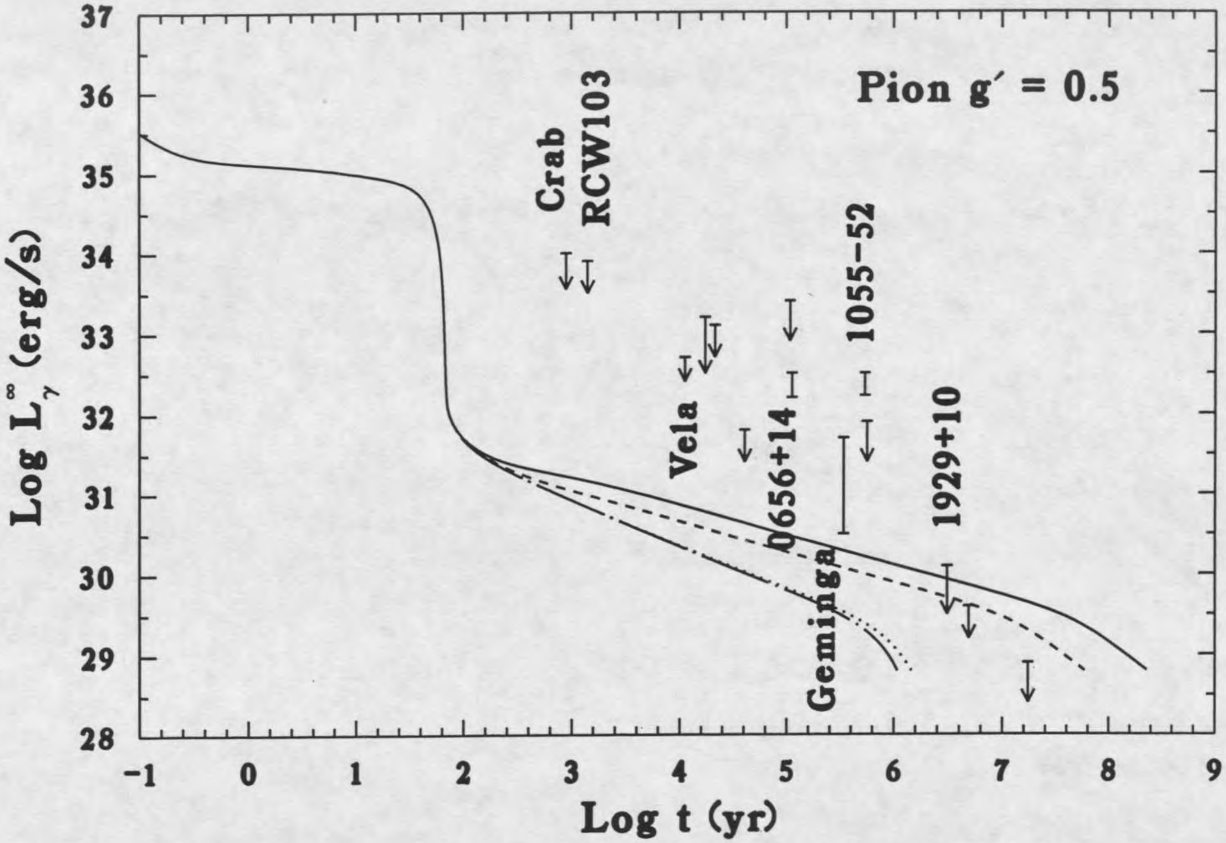

Fig(4.4) Non−Standard Cooling with Crust Breaking Heating Effect

relaxation time, the surface temperature drops thereafter, which gives the sharp decline at age 100 yr in our Fig(4.4). The dash-dotted line is the cooling curve without heating. In the other curves, the crust cracking heating effect is included, with $\epsilon_c = 0.01, 0.005$, and 0.0005, respectively, in a descending order. The larger the ϵ_0 value, the higher the temperature. In this non-standard case, the heating becomes significant as early as at age $t \sim 10^2$ yr, earlier than in the standard case. This is because the time when the temperature of the crust becomes less than $10^8 K$ is earlier than in the standard case, due to the fast cooling mechanism in the non-standard scenario.

The superfluidity of the core particles will suppress the neutrino emissivity by a factor of $\exp(-\Delta/T)$, where Δ is the superfluid energy gap, and T is temperature. By now there are several superfluid models with quite different energy gaps. Because the emissivity depends on Δ exponentially, different models will give quite different cooling curves. The energy gap depends on the nuclear interaction force and neutron effective mass m_n^*. A larger neutron effective mass gives a larger energy gap, and so does a smaller nuclear repulsion force. For standard cooling, the suppression of the neutrino emissivity by superfluidity is not as effective as in the non-standard case, and different superfluid energy gap estimations do not make a serious difference.

In our non-standard calculations, we adopt several superfluid models: Model E1, Model E2 and Model AO. Models E1 and E2 represent two extremes. In Model E1, we set the neutron effective mass to be $m_n^* = 0.8m_n$, and the smallest nuclear repulsive force is used. Thus Model E1 has the largest energy gap. In Model E2, $m_n^* = 0.7m_n$, and moreover the superfluid effect is cut off at $3\rho_0$, where pion condensation takes place (ρ_0 is the nuclear density). In Model AO (Amundsen & Ostgard 1985), a density dependent m_n^* is used. (For details, see Umeda, Nomoto, Tsuruta, Muto, Tatsumi 1993, and also see Takatsuka & Tamagaki 1979, 1980, 1982).

Fig(4.5) shows non-standard cooling with different superfluid models but without starquake heating. The solid curve represents the model which has no superfluid, the dotted curve is for superfluid Model E2, the dashed one for Model AO, and the dash dotted one for Model E1. Model E1 has the largest energy gap. We reduce the energy gap of Model E1 by $10^{0.1}$, $10^{0.3}$, $10^{0.5}$, $10^{0.7}$ to demonstrate the effect of the gap size. We note that these different curves fill the gap between the two extremes, Models E1 and E2. The four chain-dashed lines are for the energy gap $\Delta = \Delta_{E1model} \times 10^{-0.1}$, $10^{-0.3}$, $10^{-0.5}$, $10^{-0.7}$ respectively, in a descending order. We call these four models Model E1-0.1, E1-0.3, E1-0.5, E1-0.7.

In Figs(4.6), (4.7) and (4.8), we show the effects of heating due to crust breaking for Model E1, E2, and AO. In Fig(4.9) and Fig(4.10) we show the heating effect on Models E1-0.3 and E1-0.5. Two solid lines are for non-heating case, two dashed lines are for $\epsilon_c = 0.01$, two dotted lines are for $\epsilon_c = 0.005$, and two dash dotted lines are for $\epsilon_c = 0.0005$.

4.3.2 Thermal Impulse

To explore the possibility of seeing thermal impulses after a starquake, we start

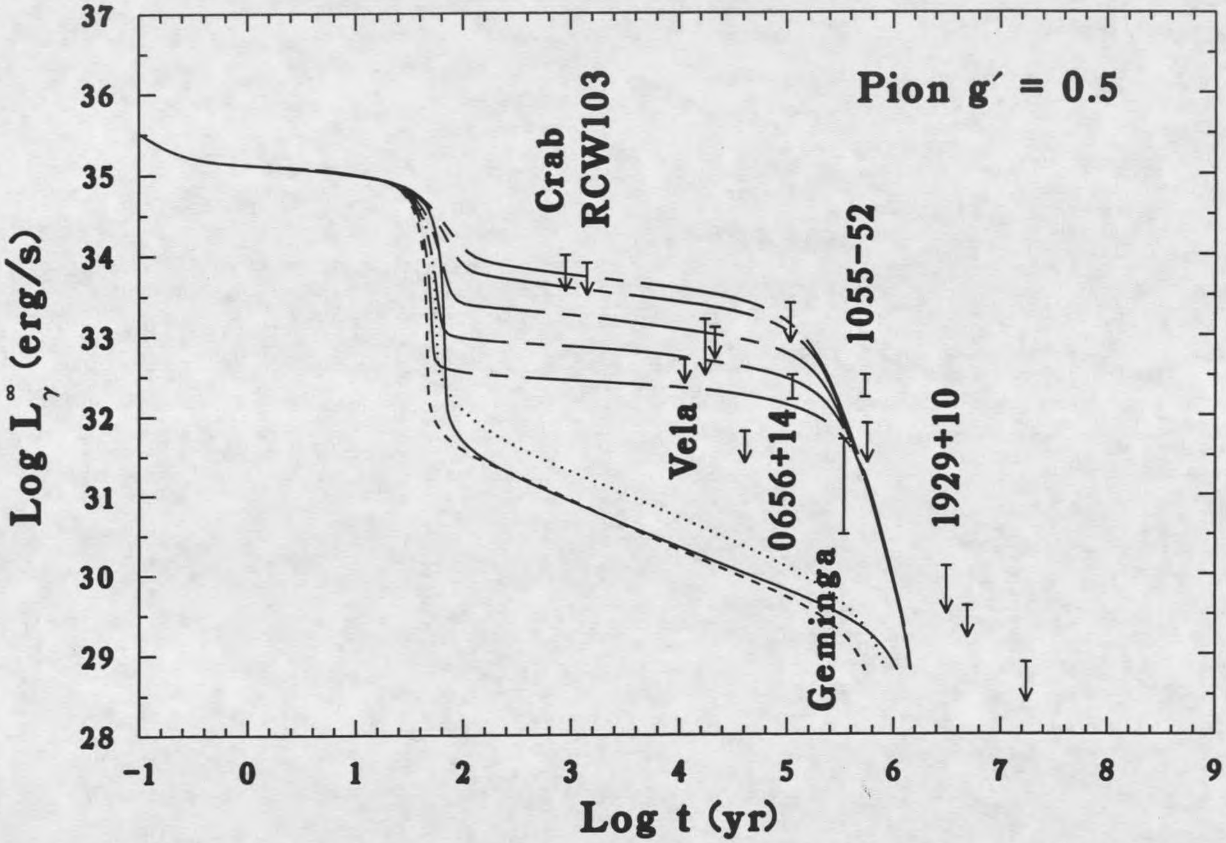

Fig(4.5) Non-Standard Cooling with Superfluidity (No Heating)

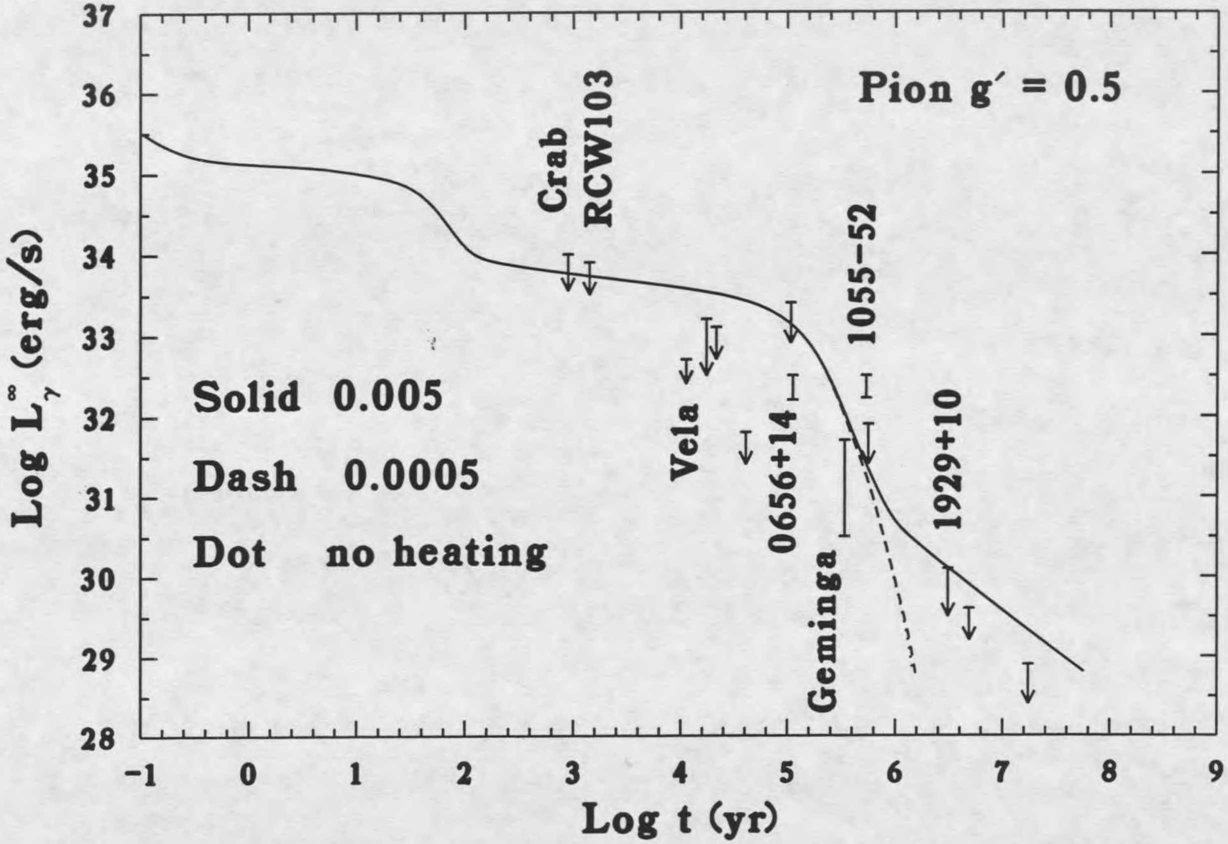

Fig(4.6) Superfluid Model E1 with Crust Breaking Heating

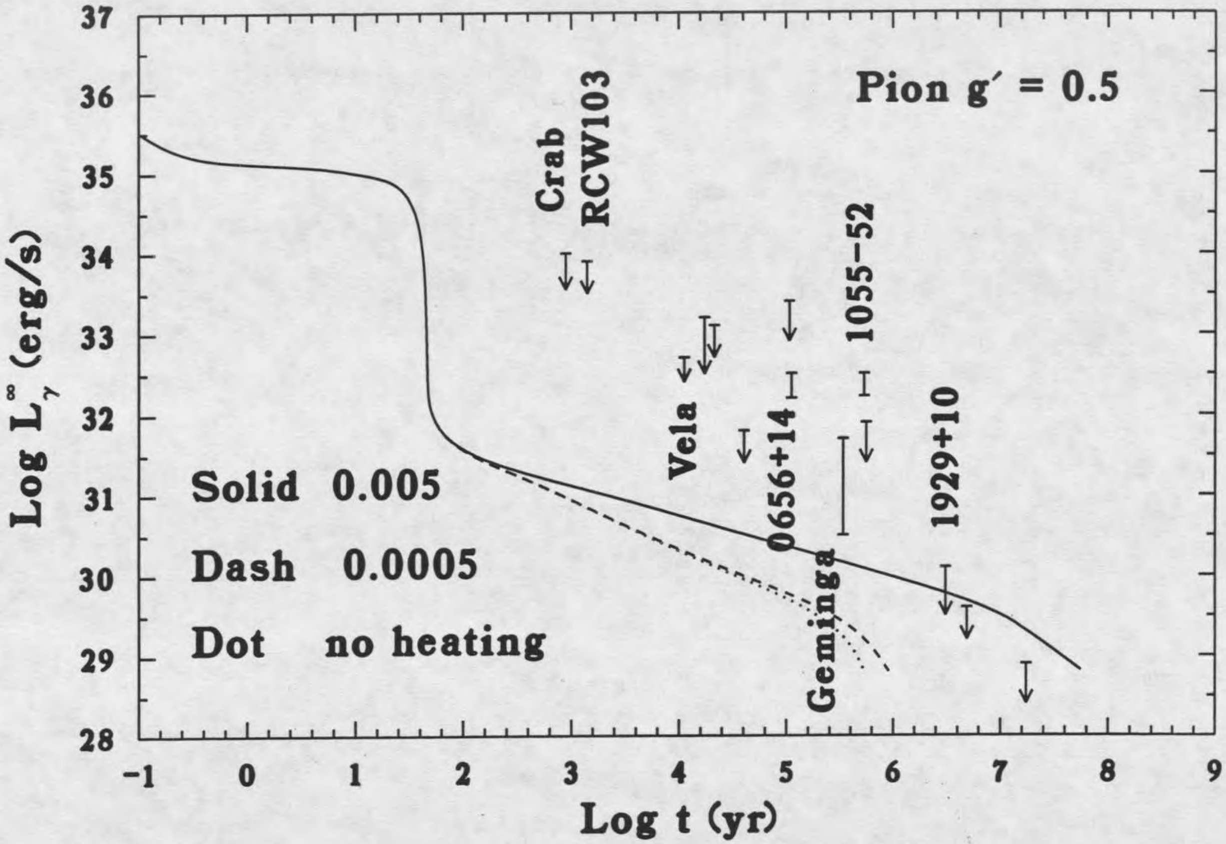

Fig(4.7) Superfluid Model E2 with Crust Breaking Heating

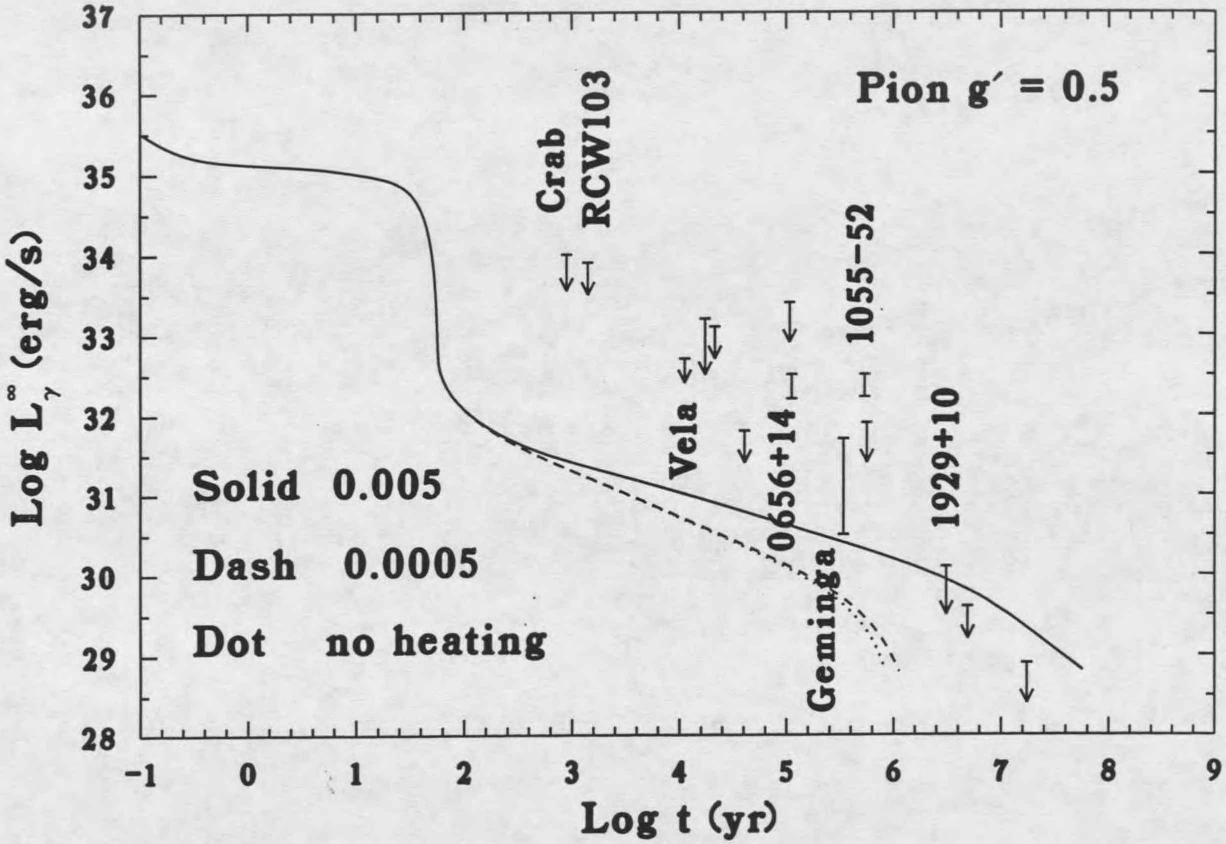

Fig(4.8) Superfluid Model AO with Crust Breaking Heating

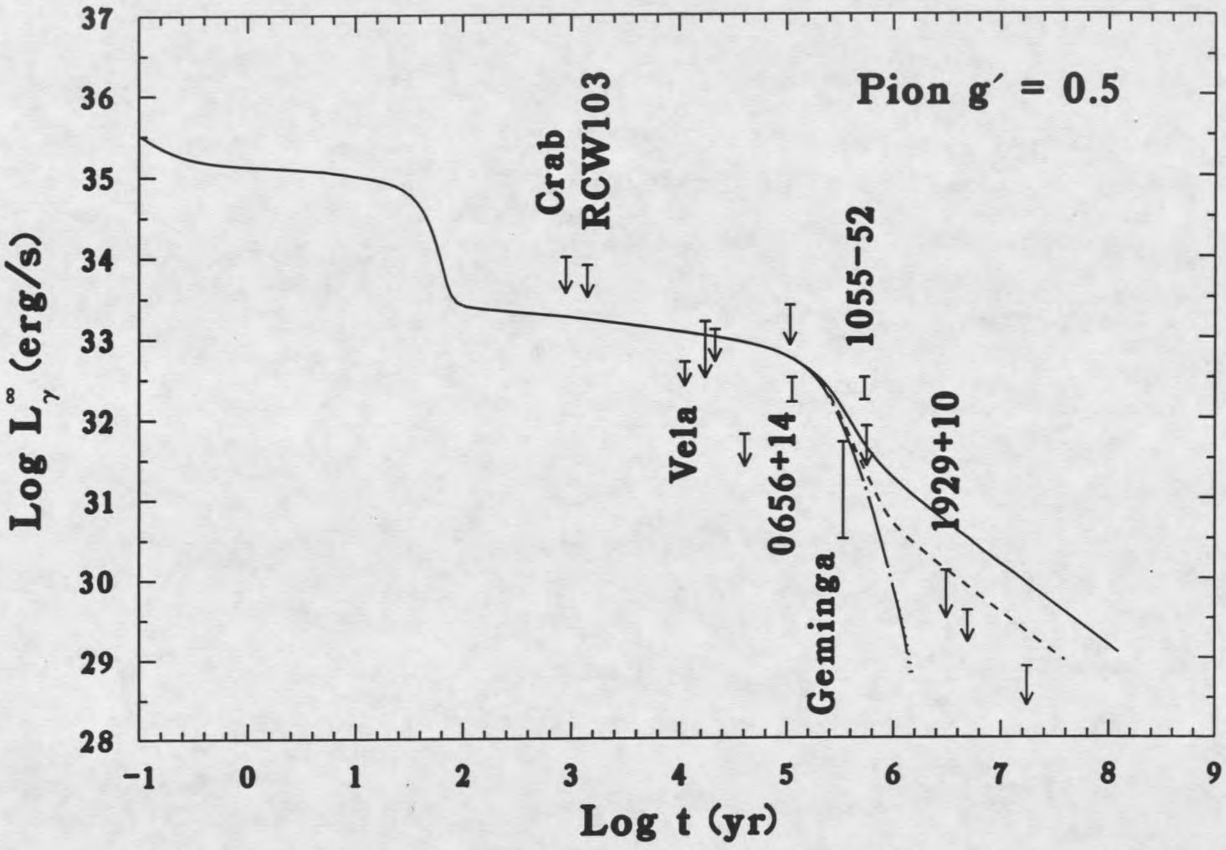

Fig(4.9) Superfluid Model E1−0.3 with Crust Breaking Heating

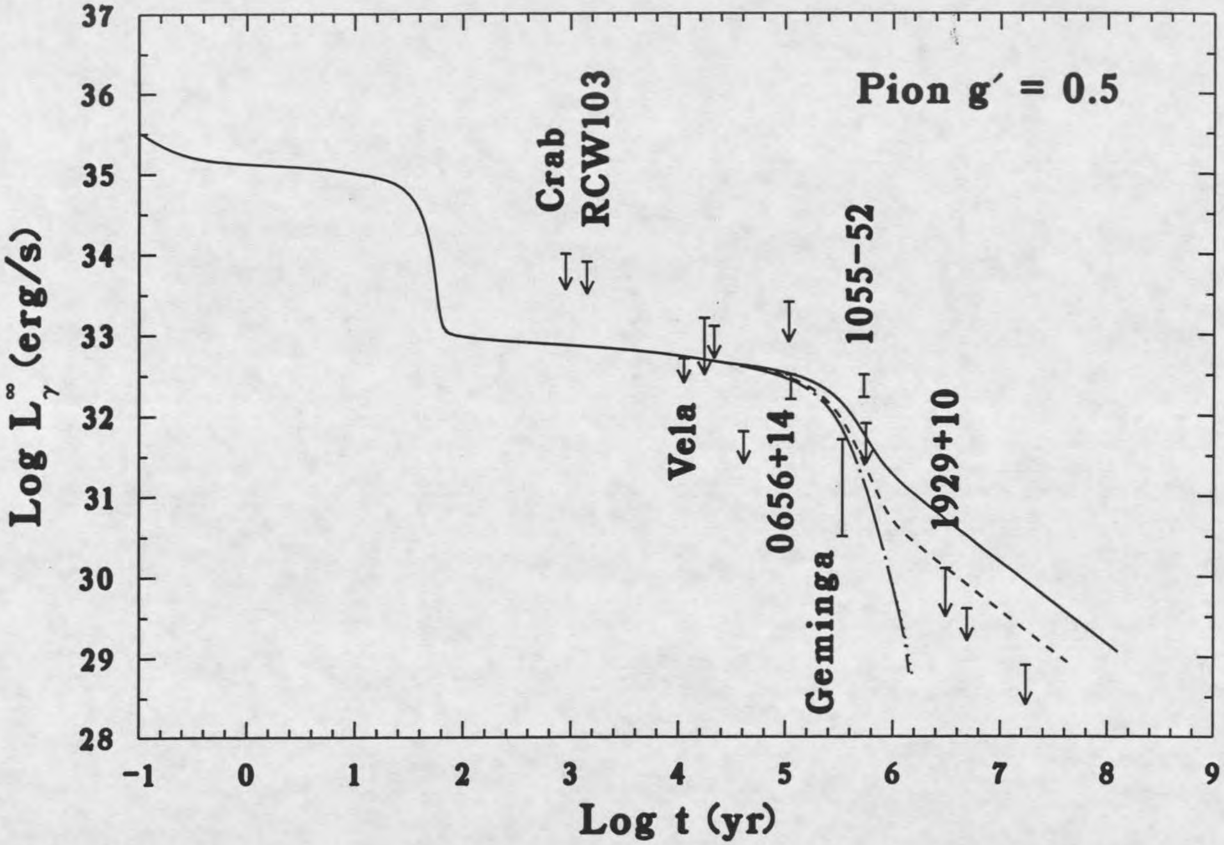

Fig(4.10) Superfluid Model E1−0.5 with Crust Breaking Heating

with Equation(4.11):

$$\Delta E = -2B\epsilon_c^2,$$

and deposit ΔE in the crust at certain age. When the thermal wave reaches the surface, the surface temperature will increase. In this chapter, we are only doing 1-dimensional simulation, and we assume that the energy of amount ΔE is deposited in the entire crust.

To model this phenomenon, we carry out the standard cooling calculation. At certain age, we deposit ΔE in the entire crustal region. Inside the crustal region, we add energy of amount E/V_c to each mesh point with V_c as the volume of the crustal region. In Fig(4.11), we show how the thermal impact changes as ΔE varies. We choose the age to be 10^5 yr, and let ΔE vary from 2×10^{47} ergs to 2×10^{49} ergs. The solid curve represents the case when no heating is included, the dashed curve is the case when ΔE is 2×10^{49} ergs, the dotted curve $\Delta E = 2 \times 10^{48}$ ergs, the chain dotted curve $\Delta E = 2 \times 10^{47}$ ergs. We can see that the larger the amount of the total energy, the higher the impulse. Also when $E = 2 \times 10^{47}$ ergs, the thermal impulse is rather small. So for the events with the total energy released smaller than 2×10^{47} ergs, it is probably impossible to detect any changes of the flux from the surface of the neutron star. It is estimated that a starquake could release about 10^{42} erg energies (Link & Epstein 1995). Then according to our calculations, such events could not possibly produce a discernible change of the surface temperature. In Fig(4.12), we show how stars' responses vary when starquakes happen at different ages. We fix ΔE to be $2 \times 10^{48} erg$, and let ΔE to be deposited at age 3.16×10^4 yr (dashed curve),

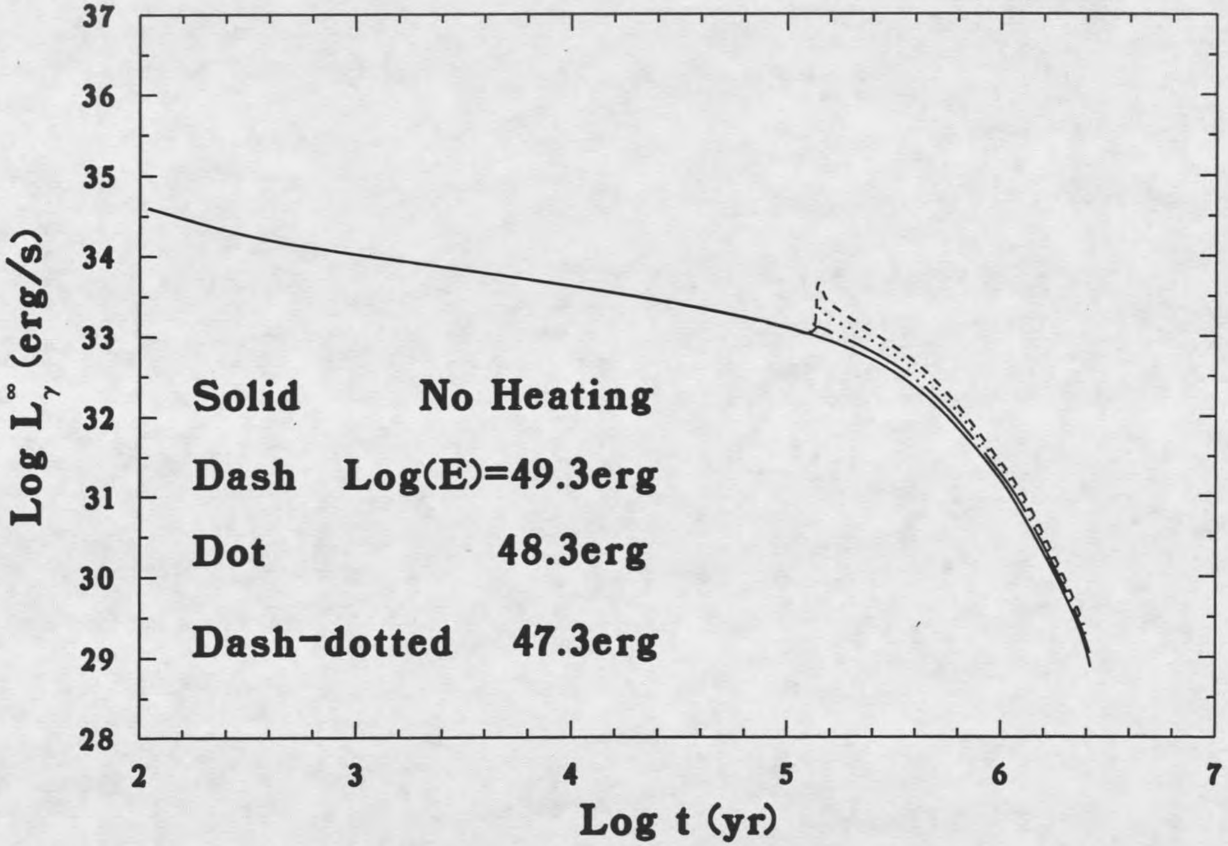

Fig(4.11) Thermal Impulses with Different Energy Depositions

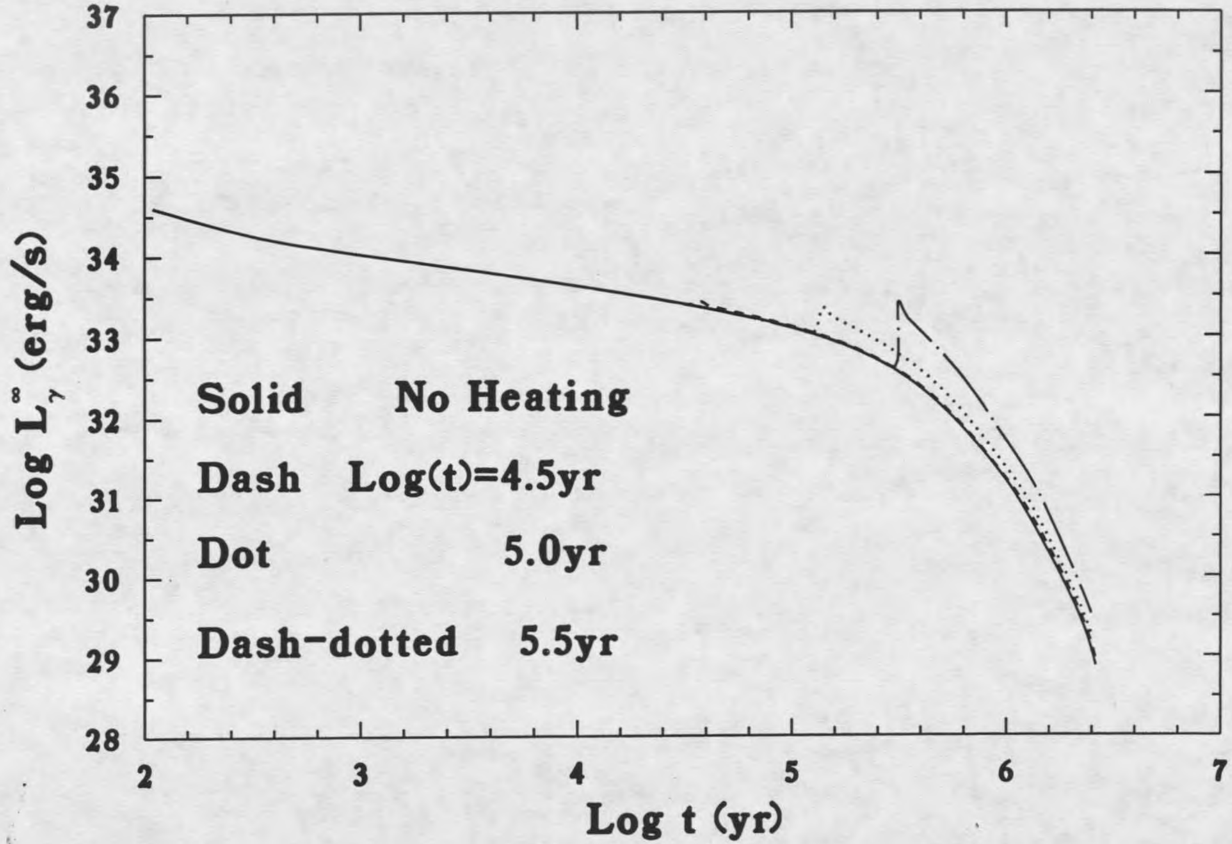

Fig(4.12) Thermal Impulses Taking Place at Different Ages, Log(E)=48.3erg

10^5 yr (dotted curve) and 3.16×10^5 yr (dash-dotted curve). Even though the same amount of energy is deposited, the star responds quite differently at different ages. At age 3.16×10^4yr, there is hardly any effect, while at age 3.16^5yr, the thermal impulse is striking. The differences in the responses of neutron stars to the energy deposition at different ages are caused by the fact that the specific heat decreases with temperature. Neutron stars of older ages have lower specific heat, thus they produce larger temperature increases with the same amount of energy depositions than younger stars.

Another possibility is that the energy is not deposited in the entire crust, but only in part of the crust. Fig(4.13) shows the results when we deposit the energy in different regions. The dash-dotted curve is the one with energy deposited in the outer crust, the dotted curve is in the inner crust, and the dashed curve in the entire crust. The dash-dotted curve shows the largest response and that is because when the energy is deposited in the outer crust, the energy density is larger due to the small volume of the outer crust, and also the outer crust is closer to the surface, so the surface temperature rises more dramatically when we deposit the energy in the outer crust than in other situations.

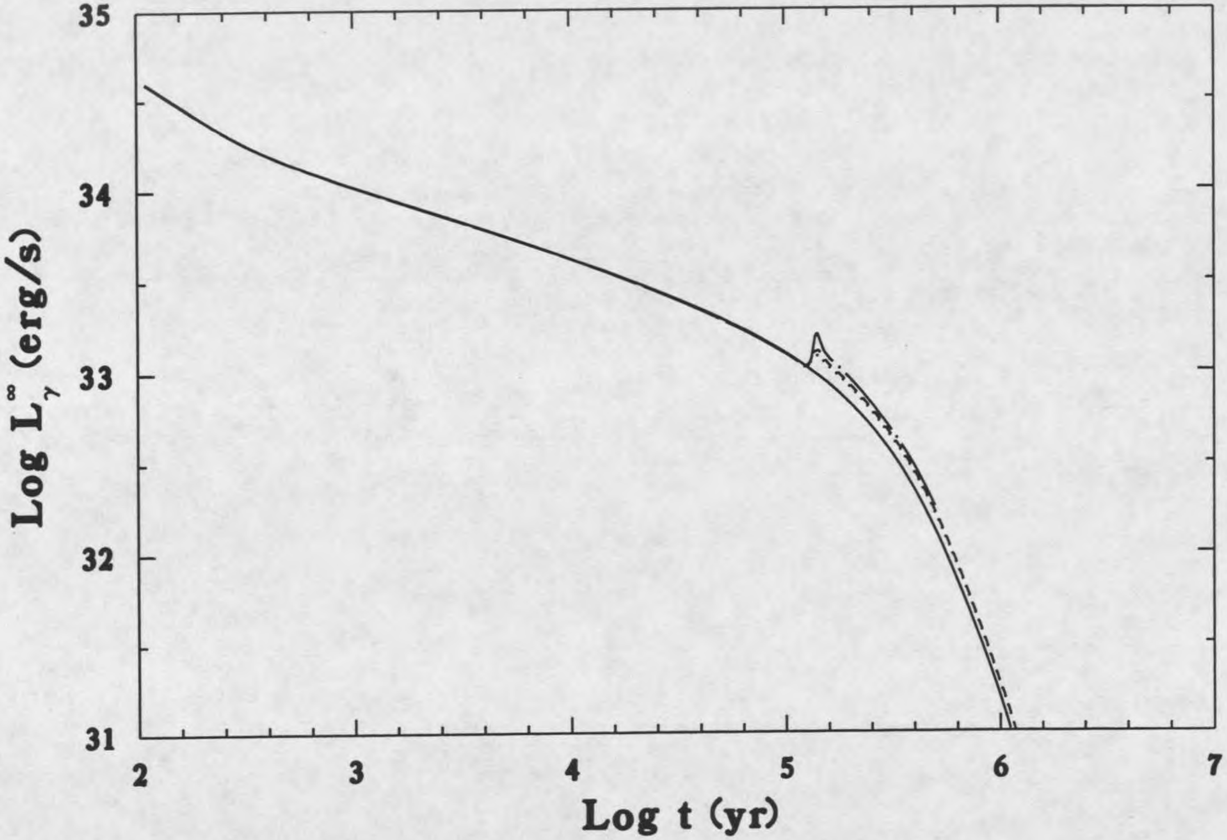

Fig(4.13) Thermal Impulses Taking Place at Different Regions, Log(E)=48.3 erg

Chapter 5

Neutron Stars as a Playground

The interior density of neutron stars can be as high as several times of nucleon density $2.8 \times 10^{14} g/cm^3$, a condition no laboratory on earth can provide so far. Thus neutron stars have been attracting attention from nuclear physicists and particle physicists. They are eager to apply their theories on neutron stars. By incorporating their theories into the thermal evolution calculations of neutron stars and by comparison with observational data, one can test those theories, and put limits to the parameters in those theories, or adjust the neutron star theory itself. In this chapter, I will talk about two such examples, the two works we've done in the past two years: axion emission (Qin et al 1995d) and neutrino magnetic dipole moment (Iwamoto et al 1995). Once a cooling code is at hand, to incorporate different theories is a fairly small task. Thus this chapter is named as: neutron stars as a playground.

5.1 Axion Emission

5.1.1 Introduction

Axions are pseudoscalar particles proposed to solve CP violation in strong interactions. The energy scale of symmetry breaking f_a is uncertain theoretically and experimentally. The unsuccessful experimental search for axions implies a very high symmetry breaking scale. There also have been numerous astrophysical and cosmological arguments concerning their possible existence. The mass of the axion m_a is related to the parameter f_a as $m_a \approx 10^{16} eV^2/f_a$ (Turner 1986). Also this symmetry breaking scale f_a determines the coupling constants. The coupling constant g_{ai} of axions to a matter field i is proportional to m_i/f_a. There are two types of axion models. One is the Kim-Shifman-Vainshtein- Zakhavarov model (KVSZ model). In KVSZ model, the axion couples to photons and hadrons, but not electrons. The other model is the Dine-Fishler-Srednicki- Zhitnitskii model (DFSZ model). In DFSZ model, the axion couples to photons, hadrons and electrons. Astrophysical and cosmological limits on the axion mass obtained from stellar evolution theories and the standard model of the early universe can be found in Sikivie 1983. In this section, we will try to derive the limit from considerations of neutron star cooling.

If axions do exist, then inside neutron stars the following axion bremsstrahlung processes are possible.

$$n + n \longrightarrow n + n + a, \tag{5.1}$$

$$p + p \longrightarrow p + p + a, \tag{5.2}$$

$$n + p \longrightarrow n + p + a. \tag{5.3}$$

Such axion emission processes would increase the cooling rate of neutron stars. In this section, we will first calculate the emissivity of the above processes. Then we will include the axion emissivity into the cooling calculations. The axion emissivity depends on the mass of axions and the coupling constants. By requiring that the cooling curve of neutron stars be compatible with the observation data, we can set some constraints on the symmetry breaking scale f_a, thus find some limits on the mass and coupling constants of axions.

5.1.2 Axion Emissivity

We start with the neutron-neutron axion bremsstrahlung process (Eq.(5.1)). Designate the four momenta of the initial two neutrons as $p_1 \equiv (E_1, \vec{p_1})$, $p_2 \equiv (E_2, \vec{p_2})$, and the final two neutrons as $p_3 \equiv (E_3, \vec{p_3})$ and $p_4 \equiv (E_4, \vec{p_4})$. Indices 1 and 3 correspond to the same neutron and, indices 2 and 4 the other, while $p_5 \equiv (E_5, \vec{p_5})$ is the four momentum for the axion.

Define:

$$\kappa \equiv p_1 - p_3, \tag{5.4}$$

$$\kappa' \equiv p_4 - p_2, \tag{5.5}$$

$$l \equiv p_1 - p_4, \tag{5.6}$$

$$l' \equiv p_3 - p_2. \tag{5.7}$$

Notice that axions are emitted thermally, so the momentum of axion $\mid p_5 \mid$ is about kT/c. In the interior of neutron stars, the momenta of neutrons are much higher than kT/c, (because $T \ll T_{fermi}$), and hence $\mid p_5 \mid \ll \mid p_4 \mid$ and $\mid p_5 \mid \ll \mid p_3 \mid$. The conservation of momentum $p_1 + p_2 = p_3 + p_4 + p_5$ simplifies to $p_1 + p_2 = p_3 + p_4$, i.e. $p_1 - p_3 = p_4 - p_2$, or $p_1 - p_4 = p_3 - p_2$. We thus find

$$\kappa' \approx \kappa, \tag{5.8}$$

and

$$l' \approx l. \tag{5.9}$$

The Feynman diagrams of process (5.1) are drawn in Fig(5.1). In Fig(5.1), the diagrams (e), (f), (g) and (h) are deduced from the diagrams (a), (b), (c) and (d), from the consideration of the indistinguishability of nucleons. The matrix element of process (5-1) is the square of the summation of the eight amplitudes corresponding to the eight diagrams in Fig(5.1) over the initial and final neutron spins.

$$\mid M(nn) \mid^2 = \sum_{\sigma_1\sigma_2\sigma_3\sigma_4} \mid M^{(a)} + M^{(b)} + M^{(c)} + M^{(d)} + M^{(a')} + M^{(b')} + M^{(c')} + M^{(d')} \mid^2 . \tag{5.10}$$

In terms of the matrix elements, the emission rate of axions can be written as:

$$\begin{aligned} \epsilon_{ann} = & \\ & \frac{1}{4V} \int \frac{d^3p_1}{8\pi^3} \int \frac{d^3p_2}{8\pi^3} \int \frac{d^3p_3}{8\pi^3} \int \frac{d^3p_4}{8\pi^3} \int \frac{d^3p_5}{8\pi^3} \\ & E_5 n(p_1) n(p_2)[1 - n(p_3)][1 - n(p_4)] \\ & V(2\pi)^4 \delta(p_3 + p_4 + p_5 - p_1 - p_2) \mid M^{(nn)} \mid^2 \\ & \frac{1}{2E_1V} \frac{1}{2E_2V} \frac{1}{2E_3V} \frac{1}{2E_4V} \frac{1}{2E_5V}, \end{aligned} \tag{5.11}$$

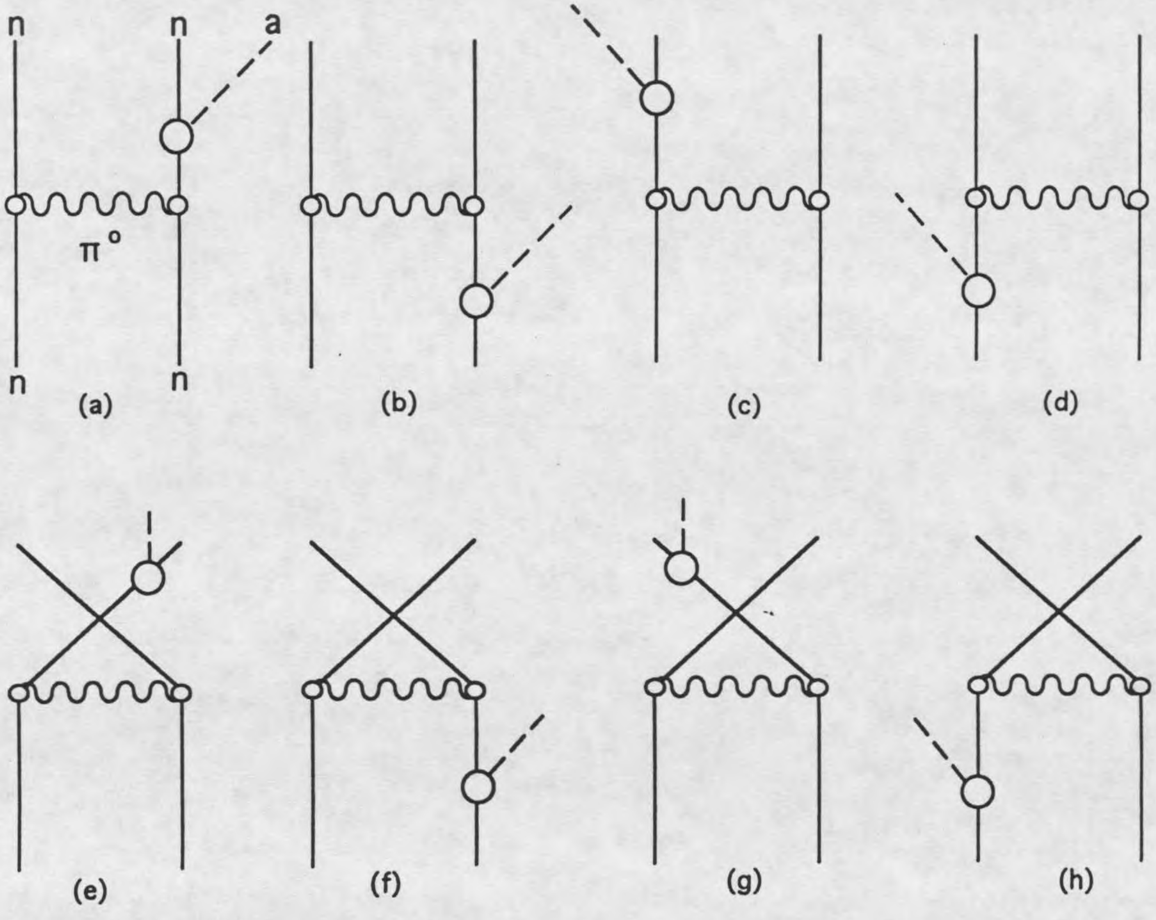

Fig(5.1) Feynman Diagram of Axion nn Bremsstrahlung Process where V is the normalization volume, and $n(p_i)$ is the distribution function for neutrons. The evaluation of the matrix element $M(nn)$ and the integration of Equation (5.11) can be found in Iwamoto 1992, they are also given in Appendix D. The expression for ϵ_{ann} is

$$\epsilon_{ann} = \frac{31}{2780\pi}\frac{g_{ann}^2}{\hbar c}(\frac{f}{m_\pi})^4[m_n^{*2}p_F(n)/\hbar^4c^6]F(\frac{m_\pi c}{2p_F(n)})(k_BT)^6. \tag{5.12}$$

Here f is about 246MeV, $g_{ann}$is the coupling constant and function F is given in Appendix D.

ϵ_{app}, the emission rate of process $p+p \longrightarrow p+p+a$, can be obtained very easily from the expression of ϵ_{ann}. The Feynman diagrams for process $p+p \longrightarrow p+p+a$ are the same as the Feynman diagrams for process $n+n \longrightarrow n+n+a$ except for the labels. If we replace n with p, the above derivation works for $p+p \longrightarrow p+p+a$. So the axion emissivity due to proton-proton bremsstrahlung is

$$\epsilon_{app} = \frac{31}{2780\pi}\frac{g_{app}^2}{\hbar c}(\frac{f}{m_\pi})^4[m_p^{*2}p_F(p)/\hbar^4c^6]F(\frac{m_\pi c}{2p_F(p)})(k_BT)^6. \tag{5.13}$$

Inside neutron stars, the Fermi momenta of protons are much smaller than the Fermi momenta of neutrons. Since

$$\frac{\epsilon_{app}}{\epsilon_{ann}} = \frac{p_F(p)F(\frac{m_\pi c}{2p_F(p)})}{p_F(n)F(\frac{m_\pi c}{2p_F(n)})}, \tag{5.14}$$

and $F(x)$ is a monotonously decreasing function, (see Fig(5.2)), $\frac{\epsilon_{app}}{\epsilon_{ann}} \ll 1$. For typical situations inside neutron stars, $\frac{\epsilon_{app}}{\epsilon_{ann}} \sim 0.1$.

Now we calculate the emissivity for process $n+p \longrightarrow n+p+a$. Fig(5.3) gives the Feynman diagrams for this process. The Feynman diagrams for this process are

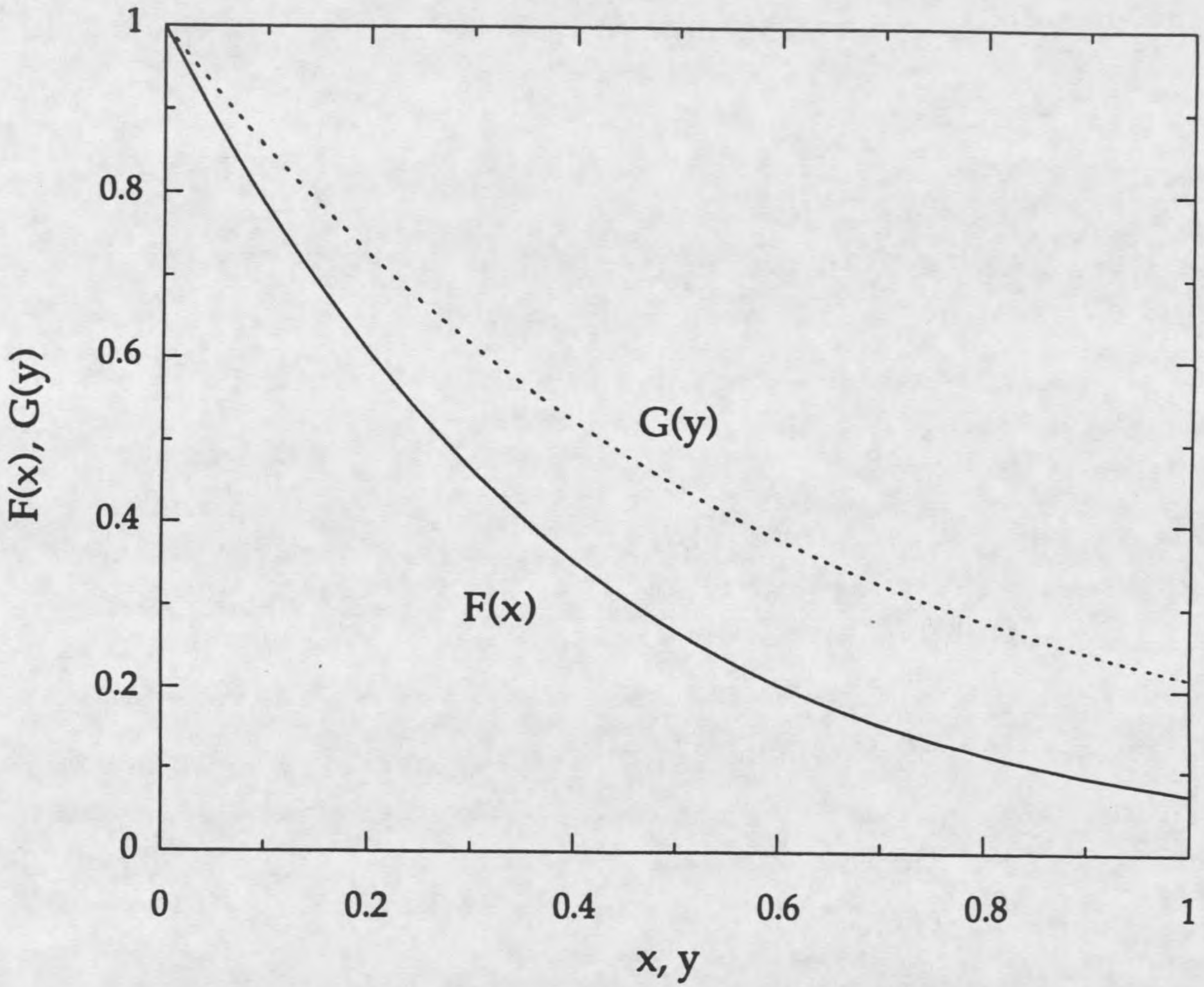

Fig(5.2)   Function F(x) and G(y)

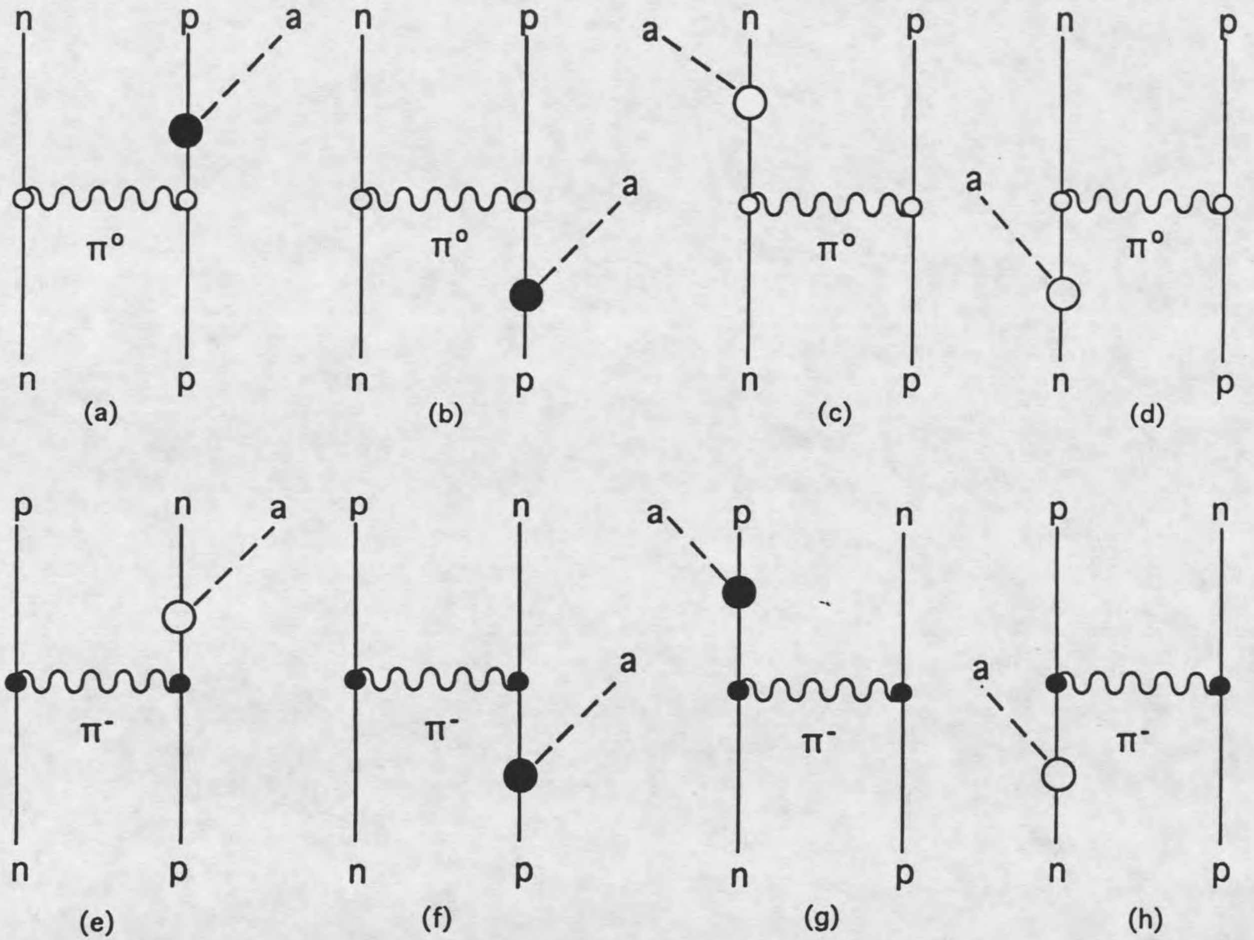

Fig(5.3) Feynman Diagram of Axion np Bremsstrahlung Process different from those for process $n + n \longrightarrow n + n + a$. Between neutrons and protons, they can exchange neutral pions or exchange charged pions. When they exchange neutral pions, they stay as the same particle as before the reaction. When they exchange charged pions, protons will become neutrons and neutrons will become protons during the reaction. Since neutrons and protons are different particles, no exchange diagrams need be considered.

The matrix element $M(np)$ is the sum of the matrix elements of each Feynman diagram for the np axion bremsstrahlung process.

$$| M(np) |^2 = \sum_{\sigma_1\sigma_2\sigma_3\sigma_4} | M^{(a)} + M^{(b)} + M^{(c)} + M^{(d)} + M^{(e)} + M^{(f)} + M^{(g)} + M^{(h)} |^2, \quad (5.15)$$

where $M^{(a)}$ to $M^{(d)}$ are the four matrix elements associated with the processes of neutral pion exchange, and $M^{(e)}$ to $M^{(h)}$ are the four matrix elements associated with the processes of charged pion exchange. From $M^{(a)}$ for diagram (a), we can easily write down $M^{(c)}$. For diagram (c), the axion is coming out of a neutron instead of a proton, so we should replace g_{app} in $M(a)$ with g_{ann}, and switch the labels. Then we have

$$M^{(c)} = \frac{g_{ann}}{g_{app}} M^{(a)}(2p, 1n, 4p, 3n, -k). \quad (5.16)$$

Similarly, we can write down $M^{(d)}$ as:

$$M^{(d)} = -\frac{g_{ann}}{g_{app}} M^{(b)}(2p, 1n, 4p, 3n, -k). \quad (5.17)$$

For diagrams (e) (f) (g) and (h), the symmetry consideration will help us write down the matrices easily. A pion can exchange either π^- or π^+, giving an extra factor of 2.

The matrices for diagrams (e) (f) (g) and (h) are related to the matrices for diagram (a), (b), (c), and (d) as:

$$\begin{aligned} M^{(e)} &= -2(g_{ann}/g_{app})M^{(a)}(1n, 2p, 4p, 3n, l), && (5.18)\\ M^{(f)} &= -2M^{(b)}(1n, 2p, 4p, 3n, l), && (5.19)\\ M^{(g)} &= -2(g_{app}/g_{ann})M^{(c)}(1n, 2p, 4p, 3n, l), && (5.20)\\ M^{(h)} &= -2M^{(d)}(1n, 2p, 4p, 3n, l). && (5.21) \end{aligned}$$

The axion emission rate for $p + n \longrightarrow p + n + a$ can be expressed as:

$$\begin{aligned} &\epsilon_{anp} = \\ &\frac{1}{V}\int\frac{Vd^3p_1}{8\pi^3}\int\frac{Vd^3p_2}{8\pi^3}\int\frac{Vd^3p_3}{8\pi^3}\int\frac{Vd^3p_4}{8\pi^3}\int\frac{Vd^3p_5}{8\pi^3} \\ &E_5 n(p_1)n(p_2)(1-n(p_3))(1-n(p_4)) \cdot \\ &V(2\pi)^4\delta(p_3+p_4+p_5-p_1-p_2) \mid M(np) \mid^2 \frac{1}{\sum_{i=1}^5(2E_iV)}. \end{aligned} \tag{5.22}$$

Perform the integral in the same way as in the case of ϵ_{ann}, we could get

$$\begin{aligned} \epsilon_{anp} &= \frac{31}{5670\pi\hbar c}(\frac{f}{m_\pi})^4[\frac{(m_N)^2 p_F(p)}{\hbar^4 c^6}](k_BT)^6 \cdot \\ &\{\frac{1}{2}(g^2+h^2)F(y) + (g^2+h^2)G(y) + \\ &(g^2+\frac{1}{2}h^2)[F(\frac{2xy}{x+y}) + F(\frac{2xy}{y-x}) + \\ &\frac{y}{x}[F(\frac{2xy}{x+y}) - F(\frac{2xy}{y-x})]]\}, \end{aligned} \tag{5.23}$$

where $x = m_\pi c/2p_F(n)$, $y = m_\pi c/2p_F(p)$, $F(x)$ is the same as in Eq.(5.12), $G(y)$ is

$$G(y) = 1 - y\arctan(\frac{1}{y}), \tag{5.24}$$

and it is shown in Fig(5.2). If we take limits $x \longrightarrow 0$ and $y \longrightarrow 0$, which are good approximations in the interior of neutron stars, then

$$\frac{\epsilon_{anp}}{\epsilon_{ann}} \sim \frac{x}{y} = \frac{p_F(p)}{p_F(n)} < 1, \tag{5.25}$$

together with Eq.(5.14), we find

$$\epsilon_{app} < \epsilon_{anp} < \epsilon_{ann}. \tag{5.26}$$

Among the axion emitting processes, the process $n + n \longrightarrow n + n + p$ is the most efficient. In Fig(5.4), we plot ϵ_a as a function of density at temperatures 10^9, 10^8 and $10^7 K$ (solid, dot, dash, respectively).

5.1.3 Results

The presence of axions increases the energy loss rate of the star. The equation for the evolution of interior temperatures is now

$$c_v \frac{dT}{dt} = -\frac{1}{4\pi r^2 e^{2\phi}} \frac{d\mathcal{L}}{dr} - e^{\phi}(\epsilon_\nu + \epsilon_a). \tag{5.27}$$

The energy lose rate includes two parts: neutrino emissivity ϵ_ν and axion emissivity $\epsilon_a = \epsilon_{ann} + \epsilon_{anp} + \epsilon_{app}$. Among the three different axion emission processes, we already showed, ϵ_{ann} is the most important one. ϵ_{ann} can be written as:

$$\epsilon_{ann} = 5.67073 \times \hbar^4 c^4 \frac{g_{ann}^2}{G^2 g_A^2} \frac{1}{(m_n^*)^2 (kT)^2} \epsilon_{nn}. \tag{5.28}$$

Here ϵ_{nn} is the emissivity of the nn bremsstrahlung process, $g_{ann} = 12 c_n m_N / f_a$ $MeVm$, $c_n = 0.537$ and m_N is the mass of neutrons. G is the weak Fermi coupling constant, $G = 8.74 \times 10^{-5} MeV fm^3$, $g_A = 1.26$, it is the axial vector renormalization,

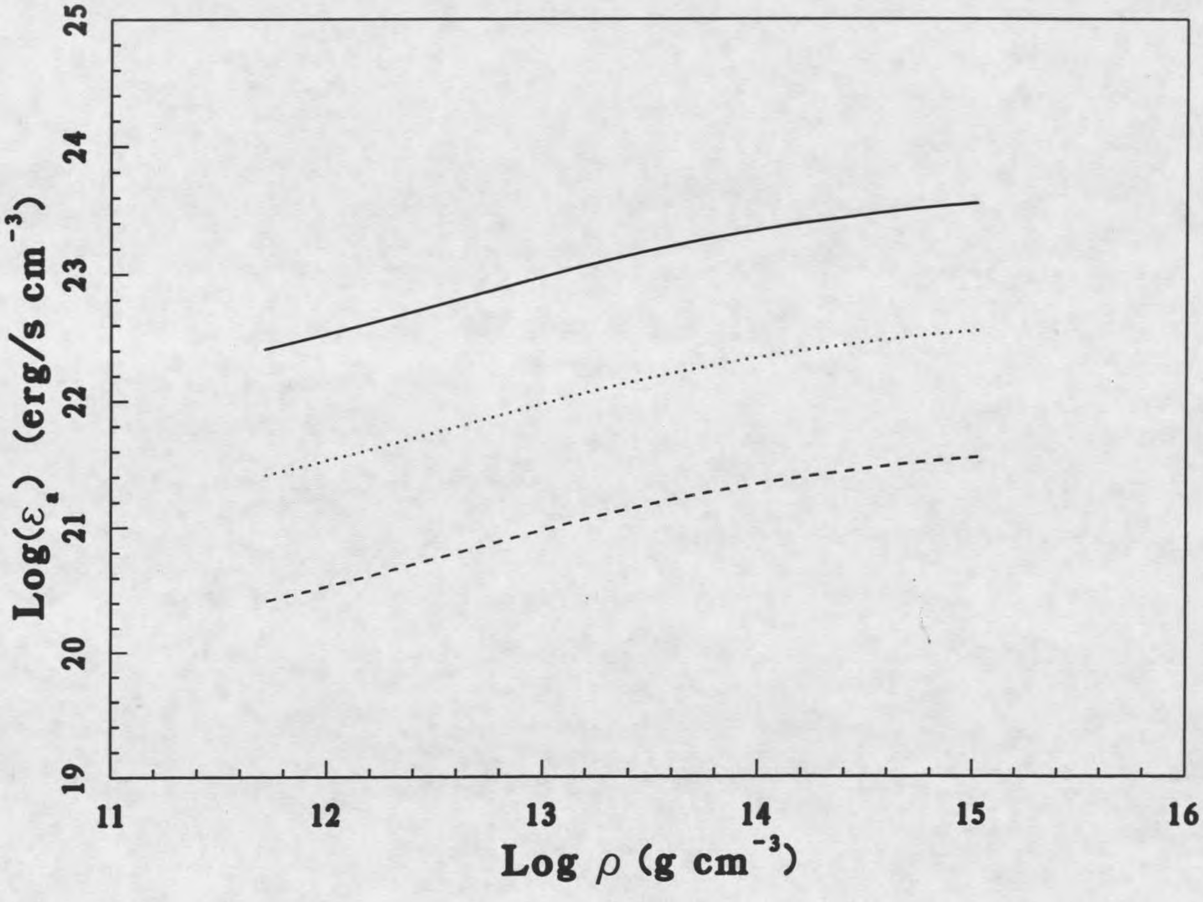

Fig(5.4) ε_a vs. ρ at T=10^9, 10^8, 10^7

m_n^* is the effective mass of neutrons, and kT is the thermal energy. When $f_a = 10^{25}m^{-1}$ and T is $10^{10}K$, ϵ_{ann} is about the same as ϵ_{nn}. Since $\epsilon_{ann}/\epsilon_{nn}$ is proportional to T^{-2}, as the temperature decreases, ϵ_{ann} becomes more important than ϵ_{nn}.

Figs(5.5), (5.6) and (5.7) show the calculation results. Fig(5.5) is for FP type neutron stars, Fig(5.6) PS type and Fig(5.7) BPS type. In all three figures, the solid curves are the standard evolutionary model with no axion emission. The dashed curves correspond to f_a equal $10^{26}m^{-1}$, which is equivalent to $1.99 \times 10^{13}MeV$. The dotted curves correspond to f_a equal $3.625 \times 10^{25}m^{-1}$ and the dash-dotted curves $10^{25}m^{-1}$. In these three figures, we plot the observed luminosity for thirteen pulsars. Three of them are detections: Geminga, PSR0656+14 and PSR1055-52, others are upper limits. Since the observational data are distributed in a wide range around the standard cooling curve, the dashed curve and the dotted curve do not pose significant disagreement with the observational data, even though they differ substantially from the standard cooling curve. When considering individual pulsars, for instance PSR1055-52, the dashed curves in all three figures fall below the observed luminosity. So the constraint on f_a obtained from this consideration is $f_a > 1.99 \times 10^{13}MeV$. Since f_a is related to the mass of axions m_a as:

$$m_a = \frac{3.7 \times 10^{16}eV^2}{f_a}, \tag{5.29}$$

that implies $m_a < 1.87 \times 10^{-3}eV$. Overall, only the chain-dotted curve with $f_a = 10^{25}m^{-1}$ goes below all the observational data in these three figures. We may consider this case as unacceptable, and that will lead to the limit $m_a < 1.87 \times 10^{-2}eV$.

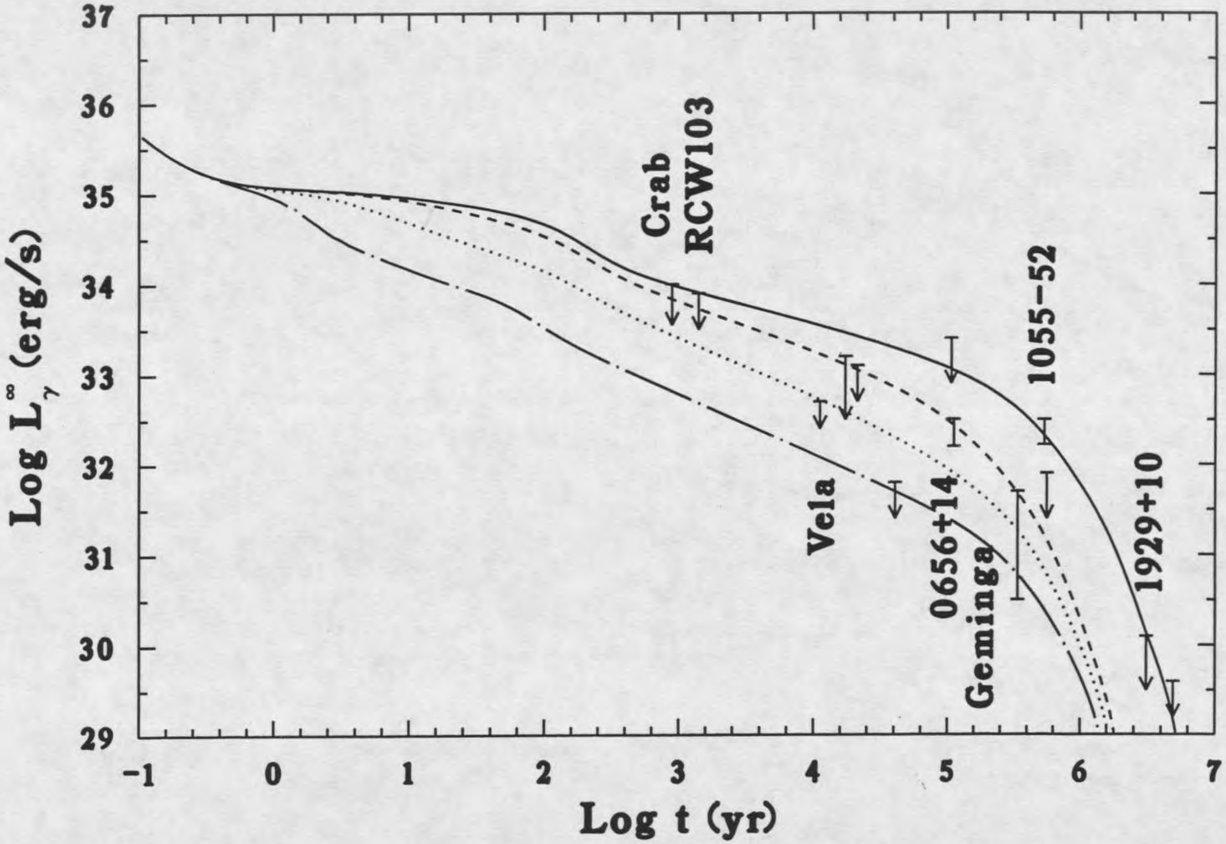

Fig(5.5) Cooling with Axion Emission, the FP Model

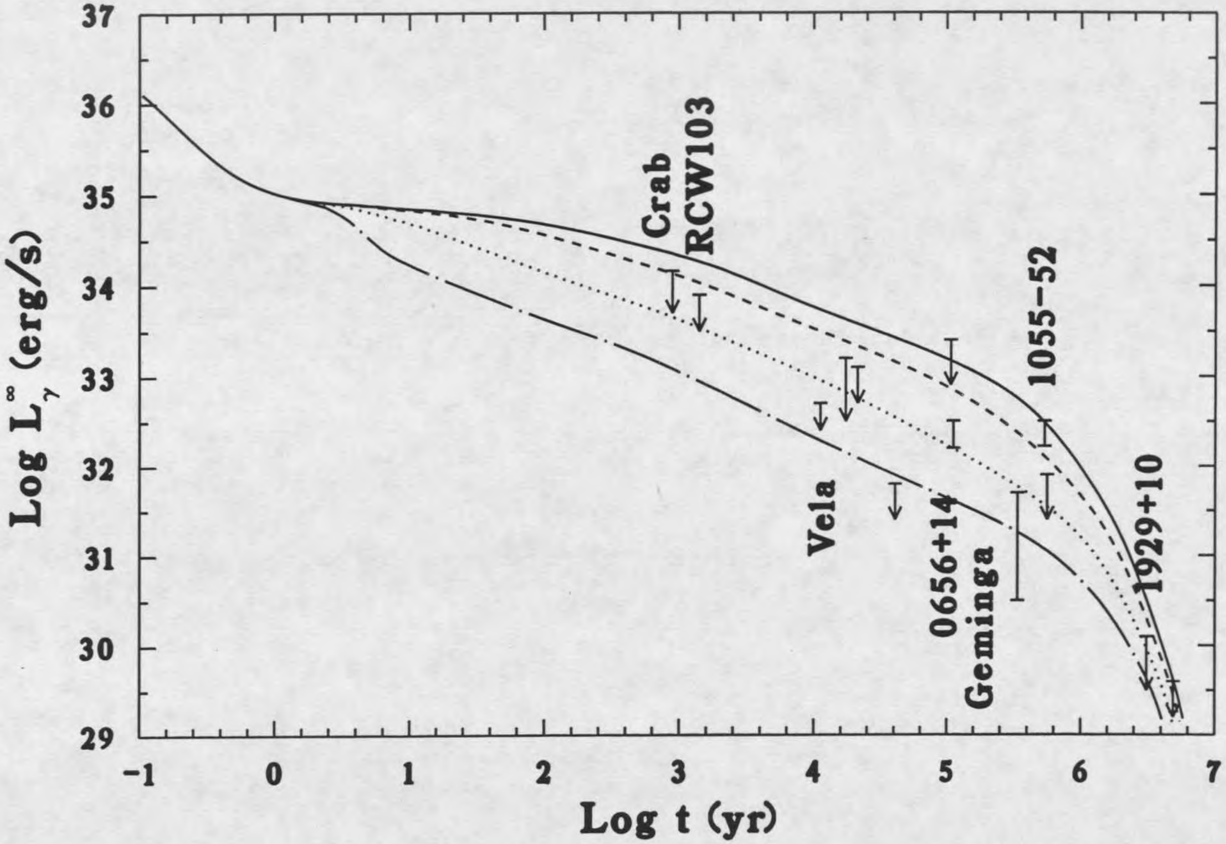

Fig(5.6) Cooling with Axion Emission, the PS Model

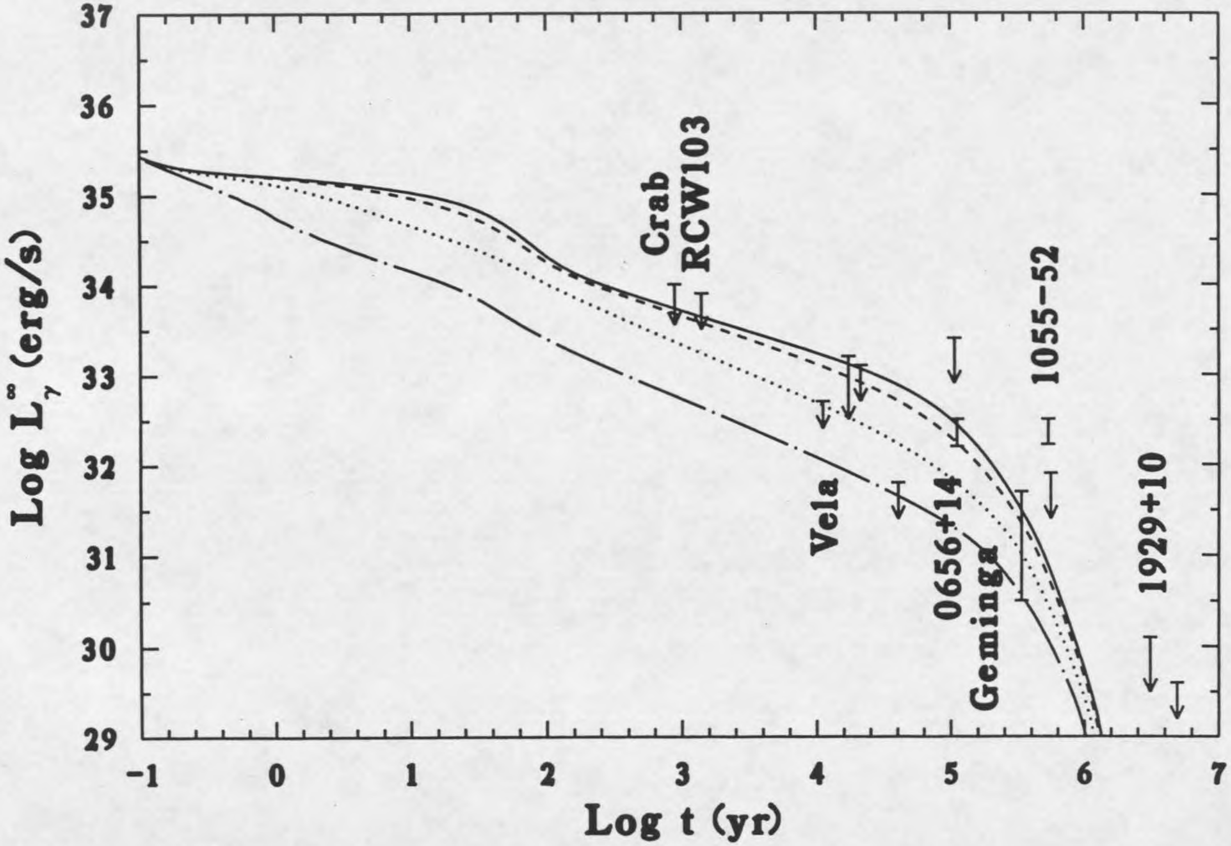

Fig(5.7) Cooling with Axion Emission, the BPS Model

5.1.4 Discussions

The inclusion of axion emissions accelerates the neutron star cooling. Since the axion emissivity is proportional to T^6 and the neutron-neutron bremsstrahlung neutrino process is proportional to T^8, the axion emission becomes more dominant over the neutrino emission as time goes on. This is shown in Figs(5.5), (5.6) and (5.7). At age $10^3 yr < t < 10^5 yr$, the differences between the standard evolutionary curve and the curves with axion emissions are the biggest. After $t > 10^5 yr$, the photon cooling which depends on temperature as $T^{2.7}$, takes over. We are fortunate to have several detections around age $10^3 < t < 10^5$ yr, and that makes it possible for us to obtain a rather stringent limit on the axion mass. In the case of neutrino magnetic dipole moment (§5.2), we are unable to obtain a limit on the neutrino magnetic moment as stringent as from other astrophysical considerations, such as the Sun, white dwarf and red giant (Iwamoto, Qin, Fukugita and Tsuruta 1995).

The limits on the axion mass have also been examined through considerations of red giant, white dwarf evolutions. The mechanisms are the same for all cases, that is the axion emission will accelerate the stellar evolutionary processes. The limit from the Sun is $m_a < 1.7eV$ (Krauss, Moody, Wilezek 1984), the limit from red giants is $m_a < 10^{-2}eV$ (Dearborn, Shramm and Steigman 1986), and white dwarf cooling gives a limit $m_a < 3 \times 10^{-2}eV$ (Raffelt 1986). Our limits are comparable and in some cases better than these results.

5.2 Neutrino Magnetic Dipole Moment

5.2.1 General Considerations

A finite neutrino magnetic moment would indicate a new interaction that breaks chiral symmetry. The present laboratory limit is $1.2 \times 10^{-9}\mu_B$ for μ neutrinos, and $1.5 \times 10^{-10}\mu_B$ for electron neutrinos, where μ_B is the Bohr magneton. With a finite neutrino magnetic dipole moment, the cross sections of many processes involving neutrinos will be quite different, and may well change the various scenarios in cosmology and stellar evolution. Astrophysical and cosmological limits on the neutrino magnetic dipole moment have been obtained from arguments about the energy loss rates of neutron stars (Iwamoto et al 1995), the Sun, red giants, white dwarfs as well as nucleosynthesis in the early universe.

In the early universe, before neutrinos decoupled from the rest of the universe, the neutrino magnetic dipole moment will make the following scattering process possible:

$$\nu_L e^- \longrightarrow \nu_R e^- \tag{5.30}$$

ν_L stands for left-handed neutrinos, ν_R right-handed neutrinos. This process will double the neutrino species and increase the expansion rate of the universe, causing an overabundance of helium (Morgan 1981). The constraint obtained from this consideration is

$$\mu_\nu < 0.52 \times 10^{-10}\mu_B/\sqrt{T_{200}}, \tag{5.31}$$

with $T_{200} = T/200MeV$.

The stellar evolution argument concerns the reaction of the plasmon decaying into $\nu_L \bar{\nu}_R$. The plasmon γ decays through the direct photon coupling with neutrino magnetic moment. Such reactions may increase the cooling rates of the Sun, red giants, white dwarfs and neutron stars. Comparison with the observation would allow limits to be placed on the value of the neutrino magnetic dipole moments.

The argument concerning the stellar evolution goes as follows. For white dwarfs, we have very good observational data. The Hyades cluster, for instance, includes 21 white dwarfs (Stothers 1971). Two distinct sequences of white dwarfs appear in this cluster. One sequence is the low mass red sequence. The other is the blue sequence. We will consider the ten blue stars only. The observed luminosity function for the blue Hyades white dwarfs is listed in Table (5.1), as the first column. The theoretical predictions assuming that the neutrino magnetic dipole moment is zero are given in the second column. If the neutrino magnetic dipole moment is nonzero, the extra energy loss due to the neutrino magnetic moment will be $0.75 \times 10^3(\kappa/10^{-10})^2$ times stronger with κ defined as $\kappa = \mu_{nu}/\mu_B$. That will accelerate the evolution process of the stars and will shift the luminosity function of the Hyades cluster to the fainter side. The observed luminosity function requires $0.75 \times 10^3(\kappa/10^{-10})^2$ to be smaller than 100. That leads to a very stringent constraint:

$$\mu_\nu < 0.37 \times 10^{-10} \mu_B. \tag{5.32}$$

For the sun, we obtain the limit by requiring that $L_{\nu,mag}$ be smaller than $L_\odot$, and this leads to:

$$\mu_\nu < 1.3 \times 10^{-9} \mu_B. \tag{5.33}$$

Table(5.1) Luminosity Function of Hyades Cluster

Log(L / L⊙)	Observed Number	Theoretical Estimation (μ_v=0)
> 1.50	0	0
-1.50 to -1.75	1	1
-1.75 to -2.00	2	2
-2.00 to -2.25	2	2
-2.25 to -2.50	3	2
-2.50 to -2.25	2	3
<-2.75	0	0

5.2.2 Constraints from Neutron Star Cooling

Plasma Neutrino Emissivity

In the following, we will concentrate on neutron star cooling. Sutherland et al (1976) gave the expressions for the rate of the plasmon decay process, assuming the neutrino magnetic dipole moment to be zero,

$$Q_l = \frac{g^2}{3\pi e^2}\frac{1}{(2\pi)^3}\frac{1}{e^{\omega_0\beta}-1}\omega_0^9\left(\frac{16}{315}\right), \tag{5.34}$$

$$\begin{aligned} Q_t &= \frac{4g^2}{3\pi e^2}\frac{\omega_0^6}{\beta^2}\frac{1}{(2\pi)^3}\sum_{n=1}^{\infty}\frac{1}{n^3} \\ &= \frac{4g^2}{3\pi e^2}\frac{\omega_0^6}{\beta^2}\frac{1}{(2\pi)^3}\frac{n^2(n+1)^2}{4}, \end{aligned} \tag{5.35}$$

with $g = 3.08 \times 10^{-12} m_e^{-2}$ as the weak coupling constant, $\omega_0^2 = 4e^2 p_F^3/3\pi E_F$, $\beta = 1/kT$. Here Q_l is the decay rate for longitudinal photons, and Q_t is for transversal photons.

Two modifications are needed. The first is that the above expressions are obtained through the V-A theory (Feynman and Gell-man 1958). Here V stands for the vector part of the interaction and A the axial vector part. The conversion to the Weinberg-Salam-Glashow theory (WSG theory) requires a factor to be multiplied to the expression of plasma neutrino emissivity from the V-A theory. The second modification is that the plasma dispersion relation in Sutherland et al (1976) is not adequate. We need a better plasma dispersion relation.

In the standard WSG model, there are two charged "intermediate" bosons W^+

and W^-, and one neutral intermediate boson Z^0. They are predicted to have masses:

$$m_W c^2 = \frac{37.3GeV}{\sin\theta_W} = 78.1 \pm 1.7GeV, \quad (5.36)$$

$$m_Z c^2 = \frac{m_W c^2}{\sin\theta_W} = 88.9 \pm 1.4GeV, \quad (5.37)$$

where the Weinberg angle θ_W is experimentally determined to be:

$$\sin^2\theta_W = 0.228 \pm 0.010. \quad (5.38)$$

All processes taking place in the neutron star interiors are at low interaction energies, $E^2/c^4 \ll m_W^2$ and m_Z^2, Under this approximation, the Hamiltonian of the WSG theory encompasses the old V-A Hamiltonian. The difference between the old and new theories at low energy levels is that in the old theory only charged current reactions were allowed, while in the new theory, in addition to the charged vector bosons W^+ and W^-, a neutral boson Z^0 also mediates the reaction. A factor of $c_V^2 + n(1-c_V)^2$ is needed to take this fact into account. Here c_V is defined as $c_V \equiv \frac{1}{2} + 2\sin^2\theta_W$, and n is the number of neutrino flavors. For electron type neutrinos, n is 0, for muon type neutrinos, n is 1, and for τ type neutrinos, n is 2. Since $c_V^2 = 0.9312 \pm 0.0031$, and $(1-c_V)^2 = 0.012$ is very small, we approximate $c_V^2 + n(1-c_V)^2$ with c_V^2.

The correct plasma dispersion relation requires a factor of $(5/6)^{3/2}$ in front of the old expression for the transverse plasma neutrino emissivity. The new plasma neutrino emission rate then is

$$Q_l' = \frac{g^2 c_V^2}{3\pi e^2}\frac{1}{(2\pi)^3}\frac{1}{e^{\omega_0\beta}-1}\omega_0^9(\frac{16}{315}), \quad (5.39)$$

$$Q_t' = (\frac{5}{6})^{3/2}\frac{4g^2}{3\pi e^2}\frac{\omega_0^6}{\beta^2}\frac{1}{(2\pi)^3}\frac{n^2(n+1)^2}{4}. \quad (5.40)$$

If neutrinos have a finite magnetic dipole moment, the above expressions need further modifications. A factor $2\pi^2\alpha^2\kappa^2\ /[G_F(m_ec^2)^2/(\hbar c)^3]^2(\hbar\omega_P/m_e^2)^2$ needs to be added. κ is defined as before, G_F is the Fermi coupling constant, and $\omega_P = (4\alpha/3\pi)^{1/2}E_F(e)/\hbar$ is the plasma frequency for relativistic degenerate electrons, α is the fine structure constant. The final form for the plasma decay rate is

$$Q_{mag} = 4.063(\frac{\kappa}{10^{-10}})^2(\rho_9/\mu_e)^{-2/3}(Q_l' + Q_t'). \tag{5.41}$$

We add this new emissivity to our neutron star evolutionary code, Since the neutrino emissivity is enhanced, the cooling of the neutron stars will be accelerated. Our results are presented in Figs(5.8), (5.9) and (5.10).

Results

Fig(5.9) shows the effect of neutrino magnetic dipole moment μ_ν of PS type of neutron stars. The solid curve is the standard evolutionary curve. Other curves incorporated the neutrino magnetic dipole moment effects. The effects of a finite neutrino magnetic moment on the plasma emissivity scale as κ^2. By varying κ, we could have different degrees of acceleration of cooling process by the neutrino magnetic dipole moment. In descending order, the parameter κ takes values as 10^{-10}, 10^{-9}, 10^{-8} and 10^{-7}. Fig(5.8) is for FP type of neutron stars. The curves are $\kappa = 0, 10^{-10}, 10^{-9}, 10^{-8}, 10^{-7}$ and 3×10^{-6} in a descending order. Fig(5.10) is for BPS type of neutron stars. The curves are the same as in Fig(5.8) except that the lowest one has κ equal to 10^{-6}. We also plot observational data in these three figures.

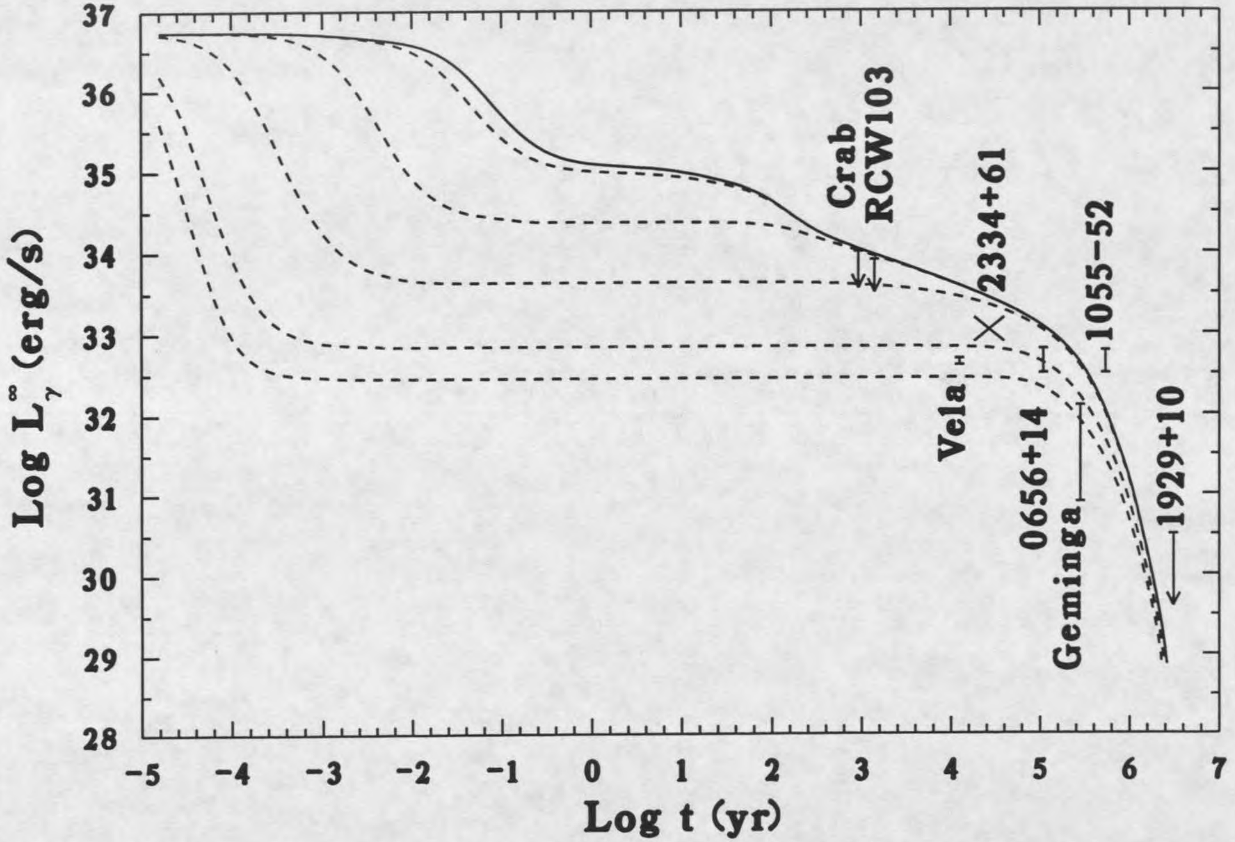

Fig(5.8) **Effects of Neutrino Magnetic Dipole Moment on Cooling, the FP Model**

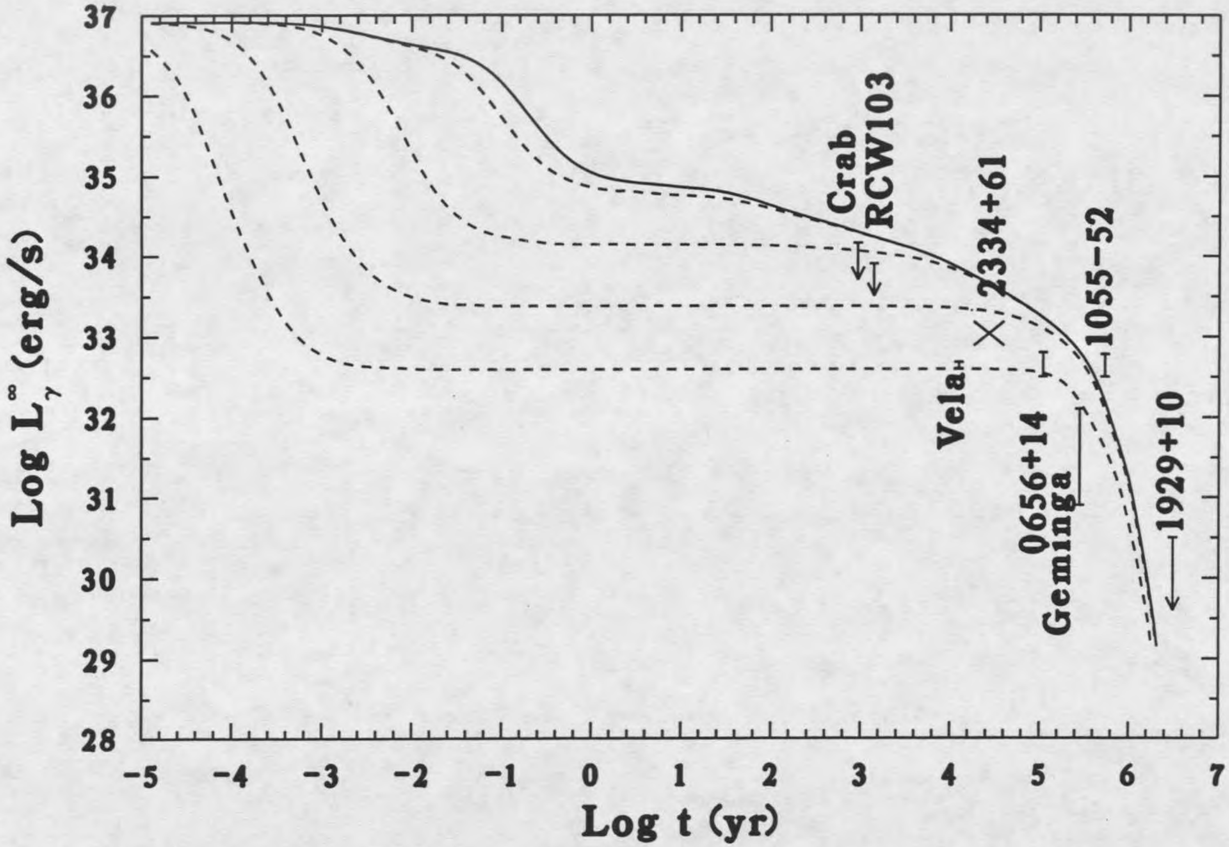

Fig(5.9) Effects of Neutrino Magnetic Dipole Moment on Cooling, the PS Model

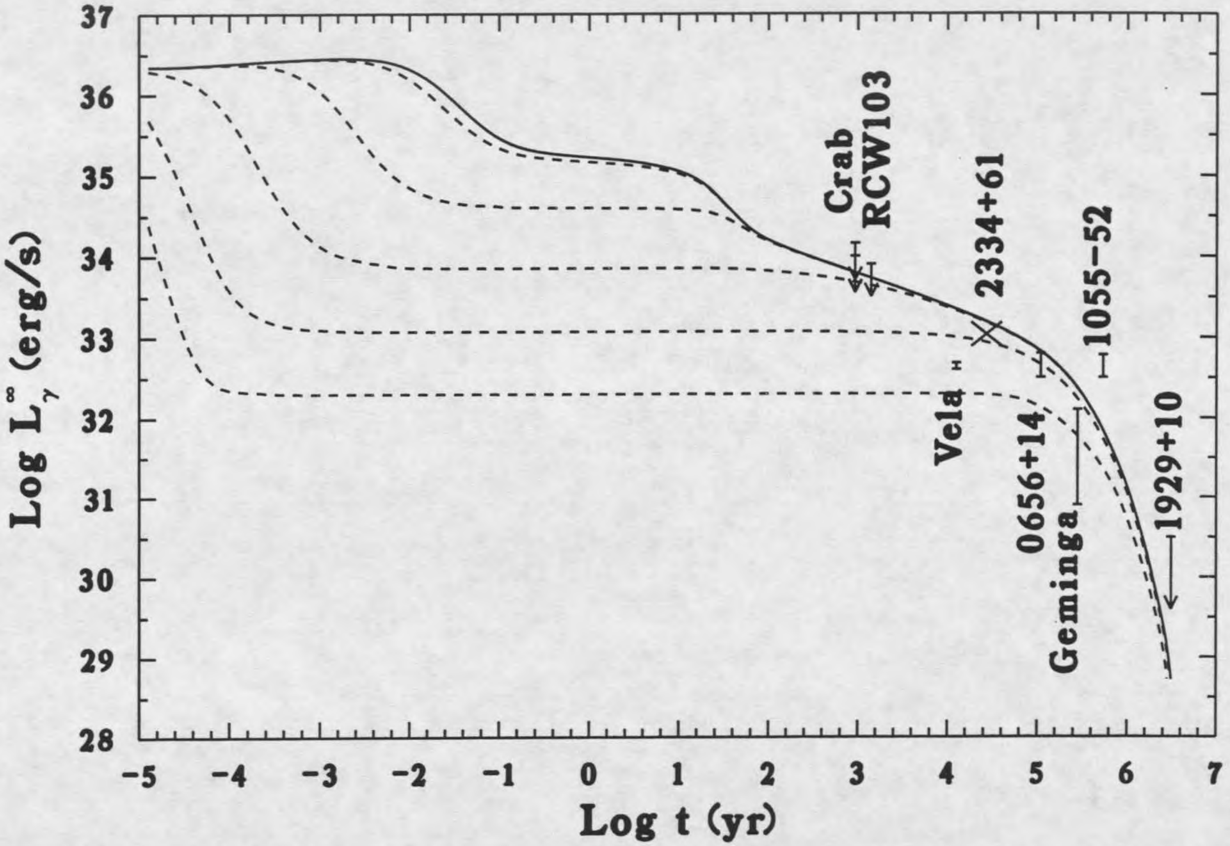

Fig(5.10) **Effects of Neutrino Magnetic Dipole Moment on Cooling, the BPS Model**

For neutron stars, unlike the cases of red giants and white dwarfs, the plasma neutrino process is not a decisive cooling process. Inside the core, modified URCA process and neutron-neutron and neutron-proton bremsstrahlung processes are the major emission mechanisms (see section §2.3.2). Only in the crust, the plasmon neutrino process dominates other neutrino emission processes. Before 10^5 yr, the interior temperature determines the surface temperature, which is related to the observed luminosity as $L_\gamma^\infty = 4\pi R^2 \sigma T_s^4$, and before thermal relaxation, it is the crust that controls the surface temperature. The thermal relaxation time for the PS Model is 6×10^4 yr; for the FP Model, it is about 600 yr; and for the BPS Model, it is about 300 yr (see §2.1). Before thermal relaxation, the surface temperature is determined by the neutrino processes in the crustal region, and the changes caused by the inclusion of neutrino magnetic dipole moment are showing at this stage. In Figs(5.8), (5.9) and (5.10), all dotted curves show dramatic accelerations in cooling at early stage. The neutrino magnetic dipole moment enhances the plasmon neutrino emissivity and quickly cools the crust. By thermal conduction, the surface temperatures drop thereafter. Thus it is not a surprise to see that the effects of cooling due to the finite neutrino magnetic dipole moment last longer in the PS Model, since PS type neutron stars have the thickest crust region. Neutron stars with a soft equation of state, such as the BPS Model, show relatively minor cooling effect. Model FP is an intermediate equation of state, therefore the cooling effect due to the finite neutrino magnetic dipole moment on the FP type of neutron stars is more pronounced than in the BPS Model, but less than the FP Model.

When the thermal relaxation state has been reached, the interior of the neutron star has uniform temperature distribution, and the surface temperature is controlled by the stronger neutrino emission processes in the central core. So after the thermal relaxation, the dashed curves in Figs(5.8), (5.9) and (5.10) become flat.

The overall disagreement between the observational data and the theoretical curves becomes worse only when μ_ν is larger than $10^{-7}\mu_B$. Thus the limit on the neutrino magnetic dipole moment obtained from the cooling consideration of neutron stars is $\mu_\nu < 10^{-7}\mu_B$. Compared with the limits obtained from other means (Eq.(5.32), (5.33) and (5.34)), our result is very weak. But however, the situation would be improved if we have observational data about young pulsars, noticing that the curve with $\kappa = 10^{-9}$ differs quite much from the curve with $\kappa = 10^{-8}$ at age $t \sim 10^3$ yr. Observational data from young pulsars ($t <\sim 10^3$) could improve the limit on μ_ν by two orders of magnitude.

5.2.3 Discussions

Because of the lack of observational data of young pulsars, we are not able to obtain a stringent limit on μ_ν. Young pulsars, such as the remnants from the recent supernovae SN1987A, SN1993J and SN1994I, are under intensive investigations now. If the thermal X-rays from the surfaces of these young pulsars are detected, that may push the limit up by two orders of magnitude. The difficulty of observing thermal X-rays from young pulsars is the thick circumstellar materials from the supernovae. However these supernova ejecta are inhomogeneous and clumpy, and they are expanding quickly, so if the line of sight passes through a thin area of the supernovae ejecta, it is quite possible to detect thermal X-rays from the surface of young pulsars.

It is worthwhile to point out another aspect of Figs(5.8), (5.9) and (5.10). These three figures show us how physical inputs about the neutrino emission processes in the crustal region would influence the cooling calculations of neutron stars. For instance, when $\mu_\nu = 10^{-10}\mu_B$, the plasma neutrino emissivity is increased by 1000 times, it slightly changes the cooling during the thermal relaxation period between $t = 10^{-1}$ to 10 yr. Only when $\mu_\nu = 10^{-9}\mu_B$, the plasma neutrino emissivity is increased by 10^5 times, do the cooling curves have significant changes. It is quite interesting to compare the three figures in this section with the three figures in the previous section. In Fig(5.5), the dashed curve has $f_a = 10^{25}m^{-1}$, that is equivalent to increasing the neutron-neutron bremsstrahlung emissivity by 0.5 times, but it shows much more alterations than the curves of $\kappa = 10^{-10}$ in Figs(5.8), (5.9) and (5.10). It is not difficult to understand when we remember the fact that the neutron-neutron bremsstrahlung neutrino process plays a more important role in the neutron star cooling than the plasmon neutrino process (see §2.2.2).

Chapter 6

Thermal X-Ray Observation of Neutron Stars

6.1 Introduction

The recent advances in the imaging X-ray telescopes have given us the opportunity of detecting thermal X-rays from the surfaces of neutron stars. According to the theoretical cooling calculations, neutron stars will maintain a surface temperature as high as a million degrees for about a million years. Thermal photons of a million degrees are in the soft X-ray range. Three X-ray satellite, EXSAT, Einstein and ROSAT, have been able to detect and observe a dozen neutron stars. In this chapter, I will first briefly describe in section §6.2 the modern technologies of X-Ray telescopes, such as the positional-sensitive proportional counter (PSPC), and the high resolution imager (HRI), which are on board ROSAT, a German satellite, and the charged-coupled devices (CCD), and the gas scintillation proportional counters (GIS), which are used on ASCA, a Japanese satellite. Data analysis is an important part of pulsar observations. Section §6.2 presents the results from our data analysis of PSR0656+14. In section §6.3, theoretical light curve calculations are described. The observed thermal X-rays from neutron stars are pulsed. Fig(6.1) is the observed light curve for the Vela Pulsar. The shapes of the pulses and the pulsed fractions of light curves depend on many factors, such as the modulation of the surface temperatures, the gravitational field, the configuration of the fields and the direction of the observation. In section §6.3, I will first explain how theoretical light curves are constructed. By comparing the theoretical results with the observation data, we are able to determine two observational parameters: the angle between the magnetic field and the rotating axis and the angle between the line of sight of the observation and the rotating axis. We also find that it is necessary to add hot spots on the surface of the neutron star in order to produce the observed large variations of the photon flux (Qin & Tsuruta 1994, Tsuruta & Qin 1994).

6.2 X-Ray Telescope

I will put emphasis on the X-ray telescopes on board the satellites such as ROSAT and ASCA.

The orbiting X-ray satellite ROSAT was launched on June 1, 1990. Before ROSAT, there are Uhuru, Einstein, EXSAT satellites, as well as X-ray rockets. The Uhuru satellite is the first to be launched which performed the all sky survey in X-rays, leading to many important discoveries, e.g. the binary X-ray sources and hot gases in clusters of galaxies and so on. The Einstein Observatory was the first to employ imaging X-Ray optics, PSPC. The PSPC detector increased the sensitivity

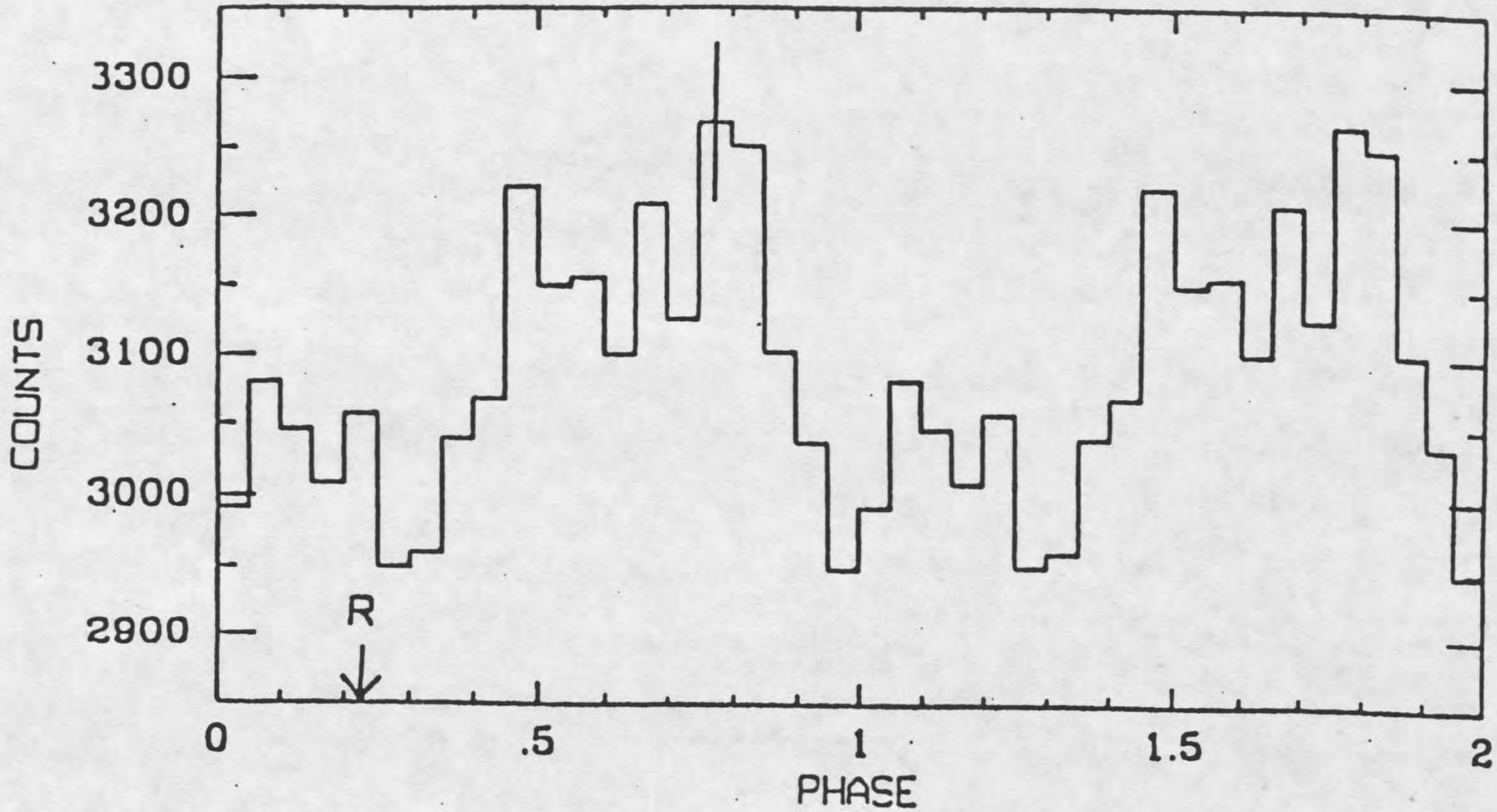

Fig(6.1) Observed Light Curve for Vela Pulsar of telescopes by three orders of magnitude over Uhuru. The ROSAT satellite has two PSPC detectors and one HRI detector. It has the unprecedented ability to locate sources and to produce fairly detailed images.

A X-ray telescope usually consists of two parts, a mirror and a detector (detectors). The mirror is used to collect photons and the detectors are used to register photon events electronically. The X-ray telescope on board ROSAT is made up of a four-fold nested Wolter type 1 mirror (see Fig(6.2)) and three detectors. The four-fold nested Wolter type 1 mirror has an aperture with diameter 83cm, and focal length 240cm. The geometrical collecting area is 1141cm^2. The mean gazing angle is 2° and the on axis resolution is 5 arcsec. A Wolter type 1 mirror consists of a paraboloid mirror and a hyperboloid mirror. The light rays from infinity will hit the paraboloid mirror first, then will be reflected towards the common focus of the paraboloid and hyperboloid mirrors. When the photons reach the hyperboloid mirror, the mirror will deflect the photons toward the other focus. In the case of the Wolter type 1 mirror, the photons are reflected twice and an image will form at the focal plane. As a contrast, a Wolter type 0 mirror has only one paraboloid mirror, and photons are only reflected once by a Wolter type 0 mirror. Wolter type 0 mirror is not able to form images from photons coming from infinity, because every point in infinity will form a ring at the focus of the paraboloid mirror. The purpose of using a hyperboloid mirror in the Wolter type 1 mirror then is to bring the ring back into focus. A four-fold nested Walter type 1 mirror consists of four sets of such co-focused mirror pairs. It increases the collecting area by four folds. The performance of the telescopes relies heavily on the collecting

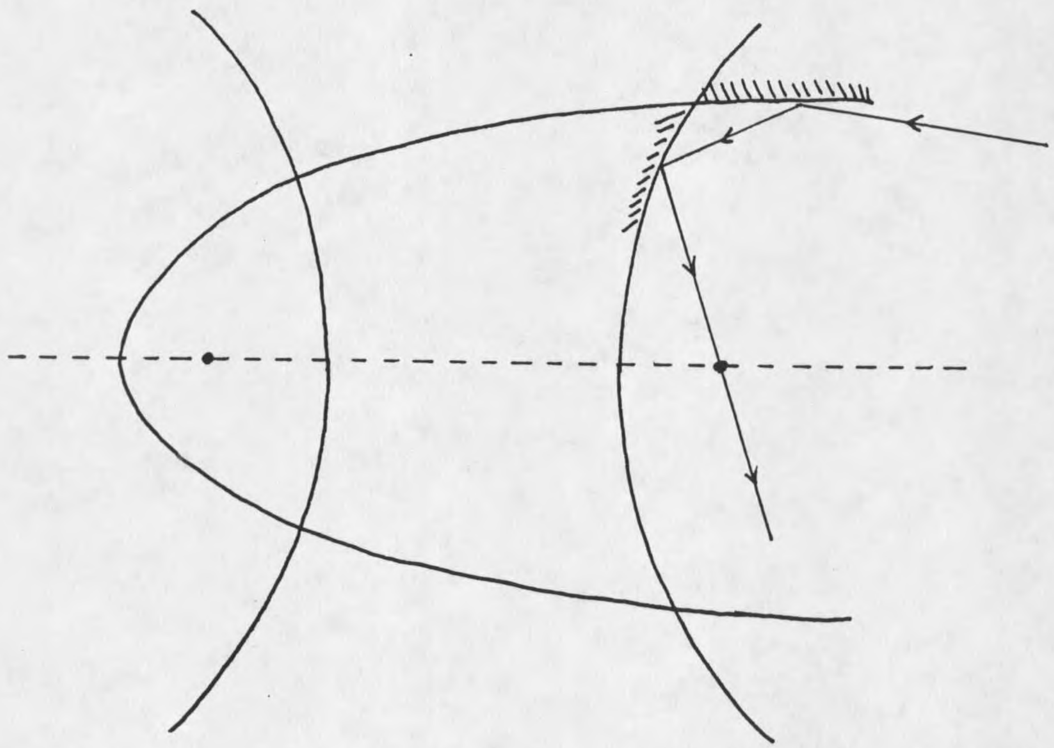

Fig(6.2) Wolter Type 1 Mirror

area. The larger the collecting area, the better.

The three detectors are posed at the focal plane of the mirror.. Two of them are PSPC detectors. The so-called PSPC detector is essentially a gas proportional counter. It is made of a ber with charged wire arrays built in. When a X-ray photon comes in through the window, it will ionize the gas molecules (argon and methane). The electric field produced by the charged wires will amplify the ionization, and cause electron avalanche. The electric circuit connected to the wires can register such events, and record informations on both position and amplitude. The position indicates the direction the photon comes in, which directly tells us the position of the source, and the amplitude indicates the energy of the incoming photon. The PSPC detectors on ROSAT have a positional resolution of 25 arcsec, and has a moderate energy resolution, $\Delta E/E \approx 0.43$ at $1.3keV$, where ΔE is the uncertainty of the energy. That will give 4 to 5 bands within the ROSAT energy detection range, from $0.1keV$ to $2.4keV$.

The other detector is HRI detector. A HRI detector is a channel plate detector. It is made of arrays of micro fiber glass channels. Each incoming photon is conducted through one channel and is led to a position sensitive read-out plate. HRI has very good positional resolution, a few arcsec, but poor energy resolution.

After ROSAT, a major achievement in X-ray astronomy is the Japanese satellite, ASCA, Advanced Satellite for Cosmology and Astrophysics. ASCA was launched on February 20, 1993 from Kagoshima Space Center in Japan. The mission is expected to last 5 years. ASCA has a wide energy range, from $0.5keV$ to $12keV$. ASCA also has very high energy resolution, 8% for GSPC and 2% for CCD at $5.69keV$. ASCA will examine (has examined) a variety of X-ray sources with moderate spatial and spectral resolutions, and with particular emphasis on the iron K band, which is very useful in active galactic nuclei (AGN) studies.

ASCA has four large area mirrors. These mirrors focus X-rays of a wide energy range onto four detectors: two X-ray sensitive charged-coupled devices(CCD) and two imaging gas-scintillation proportional counters(GSPC). CCD are also known as SIS, solid-state imaging spectrometers, and GSPC is also called GIS, gas imaging spectrometer. The four mirrors on board ASCA are attached to the top plate of EOB, Extensible Optical Bench. Each of the four telescopes is located opposite to one of the two SIS and two GIS spectrometers. The field view of ASCA's X-ray telescope is about $60arcmin$ in diameter. The mirror has a diameter of $34.5cm$ and focal length of $3.5m$.

The X-ray astronomy is relatively new compared with optical and radio astronomy. The full scale effort on X-ray Astronomy from the astrophysics society has enabled the X-ray astronomy to take an equal role with others, as indicated by the blooming fields in X-ray astronomy, such as solar X-ray physics, X-ray pulsars, AGN and interstellar clouds physics.

In section §6.2, I will focus on data analysis in the thermal X-ray observation of pulsars. Using PSR0656+14 as an example, we discuss the results from spatial, timing and spectral analyses.

6.3 Data Analysis of PSR0656+14

The detector on the satellite will register every photon event. It records the time of the events, the energies and positions of the photons, regardless of whether the photons are from the source or from the background. The data will be stored on board and will be transferred to the ground every day. Table (6.1) is an event file from ROSAT satellite (some basic corrections have been made).

The first column is the sequence number of the events, the second column is the time of the events in Julian date, and the third column is amplitude, i.e. photon energies, it is expressed in channel number. The energy range for ROSAT is $0.1keV$ to $2.4keV$. Inside this range, there are 256 channels. One channel approximately corresponds to $0.01keV$. For instance, Event No.3 has an amplitude of 78, that says the energy of this photon is about $0.78KeV$. The fourth column and the fifth column are the coordinates of the position of the photon coming in, in pixel number. The entire detector is divided into 512×512 pixels. The sixth and the seventh column are coordinates of the sky. The last column is the raw amplitudes, that is the photon energies before calibration.

Data analysis consists of three parts, spatial analysis, timing analysis and spectral analysis.

6.3.1 Spatial Analysis

With the photon event table in hand, spatial analysis is fairly easy: build up a coordinate system and draw one dot for each photon event at suitable places according

Sequence	TIME	AMPL	XPIX	YPIX	XDET	YDET	RAW_AMPL
1	25698256.7604	31	-2039	-6343	2665	706	32
2	25698635.3351	71	-2035	-6554	2674	652	72
3	25698836.8334	78	-2164	-6374	2798	539	79
4	25698866.9274	186	-2476	-6388	2621	600	172
5	25714193.8568	47	-2071	-6328	2659	740	48
6	25714206.1943	72	-2114	-6384	2605	743	72
7	25714207.8711	22	-1850	-6489	2738	677	23
8	25714229.6327	56	-2295	-6320	2469	822	56
9	25714256.6786	23	-1874	-6434	2636	791	24
10	25714263.8351	34	-2345	-6325	2375	891	35
11	25714352.9360	72	-1981	-6492	2716	649	72
12	25714369.6798	52	-2246	-6337	2620	715	52
13	25714541.6011	23	-1864	-6384	2894	592	24
14	25714615.1664	46	-2582	-6485	2404	724	48
15	25714638.0676	71	-1860	-6663	2737	636	71
16	25714695.6810	24	-2036	-6330	2613	839	25
17	25714743.0062	19	-2266	-6533	2604	674	20
18	25714852.8657	92	-2191	-6323	2815	569	93
19	25714911.1477	23	-1832	-6367	2964	581	24
20	25715033.3578	17	-2478	-6386	2377	806	18

Table(6.1) Photon Event File

to the coordinates in the event file. Fig(6.3) is what we get from the photon event table of PSR0656+14. The central black dot is the source that we are looking for, PSR0656+14, and the diffusive background is the noise. PSR0656+14's celestial coordinates are RA $6^h 59^m 48.0^s$, DEC $14°14' 24.0''$.

The spatial analysis can help us pick the point source and do background subtraction. The background subtraction of PSR0656+14 is done in the following fashion. We first draw a circle which embraces the point source, called circle 1. Suppose T is the set of all photon events that are enclosed in this circle, $T = \{$ all photon events that are enclosed in circle 1 $\}$. Draw another circle, circle 2, with the same area as circle 1, but does not contain the source. Let $B = \{$ the photon events that are enclosed in the circle 2 $\}$. B represents the background noises. $T - B$ then gives us the source photons with the background subtracted. Background subtraction is essential to spectral analysis, while for timing analysis, it is not necessary.

6.3.2 Timing Analysis

Timing analysis usually is to look for periodicity, and the Fast Fourier Transformation is the standard. But for pulsars, we know the period from radio observation to a very high accuracy. For example: PSR 1509-58's period in October,1994 is $0.1506515105966924 sec.$ and the decreasing rate of the period dP/dt is $1.5365550511561575E - 12$. The incredible high accuracy of the period is obtained by a rather simple method. Suppose the equipment for measuring frequency gives an error ΔT. If we measure one period, the accuracy of the measurement would be $\Delta T/T = \epsilon_0$. Instead, if we measure N periods, $N \gg 1$, then the accuracy becomes

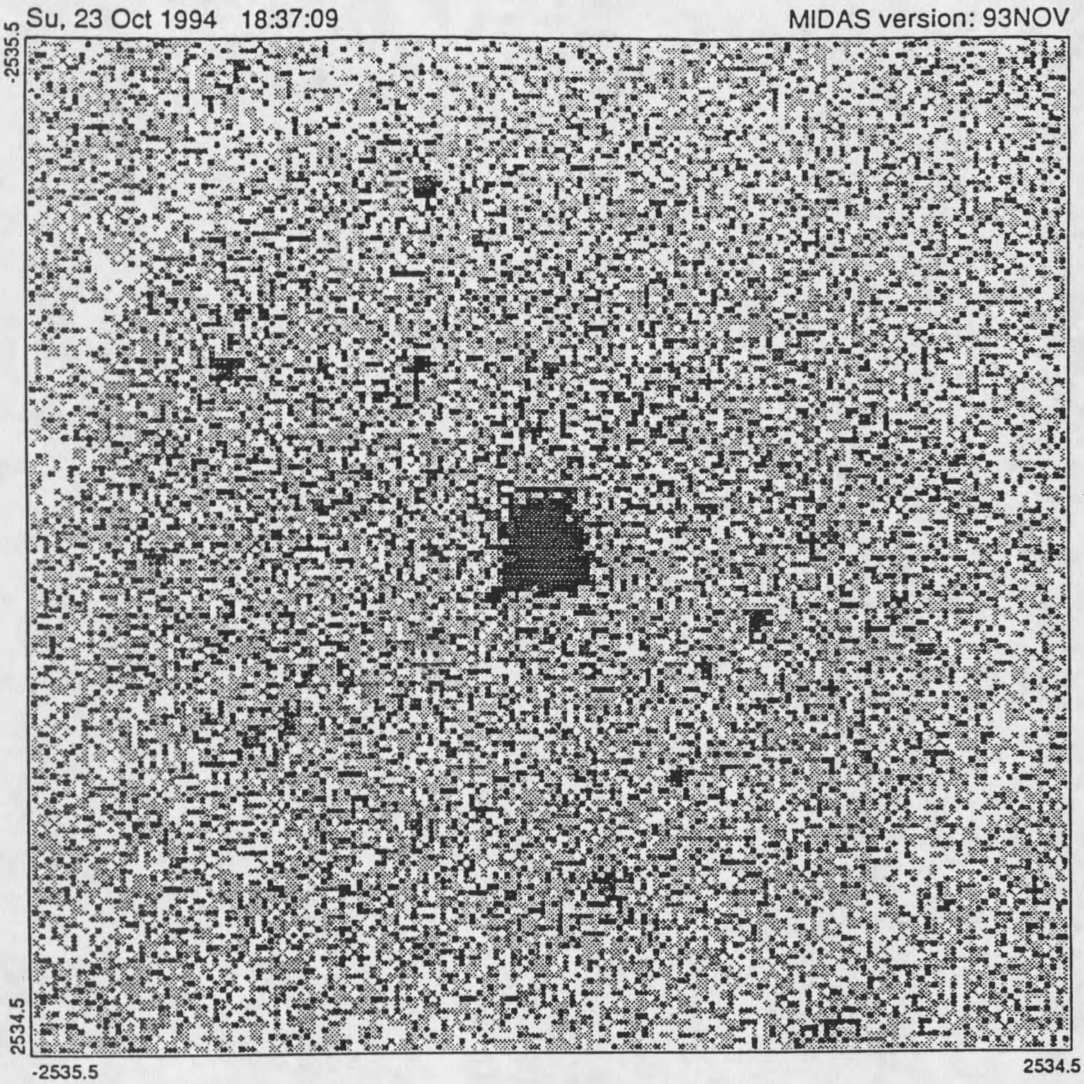

Frame : imalq
Identifier :
ITT-table : ramp.itt
Coordinates : -2535.5, 2534.5 : 2534.5, -2535.5
Pixels : 1, 1 : 512, 512
Cut values : 0, 5
User : visitor

Fig(6.3) PSR0656+14

$\Delta T/NT = \epsilon_0/N \ll \epsilon_0$, which is N times smaller.

Along the time sequence, if we fold up the photon events every 4 to 5 periods, we could construct a light curve, the periodical variations of the photon intensity. What we get for PSR0656+14 is shown in Fig(6.4). The x-axis of Fig(6.4) is the phase. The y-axis is the flux, count/sec. The black dots are observational data, and the vertical bars are measurement uncertainty. It is quite obvious that the intensity of the flux varies periodically.

6.3.3 Spectral Analysis

The two PSPC detectors used on ROSAT have relatively good energy resolutions. In the photon event table (Table 6.1), the energies of photons are listed. The goal of spectral analysis is to decide the physical processes that produced these photons. Soft X-rays from pulsars are usually considered to have two major origins: blackbody emission from the surface of the star and synchrotron radiation from the magnetosphere. If the photons are from synchrotron emission, the spectrum would fit the formula below.

$$f(E, A, \Gamma, E_0)dE = A(\frac{E}{E_0})^\Gamma dE. \tag{6.1}$$

$f(E, A, \Gamma, E_0)$ is the photon flux, E is the energy of the photon, A, E_0, and Γ are parameters needed to be fitted with the data. If the photons are from blackbody emission, the spectrum would be

$$f(E, A, T)dE = \frac{A}{c_0 \cdot T}\frac{(\frac{E}{T})^2}{e^{\frac{E}{T}} - 1}dE. \tag{6.2}$$

Here A and T are two parameters, and c_0 is a physical constant.

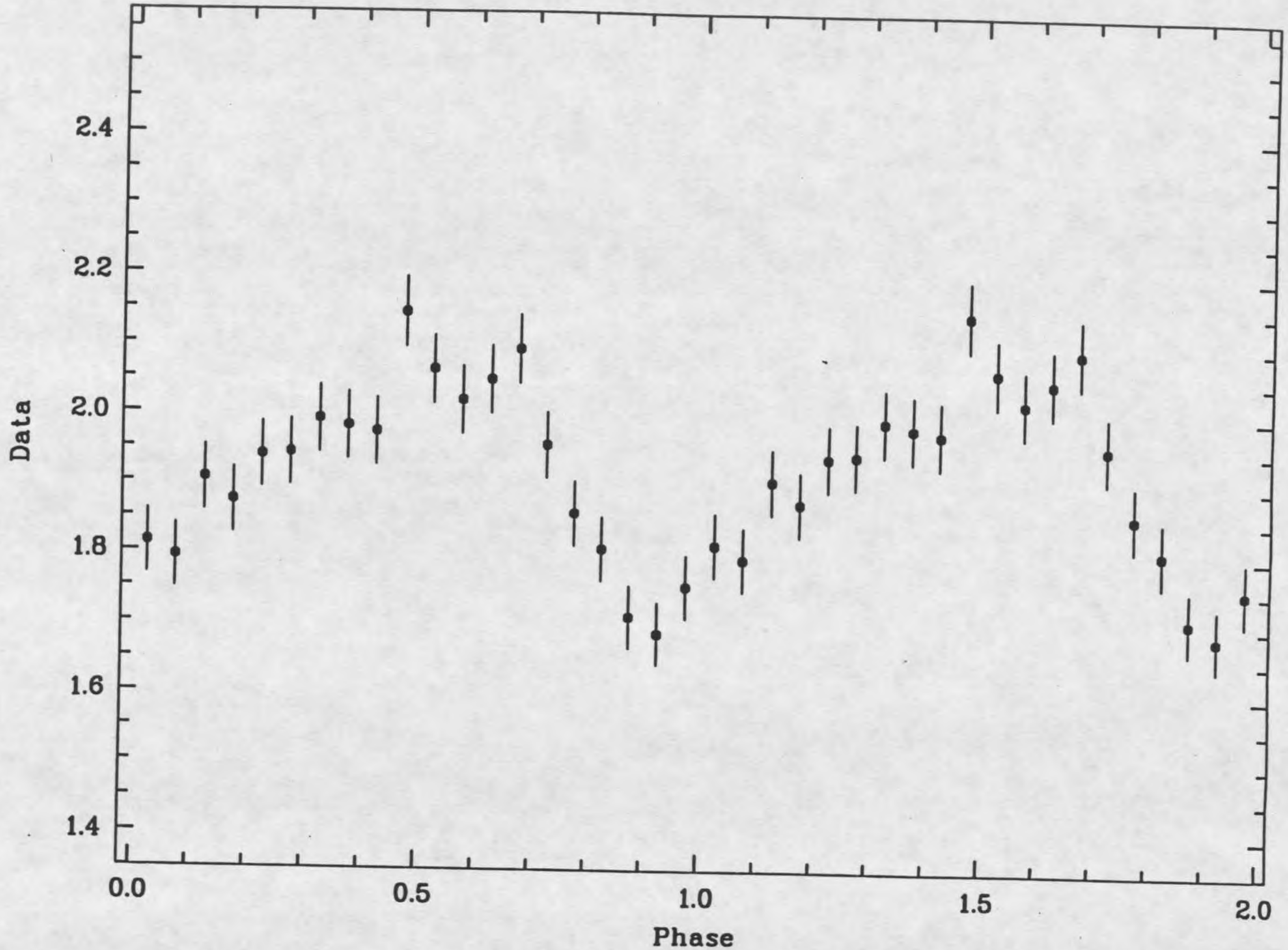

Fig(6.4) Light Curve of PSR0656+14

By adjusting the parameters, A, Γ, and E_0 in the synchrotron radiation case and A, and T in the blackbody emission case, and searching for the least standard deviation, we then are able to determine the values of these parameters. One complication in the spectral analysis is the possible multi-component radiations, that is the X-ray photons from pulsars may come from two or more different physical processes. For example, if the surface of neutron stars has a hot spot, then the spectral fit would require two blackbody models, with different temperatures. Also synchrotron radiations may co-exit with blackbody emissions, and that requires a blackbody and a power-law model.

We carried out spectral analysis for PSR0656+14. Fig(6.5) shows the results when we fit with one blackbody model. In this figure, the observation data are represented by crosses. The curves are models. The upper left figure shows the fit for the photons having passed through the detectors, the distortion at the high energy level is caused by the energy responses of the detectors. The upper right curve is the fit for the photons before passing through the detectors, so both curves are perfect blackbody radiation curves. The fit yields a blackbody temperature $0.0801 \pm 0.00313 keV$. The standard deviation is 8.26. The lower left graph shows the fitting residuals. The large positive residuals at higher energy end hints that another component of blackbody emission with a relatively higher temperature may exist. Fig(6.6) is the result when we fit PSR0656+14 with two blackbody spectrums. This time, the standard deviation is reduced to 1.3, and the large residuals at high energy end in Fig(6.5) also disappear. The fitting yields two temperatures, $0.079 \pm 0.00672\ keV$ and $0.177 \pm 0.096\ keV$.

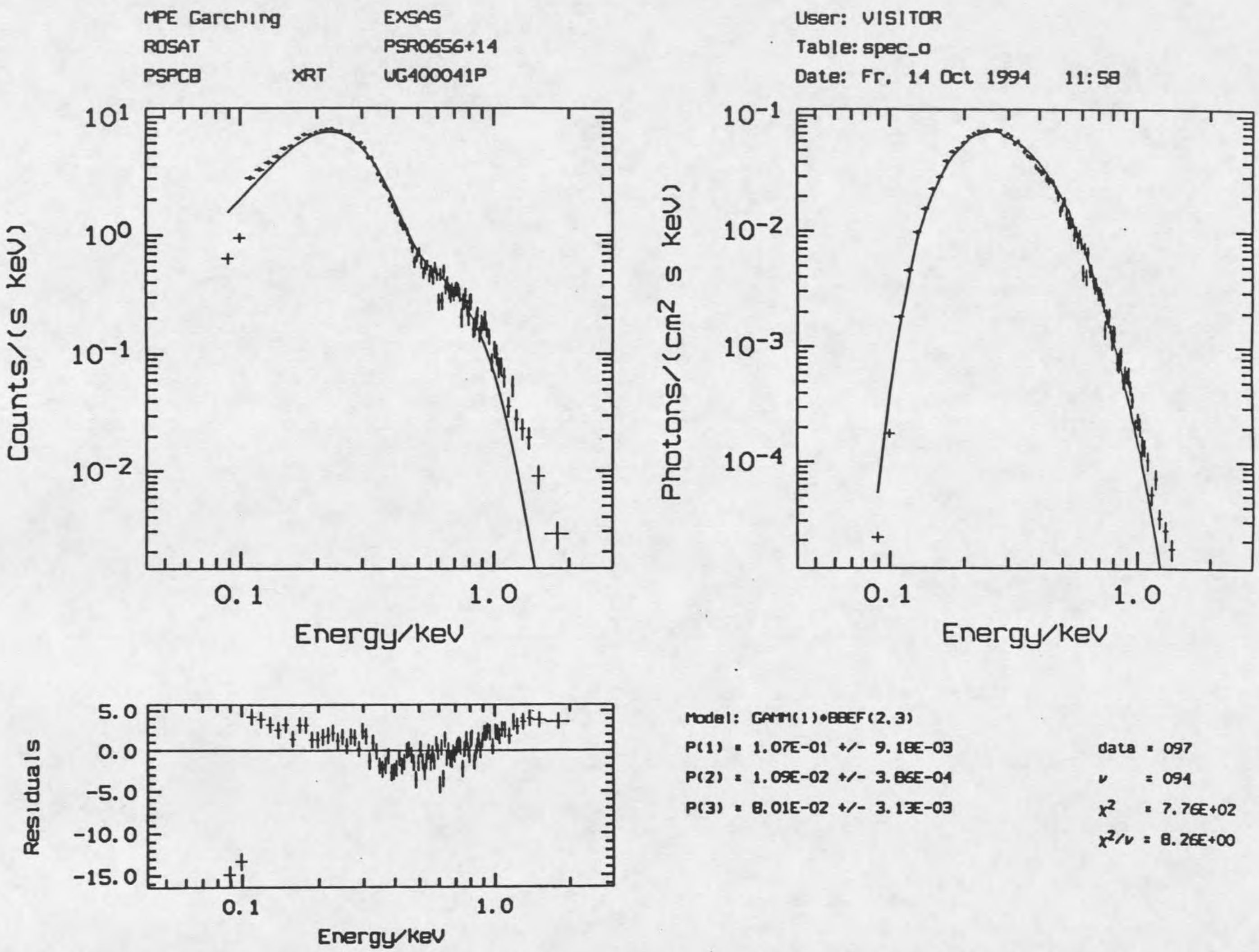

Fig(6.5) Spectral Analysis for PSR0656+14 (i)

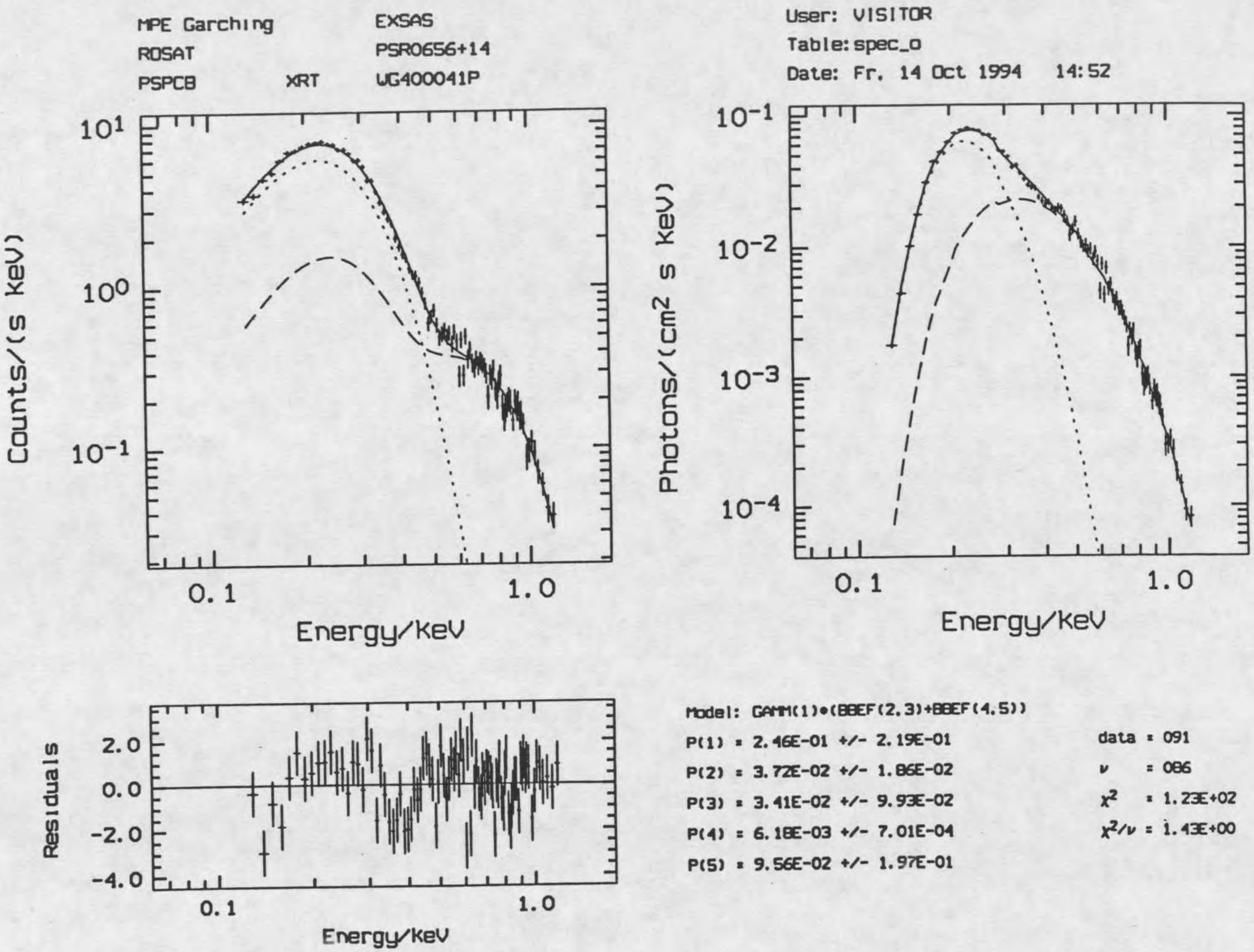

Fig(6.6) Spectral Analysis for PSR0656+14 (ii)

However the situation is somewhat inconclusive, the two blackbody model fitting is better, but not good enough to pin down the case. This is due to the poor response of the ROSAT PSPC detector at the high energy range. The detectors on board ASCA have better energy response at high energy ranges, so hopefully the data from ASCA will help us settle this issue.

In Table(6.2), we listed 11 pulsars for which we have positive detections with one or more of the imaging X-ray detectors (Ögelman 1994). Among these 11 pulsars, there are four pulsars whose spectra are dominated by a soft blackbody like component. These four pulsars are 0833-45 (Vela), 0656+14, 0630+18 (Geminga) and 1055-52. The observation shows that the soft X-rays from these four pulsars are periodic, and different pulsars have different pulse shapes. We can see from Fig(6.1) that for the light curve of the Vela Pulsar, during one phase, there are two pulses, one large, one small. The larger pulse is about 3 times wider than the smaller pulse, and the pulsed fraction is about 11%. In an effort to understand these features of light curves of thermal X-ray emission, we study how thermal emissions from the surfaces and atmosphere of neutron stars would be modulated under various conditions. This is the theme of the next section.

6.4 Theoretical Light Curves and Comparison with Observation

Fig(6.7) shows a configuration of an observation scene. The pulsar is rotating, the magnetic axis and the rotation axis are not aligned, but form an angle β. The line of

Table(6.2) Detection of Pulsars

Pulsar	Log(L) (erg/s)	Log(age)
0531+21	36.0	3.09
0540-69	36.3	3.22
1509-58	34.3	3.19
0833-45	32.7	4.05
1951+32	33.4	5.02
0656+14	32.5	5.04
0630+18	31.7	5.51
1055-52	32.5	5.73
J0437-47	30.5	8.88
1929+10	29	6.49
0950+08	29	7.24

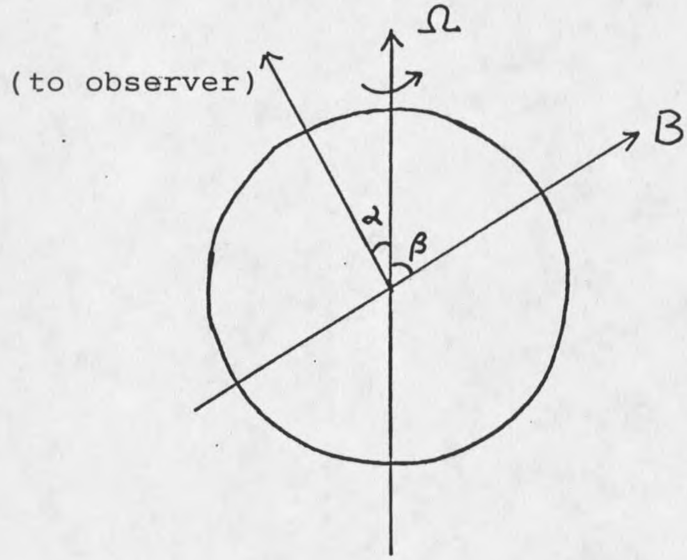

Fig(6.7) Illustration of a Observational Scene

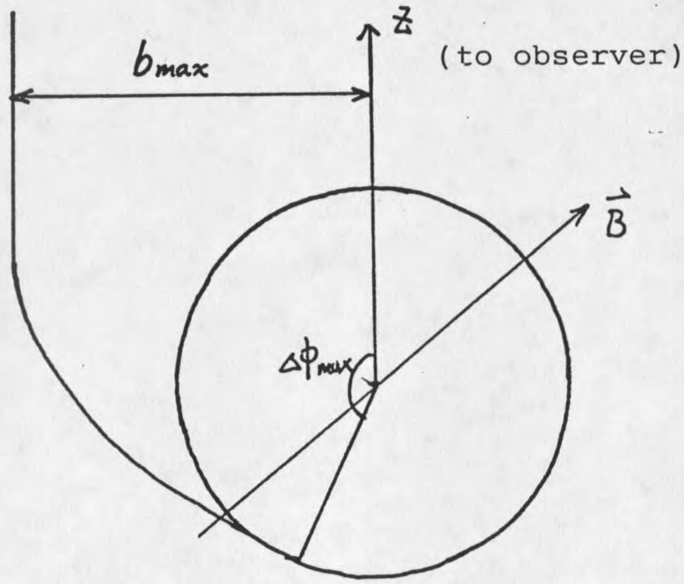

Fig(6.8) Geometry of a Photon Path near the Surface of a Neutron Star sight of the observer and the rotating axis form an angle α.

The strong magnetic field will cause a higher polar surface temperature and a lower equatorial temperature. Also the polar cap heating effect will raise the polar surface temperature further. As the neutron star rotates, the integral of the radiation over the surface of the neutron star will vary with time. Due to the general relativity effect, the photons which are able to reach the observer not only come from the half sphere facing the observer, but also the curved path of photons under strong gravitation will enable some photons from the back half of the sphere to reach the observer. In Fig(6.8), we illustrate the geometry of such a situation (Pechenick et al 1983).

In the Schwarzchild metric, for a photon moving in the equatorial plane, its path is described by the following equations. (Misner, Thorne and Wheeler 1973, P.674)

$$\frac{dt}{d\lambda} = (1-\frac{2M}{r})^{-1}, \tag{6.3}$$

$$\frac{dr}{d\lambda} = [1-\frac{b^2(1-\frac{2M}{r})}{r^2}]^{\frac{1}{2}}, \tag{6.4}$$

$$\frac{d\theta}{d\lambda} = 0, \tag{6.5}$$

$$\frac{d\phi}{d\lambda} = br^{-2}. \tag{6.6}$$

Here b is the impact parameter. Equation(6.4) and Equation(6.6) together give:

$$\frac{1}{r^2}\frac{dr}{d\phi} = \frac{\sqrt{1-\frac{b^2(1-\frac{2M}{r})}{r^2}}}{b}, \tag{6.7}$$

which leads to

$$(\frac{1}{r^2}\frac{dr}{d\phi})^2 = \frac{1}{b^2} - \frac{1-\frac{2M}{r}}{r^2}. \tag{6.8}$$

The above equation requires that $1/b^2 \geq (1-2M/r)/r^2$. On the other hand, $(1-2M/r)/r^2$ has a minimum at $r = 3M$, and decreases for $r > 3M$. Thus if the neutron star has a radius R larger than 3M, then $b \leq R/\sqrt{1-2M/R}$, and $b_{max} = R/\sqrt{1-2M/R}$. Let $b = b_{max}$, integrate Equation(6.8) from $r = R$ to $r = \infty$, and we then could get $\Delta\phi_{max}$. $\Delta\phi_{max}$ is the largest angular size of the visible part of the sphere, as shown in Fig(6.8).

$$\Delta\phi_{max} = \int_0^{\frac{M}{R}} [(1-\frac{2M}{R})(\frac{M}{R})^2 - (1-2u)u^2]^{-1/2} du, \tag{6.9}$$

with $u = M/r$.

If $M = 0$, i.e. flat spacetime, $\Delta\phi_{max} = 90°$, and exactly half of the sphere is visible to the observer. If $R/2M = 1.76$, $\Delta\phi_{max} \approx 180°$, and the entire surface is visible. When $R/2M$ is smaller than 1.76, then each part of the sphere can be seen twice during one phase. When $R/2M > 1.76$, $\Delta\Phi_{max}$ is less than 180°, but larger than 90°, and more than half of the sphere is visible at a time. In general, the visible part of the sphere is a portion of the sphere, with the center pointing to the observer and the angular size of $\Delta\phi_{max}$.

The luminosity of the visible portion is given by the following equation. Suppose it has a temperature distribution T, then

$$N = \frac{2R^2}{D^2h^3c^2} \int_0^\infty dE \int_{-\Delta\phi_{max}}^{\Delta\phi_{max}} d\phi \int_0^{2\pi} d\psi \frac{E^2 \exp(-\tau(E)) \sin\phi \cos\alpha}{\exp(E/kT) - 1}, \tag{6.10}$$

with N as the number of counts per unit area per second, R as the stellar radius, D the distance to the source, h Plank constant, c the speed of light, k Boltzman constant, E the photon energy, α the angle between the line of sight and the normal of the surface, and $\tau(E)$ the optical depth between the source and the observer, where $\tau(E)$ describes the attenuation of the signal by the interstellar medium. It can be written as $N_H\sigma_E$, where N_H is the column number density of hydrogen, we choose N_H to be $10^{20} atoms/cm^2$ and σ_E is the cross section of one hydrogen atom (Morrison and McCammon 1983). The temperature distribution is taken from our thermal calculations of strongly magnetized neutron stars.

As the neutron star rotates, the temperatures of the visible portion will not stay unchanged. During one phase, we calculate the total photon counts that can be received by the observer for 30 positions. The photon counts vary with the position. Due to the general relativity effect, the light curve for radiations from a neutron star with only temperature modulations from magnetic fields is rather flat, not enough to produce the observed pulsed fractions, 11% in the Vela Pulsar case. The flattening effects of general relativity can be understood by the fact that a relatively large portion of the surface of the neutron star is visible when the general relativity effect is included. A larger visible portion means less variations. When the entire surface is visible at once, there would be no pulsations. So we have to assume that the poles of the neutron stars are somewhat hotter, i.e. the polar cap heating effect has to be added in order to reproduce the large variations in the observed light curves.

There are four undetermined parameters in the theoretical calculations: the angle between the rotating axis and the magnetic axis, β; the angle between the rotating axis and the line of sight, α; the temperature of the hot spot and the size of the polar cap. By adjusting these parameters, we are able to construct light curves to fit the observations. Fig(6.9) is our results for the Vela Pulsar. It shows the same features as the observed light curves (Fig(6.1)). The solid curve shows the light curve without the atmosphere effects, the dotted one has the atmosphere effects included. The pulsed fraction of the dotted curve is 10%. As results of the fitting, the four parameters take values as: α is 50°, β is 65°, the hot spot is about 60° wide, and the temperatures of the hot spots are about 1.3 times as high as the original temperatures.

Another example we calculate is PSR0656 + 14. We find that α is about 25°, β is about 10°, the polar cap is 20° wide, and the temperatures are about 4.5 times higher. Vela Pulsar is younger than PSR0656+14, the polar cap heating effect on Vela Pulsar is not as strong as PSR0656+14, and that agrees with Halpern and Halpern (preprint), which states that the polar cap heating effect is stronger among older pulsars than younger pulsars.

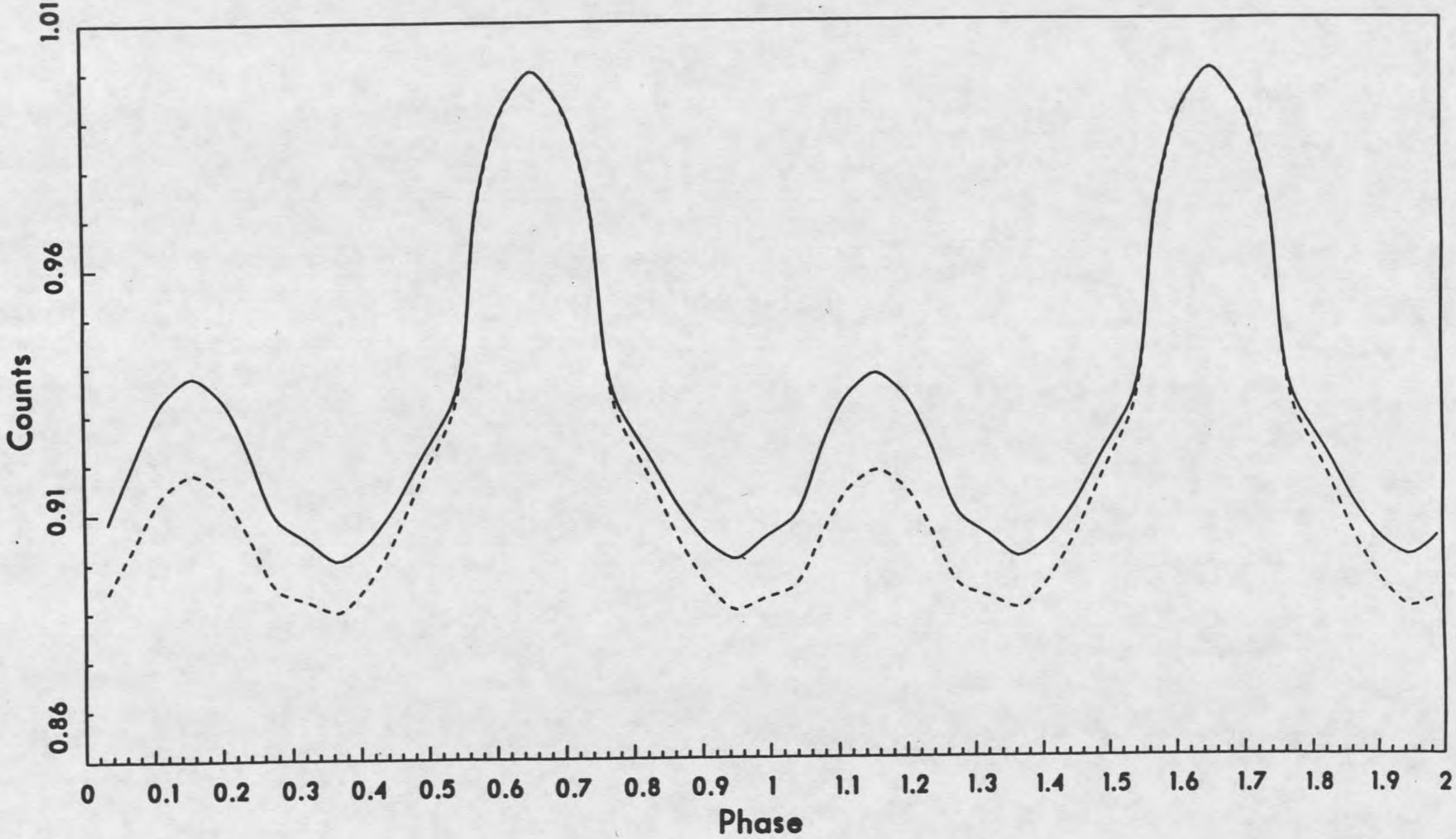

Fig(6.9) Theoretical Light Curves for Vela Pulsar

Chapter 7

Conclusion

As perceived by an ancient Chinese philosopher, "to conclude is to begin", such is the purpose of this conclusion. Here I will summarize the works I discussed in the preceding chapters, and let this summary serve as a starting point for further studies for myself (and perhaps others).

My major research work is to investigate the effects of strong magnetic fields on thermal evolution of neutron stars. We have built our own codes for this task. Chapter 2 and Chapter 3 described in detail the approaches and inputs we adopted in this project, as much as presenting our results. We find that under strong magnetic fields, the transportation properties of dense matter are no longer isotropic. The transverse heat conducting ability is significantly jeopardized, due to the Landau quantization of electrons' orbits by the strong fields, while the longitudinal heat conductivity is only slightly altered. Our investigation shows that the low heat conductivity along the transverse direction prevents rapid heat loss by the blackbody emission from the stellar surface at the later stages of neutron star cooling, and hence neutron stars with strong magnetic fields are able to maintain higher surface temperatures ($\sim 10^6 K$) for periods longer than non-magnetic neutron stars. This result proves that previous conclusions about the effects of magnetic fields on the cooling of neutron stars were not correct, the strong magnetic fields do play an important role at later stages of neutron star cooling. At the moment, our investigations of this matter are not yet complete, and they need to be carried out further, for many questions have been brought forward by our results. The following is a tentative list of some of the unsettled questions, and I am sure there would be plenty more.

- At what age will the photon cooling take over the neutrino cooling eventually?
- When will the crust of neutron stars have uniform temperatures?
- Is it possible that magnetic fields will decay as early as at about 10^6 yr, so that our magnetic warming effect will not be materialized at all?
- How different will the superfluid phenomenon and other physical processes be under the strong magnetic field? And will they affect the thermal evolution of neutron stars?
- How strong is the polar cap heating effect?
- For "strange" magnetic field configurations, such as the magnetic field does not pass through the center of the neutron stars or the two poles of the magnetic fields stay very close, e.g. the off-axis dipoles and 'sun spots' suggested by

Halpern and Ruderman (preprint) and so on, will the results change? In these cases, more powerful and faster computer codes are needed.

While cooling is the primary trend of the thermal evolution of neutron stars, heating may also become significant. Superfluidity is a natural phenomenon in a "super cool" environment, such as in the interior of neutron stars, and the consequence then is the frictional heating caused by the crustal solid and the superfluid neutrons. Also the deformation and cracking of the crusts of neutrons stars as a result of the spin down has its analogy in the crust of the Earth. In Chapter 4, I explained heating effect of crust breaking. It is found that the critical stress has to take an unrealistic value in order to fit with the observation data. So it seems that crust breaking alone is not a significant heating source, but it could co-exist with other heating mechanisms.

In Chapter 5, I discussed two examples of how particle physics could be tested by using neutron star cooling theories. One example is the axion emission. Axion is a pseudoscalar particle proposed to solve CP violation in the strong interaction. So far it has not been observed yet. Axion emission from the interior of neutron stars will accelerate cooling. The other example is the neutrino magnetic dipole moment. The finite neutrino magnetic dipole moment will increase the emission rate of the neutrinos and thus will alter the theoretical cooling curves. By comparing with the observation data, we may attain some constraints on the physical parameters in the theories. For axion emission, the physical parameter is the mass of axions m_a, and for neutrino magnetic dipole moment, it is the value of neutrino magnetic dipole moment. In the case of axion emission, we are able to obtain a limit on the mass of the axion as $m_a < 1.87^{-3} eV$. This limit is better than most of the limits from other astrophysical considerations, such as the Sun, white dwarfs and red giants. But in the case of neutrino magnetic dipole moment, our limit is $\mu_\nu < 10^{-7}\mu_B$, weaker than other results, due to the relatively poor observational data.

Chapter 6 is a chapter on thermal X-ray observations. In Chapter 6, we briefly gave account of the current situations of the thermal X-ray observations, and made another attempt to connect the observational data with the theories through the light curve construction. (Earlier we compared the theory and observation through the cooling profile) Theoretical light curve construction, together with the observation, will enable us to determine several physical parameters, such as the configuration of the magnetic fields, the relative position of the observer, and so on. What we find out is that the large amplitude variations of the observed light curves require the presence of hot spots in addition to the modulations of the surface temperatures by strong magnetic fields. But one reservation should be made here, it is that in our theoretical light curve calculations, we did not include the differential effects of magnetic fields on the two different modes of the photon transportation (flux beaming effect). These polarization effects will enhance the variation of the photon intensity, and it is possible that further studies may find that the hot spots are not necessary when these effects are included.

It may be disappointing to note that the questions brought up by our work are more than the problems we have solved, as you may have noted. One step toward the goal at infinity is no nearer to the goal. But what really matters to me is the excitement of the work and the hard labour itself. If we are condemned to roll a stone uphill forever, the only choice would be to roll the stone uphill and enjoy it.

Bibliography

[1] Adams, W.S. 1915, Pub. Astron. Soc. Pac. 27, 236.

[2] Ambartsumyan, V.A. and Saakyan, G.S. 1960, Astron. Zhur. 37, 193.

[3] Amundsen, L. and Ostgard, E. 1985, Nucl. Phys. A, 437, 487.

[4] Baade, W. and Zwicky, F. 1934, Phys. Rev. 45, 138.

[5] Baym, G. 1973, Lectures on Quantum Mechanics

[6] Baym, G., Bethe, H.A., and Pethick, C.J. 1971, Nucl. Phys. A 175, 225.

[7] Baym, G., Pethick, C. and Pines, D. 1969, Nature 224, 872.

[8] Baym, G., Pethick, C.J., and Sutherland, P. 1971, Ap. J., 170,299.

[9] Baym, G., Pines, D. 1971, Annals of Physics, 66, 816.

[10] Cameron, A.G.W., 1959, Ap. J., 130, 916.

[11] Chandrasekhar, S., 1938, An introduction to the Study of Stellar Structure, Chicago Press.

[12] Cheng, K.S., Chau, W.Y., Zhang, J.L. and Chau, H.F. 1992, Ap. J., 135, 396.

[13] Clayton, D.B., 1968, Principles of Stellar Evolution and Nucleosynthesis, McGram-Hill.

[14] Dearborn, D.S., Shramnn, D.N., and Steigman, G. 1986 Phys. Rev. Lett. 56, 26.

[15] Friedman, B., and Pandharipande, V.R. 1981, Nucl. Phys. A, 361, 502.

[16] Friman, B.L., and Maxwell, O.V. 1979, Ap. J. 232, 541.

[17] Flowers, E. and Itoh, N. 1976, Ap. J., 206, 218.

[18] Glen, G. and Sutherland, P.G. 1980, Ap. J., 239, 671.

[19] Goldreich, P. and Julian, W.H. 1969, Ap. J., 157, 869.

[20] Gold, T. 1968, Nature 218, 731.

[21] Greenstein, G. and Hartke, G.J. 1983, Ap. J. 271, 283.

[22] Halpern, J.P., and Ruderman, M. preprint.

[23] Hamada, T. and Salpeter, E.E. 1961, Ap. J., 134, 683.

[24] Hernquist, L. 1984, Ap. J. Suppl. 56, 325.

[25] Hernquist, L. 1985, Mon. Not. R. Astro. Soc. 213, 311.

[26] Hewlish, A., and Bell, J. 1968, Nature 217,709.

[27] Itoh, N., and Kohyama, K. 1983, Ap. J., 275, 858.

[28] Itoh, N., Kohyama, K., Matsumoto, N., and Seki, M. 1984a, Ap. J., 280, 787.

[29] Itoh, N., Kohyama, K., Matsumoto, N., and Seki, M. 1984b, Ap. J., 285, 304.

[30] Itoh, N., Matsumoto, N., Seki, M., and Kohyama, Y. 1984c, Ap. J., 279, 413.

[31] Iwamoto, N., preprint.

[32] Iwamoto, N., Qin, L., Fukugita, M. and Tsuruta, S. 1995, Phys. Rev. D, 51, 348.

[33] Krauss, L., Moody, J., Wilezek, F. 1984, Phys. Lett. 144B, 391.

[34] Landau, L.D. 1932, Phys. Z. Sowjetunion 1, 285.

[35] Landau, L.D. 1941, Phys. USSR 5, 71.

[36] Landau, L.D. 1947, Phys. USSR 11, 91.

[37] Link, B. and Epstein, R.I. 1995, preprint.

[38] Misner, C.W., Thorne, K.S., and Wheeler, J.A., 1973 Gravitation (San Francisco: Freeman).

[39] Morgan, J.A. 1981, Phys. Lett. 102B, 247.

[40] Morrison, R. and McCammon, D. 1983, Ap. J., 270, 119.

[41] Munakata, H., Kohyma, Y., and Itoh, N. 1985, Ap. J.,277,375.

[42] Negele, J.W. and Vantherin, D. 1972, Phys. Rev. C, 5, 1472.

[43] Nomoto, K., and Tsuruta, S. 1981, Ap. J. (Letters) 250, L19.

[44] Nomoto, K., and Tsuruta, S. 1987, Ap. J., 312, 711.

[45] Ögelman, H., 1994, preprint.

[46] Oppenheimer, J.R., and Volkoff, G.M. 1939, Phys. Rev. 55, 374.

[47] Pandharipande, V.R., and Smith, R.A. 1976, Ap. J., 208, 550.

[48] Patharia, R.K. 1986, Statistical Mechanics, Pergamon, 3rd Edition.

[49] Pavlov, G.G., and Yakovlev, D.G. 1976, Sov. Phys. JETP 43, No.3.

[50] Pechenick, K.R., Ftaclas, C., and Cohen, J.M. 1983, Ap. J., 274, 846.

[51] Qin, L., Tsuruta, S. and Umeda, H. 1995a, in preparation.

[52] Qin, L. and Tsuruta, S. 1995b, in preparation.

[53] Qin, L., Tsuruta, S., Umeda, H. and Nomoto, K. 1995c, in preparation.

[54] Qin, L., Tsuruta, S. and Iwamoto, N 1995d, in preparation.

[55] Qin, L. and Tsuruta, S. 1994, Proceedings of 7th Marcel Grossman (in press).

[56] Raffelt, G.G. 1986, Phys. Rev. D, 33, 897.

[57] Richardson, M.B., Van Horn, H.M., Ratcliff, K.F., and Malone, R.C. 1982, Ap. J., 255, 624.

[58] Shaaf, M.E. 1988, Astron., Astrophys. 205, 335.

[59] Shaaf, M.E. 1990, Astron. Astrophys. 227, 61.

[60] Shapiro, S.L. and Teukolsky, S.A. 1983, Black Holes, White Dwarfs and Neutron Stars, Wiley-Interscience.

[61] Sikirie, P. 1983, Phys. Rev. Lett. 51, 1415.

[62] Slattery, W.L., Doolen, G.D., and Dewitt, H.E. 1982, Phys. Rev. A, 26, 2255.

[63] Smolukowoski, R. and Welch, D. 1970, Phys. Rev. Lett. 24, 119.

[64] Staigman, G. 1986, Phys. Lett. B 176, 33.

[65] Stothers, R.B. 1970, Phys. Rev. Lett. 24, 538.

[66] Sugimoto, D., and Nomoto, K. 1975, Sci. Pap. Coll. Gen. Educ. Univ. Tokyo, 25,109.

[67] Sutherland et al 1976, Phys. Rev. D 13, 2700.

[68] Taktsuka, T. 1972, Progr. Theor. Phys. 48, 1517.

[69] Taktsuka, T. and Tamagaki, R. 1971, Progr. Theor. Phys. 46, 114.

[70] Tsuruta, S. 1964, PhD thesis, Columbia University.

[71] Tsuruta, S. 1974, in IAU Symposium 53, Physics of Dense Matter ed. C. Hansen (Dodrecht, Reidel).

[72] Tsuruta, S. 1975, Space Sci. Rev., 34, 199.

[73] Tsuruta, S. 1979, Phys. Rept. 56,237.

[74] Tsuruta, S., Canuto, V., Lodenquai, J., and Ruderman, M. 1972, Ap. J., 176, 739.

[75] Tsuruta, S. and Qin, L. 1994, Proceedings of 17th Texas Symposium (in press).

[76] Turner, S. 1988, Phys. Rev. Lett. 60, 1797.

[77] Umeda, H., Nomoto, K., Tsuruta, S., Muto, T.,and Tatsumi, T. 1994, Ap. J.,431.

[78] Yakovlev, D.G., and Upin, V.A. 1981, Sov. Astron. Letter 7, 88.

APPENDICES

Appendix A

Coefficients $A_{i,j}$ and $F_{i,j}$ in 1D Calculation

The following are the coefficients used in Equation(2.25) and (2.26).

$$
\begin{aligned}
A_{2k,2k} &= 1, & \text{(A.1)}\\
A_{2k+1,2k+1} &= \\
& 1 + \Delta t e^{2\phi_k} \frac{1}{c_v(T_{2k+1})} \frac{d\epsilon_\nu}{dT} - \Delta t e^{2\phi_k} \frac{\epsilon_\nu(T_{2k+1})}{{c_v}^2} \frac{dc_v}{dT} - \\
& \frac{\Delta t}{4\pi r^2 {c_v}^2} e^{2\phi} \frac{L_{2k+2} e^{2\phi_{k+1}} - L_{2k} e^{2\phi_{2k}}}{R_{k+1} - R_k} \frac{dc_v}{dT}, & \text{(A.2)}\\
A_{2k+1,2k+2} &= \frac{\Delta t}{4\pi r^2 c_v (R_{k+1} - R_k)}, & \text{(A.3)}\\
A_{2k+1,2k} &= -A_{2k+1,2k+2}, & \text{(A.4)}\\
F_{2k+1} &= -\frac{\Delta t}{4\pi r^2 c_v e_k^{2\phi}} \frac{L_{2k+2} e^{2\phi_{k+1}} - L_{2k} e^{2\phi_k}}{R_{k+1} - R_k} \\
& -\Delta t e^{2\phi_k} \frac{\epsilon_\nu}{c_v} - T_{2k+1} + {T_{2k+1}}^{old}, & \text{(A.5)}\\
A_{2k,2k+1} &= \frac{1}{2} \frac{16\sigma}{\kappa\rho T_{2k+1}} \left(\frac{T_{2k+1} + T_{2k-1}}{2}\right)^2 -
\end{aligned}
$$

$$
\begin{aligned}
& \frac{1}{2}\frac{16\sigma}{3\kappa^2\rho}\frac{d\kappa}{dT}(\frac{T_{2k+1}+T_{2k-1}}{2})^3(4\pi {R_k}^2)\frac{T_{2k+1}-T_{2k-1}}{R_{k+1}-R_k}+ \\
& \frac{16\sigma}{3\kappa\rho}(4\pi {R_k}^2)(\frac{T_{2k+1}+T_{2k-1}}{2})^3\frac{1}{R_{k+1}-R_k}, \qquad \text{(A.6)}
\end{aligned}
$$

$$
\begin{aligned}
A_{2k,2k-1} \quad = \quad & \frac{1}{2}\frac{16\sigma}{\kappa\rho T_{2k+1}}(\frac{T_{2k+1}+T_{2k-1}}{2})^2- \\
& \frac{1}{2}\frac{16\sigma}{3\kappa^2\rho}\frac{d\kappa}{dT}(\frac{T_{2k+1}+T_{2k-1}}{2})^3(4\pi {R_k}^2)\frac{T_{2k+1}-T_{2k-1}}{R_{k+1}-R_k}- \\
& \frac{16\sigma}{3\kappa\rho}(4\pi {R_k}^2)(\frac{T_{2k+1}+T_{2k-1}}{2})^3\frac{1}{R_{k+1}-R_k}, \qquad \text{(A.7)}
\end{aligned}
$$

$$
F_{2k} \quad = \quad L_{2k}-\frac{16\sigma}{3\kappa\rho}(4\pi {R_k}^2)(\frac{T_{2k+1}+T_{2k-1}}{2})^3\frac{T_{2k+1}-T_{2k-1}}{R_{2k+2}-R_{2k}}. \qquad \text{(A.8)}
$$

Appendix B

Coefficients Ξ, μ, α and β in 2D Calculation

The following are the coefficients in Equation(3.42), (3.43) and (3.44).

$$\begin{aligned}\Xi &= 1+\frac{\Delta t}{2}\frac{\partial Z_{i,j}}{\partial T}+ \\ &\Delta t\frac{\partial X_{i,j}}{\partial T}\frac{R_{i+1}^2 e^{2\phi(R_{i+1})}F_{ri+1,j}-R_i^2 e^{2\phi(R_i)}F_{ri,j}}{\Delta R}+ \\ &\frac{\Delta t}{2}(\frac{\partial Y_{i+1,j}}{\partial T})\frac{\sin\theta_j F_{\theta i+1,j}-\sin\theta_{j-1}F_{\theta i+1,j-1}}{\Delta\theta} \\ &\frac{\Delta t}{2}(\frac{\partial Y_{i+1,j}}{\partial T})\frac{\sin\theta_j F_{\theta i,j}-\sin\theta_{j-1}F_{\theta i,j-1}}{\Delta\theta}\end{aligned} \tag{B.1}$$

$$\begin{aligned}-\mu &= -\frac{1}{2\Delta R}(\frac{\partial U_{i,j}}{\partial T}+\frac{\partial U_{i+1,j}}{\partial T})T_{i,j}^3 e^{\phi(R_{i+1})}T_{i+1,j} \\ &-\frac{3}{2\Delta R}(U_{i,j}+U_{i+1,j})T_{i,j}^2 e^{\phi(R_{i+1})}T_{i+1,j} \\ &+\frac{1}{2\Delta R}(\frac{\partial U_{i,j}}{\partial T}+\frac{\partial U_{i+1,j}}{\partial T})T_{i,j}^4 e^{\phi(R_i)} \\ &+\frac{2}{\Delta R}(U_{i,j}+U_{i+1,j})T_{i,j}^3 e^{\phi(R_i)} \\ &-\frac{1}{2\Delta\theta}(\frac{\partial V_{i,j}}{\partial T}+\frac{\partial V_{i+1,j}}{\partial T})T_{i,j}^3 e^{\phi(R_i)}T_{i,j+1}\end{aligned}$$

$$
\begin{aligned}
&-\frac{3}{2\Delta\theta}(V_{i,j}+V_{i+1,j})T_{i,j}^{2}e^{\phi(R_i)}T_{i,j+1} \\
&+\frac{1}{2\Delta\theta}(\frac{\partial V_{i,j}}{\partial T}+\frac{\partial V_{i+1,j}}{\partial T})T_{i,j}^{4}e^{\phi(R_i)} \\
&+\frac{2}{\Delta\theta}(V_{i,j}+V_{i+1,j})T_{i,j}^{3}e^{\phi(R_i)},
\end{aligned} \tag{B.2}
$$

$$
\begin{aligned}
-\alpha \;=\; &-\frac{1}{4}(\frac{\partial Q_{i,j}}{\partial T}+\frac{\partial Q_{i+1,j}}{\partial T})(\frac{T_{i,j}+T_{i-1,j}}{2})^{3}\frac{e^{\phi(R_{i+1})}}{\Delta R}T_{i,j} \\
&-\frac{3}{4}(Q_{i,j}+Q_{i+1,j})(\frac{T_{i,j}+T_{i-1,j}}{2})^{2}\frac{e^{\phi(R_{i+1})}}{\Delta R}T_{i,j} \\
&+\frac{1}{2}(Q_{i,j}+Q_{i+1,j})(\frac{T_{i,j}+T_{i-1,j}}{2})^{3}\frac{e^{\phi(R_i)}}{\Delta R} \\
&+\frac{1}{4}(\frac{\partial Q_{i,j}}{\partial T}+\frac{\partial Q_{i+1,j}}{\partial T}(\frac{T_{i,j}+T_{i-1,j}}{2})^{3}\frac{e^{\phi(R_{i+1})}}{\Delta R}T_{i-1,j} \\
&+\frac{3}{4}(Q_{i,j}+Q_{i+1,j})(\frac{T_{i,j}+T_{i-1,j}}{2})^{2}\frac{e^{\phi(R_{i+1})}}{\Delta R}T_{i-1,j} \\
&-\frac{1}{8\Delta\theta}(\frac{\partial W_{i,j}}{\partial T}+\frac{\partial W_{i+1,j}}{\partial T})(\frac{T_{i,j}+T_{i-1,j}}{2})^{3}e^{\phi(R_{i+1})}T_{i,j+1} \\
&-\frac{3}{8\Delta\theta}(W_{i,j}+W_{i+1,j})(\frac{T_{i,j}+T_{i-1,j}}{2})^{2}e^{\phi(R_{i+1})}T_{i,j+1} \\
&+\frac{1}{8\Delta\theta}(\frac{\partial W_{i,j}}{\partial T}+\frac{\partial W_{i+1,j}}{\partial T})(\frac{T_{i,j}+T_{i-1,j}}{2})^{3}e^{\phi(R_{i+1})}T_{i,j-1} \\
&+\frac{3}{8\Delta\theta}(W_{i,j}+W_{i+1,j})(\frac{T_{i,j}+T_{i-1,j}}{2})^{2}e^{\phi(R_{i+1})}T_{i,j-1},
\end{aligned} \tag{B.3}
$$

and

$$
-\beta = -\alpha - 2 + \frac{1}{2}(Q_{i,j}+Q_{i+1,j})(\frac{T_{i,j}+T_{i-1,j}}{2})^{3}\frac{e^{\phi(R_i)}}{\Delta R} \tag{B.4}
$$

Appendix C

Matrix Inversion Code in 2D Calculation

Here we include the subroutines we construct for matrix inversions in 2D calculations. The AD matrix refers to submatrices 1, 4 , 7, while ATU matrix refers to submatrices 2 and 5 and ATL submatrices 3 and 6 (see Equation(3.47)). The elements in the AD matrix have a form that looks like

$$ad(i,j,k). \tag{C.1}$$

The symbol i indicates the row inside a block matrix, which ranges from 1 to 3×150, j indicates how far away the element is from the diagonal. It ranges from -2 to 2. For example, if the middle index is 0, that means the element is the diagonal element. If it is -1, then it is the one next to the diagonal element at left. If it is 2, then it is one element away from the diagonal element at right. The letter k indicates the column of the block matrix. Same indexing structures applies to ATU and ATL.

```
subroutine dfdt(n,nme)
implicit real*8(a-h,o-z)
```

```
common/b/b(600,3)
common/lu/rl(600,-6:6,2,3),ru(600,-6:6,2,3)
common/ft/x(600,3)
dimension y(600,3)
y(1,1) = b(1,1)/rl(1,0,1,1)
do j =1,n
do i = 1,3*nme+2
if(i.eq.1.and.j.eq.1) go to 8
jj = 2*n
if(i-1.lt.2*n) jj = i-1
jj = -jj
jk=2*n
if(3*nme+2-i.lt.2*n) jk = 3*nme+2-i
y(i,j) = b(i,j)
do l = jj,-1
y(i,j) = y(i,j) -rl(i,l,1,j)*y(i+l,j)
enddo
if(j.eq.1) go to 8
do l = jj,jk
y(i,j) = y(i,j) -rl(i,l,2,j)*y(i+l,j-1)
enddo
8 continue
enddo
enddo
x(3*nme+2,n) = y(3*nme+2,n)/ru(3*nme+2,0,1,n)
do j = n, 1, -1
do i = 3*nme+2, 1, -1
```

```
if(i.eq.3*nme+2.and.j.eq.n) go to 17
jj = 2*n
if(i-1.lt.jj) jj = i-1
jj = -jj
jk = 2*n
if(3*nme+2-i.lt.jk) jk = 3*nme+2-i
x(i,j) = y(i,j)
do l = 1,jk
x(i,j) = x(i,j) - ru(i,l,1,j)*x(i+l,j)
enddo
if(j.eq.n) go to 16
do l = jj,jk
x(i,j) = x(i,j) -ru(i,l,2,j)*x(i+l,j+1)
enddo
16 x(i,j) = x(i,j)/ru(i,0,1,j)
17 continue
enddo
enddo
return
end
subroutine inver(n,nme)
implicit real*8(a-h,o-z)
common/matrix/a(600,-6:6,3) atl(600,-6:6,3),atu(600,-6:6,3)
common/lu/rl(600,-6:6,2,3),ru(600,-6:6,2,3)
do j =1,n
do k = -2*n,2*n
do i =1,600
```

```
rl(i,k,1,j) = 0.
rl(i,k,2,j) = 0.
ru(i,k,1,j) = 0.
ru(i,k,2,j) = 0.
enddo
enddo
enddo
do j = 1,n
call lude(n,j,nme)
if(j.eq.n) then
c**********solve matrix ru(,,2,j)***********
call solve(n,j,2,nme)
c**********solve matrix rl(,,2,j)***********
call solve(n,j+1,1,nme)
endif
enddo
return
end
subroutine solve(n,k0,index,nme)
implicit real*8(a-h,o-z)
common/matrix/a(600,-6:6,3),atl(600,-6:6,3),atu(600,-6:6,3)
common/lu/rl(600,-6:6,2,3),ru(600,-6:6,2,3)
if(index.eq.2) then
do j=0,2*n
ru(1,j,2,k0) = atu(1,j,k0)/rl(1,0,1,k0)
enddo
do i = 2,3*nm3+2
```

```
jj = 2*n
if(i-1.lt.2*n) jj = i-1
jj = -jj
jk = 2*n
if (3*nme+2-i.lt.2*n) jk = 3*nme+2-i
do j = jj,jk
ru(i,j,2,k0) = atu(i,j,k0)
do 29 l = jj,-1
if(abs(j-l).gt.2*n.or.j-l.gt.3*nme+2-i-l.or.j-l.lt.1-i-l)
go to 29
ru(i,j,k0) = ru(i,j,2,k0)/rl(i,0,1,k0)
29 continue
ru(i,j,2,k0) = ru(i,j,2,k0)/rl(i,0,1,k0)
enddo
enddo
endif
if (index,eq,1) then
do i = 1,3*nme+2
jj = 2*n
if(i-1.lt.jj) jj = i-1
jj = -jj
jk = 2*n
if(3*nme+2-i.lt.jk) jk = 3*nme+2-i
do j = jj,jk
rl(i,j,2,k0) = atl(i,j,k0)
do 23 l = jj,j-1
if(j-l.gt.2*n.or.j-l.gt.3*nme+2-i-l) go to 23
```

```
rl(i,j,2,k0) = rl(i,j,2,k0) - rl(i,l,2,k0)*ru(l+i,j-l,1,k0-1)
23 continue
rl(i,j,2,k0) = rl(i,j,2,k0)/ru(j+i,0,1,k0-1)
enddo
enddo
endif
return
end
subroutine lude(n,k0,nme)
implicit real*8(a-h,o-z)
common/matrix/a(600,-6:6,3),atl(600,-6:6,3),atu(600,-6:6,3)
common/lu/rl(600,-6:6,2,3),ru(600,-6:6,2,3)
dimension s(600,-6:6)
if(k0.ne.1) then
do i = 1,3*nme+2
jj = 2*n
if(i-1.lt.2*n) jj = i-1
jj = -jj
jk = 2*n
if(3*nme+2-i.lt.2*n) jk = 3*nme+2-i
do j = jj,jk
s(i,j) = 0.
do k = jj,jk
if( abs(j-k).gt.2*n.or.j-k.lt.1-i-k.or.j-k.gt.3*nme+2-i-k) go to 7
s(i,j) = s(i,j) + rl(i,k,2,k0)*ru(k+i,j-k,2,k0-1)
7 enddo
enddo
```

```
endif
do 11 i = 1,3*nme+2
rl(i,0,1,k0) = 1.
jk = 2*n
if(3*nme+2-i.lt.2*n) jk = 3*nme+2-i
jj = 2*n
if(i-1.lt.2*n) jj = i-1
jj =-jj
do j = jj,-1
h= a(i,j,k0)
if(k0.ne.1) h = a(i,j,k0) -s(i,j)
rl(i,j,1,k0) = h
do 37 l = jj,j-1
if(j-l.gt.2*n.or.j-l.gt.3*nme+2-i-l) go to 37
rl(i,j,1,k0) = rl(i,j,1,k0) -rl(i,l,1,k0)*ru(l+i,j-l,1,k0)
37 continue
rl(i,j,1,k0) = rl(i,j,1,k0)/ru(i+j,0,1,k0)
enddo
do j = 0,jk
h = a(i,j,k0)
if(k0.ne.1) h = a(i,j,k0) - s(i,j)
ru(i,j,1,k0) = h
do 34 l = jj,-1
if(j-l.gt.2*n.or.j-l.gt.3*nme+2-i-l) go to 34
ru(i,j,1,k0) = ru(i,j,1,k0) - rl(i,l,1,k0)*ru(i+l,j-l,1,k0)
34 continue
enddo
```

```
11 continue
return
end
```

Appendix D

Derivation of Axion Emissivity ϵ_{ann}

Here we explain how to calculate the axion emissivity ϵ_{ann}. Using non-relativistic Feynman rules, we can write down the expression for the matrix element $M^{(a)}$.

$$\begin{aligned} -iM^{(a)} &= -g_{ann}(f/m_\pi)^2 2m \frac{1}{|\vec{K}|^2 + m_\pi^2} \\ & (1/q^\circ) W_3^+ (\vec{K} \cdot \vec{\sigma}) W_1 W_4^+ (\vec{q} \cdot \vec{\sigma})(\vec{K} \cdot \vec{\sigma}) W_2, \end{aligned} \tag{D.1}$$

where W_i's are non-relativistic two-component Pauli spinors for neutrons.

Similarly, for diagram(b), we have:

$$\begin{aligned} -iM^{(b)} &= g_{ann}(f/m_\pi)^2 2m \frac{1}{|\vec{K}|^2 + m_\pi^2} \\ & (1/q^\circ) W_3^+ (\vec{K} \cdot \vec{\sigma}) W_1 W_4^+ (\vec{K} \cdot \vec{\sigma})(\vec{q} \cdot \vec{\sigma}) W_2. \end{aligned} \tag{D.2}$$

$$\tag{D.3}$$

Notice the symmetry between diagrams (c) and (a), and then the matrix for diagram(c) can be easily obtained from the matrix for diagram (a), if we only interchange the particle label 1 to 2, and 3 to 4, and also replace $\vec{k} \equiv p_1 - p_3$ with $-\vec{k}' \equiv p_2 - p_4 \equiv -\vec{k}$. The matrix for diagram (d) can be obtained from the matrix for diagram (b), doing the same thing. Hence:

$$M^{(c)} = M^{(a)}(2,1,4,3,-k), \tag{D.4}$$

$$M^{(d)} = M^{(b)}(2,1,4,3,-k). \tag{D.5}$$

The matrices for the diagrams in Group (α') are quite similar to the matrices for the diagrams in Group (α) from the considerations of symmetry. We only need to interchange labels 3 and 4, and replace $\vec{k} = p_1 - p_3$ with $\vec{l} = p_1 - p_4$ to obtain the matrix for the diagram in Group (α') from the matrices for the diagrams in Group (α).

$$M^{(e)} = -M^{(a)}(1,2,4,3,l), \tag{D.6}$$

$$M^{(f)} = -M^{(b)}(1,2,4,3,l), \tag{D.7}$$

$$M^{(g)} = -M^{(c)}(1,2,4,3,l), \tag{D.8}$$

$$M^{(h)} = -M^{(d)}(1,2,4,3,l). \tag{D.9}$$

The minus sign is due to the antisymmetric wavefunctions of the fermions.

The summation of equation(5.10) involves 64 terms. Fortunately, there are some symmetries which make life simpler. When we add $M^{(a)}$, $M^{(b)}$, $M^{(c)}$, $M^{(d)}$ together, we get

$$\begin{aligned}
&-i(M^{(a)} + M^{(b)} + M^{(c)} + M^{(d)}) = \\
&\quad -4im_N(f/m_\pi)^2(g_{ann}/q^\circ)\frac{1}{|\vec{k}|^2 + m_\pi^2} \\
&\quad [\, W_3^+(\vec{K} \cdot \vec{\sigma})W_1 W_4^+(\vec{q} \times \vec{k}) \cdot \vec{\sigma} W_2 + \\
&\quad W_3^+(\vec{q} \times \vec{k}) \cdot \vec{\sigma} W_1 W_4^+(\vec{k} \cdot \vec{\sigma}) W_2].
\end{aligned} \tag{D.10}$$

Adding $M^{(e)} + M^{(f)} + M^{(g)} + M^{(h)}$ yields:

$$-i(M^{(e)} + M^{(f)} + M^{(g)} + M^{(h)}) =$$

$$-4im_N(f/m_\pi)^2(g_{ann}/q^\circ)\frac{1}{|\vec{l}|^2+m_\pi^2}$$
$$[\,W_4^+(\vec{l}\cdot\vec{\sigma})W_1W_3^+(\vec{q}\times\vec{l})\cdot\vec{\sigma}W_2+$$
$$W_4^+(\vec{q}\times\vec{l})\cdot\vec{\sigma}W_1W_3^+(\vec{l}\cdot\vec{\sigma})W_2]. \tag{D.11}$$

To calculate $|\ M(nn)\ |^2$, we need to add Equation(D.10) and Equation(D.11), and then square the sum. The final result is

$$\begin{aligned}
|\ M^{(1)}(nn)\ |^2\ (\vec{q}) &= \sum_{\sigma_1\sigma_2\sigma_3\sigma_4} |\ M^{(a)}+\cdots+M^{(h)}\ |^2 \\
&= 128m_N^2(f/m_\pi)^4g_{ann}^2[1/(q^\circ)^2]\cdot \\
&\quad [(\vec{q}\times\vec{k})^2\frac{|\vec{k}|^2}{(|\vec{k}|^2+m_\pi^2)^2}+(\vec{q}\times\vec{l})^2\frac{|\vec{l}|^2}{(|\vec{l}|^2+m_\pi^2)^2}+ \\
&\quad 2([\vec{q}\cdot(\vec{k}\times\vec{l})]^2-(\vec{q})^2(\vec{k}\cdot\vec{l})^2+(\vec{q}\cdot\vec{k})(\vec{q}\cdot\vec{l})(\vec{k}\cdot\vec{l}))\cdot \\
&\quad [\frac{1}{(|\vec{k}|^2+m_\pi^2)(|\vec{l}|^2+m_\pi^2)}]\,]
\end{aligned} \tag{D.12}$$

Averaging over the directions of the axion's momentum $\vec{q}$ gives:

$$\begin{aligned}
\frac{1}{4\pi}\int |\ M^{(1)}(nn)\ |^2\, d\Omega &= \frac{256}{3}m_N^2(\frac{f}{m_\pi})^4g_{ann}^2 \\
&\quad [\frac{|\vec{k}|^4}{(|\vec{k}|^2+m_\pi^2)^2}+\frac{|\vec{l}|^4}{(|\vec{l}|^2+m_\pi^2)^2}+ \\
&\quad \frac{(\vec{k}\times\vec{l})^2}{(|\vec{k}|^2+m_\pi^2)(|\vec{l}|^2+m_\pi^2)}\,].
\end{aligned} \tag{D.13}$$

In terms of the matrix elements, the emission rate of axions can be written as:

$$\begin{aligned}
&\epsilon_{ann} = \\
&\frac{1}{4V}\int\frac{d^3p_1}{8\pi^3}\int\frac{d^3p_2}{8\pi^3}\int\frac{d^3p_3}{8\pi^3}\int\frac{d^3p_4}{8\pi^3}\int\frac{d^3p_5}{8\pi^3} \\
&E_5n(p_1)n(p_2)[1-n(p_3)][1-n(p_4)] \\
&V(2\pi)^4\delta(p_3+p_4+p_5-p_1-p_2)\ |\ M^{(1)}\ |^2 \\
&\frac{1}{2E_1V}\frac{1}{2E_2V}\frac{1}{2E_3V}\frac{1}{2E_4V}\frac{1}{2E_5V}
\end{aligned} \tag{D.14}$$

where V is the normalization volume, and $n(p_i)$ is the distribution function for neutrons. Since neutrons inside the cores of the neutron stars are degenerate but non-relativistic, $d^3p_i = d\Omega_i m_n^*(n) p_i dE_i$, and then:

$$\begin{aligned}
\epsilon_{ann} &= \frac{2}{3}\frac{1}{(2\pi)^{11}}(m_n^*)^2 p_F^4(n)(\frac{f}{m_\pi})^4 g_{ann}^2 \\
&\int d\Omega_1 \int d\Omega_2 \int d\Omega_3 \int d\Omega_4 \int d\Omega_5 \delta(p_3+p_4+p_5-p_1-p_2) \\
&\cdot[\frac{|\vec{k}|^4}{(|\vec{k}|^2+m_\pi^2)^2}+\frac{|\vec{l}|^4}{(|\vec{l}|^2+m_\pi^2)^2}+\frac{|\vec{k}|^2|\vec{l}|^2}{(|\vec{k}|^2+m_\pi^2)(|\vec{l}|^2+m_\pi^2)}]\cdot \\
&\int_0^\infty dE_1 \int_0^\infty dE_2 \int_0^\infty dE_3 \int_0^\infty dE_4 \int_0^\infty dE_5 \delta(E_3+E_4+E_5-E_1-E_2) \\
&E_5^2 n(E_1) n(E_2)(1-n(E_3))(1-n(E_4)), \qquad \text{(D.15)}
\end{aligned}$$

with

$$n(E_i) = \frac{1}{1+\exp(E_i-\mu_i)/kT}. \qquad \text{(D.16)}$$

Define :

$$\begin{aligned}
x_i &= (E_i-\mu_i)/k_BT \quad \mathrm{i} = 1,2, \\
x_i &= -(E_i-\mu_i)/k_BT \quad \mathrm{i} = 3,4, \\
y_5 &= E_5/k_BT.
\end{aligned} \qquad \text{(D.17)}$$

Then the integral over the energy part becomes:

$$\begin{aligned}
&\int_0^\infty dE_1 \int_0^\infty dE_2 \int_0^\infty dE_3 \int_0^\infty dE_4 \int_0^\infty dE_5 \delta(E_3+E_4+E_5-E_1-E_2) \\
&n(E_1)n(E_2)(1-n(E_3))(1-n(E_4)) = \\
&\int_{-\frac{\mu_1}{k_BT}}^\infty dx_1 \int_{-\frac{\mu_2}{k_BT}}^\infty dx_2 \int_{-\infty}^{\frac{\mu_3}{k_BT}} dx_3 \int_{-\infty}^{\frac{\mu_4}{k_BT}} dx_4 \int_0^\infty dy_5 y_5^2 \\
&\delta(\mu_3 - k_BTx_3 + \mu_4 - k_BTx_4 + k_Ty_5 - \mu_1 - k_BTx_1 - \mu_2 - k_BTx_2) \\
&\frac{1}{1+e^{x_1}}\frac{1}{1+e^{x_2}}(1-\frac{1}{1+e^{-x_3}})(1-\frac{1}{1+e^{-x_4}}). \qquad \text{(D.18)}
\end{aligned}$$

With $1-(1/1+e^{-x_3}) = 1/1+e^{x_3}$ and $\mu_3 = \mu_4 = \mu_1 = \mu_2$, the above integral becomes:

$$\text{The integral} = (k_BT)^7 \int_0^\infty y_5^2 dy_5 \int_0^\infty \frac{1}{1+e^{x_1}}dx_1 \int_0^\infty \frac{1}{1+e^{x_2}}dx_2$$

$$\begin{aligned}
&\int_0^\infty \frac{1}{1+e^{x_3}}dx_3 \int_0^\infty \frac{1}{1+e^{x_4}}dx_4\delta(k_BT(y_5-\sum_{i=1}^{4}x_i) \\
= &\ (k_BT)^6\int_0^\infty dy_5 y_5^2(1/6)y_5\frac{y_5^2+4\pi^2}{e^{y_5}-1} \\
= &\ \frac{62\pi^6}{945}(k_BT)^6. \qquad \text{(D.19)}
\end{aligned}$$

The integral over the angular part can be performed as follows. First express the integral with three terms.

$$\begin{aligned}
&\int d\Omega_1\int d\Omega_2\int d\Omega_3\int d\Omega_4\int d\Omega_5\delta(p_3+p_4+p_5-p_1-p_2)\cdot \\
&\{\frac{|\vec{k}|^4}{(|\vec{k}|^2+m_\pi^2)^2}+\frac{|\vec{l}|^4}{(|\vec{l}|^2+m_\pi^2)^2}+\frac{|\vec{k}|^2|\vec{l}|^2}{(|\vec{k}|^2+m_\pi^2)(|\vec{l}|^2+m_\pi^2)}\} \\
&= A_1+A_2+A_3, \qquad \text{(D.20)}
\end{aligned}$$

with

$$\begin{aligned}
A_1 = &\int d\Omega_1\int d\Omega_2\int d\Omega_3\int d\Omega_4\int d\Omega_5 \\
&\delta(p_3+p_4+p_5-p_1-p_2)\cdot\frac{|\vec{k}|^4}{(|\vec{k}|^2+m_\pi^2)^2}, \qquad \text{(D.21)}
\end{aligned}$$

$$\begin{aligned}
A_2 = &\int d\Omega_1\int d\Omega_2\int d\Omega_3\int d\Omega_4\int d\Omega_5 \\
&\delta(p_3+p_4+p_5-p_1-p_2)\cdot\frac{|\vec{l}|^4}{(|\vec{l}|^2+m_\pi^2)^2}, \qquad \text{(D.22)}
\end{aligned}$$

and

$$\begin{aligned}
A_3 = & \\
&(\frac{f}{m_\pi})^4 g_{ann}^2\int d\Omega_1\int d\Omega_2\int d\Omega_3\int d\Omega_4\int d\Omega_5 \\
&\delta(p_3+p_4+p_5-p_1-p_2)\cdot\frac{|\vec{k}|^2|\vec{l}|^2}{(|\vec{k}|^2+m_\pi^2)(|\vec{l}|^2+m_\pi^2)}. \qquad \text{(D.23)}
\end{aligned}$$

Begin with A_1. $\int d\Omega_3 = 2\pi \int d\cos\theta_B$, and

$$\int_{-1}^{+1} d\cos\theta_B = \int_0^{2p_F(n)} \frac{|\vec{k}|\, d|\vec{k}|}{|\vec{p_1}| \cdot |\vec{p_3}|}. \tag{D.24}$$

Since

$$|\vec{p_1}| \approx |\vec{p_3}| \approx p_F(n), \tag{D.25}$$

so

$$\int_{-1}^{+1} d\cos\theta_B = \int_0^{2p_F(n)} \frac{|\vec{k}|\, d|\vec{k}|}{p_F(n)^2}. \tag{D.26}$$

Substituting Equation(D.26) back into the integral for A_1 yields:

$$\begin{aligned} A_1 &= \int\int\int\int d\Omega_1 d\Omega_2 d\Omega_4 d\Omega_5 \int d\cos\theta_B 2\pi \\ &\quad \delta(p_3 + p_4 + p_5 - p_1 - p_2) \frac{|\vec{k}|^4}{(|\vec{k}|^2 + m_\pi^2)^2} \\ &= \int\int\int d\Omega_1 d\Omega_2 d\Omega_4 \int \frac{2\pi |\vec{k}|\, d|\vec{k}|}{|p_F(n)^2|} \int d\Omega_5 \\ &\quad \delta(p_3 + p_4 + p_5 - p_1 - p_2) \frac{|\vec{k}|^4}{(|\vec{k}|^2 + m_\pi^2)^2}. \end{aligned} \tag{D.27}$$

Since p_5 is very small compared with the momenta of neutrons, $\delta(p_3 + p_4 + p_5 - p_1 - p_2) \approx \delta(p_3 + p_4 - p_1 - p_2)$, and

$$\delta(p_3 + p_4 - p_1 - p_2) \approx \delta(|p_4| - |\vec{k} + \vec{p_2}|)/|p_4|^2\, \delta(\Omega_4 - \Omega_2). \tag{D.28}$$

Carrying out the integral, we get:

$$A_1 = \frac{128\pi^4}{p_F^3(n)} F(\frac{m_\pi c}{2p_F(n)}), \tag{D.29}$$

with

$$F(x) = 1 - (3/2)x \arctan(1/x) + x^2/2(1 + x^2). \tag{D.30}$$

F(x) is shown in Fig(5.2). Similarly, we find

$$A_2 = A_3 = A_1 = \frac{128\pi^4}{p_F^3(n)} F(\frac{m_\pi c}{2p_F(n)}). \tag{D.31}$$

Finally, we can write down the expression for ϵ_{ann} as:

$$\epsilon_{ann} = \frac{31}{2780\pi} \frac{g_{ann}^2}{\hbar c} (\frac{f}{m_\pi})^4 [m_n^{*2} p_F(n)/\hbar^4 c^6] F(\frac{m_\pi c}{2p_F(n)}) (k_B T)^6. \tag{D.32}$$